batteries

Special Issue Reprint

Towards a Smarter Battery Management System

3rd Edition

Edited by
Zhi Cao, Chris Mi and Naser Vosoughi Kurdkandi

mdpi.com/journal/batteries

MDPI

Towards a Smarter Battery Management System: 3rd Edition

Towards a Smarter Battery Management System: 3rd Edition

Guest Editors

Zhi Cao
Chris Mi
Naser Vosoughi Kurdkandi

MDPI

Basel • Beijing • Wuhan • Barcelona • Belgrade • Novi Sad • Cluj • Manchester

Guest Editors

Zhi Cao
Department of Electrical and Computer Engineering
San Diego State University
San Diego, CA
USA

Chris Mi
Department of Electrical and Computer Engineering
San Diego State University
San Diego, CA
USA

Naser Vosoughi Kurdkandi
Department of Electrical and Computer Engineering
San Diego State University
San Diego, CA
USA

Editorial Office
MDPI AG
Grosspeteranlage 5
4052 Basel, Switzerland

This is a reprint of the Special Issue, published open access by the journal *Batteries* (ISSN 2313-0105), freely accessible at: https://www.mdpi.com/journal/batteries/special_issues/HA19T676GN.

For citation purposes, cite each article independently as indicated on the article page online and as indicated below:

Lastname, A.A.; Lastname, B.B. Article Title. *Journal Name* **Year**, *Volume Number*, Page Range.

ISBN 978-3-7258-8989-1 (Hbk)
ISBN 978-3-7258-8990-7 (PDF)
https://doi.org/10.3390/books978-3-7258-8990-7

© 2026 by the authors. Articles in this reprint are Open Access and distributed under the Creative Commons Attribution (CC BY) license. The reprint as a whole is distributed by MDPI under the terms and conditions of the Creative Commons Attribution-NonCommercial-NoDerivs (CC BY-NC-ND) license (https://creativecommons.org/licenses/by-nc-nd/4.0/).

Contents

Marek Bobček, Róbert Štefko, Július Šimčák and Zsolt Čonka
A Novel Approach to Day-Ahead Forecasting of Battery Discharge Profiles in Grid Applications Using Historical Daily
Reprinted from: *Batteries* **2025**, *11*, 370, https://doi.org/10.3390/batteries11100370 . . . . . **1**

Zhi Cao, Naser Vosoughi Kurdkandi and Chris Mi
Techno-Economic and Environmental Viability of Second-Life EV Batteries in Commercial Buildings: An Analysis Using Real-World Data
Reprinted from: *Batteries* **2025**, *11*, 412, https://doi.org/10.3390/batteries11110412 . . . . . **11**

Francesco Maria Tiburtini, Francesco Lo Franco and Mattia Ricco
Multi-Objective Sizing Method for PV-BESS Integration with EV ChargingStations and Analysis Across Different Parking Scenarios
Reprinted from: *Batteries* **2025**, *11*, 422, https://doi.org/10.3390/batteries11110422 . . . . . **26**

Maharani Putri, Dat Nguyen Khanh, Kun-Che Ho, Shun-Chung Wang and Yi-Hua Liu
Hybrid Deep Learning Approach for Fractional-Order Model Parameter Identification of Lithium-Ion Batteries
Reprinted from: *Batteries* **2025**, *11*, 452, https://doi.org/10.3390/batteries11120452 . . . . . **53**

Mattia Ribera, Emanuele Fedele, Pasquale Franzese, Luigi Piegari, Lorenzo Codecasa and DiegoIannuzzi
State of Health Estimation of Lithium Cobalt Oxide Batteries Based on ARX Identification Across Different Temperatures
Reprinted from: *Batteries* **2026**, *12*, 2, https://doi.org/10.3390/batteries12010002 . . . . . **78**

Liye Wang, Jinlong Wu, Chunxiao Ma, Xianzhong Sun, Lifang Wang and Chenglin Liao
Coupling Model and Early-Stage Internal Short Circuits Fault Diagnosis for Gel Electrolyte Lithium-Ion Batteries
Reprinted from: *Batteries* **2026**, *12*, 45, https://doi.org/10.3390/batteries12020045 . . . . . **98**

Sang Hoon Park and Seon Hyeog Kim
Physics-Informed Transformer Using Degradation-Sensitive Indicators for Long-Term State-of-Health Estimation of Lithium-Ion Batteries
Reprinted from: *Batteries* **2026**, *12*, 48, https://doi.org/10.3390/batteries12020048 . . . . . **122**

Moayad Albakri and Ahmed Darwish
A Review of Modelling, State of Charge Estimation and Management Methods of EV Lithium-Ion Batteries
Reprinted from: *Batteries* **2026**, *12*, 92, https://doi.org/10.3390/batteries12030092 . . . . . **140**

Xuguang Zhang, Michael C. Halbig, Mrityunjay Singh, Amjad Almansour and Yi Zheng
Geometry-Regulated Thermal Performance of Sedimentation-Stable MicroPCM Composite Capsules for Battery Thermal Management Systems Fabricated via 3D Printing
Reprinted from: *Batteries* **2026**, *12*, 144, https://doi.org/10.3390/batteries12040144 . . . . . **172**

Aleksandar Dimovski, Matteo Spiller, Mershad Pakjoo, Giulio Cantoni, Giacomo Gorni, Luigi Piegari and Marco Merlo
Data-Driven Modeling of Auxiliary Consumption in Utility-Scale BESS
Reprinted from: *Batteries* **2026**, *12*, 288, https://doi.org/10.3390/batteries12080288 . . . . . **187**

batteries

MDPI

Article

A Novel Approach to Day-Ahead Forecasting of Battery Discharge Profiles in Grid Applications Using Historical Daily

Marek Bobček, Róbert Štefko, Július Šimčák * and Zsolt Čonka

Faculty of Electrical Engineering and Informatics, Technical University of Košice, 040 01 Košice, Slovakia; marek.bobcek@tuke.sk (M.B.); robert.stefko@tuke.sk (R.Š.); zsolt.conka@tuke.sk (Z.Č.)
* Correspondence: julius.simcak@tuke.sk

Abstract

This paper presents a day-ahead forecasting approach for discharge profiles of a 0.5 MW battery energy storage system connected to the power grid, utilizing historical daily discharge profiles collected over one year to capture key operational patterns and variability. Two forecasting techniques are employed: a Kalman filter for dynamic state estimation and Holt's exponential smoothing method enhanced with adaptive alpha to capture trend changes more responsively. These methods are applied to generate next-day discharge forecasts, aiming to support better battery scheduling, improve grid interaction, and enhance overall energy management. The accuracy and robustness of the forecasts are evaluated against real operational data. The results confirm that combining model-based and statistical techniques offers a reliable and flexible solution for short-term battery discharge prediction in real-world grid applications.

Keywords: battery; prediction; power grid; consumption energy; Kalman filter; Holt's exponential smoothing

1. Introduction

Battery energy storage systems (BESSs) play a critical role in modern power grids by providing flexibility, supporting renewable integration, and enhancing grid stability. As electricity generation from intermittent sources like solar and wind continues to grow, the need for dynamic storage solutions becomes increasingly important. BESS can shift energy temporally, mitigate peak demand, and offer ancillary services such as frequency regulation or load balancing [1]. However, the efficient operation of such systems depends heavily on accurate forecasting of their charge and discharge behaviour. In grid-connected scenarios, day-ahead prediction of battery activity is essential for effective scheduling, market participation, and ensuring that storage assets are used optimally. This paper addresses the challenge of day-ahead discharge forecasting by employing historical operational data and adaptive modeling techniques [2]. Accurate day-ahead forecasting of battery discharge is vital for maximizing the economic and operational benefits of energy storage systems within the grid. Precise predictions enable better scheduling of charging and discharging cycles, allowing operators to respond effectively to market price signals, optimize participation in energy and ancillary service markets, and avoid penalties associated with forecast errors. Moreover, accurate forecasts help ensure system reliability by allowing grid operators to plan for demand fluctuations and maintain reserve margins [3,4]. Inaccurate or overly conservative forecasts can lead to suboptimal use of storage capacity, missed

revenue opportunities, or even contribute to grid instability. By improving forecast precision, battery operators can enhance system responsiveness, reduce operational costs, and increase the overall efficiency and value of BESS in grid-connected environments [5–7]. This study's primary contribution is not a new forecasting algorithm, but rather a systematic evaluation of two well-established and practically relevant methods under different grid conditions. Unlike previous research that often considers either high-accuracy machine learning models or traditional statistical approaches in isolation, this work emphasizes the balance between accuracy, robustness, and computational efficiency, offering practical insights for real-world BESS operation.

2. Data Description and Preprocessing

The battery system analysed in this study is a grid-connected lithium-ion energy storage unit with a nominal power capacity of 0.5 MW. It is installed at a substation operating at 110 kV, allowing it to interact directly with the high-voltage distribution grid. The system primarily supports local grid stability and optimizes energy flows in response to market and operational signals. The battery is managed through an automated control system that regulates its charging and discharging behaviour based on real-time grid conditions and predefined strategies [8–10]. Over the course of one year, the system's discharge data was recorded at regular intervals, resulting in a comprehensive set of daily discharge profiles. These profiles reflect various operating modes influenced by seasonal demand patterns, grid requirements, and external factors such as energy prices or renewable generation availability. This historical dataset serves as the foundation for developing and validating the forecasting methods presented in this work.

The dataset used in this study consists of daily discharge diagrams representing the battery's power output over 24 h periods, recorded at fixed time intervals. Each diagram captures the dynamic behaviour of the battery in response to grid demands and control signals throughout the day. The raw data, originally sampled at one-minute resolution, was aggregated into 15 min intervals to reduce noise and computational complexity while preserving key operational patterns. Prior to modelling, the data underwent preprocessing steps including outlier removal, handling of missing values, and normalization to ensure consistency across the dataset. Each day was treated as an individual time series, forming a matrix of daily profiles spanning one full year. These prepared diagrams were then used as input for the forecasting models, enabling the system to learn from historical discharge behaviour and make informed day-ahead predictions [11–14].

3. Forecasting Methodology

To accurately predict the day-ahead discharge behaviour of battery energy storage systems (BESS), this study employs two complementary time series forecasting approaches: the Kalman filter and Holt's linear trend method with adaptive smoothing. In the field of time series forecasting, a wide range of methods has been applied, including statistical approaches such as ARIMA and SARIMA, as well as advanced machine learning models like recurrent neural networks (e.g., LSTM, GRU) or hybrid approaches combining state estimation with neural predictors [15,16]. While these methods can achieve high prediction accuracy, they are often computationally demanding, require extensive parameter tuning, and are not always well suited for real-time grid applications where robustness and simplicity are equally important.

Against this background, the Kalman filter and Holt's model were selected for their ability to model dynamic, time-dependent processes while remaining computationally efficient and relatively easy to implement in practice. The Kalman filter is particularly effective in noisy environments, providing recursive state updates and reliable tracking of

system dynamics. Holt's method, extended with an adaptive smoothing parameter, allows for flexible modelling of linear trends and improves responsiveness to abrupt changes in discharge behaviour. By combining these two approaches, this study aims to achieve a balance between stability, adaptability, and practical applicability, offering a lightweight yet effective solution for day-ahead BESS discharge forecasting in real grid conditions.

3.1. Mathematical Formulation of the Kalman Filter

The Kalman filter is a recursive estimation algorithm widely used for real-time tracking and forecasting of dynamic systems. In the context of BESS discharge forecasting, it enables continuous estimation of the system's state—specifically, the battery's capacity or output—by optimally combining prior predictions with noisy measurements. The filter operates in two phases: a prediction step and a correction step, allowing it to adjust to real-world conditions and uncertainties.

Prediction step:

$$\hat{C}_{k|k-1} = \hat{C}_{k-1|k-1} + u_k \tag{1}$$

$$P_{k|k-1} = P_{k-1|k-1} + Q \tag{2}$$

Here, $\hat{C}_{k|k-1}$ is the predicted capacity before measurement, u_k is the known change in capacity (e.g., from a control signal or schedule), and P denotes the covariance of the estimation error [17,18].

Correction step:

$$K_k = \frac{P_{k|k-1}}{P_{k|k-1} + R} \tag{3}$$

$$\hat{C}_{k|k} = \hat{C}_{k|k-1} + K_k \cdot \left(z_k - \hat{C}_{k|k-1}\right) \tag{4}$$

$$P_{k|k} = (1 - K_k) * P_{k|k-1} \tag{5}$$

In this step, z_k is the observed discharge value, R is the measurement noise covariance, Q is the process noise covariance, and K_k is the Kalman gain, which determines how much the prediction is corrected based on new measurements. This method is particularly effective in systems where both the underlying process and the measurements are affected by noise, and it is well suited for adaptive day-ahead forecasting in dynamic environments [17,18].

3.2. Mathematical Formulation of the Holt's Linear Model

Holt's linear trend model is an extension of exponential smoothing that captures both the level and trend components of a time series. To enhance its responsiveness to abrupt changes in discharge behaviour, the model is extended with an adaptive smoothing parameter α_t, which adjusts based on the forecast error [19,20].

Level component:

$$l_t = \alpha * y_t + (1 - \alpha) * (l_{t-1} + b_{t-1}) \tag{6}$$

Trend component:

$$b_t = \beta * (l_t - l_{t-1}) + (1 - \beta) * b_t - 1 \tag{7}$$

Forecast:

$$\hat{y}_{t+1} = l_t + b_t \tag{8}$$

where:

y_t—is the observed discharge value at time t;

l_t—is the estimated level (smoothed capacity);
b_t—is the estimated trend (rate of change);
$\hat{y}_{t+1}$—is the forecast for the next time step.

To make the model adaptive, the smoothing coefficient α_t is dynamically adjusted using a function f based on the current forecast error:

$$\alpha_t = \max(a_{min}, f(|y_t - \hat{y}_t|)) \quad (9)$$

This mechanism increases the sensitivity of the model during periods of high prediction error, enabling quicker adaptation to changing battery discharge patterns [19–24].

4. Evaluation and Results

To evaluate the performance and robustness of the proposed forecasting methods, simulations were conducted under three controlled variability scenarios, reflecting different levels of daily discharge fluctuations. The simulations aimed to represent realistic operational changes in the battery's daily discharge profiles while testing the adaptability and accuracy of the Kalman filter and Holt's adaptive trend model.

4.1. Simulation Setup

The battery system, with a nominal capacity of 0.5 MW, was simulated over a one-year period using historical discharge data, into which artificial day-to-day variability was introduced. Three distinct scenarios were defined to reflect different operating conditions:

- Low Variability (±10 kW): Represents stable grid support with minimal changes in discharge between days.
- Moderate Variability (±50 kW): Simulates moderate fluctuations, possibly driven by seasonal renewable integration or variable load support.
- High Variability (±90 kW): Emulates highly dynamic operational environments such as price-driven arbitrage or response to volatile grid conditions.

Each scenario was constructed by modifying the maximum discharge level of each day by a random value within the defined bounds, relative to the previous day. This approach enabled us to stress-test the forecasting models under different rates of change while maintaining the temporal structure of actual operational data.

4.2. Simulation Results

To visualize and assess the accuracy of the forecasting models, a set of simulation plots was generated for each variability scenario. These figures present a comparison between the actual measured battery discharge and the predicted values produced by the Kalman filter and Holt's adaptive trend model. By focusing on selected time intervals, the plots allow for a detailed inspection of model performance under varying operational conditions. The first scenario illustrates a low-variability case, where daily changes in discharge do not exceed ±10 kW. This baseline scenario serves to evaluate how well each model can capture and replicate stable daily discharge patterns with minimal fluctuations.

Figure 1 shows a typical daily battery discharge profile for a 0.5 MW system, where the power output gradually decreases throughout the day and then recovers. This curve illustrates a standard daily charge–discharge cycle under stable operating conditions with only minor fluctuations between days.

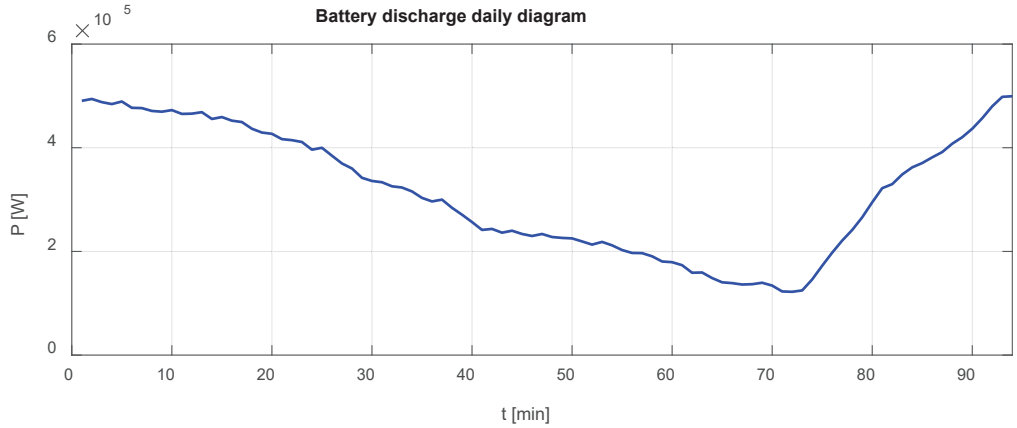

Figure 1. Daily 10 kW change.

Figure 2 compares the actual measured discharge power with the forecast generated by the Kalman filter. The prediction closely follows the measured values, even when zoomed in over multiple consecutive days. This demonstrates that the Kalman filter effectively captures the daily discharge pattern in environments with minimal day-to-day variation.

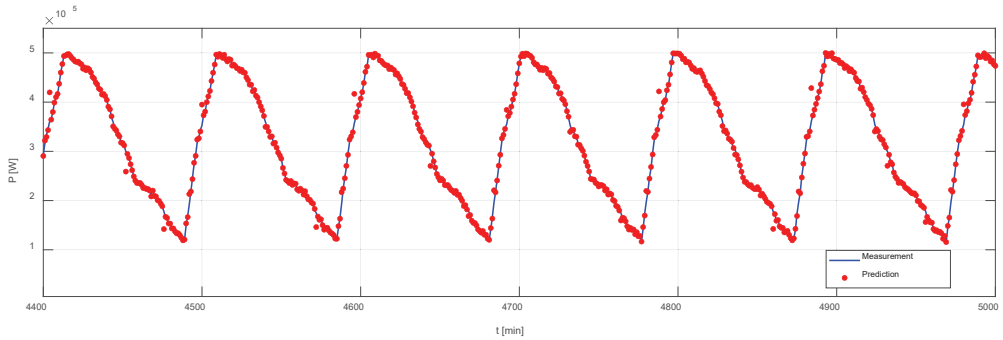

Figure 2. Kalman 10 kW change.

Figure 3 presents the forecast produced by the Holt's model with adaptive alpha. Here, as well, the predicted curve aligns very well with the measurements, with only minor deviations or delays occurring occasionally. In this low-variability scenario (±10 kW), Holt's model also achieves high prediction accuracy.

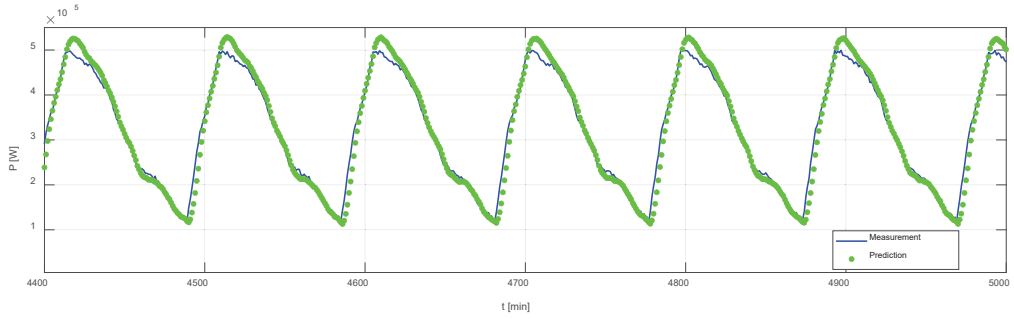

Figure 3. Holt's 10 kW change.

To evaluate forecasting performance under moderately dynamic conditions, the second scenario introduces daily variations of up to ±50 kW in battery discharge. This level of variability represents a more realistic operating environment, where external factors such as fluctuating grid demand or renewable generation begin to influence the system more significantly. The following figures provide a visual comparison between measured discharge

data and predictions from both the Kalman filter and Holt's adaptive model, highlighting how each method responds to mid-range changes in the battery's daily discharge pattern.

Figure 4 presents a daily battery discharge profile under moderate variability conditions, where discharge patterns fluctuate up to ±50 kW between consecutive days. The profile still follows a recognizable daily cycle, but includes visible noise and irregularities, reflecting more dynamic grid conditions compared to the low-variability scenario.

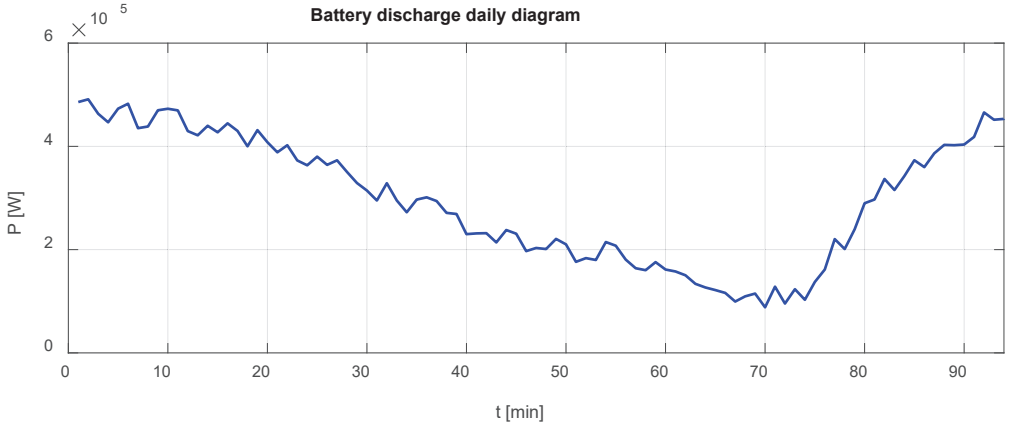

Figure 4. Daily 50 kW change.

Figure 5 shows the performance of the Kalman filter in forecasting daily discharge during this scenario. Despite increased variability, the predicted values (orange) remain closely aligned with the actual measurements (blue), showing that the Kalman filter retains high accuracy and effectively smooths noise while adjusting to moderate changes in the discharge curve.

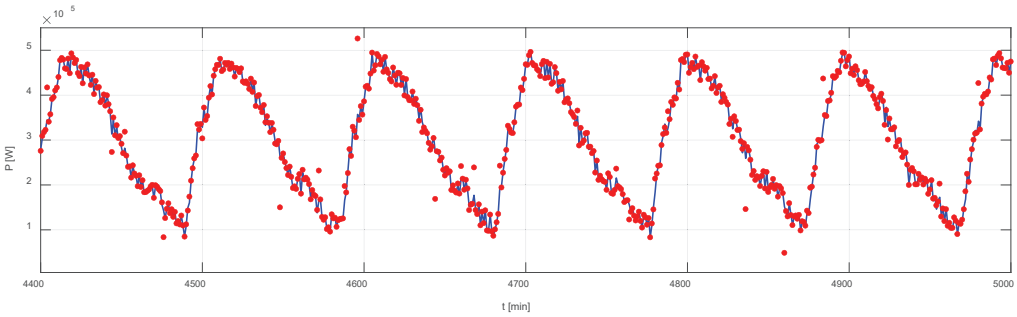

Figure 5. Kalman 50 kW change.

Figure 6 displays the prediction results using Holt's adaptive model. Compared to the Kalman filter, Holt's predictions show slightly larger deviations from the measured values, especially around peak and trough regions. Although the model tracks the general trend, the adaptive smoothing does not fully compensate for the increased variability, resulting in greater forecast errors. Overall, these plots illustrate that while both models can follow the daily discharge pattern under moderate variability, the Kalman filter continues to provide more accurate and stable predictions, whereas Holt's model begins to show limitations in capturing the full extent of dynamic fluctuations.

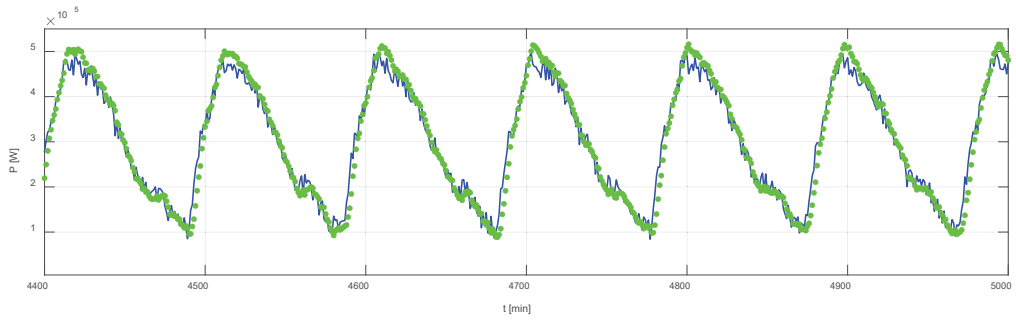

Figure 6. Holt's 50 kW change.

To evaluate the robustness of the forecasting models under highly dynamic conditions, the third simulation scenario introduces a ±90 kW change in daily battery discharge values. This scenario simulates a more volatile grid environment, such as during extreme fluctuations in renewable generation or load demand. The following figures illustrate the system's actual discharge behaviour and compare the prediction accuracy of the Kalman filter and Holt's adaptive model under this high-variability setting.

Figure 7 shows the daily battery discharge profile with high variability. The discharge curve displays significant fluctuations and irregular dips throughout the day, reflecting rapidly changing system conditions and a more erratic power demand-response behaviour.

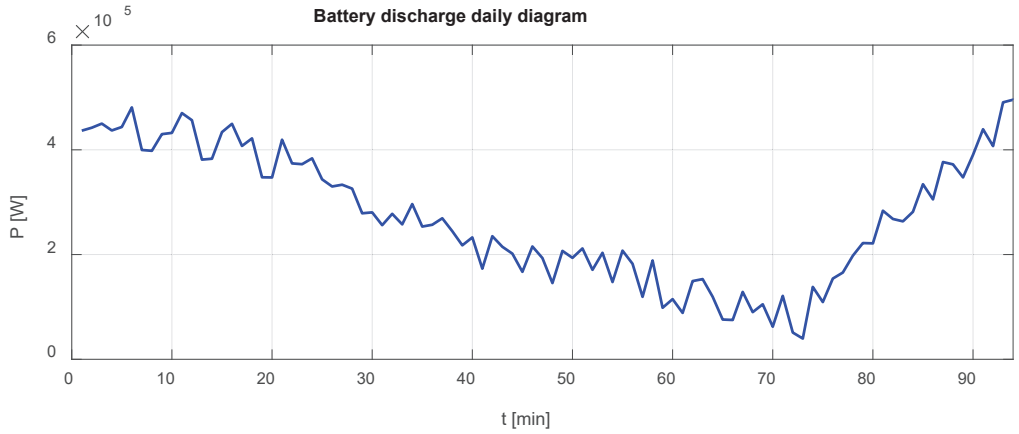

Figure 7. Daily 90 kW change.

Figure 8 presents the Kalman filter's forecasting performance under this scenario. Despite the increased noise and instability in the discharge profile, the Kalman filter manages to closely track the measured values, maintaining a consistent prediction pattern with minor deviations. Its recursive correction mechanism allows it to remain stable, though slightly conservative in reacting to sharp shifts.

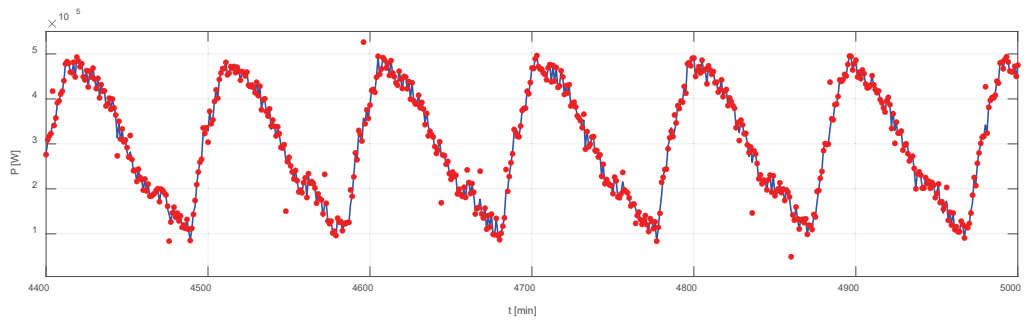

Figure 8. Kalman 90 kW change.

Figure 9 displays the results of Holt's adaptive model. While it generally follows the trend of the actual measurements, the prediction shows higher error margins compared to the Kalman filter. The model exhibits more noticeable overshooting and lagging, especially during steep changes, as it tries to adjust its smoothing parameters dynamically. These visual differences align with the quantitative evaluation, where Holt's model produces a significantly higher error rate under high variability.

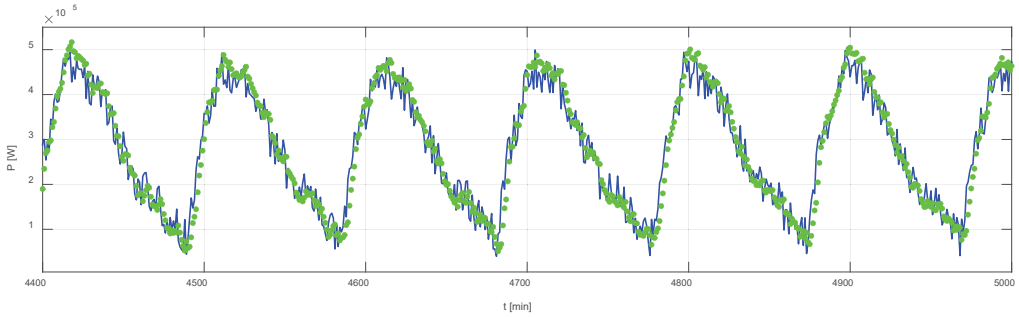

Figure 9. Holt's 90 kW change.

4.3. Evaluation Metrics

To quantify forecasting accuracy, the following standard time series evaluation metrics were used [2]:

- Mean Absolute Error (MAE);
- Root Mean Squared Error (RMSE);
- Mean Absolute Percentage Error (MAPE).

Table 1 presents a comparison of forecasting accuracy for the Kalman filter and Holt's adaptive model across three battery discharge variability scenarios. The metrics used to assess performance are Mean Absolute Error (MAE), Root Mean Squared Error ($RMSE$) and Mean Absolute Percentage Error ($MAPE$).

$$MAE = \frac{1}{n}\sum_{i=1}^{n}|y_i - \hat{y}_i| \tag{10}$$

$$RMSE = \sqrt{\frac{1}{n}\sum_{i=1}^{n}(y_i - \hat{y}_i)^2} \tag{11}$$

$$MAPE = \frac{100}{n}\sum_{i=1}^{n}\left|\frac{y_i - \hat{y}_i}{y_i}\right| \tag{12}$$

where y_i are the actual values and $\hat{y}_i$ are the predicted values.

Table 1. Comparison of charging curve applications for the applied methods.

Variability Scenario	Method	MAE (kW)	RMSE (kW)	MAPE (%)
10 kW	Kalman	4.812	8.482	1.82
	Holt's	15.559	22.205	5.26
50 kW	Kalman	23.146	29.326	8.73
	Holt's	21.489	27.600	8.56
90 kW	Kalman	44.306	53.527	16.66
	Holt's	30.389	37.196	14.21

In the low variability scenario (±10 kW), the Kalman filter clearly outperforms Holt's method, achieving an MAE of 4.812 kW and a MAPE of 1.82%, compared to Holt's results of 15.559 kW MAE and 5.26% MAPE. This confirms the Kalman filter's strength in stable

operating conditions, where its recursive update process ensures precise tracking with minimal error. In the medium variability case (±50 kW), Holt's model slightly outperforms the Kalman filter in terms of MAE (21.489 kW vs. 23.146 kW), despite the Kalman filter having a marginally higher MAPE (8.73% vs. 8.56%) and a higher RMSE. This suggests that Holt's adaptive mechanism was able to slightly better capture the moderate fluctuations in discharge, but both models experienced increased error due to the greater unpredictability. In the high variability scenario (±90 kW), performance diverged more significantly. Kalman's MAE rose to 44.306 kW and MAPE to 16.66%, while Holt's MAE was 30.389 kW and MAPE 14.21%. Despite Kalman's stability in noise handling, it lagged in responding to rapid fluctuations, allowing Holt's model to better adapt under highly dynamic conditions.

5. Conclusions

This evaluation highlights that forecasting model selection should be based on the expected level of operational variability. The Kalman filter is highly reliable in low-variability environments, providing consistent, accurate predictions with low error margins. However, as variability increases, its conservative nature limits responsiveness, reducing accuracy. Conversely, Holt's adaptive method becomes more advantageous in highly dynamic scenarios, owing to its flexible trend and level adjustment, enabling it to react more quickly to sudden shifts in discharge patterns. The presented approach improves battery discharge prediction accuracy, which, in turn, supports enhanced power grid stability. By enabling more reliable load balancing and energy storage management, this method contributes to the efficient integration of renewable energy sources and optimization of grid operations, offering practical benefits for modern power systems. An optimal strategy may involve hybrid or switching models that adapt forecasting techniques in real time, depending on recent variability trends—balancing stability with flexibility for improved overall system performance. In conclusion, the presented approach enhances battery discharge prediction accuracy and supports improved power grid stability.

Author Contributions: Conceptualization, J.Š.; Methodology, M.B.; Software, M.B.; Validation, R.Š. and Z.Č.; Investigation, J.Š.; Data curation, R.Š.; Writing—original draft, M.B. and J.Š.; Writing—review & editing, M.B. and J.Š.; Supervision, Z.Č.; Project administration, Z.Č.; Funding acquisition, Z.Č. All authors have read and agreed to the published version of the manuscript.

Funding: This research was funded by the Slovak Ministry of Education, Science, Research and Sport of the Slovak Republic and the Slovak Academy of Sciences VEGA 1/0627/24.

Data Availability Statement: The original contributions presented in this study are included in the article. Further inquiries can be directed to the corresponding authors.

Conflicts of Interest: The authors declare no conflict of interest.

References

1. Kwon, K.; Lee, H.-B.; Kim, N.; Park, S.; Joshua, S.R. Integrated Battery and Hydrogen Energy Storage for Enhanced Grid Power Savings and Green Hydrogen Utilization. *Appl. Sci.* **2024**, *14*, 7631. [CrossRef]
2. Zhan, R.; Wan, J. Iterated Unscented Kalman Filter for Passive Target Tracking. *IEEE Trans. Aerosp. Electron. Syst.* **2007**, *43*, 1155–1163. [CrossRef]
3. Altay, N.; Rudisill, F.; Litteral, L. Adapting Wright's modification of Holt's method to forecasting intermittent demand. *Int. J. Prod. Econ.* **2008**, *111*, 389–408. [CrossRef]
4. Sugiarto, V.C.; Sarno, R.; Sunaryono, D. Sales forecasting using Holt-Winters in Enterprise Resource Planning at sales and distribution module. In Proceedings of the 2016 International Conference on Information & Communication Technology and Systems (ICTS), Surabaya, Indonesia, 12 October 2016; pp. 8–13. [CrossRef]
5. Lee, K.-T.; Dai, M.-J.; Chuang, C.-C. Temperature-Compensated Model for Lithium-Ion Polymer Batteries With Extended Kalman Filter State-of-Charge Estimation for an Implantable Charger. *IEEE Trans. Ind. Electron.* **2018**, *65*, 589–596. [CrossRef]

6. Wei, M.; Ye, M.; Zhang, C.; Lian, G.; Xia, B.; Wang, Q. Robust state of charge estimation of $LiFePO_4$ batteries based on Sage_Husa adaptive Kalman filter and dynamic neural network. *Electrochim. Acta* **2024**, *477*, 143778. [CrossRef]
7. Zhang, J.; Xiao, B.; Niu, G.; Xie, X.; Wu, S. Joint estimation of state-of-charge and state-of-power for hybrid supercapacitors using fractional-order adaptive unscented Kalman filter. *Energy* **2024**, *294*, 130942. [CrossRef]
8. Jiang, H. Research on SOC estimation of residual power of lithium-ion batteries for electric vehicles based on extended Kalman filtering algorithm. *Appl. Math. Nonlinear Sci.* **2023**, *8*, 2849–2860. [CrossRef]
9. Kaczorowska, D.; Rezmer, J.; Jasinski, M.; Sikorski, T.; Suresh, V.; Leonowicz, Z.; Kostyla, P.; Szymanda, J.; Janik, P. A Case Study on Battery Energy Storage System in a Virtual Power Plant: Defining Charging and Discharging Characteristics. *Energies* **2020**, *13*, 6670. [CrossRef]
10. Zhang, D.; Shafiullah, G.; Das, C.K.; Wong, K.W. Optimal Allocation of Battery Energy Storage Systems to Enhance System Performance and Reliability in Unbalanced Distribution Networks. *Energies* **2023**, *16*, 7127. [CrossRef]
11. Pu, L.; Wang, C. Combined State-of-Charge Estimation Method for Lithium-Ion Batteries Using Long Short-Term Memory Network and Unscented Kalman Filter. *Energies* **2025**, *18*, 1106. [CrossRef]
12. Qi, J.; Li, P.; Dong, Y.; Fu, Z.; Wang, Z.; Yi, Y.; Tian, J. Remaining Available Energy Prediction for Energy Storage Batteries Based on Interpretable Generalized Additive Neural Network. *Batteries* **2025**, *11*, 276. [CrossRef]
13. Hussain, Q.; Yun, S.; Jeong, J.; Lee, M.; Kim, J. Prediction of Remaining Useful Life of Battery Using Partial Discharge Data. *Electronics* **2024**, *13*, 3475. [CrossRef]
14. Jiang, Y.; Song, W. Predicting the Cycle Life of Lithium-Ion Batteries Using Data-Driven Machine Learning Based on Discharge Voltage Curves. *Batteries* **2023**, *9*, 413. [CrossRef]
15. Zhou, J.; Tong, X.; Zhou, J.; Bai, S.; Liu, R.; Zhao, H. Application of a Hybrid ARIMA-LSTM Model Based on the LightGBM in Grid Frequency Prediction. In Proceedings of the 2024 3rd Asian Conference on Frontiers of Power and Energy (ACFPE), Chengdu, China, 2–4 April 2024; Chen, L., Liu, Y., Eds.; IEEE: Piscataway, NJ, USA, 2024; pp. 409–413. [CrossRef]
16. Oladapo, B.I.; Olawumi, M.A.; Omigbodun, F.T. Machine Learning for Optimising Renewable Energy and Grid Efficiency. *Atmosphere* **2024**, *15*, 1250. [CrossRef]
17. György, K.; Kelemen, A.; Dávid, L. Unscented Kalman Filters and Particle Filter Methods for Nonlinear State Estimation. *Procedia Technol.* **2014**, *12*, 65–74. [CrossRef]
18. Wang, H.; Zheng, X.; Li, H. Kalman Filtering With Unlimited Sensing. In Proceedings of the ICASSP 2024—2024 IEEE International Conference on Acoustics, Speech and Signal Processing (ICASSP), Seoul, Republic of Korea, 14–19 April 2024; pp. 9826–9830. [CrossRef]
19. Al-Gounmeein, R.; Ismail, M.T.; Al-Hasanat, B.; Awajan, A. Improving models accuracy using Kalman filter and Holt-Winters approaches based on ARFIMA models. *IAENG Int. J. Appl. Math.* **2023**, *53*, 869–878.
20. Maia, A.L.S.; de Carvalho, F.D.A. Holt's exponential smoothing and neural network models for forecasting interval-valued time series. *Int. J. Forecast.* **2011**, *27*, 740–759. [CrossRef]
21. Aimran, A. A comparison between single exponential smoothing (SES), double exponential smoothing (DES), holt's (brown) and adaptive response rate exponential smoothing (ARRES) techniques in forecasting Malaysia population. *Glob. J. Math. Anal.* **2014**, *2*, 276–280. [CrossRef]
22. Li, G.; Mao, Q.; Yang, F. Extended Kalman Filter Algorithm for Accurate State-of-Charge Estimation in Lithium Batteries. *Processes* **2024**, *12*, 1560. [CrossRef]
23. Khalid, A.; Kashif, S.A.R.; Ain, N.U.; Awais, M.; Ali Smieee, M.; Carreño, J.E.M.; Vasquez, J.C.; Guerrero, J.M.; Khan, B. Comparison of Kalman Filters for State Estimation Based on Computational Complexity of Li-Ion Cells. *Energies* **2023**, *16*, 2710. [CrossRef]
24. Hu, L.; Hu, R.; Ma, Z.; Jiang, W. State of Charge Estimation and Evaluation of Lithium Battery Using Kalman Filter Algorithms. *Materials* **2022**, *15*, 8744. [CrossRef]

Disclaimer/Publisher's Note: The statements, opinions and data contained in all publications are solely those of the individual author(s) and contributor(s) and not of MDPI and/or the editor(s). MDPI and/or the editor(s) disclaim responsibility for any injury to people or property resulting from any ideas, methods, instructions or products referred to in the content.

batteries

MDPI

Article

Techno-Economic and Environmental Viability of Second-Life EV Batteries in Commercial Buildings: An Analysis Using Real-World Data

Zhi Cao, Naser Vosoughi Kurdkandi and Chris Mi *

Department of Electrical and Computer Engineering, San Diego State University, San Diego, CA 92182, USA; zcao2@sdsu.edu (Z.C.); nvosoughikurdkandi@sdsu.edu (N.V.K.)
* Correspondence: cmi@sdsu.edu

Abstract

The rapid growth of electric vehicle markets is producing large volumes of retired lithium-ion batteries retaining 70–80% of their original capacity, suitable for stationary energy storage. This study assesses the techno-economic and environmental viability of second-life battery energy storage systems (SLBESS) in a California commercial building, using one year of operational data. SLBESS performance is compared with equivalent new battery systems under identical dispatch strategies, building load profiles, and time-of-use tariff structures. A dispatch-aware framework integrates multi-year battery simulations, degradation modeling, electricity cost analysis, and life cycle assessment based on marginal grid emissions. The economic analysis quantifies the net present value (NPV), internal rate of return (IRR), and operational levelized cost of storage ($LCOS_{op}$). Results show that SLBESS achieve 49.2% higher NPV, 41.9% higher IRR, and 13.8% lower $LCOS_{op}$ than new batteries, despite their lower round-trip efficiency. SLBESS reduce embodied emissions by 41% and achieve 8% lower carbon intensity than new batteries. Sensitivity analysis identifies that economic outcomes are driven primarily by financial parameters (incentives, acquisition cost) rather than technical factors (degradation, initial health), providing a clear rationale for policies that reduce upfront costs. Environmentally, grid emission factors are the dominant driver. Battery degradation rate and initial state of health have minimal impact, suggesting that technical concerns may be overstated. These findings provide actionable insights for deploying cost-effective, low-carbon storage in commercial buildings.

Keywords: second-life battery; techno-economic analysis; life cycle assessment; commercial buildings; demand charge management; battery energy storage

1. Introduction

The rapid growth of the electric vehicle (EV) market has led to an unprecedented increase in the number of retired batteries. Although these batteries are unsuitable for high-performance automotive applications once their state of health (SOH) declines to 70–80%, they retain significant residual capacity and can deliver an additional 5–10 years of service in less demanding stationary energy storage applications [1–3]. Commercial buildings with on-site photovoltaic (PV) systems represent promising candidates for second-life battery (SLB) deployment. These buildings typically exhibit predictable load profiles, face significant demand charges, and increasingly seek to integrate renewable generation. When properly managed, SLB systems can lower electricity costs, improve PV self-consumption,

and enhance grid flexibility, while extending the useful life of EV batteries and reducing their embodied carbon footprint [4].

However, the viability of SLBs in commercial contexts remains uncertain due to limited evidence regarding their technical performance, economic competitiveness, and environmental benefits. Declining new battery costs, logistics and testing requirements, limited data on degradation, and challenges in regulatory compliance further hinder large-scale adoption [5–7]. Extensive research has been conducted on the viability assessment of second-life batteries, employing both techno-economic analysis (TEA) and life cycle assessment (LCA) frameworks. Several studies have assessed the cost competitiveness and market potential of SLBs under varying assumptions of repurposing cost and electricity price. Rallo et al. analyzed real-world stationary storage systems in Spain and highlighted that aging dynamics significantly affect return on investment, emphasizing the need to account for degradation behavior in feasibility studies [8]. Steckel et al. used a Levelized Cost of Storage (LCOS) approach for utility-scale systems, emphasizing that SLB viability is highly sensitive to electricity market dynamics and processing cost [9]. Fallah et al. conducted a comparative techno-economic evaluation of used batteries across grid-based scenarios, finding that profitability can be maintained when the acquisition cost remains below approximately 25% of the new cell price, particularly for younger retired batteries with higher remaining capacity [10]. Lieskoski et al. examined the business potential of repurposing Tesla Model S/X batteries in Finland and found that pack- or module-level repurposing can be economically viable, while full disassembly to the cell level remains uneconomical due to labor costs [11]. Zhuang et al. developed a techno-economic decision support model showing that second-life battery value varies significantly by application ($23–273/kWh), with economic viability determined more by policy incentives and repurposing costs than by battery degradation characteristics [12]. Turan et al. demonstrated through dynamic degradation modeling and comprehensive cost analysis that second-life batteries achieve economic viability at 34–54% of new battery costs in off-grid applications, with sensitivity analysis identifying new battery purchase price as the dominant factor in SLB market pricing [13].

Environmental studies consistently demonstrate that SLBs yield substantial carbon and resource savings compared with new batteries. Cusenza et al. integrated load-match analysis and LCA to evaluate the reuse of EV batteries in nearly zero-energy buildings, showing that a 46 kWh second-life battery system enhanced both energy self-consumption and environmental performance [14]. Kamath et al. evaluated SLBs in residential and utility-level PV applications across the U.S. and found that SLBs reduced levelized electricity costs by 12–57% and life-cycle carbon emissions by 7–31% relative to new batteries [15]. Cheng et al. linked degradation, performance, and sustainability indicators, showing that higher initial SOH improves environmental outcomes [16]. Saez de Bikuña et al. found that automation and policy incentives such as tax credits and carbon pricing are crucial for maintaining SLB competitiveness [17].

Most prior studies, however, rely on static annual models that compute aggregate financial and environmental indicators using assumed average throughput, fixed performance parameters, and uniform operational patterns. Such approaches fail to capture the time-resolved dynamics of battery dispatch, including hourly variations in electricity prices, solar generation, building loads, and degradation trajectories. Moreover, few studies offer counterfactual comparisons between second-life and new battery systems operating under identical conditions, namely the same load profiles, tariff structures, control strategies, and operational constraints, making it difficult to isolate the true techno-economic and environmental trade-offs of battery reuse.

This study addresses these gaps through a comprehensive, dispatch-aware evaluation of a second-life battery energy storage system (SLBESS) deployed in a California commercial building. Using one year of high-resolution operational data, the study integrates TEA and LCA to evaluate both financial and environmental viability under real-world conditions.

A time-series battery simulation model is developed to operate at one-minute resolution over a 10-year period, using measured data on building load profiles, rooftop PV generation, time-of-use (TOU) tariffs, and empirically validated battery degradation models. This approach captures the temporal dynamics of battery dispatch, including demand charge management and energy arbitrage, and quantifies their cumulative effects on economic returns and system performance. The framework quantifies net present value (NPV), internal rate of return (IRR), and operational levelized cost of storage ($LCOS_{op}$) while accounting for degradation effects and system availability. Second-life and new battery systems are evaluated under identical operational conditions, including the same building, PV system, load profile, tariff structure, control algorithm, and evaluation period, allowing rigorous isolation of the economic and environmental implications of battery reuse. The environmental assessment employs a cradle-to-grave LCA boundary incorporating marginal grid emission factors to quantify avoided emissions from battery discharge, as well as embodied impacts from repurposing, transportation, balance-of-system components, and end-of-life recycling credits. While the case study is site-specific, the methodological framework developed here is designed to be generalizable and can be adapted to other geographies by incorporating local load profiles, tariff structures, and grid emission factors.

Comprehensive sensitivity analyses across technical, economic, and policy parameters identify the key drivers of SLBESS viability and quantify associated uncertainty, revealing that policy incentives and acquisition costs dominate economic outcomes, whereas grid emission factors largely determine environmental performance. This study delivers actionable insights for building owners, policymakers, and technology providers aiming to evaluate and accelerate SLB deployment in commercial applications.

2. System Description and Data

2.1. Case Study Site

This study investigates a commercial building in San Diego, California, equipped with on-site PV generation and subject to a TOU tariff structure that includes both energy and demand charges. The site is representative of commercial buildings with high demand charges, predictable load profiles, and significant on-site solar generation, which are the conditions conducive to battery storage deployment.

Figure 1 illustrates the system architecture and power flow paths at the study site. The battery energy storage system consists of repurposed EV packs assembled into racks and connected to the building's distribution panel through a three-phase power conversion system (PCS). An energy management system (EMS) coordinates all components and executes various dispatch strategies, including rule-based heuristics and model predictive control (MPC). Energy flows include: (i) bidirectional power exchange between the building and the utility grid; (ii) bidirectional charging and discharging of the SLBESS; and (iii) unidirectional PV generation to the building, grid, or battery storage. This architecture enables flexible management of peak demand reduction, energy arbitrage, and PV integration.

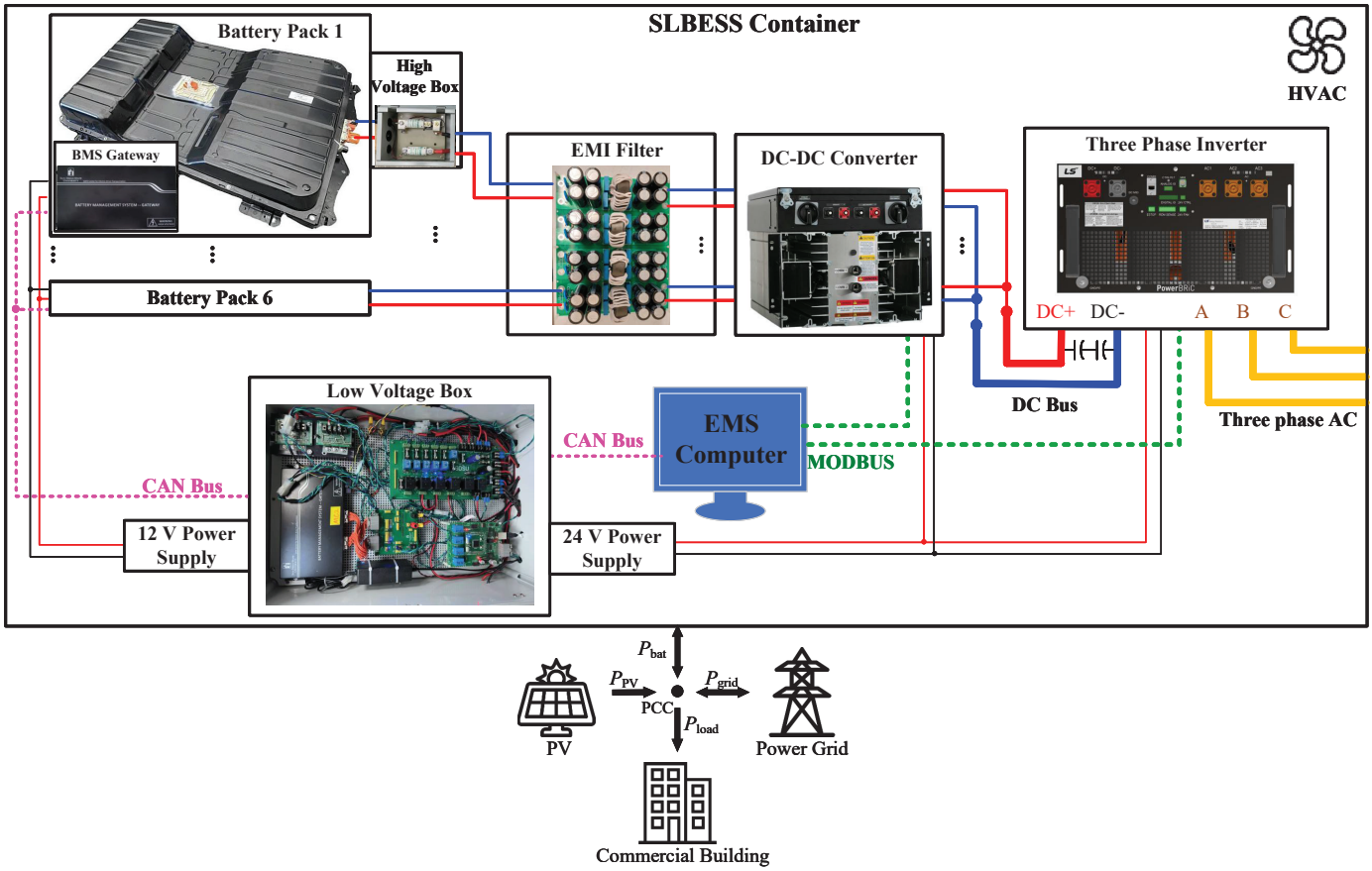

Figure 1. System schematic showing SLBESS architecture with repurposed EV battery packs, PCS, BMS gateway, EMS, and bidirectional AC/DC power flows between the building, grid, PV system, and battery storage at the point of common coupling (PCC).

2.2. Dataset

High-resolution operational data were recorded at one-minute intervals over a 12-month period. The dataset includes building load, PV generation, battery power, net load, system operating states, and environmental conditions (ambient and internal temperatures). Figure 2 shows the average daily profiles of building load and PV generation over the year. The building demonstrates consistent daily load patterns with pronounced peaks during business hours. PV generation leads to periods of negative net load at midday, indicating excess solar production available for battery charging or export to the grid. This combination of high demand charges and abundant midday PV makes the site ideal for demand charge management and PV self-consumption optimization. Table 1 summarizes key statistical characteristics of building load and PV generation.

Table 1. Summary statistics of building load and PV generation.

Statistical Indicator	Value	Unit
Average load	52.44	kW
Maximum load	158.51	kW
Minimum load	17.05	kW
Load factor	0.33	-
PV rated capacity	200	kW
Average PV generation power	48.99	kW
Maximum PV generation power	259.07	kW
PV capacity factor	0.19	-

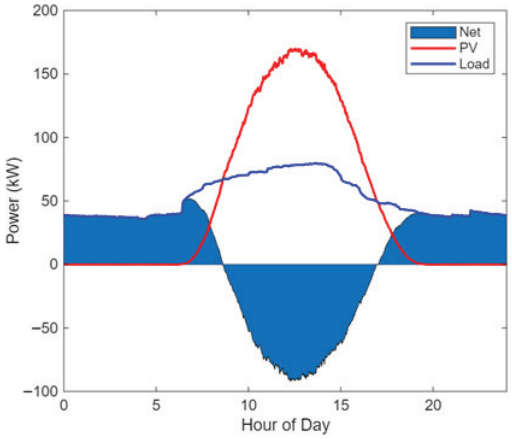

Figure 2. Average daily load and PV profile.

3. Methodology

This study introduces an integrated framework to evaluate the techno-economic and environmental viability of SLBESS in commercial buildings. The dispatch-aware framework uses one year of measured data on building load, PV generation, and battery operation from the study site. Figure 3 illustrates the overall research framework.

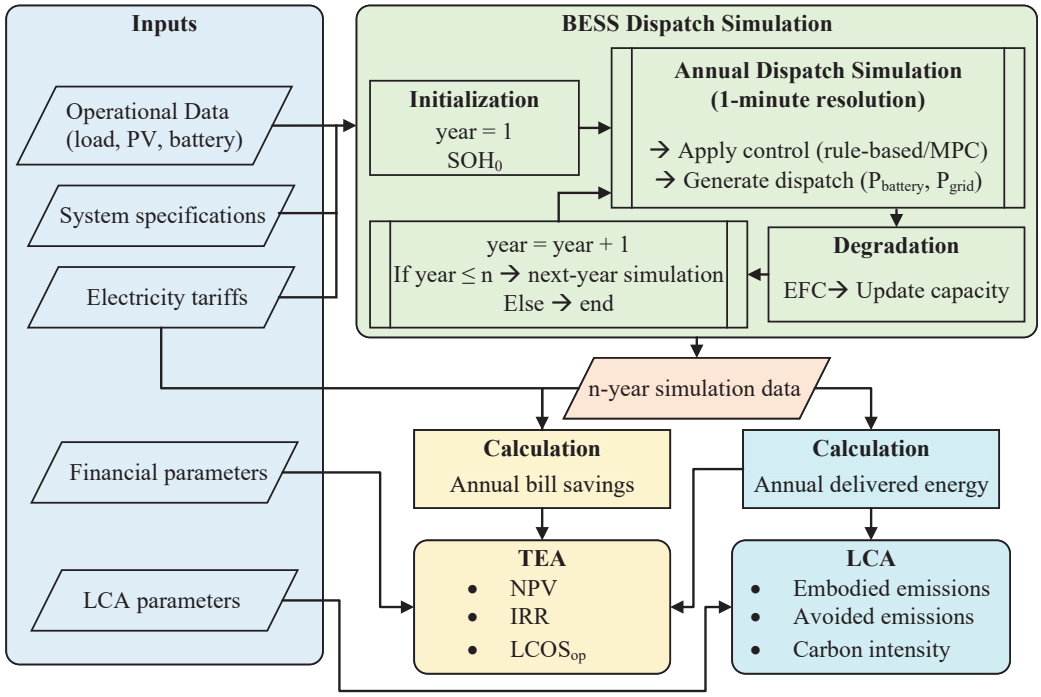

Figure 3. Integrated methodological framework showing battery dispatch simulation with annual degradation updates, followed by techno-economic assessment and life cycle assessment tracks.

The framework incorporates system specifications, high-resolution operational data, tariff structures, financial parameters, and life cycle inventories as primary inputs. The battery dispatch simulation employs dynamic modeling to track the state of charge (SOC), enforce power and energy constraints, and apply control strategies (rule-based or MPC) at one-minute resolution. For the details of system modeling and constraints, readers can refer to literature [18]. The simulation proceeds year by year, updating battery capacity based on equivalent full cycles (EFC) and applying degradation models (Section 4.1). The multi-year simulation generates time-series data on battery dispatch, grid power, and delivered energy, which serve as inputs to both techno-economic and environmental assessments.

These simulation data are analyzed through two tracks:

- TEA quantifies bill savings under demand and TOU tariffs, calculates project-level NPV and IRR, and defines $LCOS_{op}$, which accounts for degradation and downtime impacts.
- LCA employs a cradle-to-grave boundary to capture the embodied impacts of repurposing, balance-of-system (BOS) components, transportation, charging electricity, avoided grid emissions, and end-of-life recycling credits.

Both analyses are extended through sensitivity analyses that vary technical, economic, and policy parameters to characterize uncertainty and identify key drivers of SLBESS viability. The results are synthesized into integrated insights to inform building owners, policymakers, and technology providers about the conditions under which SLBESS deployment becomes both financially and environmentally favorable.

3.1. System Boundary

The system boundary follows a cradle-to-grave perspective and includes:

- SLB collection, testing, and repurposing.
- Transportation to the installation site.
- BOS, PCS, and EMS production and installation.
- Use-phase operation, including availability, round-trip efficiency (RTE) and degradation.
- End-of-life dismantling and recycling, including material recovery credits.

3.2. Techno-Economic Assessment

The techno-economic assessment quantifies the financial viability of SLB systems over an n-year project lifetime. Three key metrics are considered: bill savings, NPV, and $LCOS_{op}$.

3.2.1. Electricity Bill Model

Electricity bills include energy charges and demand charges under the utility's TOU tariff. The energy charge is based on total electricity consumption and varies by time period:

$$C_E = \Delta t \sum_{t=0}^{T-1} \left[c_{\text{imp}}(t) \max(P_{\text{grid}}(t), 0) + c_{\text{exp}}(t) \min(P_{\text{grid}}(t), 0) \right] \tag{1}$$

where Δt is the time interval, T is the total number of time steps in each billing cycle, $P_{\text{grid}}(t)$ is net grid power (positive for import, negative for export), $c_{\text{imp}}(t)$ is the import electricity price (\$/kWh), and $c_{\text{exp}}(t)$ is the export price (\$/kWh). The formulation ensures that energy charges are calculated separately for import and export, accounting for different pricing structures.

The demand charge is based on the peak 15-min average power import during the entire billing cycle:

$$C_D = c_d(t^*) \cdot \max_{t \in \mathcal{T}} P_{\text{imp}}(t) \tag{2}$$

where $c_d(t^*)$ is the demand charge rate (\$/kW) corresponding to time t^* when peak grid import occurs, $\mathcal{T}$ represents all 15-min time windows within the billing period, and $P_{\text{imp}}(t) = \max(P_{\text{grid}}(t), 0)$ is the grid import power averaged over 15-min windows. This formulation captures the time-dependent nature of demand charges, which often vary between on-peak and off-peak periods.

The total electricity cost combines both components:

$$C_{\text{total}} = C_E + C_D \tag{3}$$

Bill savings S_{bill} are computed as the difference between baseline (no storage) and storage cases.

3.2.2. Net Present Value

The project NPV accounts for upfront capital expenditure (CAPEX), operations and maintenance (O&M) costs, bill savings, residual value, and financial incentives:

$$\text{NPV} = -(1-s)C_{\text{capex}} - \sum_{t=0}^{n} \frac{C_{O\&M}(t)}{(1+r)^t} + \sum_{t=1}^{n} \frac{S_{\text{bill}}(t)}{(1+r)^t} + \frac{C_{\text{res}}}{(1+r)^n}, \tag{4}$$

where C_{capex} is capital expenditure, $C_{O\&M}$ is operating cost, S_{bill} is annual bill savings, C_{res} is residual value, r is the discount rate, and s is the incentive fraction applied to CAPEX.

The internal rate of return (IRR) is defined as the discount rate r that results in a zero NPV.

3.2.3. Operational LCOS_{op}

LCOS_{op} quantifies the effective cost per kilowatt-hour of energy delivered to the building under real operational conditions:

$$\text{LCOS}_{\text{op}} = \frac{(1-s)C_{\text{capex}} + \sum_{t=0}^{n} \frac{C_{O\&M}(t)}{(1+r)^t} - \frac{C_{\text{res}}}{(1+r)^n}}{\sum_{t=1}^{n} \frac{E_{\text{del}}(t)}{(1+r)^t}}. \tag{5}$$

This metric inherently accounts for round-trip efficiency, system availability, and capacity degradation through the denominator $E_{\text{del}}(t)$, which represents actual energy throughput rather than nameplate capacity.

3.3. Environmental Assessment

The LCA quantifies net life-cycle greenhouse gas (GHG) emissions associated with the battery energy storage. The total impact is calculated as:

$$I_{\text{net}} = I_{\text{embodied}} + I_{\text{transport}} + I_{\text{charge}} - I_{\text{avoided}} - I_{\text{recycling}} \tag{6}$$

where I_{embodied} denotes emissions from repurposing activities (e.g., testing and refurbishment) and the manufacturing of BOS, PCS, and EMS components. $I_{\text{transport}}$ represents emissions associated with transportation and site delivery. I_{charge} represents grid-related emissions incurred during battery charging from the grid. I_{avoided} represents avoided grid emissions resulting from battery discharging. $I_{\text{recycling}}$ represents credits for material recovery at the end of life.

Battery charging emissions and avoided emissions are computed using a marginal emission factor μ, which represents the carbon intensity of displaced grid generation:

$$I_{\text{charge}}(t) - I_{\text{avoided}}(t) = \mu \left[P_{\text{dis}}(t) - P_{\text{ch,grid}}(t)\right] \Delta t \tag{7}$$

where $P_{\text{dis}}(t)$ is the battery discharging power, and $P_{\text{ch,grid}}(t)$ is charging power sourced from the grid (charging from PV is considered carbon-neutral within the system boundary), and μ is the marginal emission factor $\text{kgCO}_2\text{e/kWh}$ for the California grid.

The final carbon intensity (CI) of delivered energy is:

$$CI = \frac{I_{\text{net}}}{\sum_t E_{\text{del}}(t)} \quad [\text{kgCO}_2\text{e/kWh}]. \tag{8}$$

4. Results and Discussion

4.1. Simulation Parameters and Setup

Table 2 summarizes the simulation parameters. The sensitivity range column specifies the bounds used in the uncertainty analysis (Section 4.3). The simulation parameters used in this study were compiled from a combination of existing literature and publicly available industrial data [9,15,19,20].

Table 2. Simulation parameters.

Parameter	Second-Life Battery	Sensitivity Analysis Range	New Battery
Initial SOH (%)	80	(70, 90)	100
Initial energy (kWh)	362	(100, 600)	362
Round-trip efficiency (%)	86	(80, 93)	92
SoC range (%)	10–90	-	10–90
Degradation rate (%/1000 EFC)	6.3	(4, 8)	-
System Availability (%)	98	(96, 100)	98
Core cost ($/kWh)	100	(50, 200)	200
O&M cost (% of C_{capex})	2.5	(1, 4)	2.0
Discount rate (%)	8	(5, 10)	8
Incentive rate (%)	25	(0, 50)	25
Inflation rate (%)	2.5	-	2.5
Residual value rate (%)	5	(0, 10)	20
Marginal emission factor ($kgCO_2e/kWh$)	0.291	(0.10, 0.49)	0.291
Battery embodied emissions ($kgCO_2e/kWh$)	70	-	120
Battery transport emissions ($kgCO_2e/kWh$)	5	-	5
BOS embodied emissions ($kgCO_2e/kWh$)	32	-	32
PCS embodied emissions ($kgCO_2e/kWh$)	28	-	28
Expected Lifetime (years)	10	-	10

The system's maximum power is set to one-fourth of its energy capacity, consistent with standard 4-h energy storage configurations. Although second-life and new batteries begin with the same initial capacity (362 kWh), they differ in their initial states of health. Second-life batteries start at 80% SOH while new batteries start at 100% SOH. Accordingly, all SOH and EFC calculations are referenced to the rated full capacity. For SLB systems with 362 kWh at 80% SOH, the rated full capacity is calculated as 362/0.8 = 452.5 kWh. For new systems at 100% SOH, the rated full capacity remains 362 kWh. All subsequent degradation metrics and EFC counts are normalized to these rated full capacities.

The round-trip efficiency of second-life batteries (86%) is lower than new batteries (92%) due to increased internal resistance from previous cycling. The SOH degradation model for new batteries is given by:

$$\mathrm{SOH} = 100 - a(1 - e^{-b \times \mathrm{EFC}}) - c \times \mathrm{EFC} \tag{9}$$

where coefficients $a = 5.6038, b = 0.01, c = 0.0063$ are fitted from laboratory cycling test data [21]. This semi-empirical model captures the two-phase degradation behavior typical of lithium-ion batteries, combining an exponential term for rapid initial degradation with a linear term for the slower, long-term capacity fade.

For second-life batteries, a linear degradation model is used, based on field and laboratory data, assuming a capacity fade of 6.3% per 1000 EFCs. The linear degradation assumption for second-life batteries represents the empirically observed post-knee aging phase reported in [21], where capacity fade proceeds approximately linearly below 75% SOH. While other studies identify nonlinear degradation behaviors across chemistries [22], this work employs a constant rate to simplify comparison between systems. The sensitivity

range of 4–8% per 1000 EFC encompasses this variability, ensuring robustness of the techno-economic and environmental trends despite model simplification.

The EFC is calculated as the cumulative energy throughput divided by the rated full capacity:

$$\mathrm{EFC} = \frac{\sum_t E_{\mathrm{throughput}}(t)}{E_{\mathrm{rated,full}}} \tag{10}$$

where $E_{\mathrm{throughput}}(t)$ is the energy charged or discharged at time step t.

System availability accounts for unplanned outages and maintenance windows. In the simulation, downtime periods are randomly distributed throughout the year. During these intervals, the battery is excluded from dispatch, and the building operates without storage support.

The core cost of SLBs includes collection, testing, and refurbishment, while the cost of new batteries reflects pack manufacturing prices. A lump-sum core cost is used to avoid unnecessary parameter expansion and focuses the analysis on dominant techno-economic factors. O&M costs are expressed as annual percentages of CAPEX: 2.5% for SLBs and 2.0% for new batteries, reflecting the added complexity of managing heterogeneous second-life packs. The incentive rate represents a generic upfront capital cost reduction used for analytical purposes and is not linked to any specific policy. Residual value reflects end-of-life salvage potential: 20% for new batteries, assuming second-life repurposing, and 5% for SLBs, limited to material recovery.

A marginal emission factor of 0.291 $\mathrm{kgCO_2e/kWh}$ represents the average marginal emission intensity of the California grid. The embodied emissions of SLBs account only for testing and refurbishment, and are significantly lower than those of new batteries, which include the full manufacturing burden. Transport emissions, as well as embodied emissions from BOS and PCS components, are assumed to be identical for both systems.

Sensitivity analysis explores the parameter ranges shown in the table to quantify uncertainty bounds and identify key drivers of system viability.

4.2. SLB vs. New Battery Counterfactual Analysis

Figure 4 presents the comparative operational performance of both systems over the 10-year project lifetime under identical dispatch conditions. Figure 4a,b illustrate the capacity and SOH trajectories. The second-life battery capacity declines from 362 kWh to approximately 303 kWh by year 10, corresponding to 67% SOH relative to its rated full capacity. The new battery capacity declines from 362 kWh to approximately 285 kWh, maintaining 79% SOH. Although both systems begin with identical usable capacity, the new battery experiences greater absolute capacity loss due to the rapid initial fade followed by linear degradation, as captured in Equation (9). In contrast, the second-life battery follows a steadier linear decline, having already undergone the early-life accelerated degradation phase during its first-life automotive application.

Figure 4c shows that annual delivered energy decreases as capacity degrades. The second-life battery delivers more annual energy than the new battery during years 2–10, due to its higher remaining capacity. In year 1, when both systems have identical capacity, the new battery delivers slightly more energy due to its higher round-trip efficiency.

Figure 4d illustrates annual bill savings, showing that new systems generate approximately \$21,213–\$19,515 per year over the 10-year period, while SLB systems yield \$20,599–\$19,424 annually. Although operating with higher usable capacity in years 2–10, SLB generate slightly lower annual savings than new batteries throughout the project due to lower round-trip efficiency, which diminishes both energy arbitrage value and demand charge reduction potential. Table 3 summarizes the comparative economic performance. A lower upfront investment allows SLB systems to achieve superior project-level economics,

despite lower operational revenue. With a 23.3% lower initial investment, SLB systems deliver an NPV of $45,358 compared to $30,401 for new systems, representing a 49.2% improvement. The IRR reaches 14.4% for SLB systems versus 10.2% for new batteries, corresponding to a 41.2% relative increase. The operational levelized cost is $183/MWh for SLB systems, compared to $212/MWh for new systems, representing a 13.7% reduction. These results demonstrate that the capital cost advantage of repurposed batteries outweighs the operational revenue penalty associated with lower efficiency.

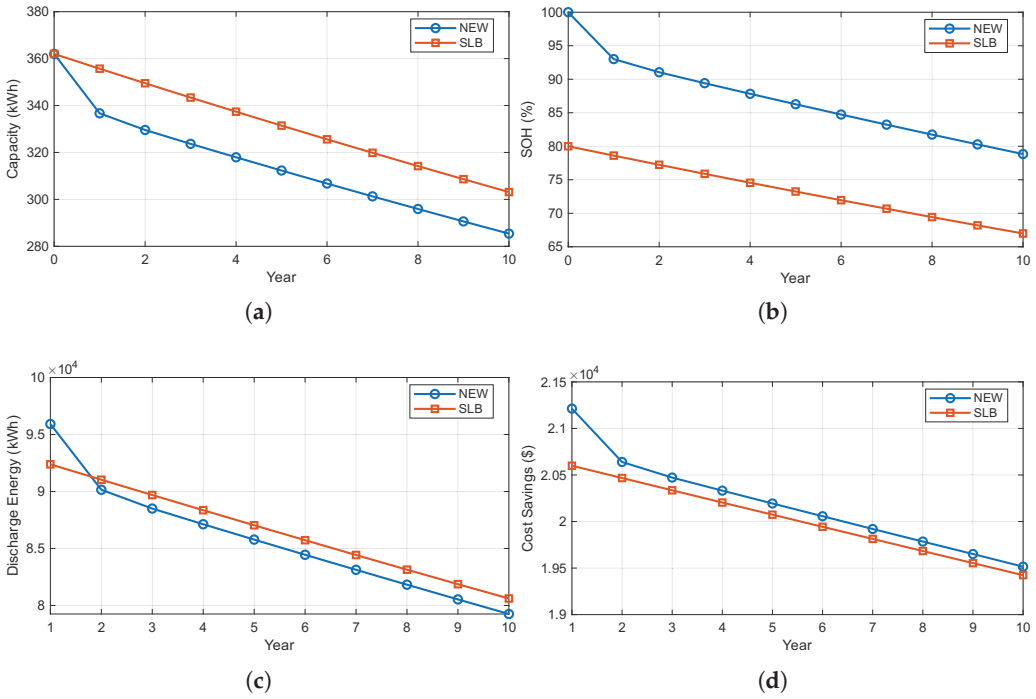

Figure 4. Annual operational performance: (**a**) Capacity trajectory. (**b**) SOH trajectory. (**c**) Delivered energy. (**d**) Cost savings (Revenue).

Table 3. Economic performance comparison between new and SLB systems under rule-based dispatch over 10-year project lifetime.

Metric	New Battery	Second-Life Battery	Advantage
Initial Investment ($)	116,745	89,595	−23.3%
NPV @ 10 years ($)	30,401	45,358	+49.2%
IRR (%)	10.2	14.4	+41.9%
$LCOS_{op}$ ($/MWh)	212	183	−13.8%

Table 4 presents the comparative environmental performance of both systems. Embodied emissions for SLB systems are 41.2% lower than those of new systems, as repurposing avoids the manufacturing burden associated with new cell production. The carbon intensity of delivered energy is -0.25 $kgCO_2e/kWh$ for SLB and -0.23 $kgCO_2e/kWh$ for new systems. The more negative value for SLB systems indicates that, despite lower efficiency, substantially reduced embodied emissions enable an 8.7% improvement in carbon intensity per kilowatt-hour delivered.

Figure 5a shows that annual avoided emissions range from approximately 27,000 $kgCO_2e$ in year 1 to 23,000 $kgCO_2e$ in year 10 for both systems. SLB systems achieve slightly higher avoided emissions than new systems in years 2–10 due to greater energy throughput, except in year 1, when the higher efficiency of new systems compensates for equal initial capacity. Cumulative net emissions in Figure 5b indicate carbon

payback within the first year for both systems, with SLB systems exhibiting slightly better cumulative performance due to lower embodied emissions.

Table 4. Environmental performance comparison between new and SLB systems under rule-based dispatch over 10-year project lifetime.

Metric	New Battery	Second-Life Battery	Advantage
Battery embodied emissions ($kgCO_2e$)	43,440	25,340	−41.2%
Transport emissions ($kgCO_2e$)	1810	1810	-
BOS embodied emissions ($kgCO_2e$)	11,584	11,584	-
PCS embodied emissions ($kgCO_2e$)	2534	2534	-
Carbon intensity ($kgCO_2e/kWh$)	−0.23	−0.25	−8.0%

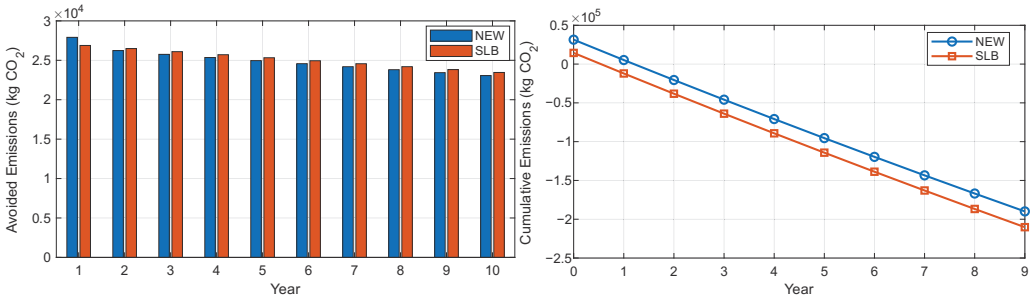

(**a**) (**b**)

Figure 5. Annual GHG emissions: (**a**) Avoided emissions. (**b**) Cumulative emissions.

This comparison highlights that the lower acquisition cost and reduced embodied emissions of SLBESS outweigh its technical performance limitations, resulting in superior economic returns and competitive environmental outcomes for commercial building applications.

4.3. Sensitivity Analysis

4.3.1. Impact of Control Strategy

Advanced control strategies can enhance SLBESS economic performance by optimizing dispatch relative to TOU tariff structures and PV generation patterns. Table 5 compares the performance of rule-based and MPC strategies for SLBESS over the 10-year project lifetime. Under MPC, SLBESS achieves an NPV of $56,914, compared to $45,358 under rule-based control, representing a 25.5% improvement. The IRR increases from 14.4% to 16.6%, while $LCOS_{op}$ decreases from $183/MWh to $173/MWh. The carbon intensity becomes less negative (from −0.25 to −0.23 $kgCO_2e/kWh$), indicating slightly lower net carbon reduction per kWh delivered, as MPC's increased throughput generates proportionally more charging emissions. These results demonstrate that advanced control strategies can extract additional value from SLBESS through improved forecasting and dispatch optimization.

Table 5. Performance comparison with different control strategies.

Metric	Rule-Based	MPC	Advantage
NPV @ 10 years ($)	45,358	56,914	+25.5%
IRR (%)	14.4	16.5	+14.6%
$LCOS_{op}$ ($/MWh)	183	173	−5.5%
Carbon intensity ($kgCO_2e/kWh$)	−0.25	−0.23	+8.0%

4.3.2. Key Parameter Sensitivities

Figure 6 presents tornado diagrams quantifying the sensitivity of key performance metrics, including NPV, $LCOS_{op}$, and carbon intensity, to variations in technical, economic,

and environmental parameters for SLBESS. Each parameter is varied across the range defined in Table 2, while all other variables are held at baseline values.

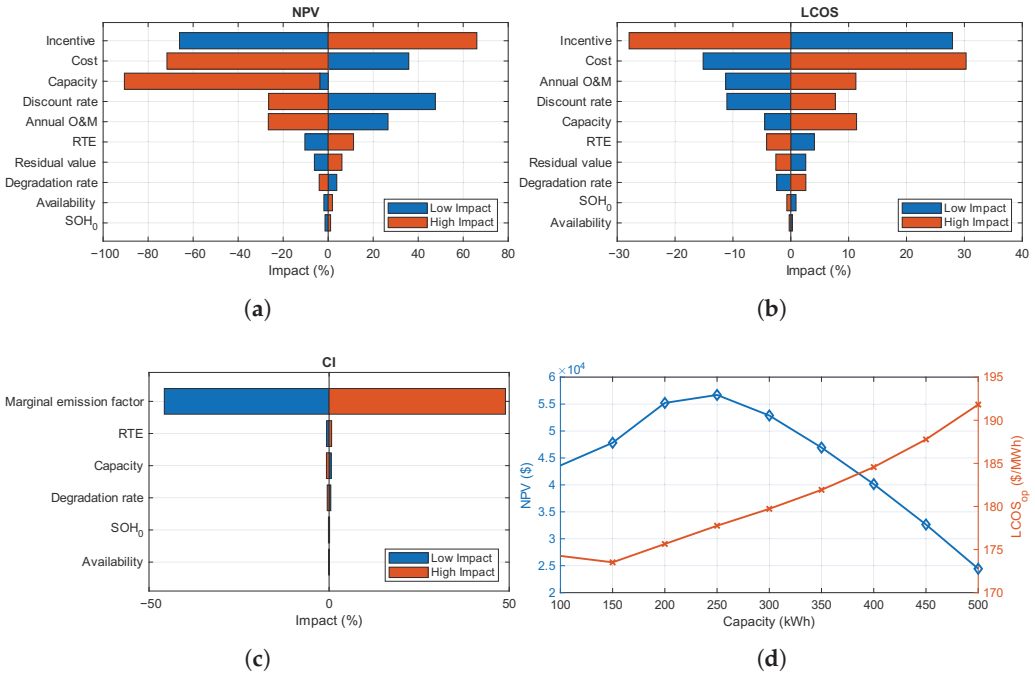

Figure 6. Sensitivity analysis: (**a**) tornado diagram of NPV. (**b**) tornado diagram of $LCOS_{op}$. (**c**) tornado diagram of carbon intensity. (**d**) economic metrics with different capacities.

NPV sensitivity: The incentive rate is the dominant factor, producing NPV variations from −66% to +66% across the 0–50% range, followed by the core cost ($50–$200/kWh), which results in an NPV variation from 36% to −71%. Capacity exhibits a nonlinear impact, as illustrated in Figure 6d: NPV peaks at intermediate capacities (250 kWh), where system size balances revenue potential against capital expenditures. Undersized systems fail to capture available PV and demand charge reduction opportunities, while oversized systems incur excessive capital expenditures without proportional revenue gains, due to limited building load and solar generation. This finding underscores the importance of sizing storage to the local PV-to-load ratio. Discount rate, O&M, and round-trip efficiency exhibit moderate influence. Degradation rate, initial SOH, residual value, and availability demonstrate minimal sensitivity ($<\pm 10\%$), suggesting that moderate variations in battery condition do not substantially affect project viability.

$LCOS_{op}$ sensitivity: Incentive rate and core cost remain the most influential factors, while round-trip efficiency and O&M costs gain relative importance due to their direct effect on energy delivered.

Carbon intensity: The marginal emission factor overwhelmingly dominates, with a range of 0.10–0.49 $kgCO_2e/kWh$ yielding carbon intensity values from −0.38 to −0.15 $kgCO_2e/kWh$, representing a 95% swing. This highlights that the climate value of SLBESS is highly dependent on grid carbon intensity, with greater benefits achieved in fossil-fuel-dominant grids. Round-trip efficiency ranks second, while capacity and degradation rates exhibit minimal influence, as both embodied and avoided emissions scale proportionally with throughput.

The sensitivity analysis reveals distinct parameter hierarchies across economic and environmental performance dimensions. Economic viability is primarily driven by financial parameters, including incentives, capital cost, and discount rate, while environmental outcomes are dominated by grid emission factors and round-trip efficiency. Technical

parameters frequently cited as barriers to second-life adoption, such as degradation rate, SOH, and availability, exhibit low sensitivity across all metrics, suggesting that concerns about battery condition may be overstated relative to economic and policy factors. The critical influence of the incentive rate on both NPV and $LCOS_{op}$ highlights the enabling role of policy support, while the dominance of the marginal emission factor underscores the importance of region-specific environmental assessments.

4.4. Discussion

This dispatch-aware assessment, based on one year of high-resolution operational data, demonstrates that SLBESS can deliver superior economic and environmental performance in commercial buildings, despite reduced technical specifications. Counterfactual analysis reveals that acquisition cost and policy incentives are the primary drivers of system viability. Sensitivity results show that commonly cited barriers to second-life adoption, including degradation rate, SOH, and availability, exhibit minimal impact within realistic ranges. Specifically, the low sensitivity of $LCOS_{op}$ and NPV to the degradation rate suggests that the economic impact of potential non-linear degradation is likely minimal over the project's 10-year horizon, as financial returns are dominated by early-year performance. System sizing, grid carbon intensity, and control strategy emerge as more critical to performance than battery condition. These findings suggest that SLBESS deployment in commercial buildings is economically and environmentally viable under supportive policy and market conditions. Acquisition cost, incentive availability, and grid carbon intensity are the critical enablers. Although the study on a single commercial building in San Diego gives location-specific results of NPV, IRR and carbon intensity, the comparative advantage of SLBBESS over new batteries and the sensitivity analysis trends are expected to hold in regions with similar conditions. In addition, the proposed framework is portable and can be applied to other sites by substituting location-specific inputs.

Several limitations should be acknowledged: (1) This study is based on a single commercial building in San Diego, which may not represent the diversity of climates, building types, or tariff structures. (2) Battery degradation was modeled using empirical cycling data rather than physics-based electrochemical models or advanced machine learning approaches, introducing uncertainty in long-term performance projections, particularly when extrapolating across diverse operational conditions and heterogeneous battery populations. (3) LCA results depend on region-specific emission factors and assumptions regarding second-life burden allocation. (4) The economic analysis assumes stable tariffs and incentive programs, both of which are subject to policy changes. (5) One year of operational data is repeated across the project lifetime, not accounting for year-to-year variations in load profiles or tariff structures.

Future work should extend this study in several directions: (1) Multi-site validation across diverse climates, building types, and utility rate structures to improve generalizability; (2) Integration of physics-based and data-driven degradation models to improve lifetime prediction accuracy. Recent AI-enabled frameworks address data scarcity, heterogeneity, and cross-condition prediction challenges for battery reuse and recycling [23]. Integrating such advanced models could further improve long-term performance projections in future work. (3) Prospective analyses that incorporate dynamic electricity prices, evolving grid emission factors, and projected technology cost trajectories; (4) Assessment of hybrid revenue models that combine bill savings with grid services such as frequency regulation, demand response, and capacity markets; (5) Evaluation of regulatory pathways, safety certification, and standardization frameworks to accelerate commercial-scale deployment.

5. Conclusions

This study evaluated the techno-economic and environmental viability of second-life battery energy storage systems in commercial buildings, using one year of high-resolution operational data from a case study in San Diego, California. A comparative assessment against equivalent new battery systems under identical operating conditions provides field-validated insights into deployment viability.

SLBESS demonstrates superior economic performance despite lower technical specifications, achieving 49% higher NPV, 42% higher IRR, and 14% lower operational levelized cost of storage over a 10-year project lifetime. The lower acquisition cost of SLBESS outweighs efficiency penalties, demonstrating that the economic advantages of repurposing can offset performance limitations. Environmentally, SLBESS reduces embodied emissions by 41% and achieves 9% lower carbon intensity, with carbon payback occurring within the first year.

Sensitivity analysis shows that economic viability depends primarily on financial parameters, such as incentive rate and acquisition cost, while environmental outcomes are dominated by grid emission factors. Parameters frequently cited as barriers to second-life adoption, such as degradation rate, SOH, and availability, exhibit minimal sensitivity, suggesting that technical concerns may be overstated relative to economic and policy drivers. This hierarchy of parameters offers an actionable guide: policymakers should focus on financial incentives to accelerate deployment, while developers should target regions with carbon-intensive grids to maximize environmental benefits. The minimal sensitivity to battery degradation suggests that design standards can be relaxed, reducing repurposing costs.

These findings demonstrate that second-life batteries can provide cost-effective, low-carbon energy storage in commercial buildings, with acquisition cost and grid carbon intensity emerging as critical enablers under favorable policy conditions. The dispatch-aware framework developed here offers actionable insights for stakeholders considering second-life battery deployment.

Author Contributions: Conceptualization, C.M. and Z.C.; methodology, Z.C. and C.M.; software, Z.C.; validation, Z.C.; formal analysis, Z.C.; investigation, Z.C. and N.V.K.; resources, C.M.; data curation, Z.C.; writing—original draft preparation, Z.C. and N.V.K.; writing—review and editing, Z.C., C.M. and N.V.K.; visualization, Z.C.; supervision, C.M.; project administration, C.M.; funding acquisition, C.M. All authors have read and agreed to the published version of the manuscript.

Funding: This research was funded by the California Energy Commission, via grant number EPC-19-053.

Data Availability Statement: Data is available on request from the corresponding author.

Conflicts of Interest: The authors declare no conflicts of interest.

References

1. Neigum, K.; Wang, Z. Technology, Economic, and Environmental Analysis of Second-Life Batteries as Stationary Energy Storage: A Review. *J. Energy Storage* **2024**, *103*, 114393. [CrossRef]
2. Aguilar Lopez, F.; Lauinger, D.; Vuille, F.; Müller, D.B. On the Potential of Vehicle-to-Grid and Second-Life Batteries to Provide Energy and Material Security. *Nat. Commun.* **2024**, *15*, 4179. [CrossRef] [PubMed]
3. Patel, A.N.; Lander, L.; Ahuja, J.; Bulman, J.; Lum, J.K.H.; Pople, J.O.D.; Hales, A.; Patel, Y.; Edge, J.S. Lithium-Ion Battery Second Life: Pathways, Challenges and Outlook. *Front. Chem.* **2024**, *12*, 1358417. [CrossRef] [PubMed]
4. Rufino Júnior, C.A.; Riva Sanseverino, E.; Gallo, P.; Koch, D.; Kotak, Y.; Schweiger, H.G.; Zanin, H. Towards a Business Model for Second-Life Batteries: Barriers, Opportunities, Uncertainties, and Technologies. *J. Energy Chem.* **2023**, *78*, 507–525. [CrossRef]
5. Catsaros, O. *Lithium-Ion Battery Pack Prices See Largest Drop Since 2017, Falling to $115 per Kilowatt-Hour: BloombergNEF*; BloombergNEF: London, UK, 2024.

6. Gharebaghi, M.; Rezaei, O.; Li, C.; Wang, Z.; Tang, Y. A Survey on Using Second-Life Batteries in Stationary Energy Storage Applications. *Energies* **2025**, *18*, 42. [CrossRef]
7. Akram, M.N.; Abdul-Kader, W. Repurposing Second-Life EV Batteries to Advance Sustainable Development: A Comprehensive Review. *Batteries* **2024**, *10*, 452. [CrossRef]
8. Rallo, H.; Canals Casals, L.; De La Torre, D.; Reinhardt, R.; Marchante, C.; Amante, B. Lithium-Ion Battery 2nd Life Used as a Stationary Energy Storage System: Ageing and Economic Analysis in Two Real Cases. *J. Clean. Prod.* **2020**, *272*, 122584. [CrossRef]
9. Steckel, T.; Kendall, A.; Ambrose, H. Applying Levelized Cost of Storage Methodology to Utility-Scale Second-Life Lithium-Ion Battery Energy Storage Systems. *Appl. Energy* **2021**, *300*, 117309. [CrossRef]
10. Fallah, N.; Fitzpatrick, C. How Will Retired Electric Vehicle Batteries Perform in Grid-Based Second-Life Applications? A Comparative Techno-Economic Evaluation of Used Batteries in Different Scenarios. *J. Clean. Prod.* **2022**, *361*, 132281. [CrossRef]
11. Lieskoski, S.; Tuuf, J.; Björklund-Sänkiaho, M. Techno-Economic Analysis of the Business Potential of Second-Life Batteries in Ostrobothnia, Finland. *Batteries* **2024**, *10*, 36. [CrossRef]
12. Zhuang, J.; Bach, A.; van Vlijmen, B.H.C.; Reichelstein, S.J.; Chueh, W.; Onori, S.; Benson, S.M. Technoeconomic Decision Support for Second-Life Batteries. *Appl. Energy* **2025**, *390*, 125800. [CrossRef]
13. Turan, F.; Boynuegri, A.R.; Durmaz, T. Comprehensive Technical and Economic Evaluations of Using Second-Life Batteries as Energy Storage in off-Grid Applications: A Customized Cost Analysis. *J. Energy Storage* **2025**, *120*, 116379. [CrossRef]
14. Cusenza, M.A.; Guarino, F.; Longo, S.; Mistretta, M.; Cellura, M. Reuse of Electric Vehicle Batteries in Buildings: An Integrated Load Match Analysis and Life Cycle Assessment Approach. *Energy Build.* **2019**, *186*, 339–354. [CrossRef]
15. Kamath, D.; Shukla, S.; Arsenault, R.; Kim, H.C.; Anctil, A. Evaluating the Cost and Carbon Footprint of Second-Life Electric Vehicle Batteries in Residential and Utility-Level Applications. *Waste Manag.* **2020**, *113*, 497–507. [CrossRef] [PubMed]
16. Cheng, M.; Ran, A.; Zheng, X.; Zhang, X.; Wei, G.; Zhou, G.; Sun, H. Sustainability Evaluation of Second-Life Battery Applications in Grid-Connected PV-battery Systems. *J. Power Sources* **2022**, *550*, 232132. [CrossRef]
17. Saez de Bikuña, K.; Pierobon, M.; Soldati, C.; Vale, M.; Picone, N. Repurposing of Electric Vehicle Batteries for Second Life Stationary Applications in Residential Photovoltaic Systems: An Environmental and Economic Sustainability Assessment. *Int. J. Environ. Res.* **2025**, *19*, 119. [CrossRef]
18. Hasan, A.S.M.J.; Enriquez-Contreras, L.F.; Yusuf, J.; Ula, S. A Comprehensive Building Load Optimization Method from Utility Rate Structure Perspective with Renewables and Energy Storage. In Proceedings of the 2021 International Conference on Smart Energy Systems and Technologies (SEST), Vaasa, Finland, 6–8 September 2021; pp. 1–6. [CrossRef]
19. Dong, Q.; Liang, S.; Li, J.; Kim, H.C.; Shen, W.; Wallington, T.J. Cost, Energy, and Carbon Footprint Benefits of Second-Life Electric Vehicle Battery Use. *iScience* **2023**, *26*, 107195. [CrossRef] [PubMed]
20. BESS Costs Analysis: Understanding the True Costs of Battery Energy Storage Systems, 2024. Available online: https://exencell.com/blogs/bess-costs-analysis-understanding-the-true-costs-of-battery-energy-storage-systems (accessed on 6 November 2025).
21. Gao, W.; Cao, Z.; Fu, Y.; Turchiano, C.; Kurdkandi, N.V.; Gu, J.; Mi, C. Comprehensive Study of the Aging Knee and Second-Life Potential of the Nissan Leaf e+ Batteries. *J. Power Sources* **2024**, *613*, 234884. [CrossRef]
22. Fischer, M.; Brand, M.J.; Karger, A.; Gomez, M.R.; Rehm, M.; Natterer, J.; Jossen, A. How Degradation of Lithium-Ion Batteries Impacts Capacity Fade and Resistance Increase: A Systematic, Correlative Analysis. *J. Power Sources* **2025**, *656*, 237921. [CrossRef]
23. Tao, S.; Guo, R.; Lee, J.; Moura, S.; Canals Casals, L.; Jiang, S.; Shi, J.; Harris, S.; Zhang, T.; Yung Chung, C.; et al. Immediate Remaining Capacity Estimation of Heterogeneous Second-Life Lithium-Ion Batteries via Deep Generative Transfer Learning. *Energy Environ. Sci.* **2025**, *18*, 7413–7426. [CrossRef]

Disclaimer/Publisher's Note: The statements, opinions and data contained in all publications are solely those of the individual author(s) and contributor(s) and not of MDPI and/or the editor(s). MDPI and/or the editor(s) disclaim responsibility for any injury to people or property resulting from any ideas, methods, instructions or products referred to in the content.

batteries

MDPI

Article

Multi-Objective Sizing Method for PV-BESS Integration with EV Charging Stations and Analysis Across Different Parking Scenarios

Francesco Maria Tiburtini [1], Francesco Lo Franco [2] and Mattia Ricco [1,*]

[1] Department of Electrical, Electronic, and Information Engineering "Guglielmo Marconi" (DEI), University of Bologna, 40136 Bologna, Italy; francesco.tiburtini2@unibo.it
[2] Syniergy S.r.l., 40128 Bologna, Italy; f.lofranco@syniergy.it
* Correspondence: mattia.ricco@unibo.it

Abstract

The growing adoption of electric vehicles (EVs) is driving the expansion of charging networks. Local photovoltaic (PV) systems combined with battery energy storage systems (BESS) have emerged as promising solutions to mitigate the impact of charging demand on the grid and reduce the environmental impact of EV charging. In this context, proper sizing of PV-BESS systems is crucial to maximize their integration with charging hubs (CHs) and ensure optimal performance. This paper proposes a multi-objective sizing method to optimize the energy and economic performance of PV-BESS systems in EV charging hubs. Sizing optimization is performed using a Non-Dominated Sorting Genetic Algorithm-II. The method is applied to four CH scenarios characterized by variations in energy demand, user behavior, and location. Results indicate that while optimal PV size remains relatively consistent across scenarios, the ideal BESS configuration varies with each scenario's characteristics. Optimized PV-BESS integration significantly improves energy performance, increasing system self-sufficiency by up to +72%. From an economic point of view, results show that in some cases, smaller BESS capacities are more advantageous due to lower capital costs, while in others, larger BESS sizes reduce overall costs by up to −50%, significantly cutting utility expenses despite higher initial investment.

Keywords: photovoltaic systems; battery energy storage systems; electric vehicles; charging stations; sizing optimization; multi-objective optimization

1. Introduction

The number of electric vehicles (EVs) is expected to grow significantly in the coming years as the transition to cleaner and more sustainable transportation accelerates. In Europe, according to [1], the share of electric vehicles is expected to rise to up to 38% by 2035. While EV represent a concrete solution for reducing pollutants and greenhouse gas emissions, this growth in EV share will lead to an increase in the number of charging hubs (CHs) needed to support EV load demand. However, the energy provided by the grid for EV charging is predominantly generated from fossil fuels rather than renewable sources [2]. The reliance on fossil-fuel-based grid power for charging undermines the potential of EVs to completely eliminate carbon emissions. Moreover, as reported in [3], the increasing number of charging stations may lead to higher peak demand in the coming years, potentially causing line and transformer overloads and stability problems within the distribution grid.

To mitigate these issues, the integration of local photovoltaic (PV) systems has proven to be a promising option, although it also presents certain challenges. Due to the inherent intermittency of PV production, there may be a mismatch between energy generation and EV charging demands. This mismatch between production and load forces reliance on the grid to meet the load. For this reason, the integration of a battery energy storage system (BESS) with PV system can help reduce grid dependency by serving as an energy buffer, storing excess energy generated during the day and releasing it when the load exceeds generation, thereby reducing the environmental impact of EV charging and relieving stress on the distribution grid [3]. Moreover, the growing demand for clean transportation further emphasizes the need for sustainable energy solutions, especially when considering that some European countries are already moving towards mandatory installation of photovoltaic panels even for small-/medium-sized car parks [4]. For these reasons, it is essential to optimize the energy performance of the CHs, by minimizing the reliance on grid energy [5]. Moreover, ensuring the economic viability of the PV-BESS system is crucial for adoption by CHs stakeholders, making it important to consider both energy performance and financial feasibility. In this context, proper sizing of the PV-BESS system is crucial. It ensures optimal utilization of the PV-generated energy while minimizing operational costs. In fact, oversizing the system can lead to increased capital expenditures and reduced profitability, whereas undersizing risks system inefficiencies and potential failure [6].

Several studies have explored the optimal sizing of PV–BESS systems integrated with EV charging hubs. The optimal system size is determined by considering one or more objective functions. Among these, many works have employed cost-based indicators such as the Levelized Cost of Energy (LCOE) to evaluate system performance, representing the average cost of the energy supplied to EVs. For instance, Khawaja et al. [6] proposed an optimal cost-based model for grid-connected PV–BESS sizing, while Dai et al. [7] applied a particle swarm optimization approach to minimize LCOE. Other studies assessed economic performance through the annualized system cost: Liu et al. [8] analyzed PV–BESS integration in fast charging stations, including battery degradation, and Zhou et al. [9] proposed an optimization framework for smart households under different price mechanisms. Finally, Yan et al. [10] and Nafeh et al. [11] minimized the total system cost, which accounts for both investment and operating expenses over the system lifetime. On the other hand, energy performance has not been sufficiently explored. In fact, only a small number of studies have addressed this, but they do not take into account the specific load caused by EV charging. In ref. [12], an energy-based optimization approach to size integrated PV-BESS systems for residential and commercial settings is proposed. The target is to properly size the system to minimize buying and selling energy from/to the grid. The proposed methodology evaluates various PV and BESS configurations based on real annual load data, optimizing the amount of energy stored into the battery to reduce energy exchanged with the grid. The results demonstrate that PV-BESS systems can significantly reduce gross energy consumption, achieving reductions of approximately 80% for residential users and 40% for commercial users. However, this approach focuses only on energy optimization, without considering the system's economic performance. To achieve this, in ref. [13] the authors developed a sizing tool for hybrid PV-BESS systems aimed at optimizing both the energy and economic performance by minimizing both the degree of energy exchange with the grid and the cost of the investment. The study focuses on a building scenario and employs a particle swarm optimization algorithm to reduce computational time while providing efficient solutions. However, this study, like the previous one, does not specifically account for the load associated with electric vehicle charging, which is more variable and fluctuating than traditional building loads. In conclusion, none of the studies reviewed

above has addressed the optimal sizing of PV-BESS systems integrated with EV charging hubs to optimize both energy and economic performance.

In addition, studies in the literature addressing the sizing of PV-BESS systems for EV charging hubs often fail to consider the specific characteristics of the CH location. Instead, most of these studies model the load of charging hubs as generic, without accounting for location specific factors that influence energy demand. For instance, Liu et al. [8] and Yan et al. [10] optimized photovoltaic and battery capacities for fast charging stations using predefined or stochastic EV arrival patterns, without distinguishing between different hub typologies. Similarly, Nafeh et al. [11] and Fang et al. [14] proposed techno-economic optimization models for PV–BESS systems, yet based their analysis on synthetic or generalized EV demand profiles instead of measured data representative of specific locations. This simplification ignores important factors, such as vehicle type, arrival time, charging power, and duration, which significantly impact energy demand [15]. To overcome this limitation, sizing of PV-BESS systems for CH integration must consider the unique load characteristics determined by the station's location. In this sense, in ref. [16], the authors proposed a multi-objective optimization approach aimed at reducing both the system cost and the pollutant emissions for the optimal sizing of PV-BESS system in a ultra-fast charging station of EVs, designed to serve EVs during medium- or long-distance travels, typically installed along motorways. The authors in ref. [17] focused on the optimal sizing of a PV-BESS system and its power management to minimize the overall energy cost. The effectiveness of the proposed model was demonstrated by considering as the load a charging hub with three EV chargers located at an office building. However, these studies consider only a single location, without comparing multiple scenarios that would allow an analysis of how the specific charging hub scenario impacts the optimal PV-BESS sizing. This gap highlights the need for a comparative approach to evaluate the influence of varying locations and operational conditions on optimal system configurations.

In the context of PV-BESS optimal sizing, accurately assessing the system's economic performance requires a precise calculation of the battery's lifetime, based on its characteristics and operation, as BESS related costs represent a significant portion of the system's total cost. However, many studies often overlook this or use simplified models. For instance, Leone et al. [16], Dai et al. [7], Islam et al. [18], and Alshammari et al. [19] assumed fixed battery lifetimes of 20, 10, 4, and 25 years, respectively, irrespective of the actual operating conditions. While this approach simplifies the analysis, it is sub-optimal because it does not take into account the actual effects of operating conditions. The latter have a significant impact on the actual life of a battery and therefore on its economics and replacement schedule. By using a fixed lifetime assumption, the analysis may overestimate or underestimate the economic performance of the system, leading to inaccurate conclusions and potentially suboptimal system designs. In the literature, battery lifetime estimation models were proposed. In [6], battery degradation is modeled using a simple annual percentage factor, applied uniformly to calculate the available capacity over time. However, this approach does not account for key operational variables such as charge/discharge cycles, depth of discharge, thereby limiting its accuracy. In ref. [20], the battery lifetime is estimated using a simplified approach that calculates the number of cycles based on cumulative SOC variations and a fixed depth of discharge of 80%. The battery is considered exhausted once the number of cycles reaches 3000, while this method is computationally efficient, it lacks accuracy as it does not account for variations in depth of discharge across different cycles, which have a varying impact on the overall battery lifetime. The model calculates cyclical degradation, but in addition to usage cycles, battery degradation is also influenced by periods of inactivity during which the battery is not in use. This type of degradation is known as calendar aging, and it is influenced by factors such as temperature, downtime

duration, and state of charge during downtimes, further impacting the overall battery life. In this sense, the authors in ref. [17], in addition to cyclic degradation, propose a model where calendar degradation is treated as a fixed parameter, set at 2% per year, while this approach simplifies the analysis, it overlooks the potential fluctuations in calendar degradation that may arise from operational factors, thus failing to capture its variability over time. In conclusion, generally, BESS lifetime loss is ignored or simplified in several studies concerning the sizing of PV-BESS systems integrated with EV charging hubs. However, since the BESS replacement cost represents a significant expense over the system's lifetime, it is necessary to establish a precise BESS model that takes into account this loss.

To the best of the author's knowledge, none of the reviewed papers addresses the multi-objective sizing optimization of PV-BESS systems combined with EV charging hubs, considering both energy and economic performance. Furthermore, the papers analyzed in this context consider either a generic CH load or a single CH site load, but do not consider multiple CH sites simultaneously. Finally, the literature review revealed that papers often fail to accurately estimate the lifetime of BESS, taking into account its characteristics and operation. To address these current limitations regarding the sizing optimization of PV-BESS systems integrated with EV charging hubs aiming to maximize both energy and economic performance, this paper proposes a framework to maximize, on one side, the energy independence of the CH from the grid, and on the other side, to maximize the economic profitability for the CH's stakeholders by minimizing the cost of the energy supplied to EVs. Furthermore, various charging locations are evaluated to explore a wider range of scenarios in various real-world contexts enabling an assessment of the impact on system sizing and performance across different scenarios. The EV power demand is calculated using a probabilistic approach based on real-world data on vehicle arrival and departure times from four different car parks, specifically, a paid public car park, a workplace car park, a municipal car park, and a mall car park. Finally, to improve the accuracy of BESS lifespan estimation compared to previous studies, a BESS degradation model is proposed that estimates battery life by considering both cyclic and calendar degradation based on real operating conditions. Photovoltaic power production data were sourced from the Photovoltaic Geographical Information System (PVGIS) to obtain realistic solar generation with a time resolution of 15 min. To simulate the power exchange between the system components, a battery power flows model has been developed. This model aims for evaluating the performance of the PV-BESS system, as it enables the calculation of energy flows and SOC variations. Finally, the resulting multi-objective optimization problem is solved using a metaheuristic approach. To identify the most suitable method for this class of problems, three state-of-the-art multi-objective algorithms are compared: Non-dominated Sorting Genetic Algorithm II (NSGA-II), Multi-Objective Evolutionary Algorithm based on Decomposition (MOEA/D), and Multi-Objective Particle Swarm Optimization (MOPSO). A comprehensive statistical analysis demonstrates that NSGA-II achieves superior stability and computational efficiency while maintaining equivalent Pareto front quality to competing approaches, making it the reference algorithm for system sizing across all scenarios.

The rest of the paper is organized as follows. Section 2 presents the data used for the simulation, the battery power flows model, and the degradation model. In Section 3 the objective functions are presented and the multi-objective problem is defined. Energy and economic results are presented and described in Section 4. Finally, Section 5 presents the conclusions.

2. System Modeling

In this section, the system under study is introduced, providing a full overview of the key components involved. Figure 1 shows the system under analysis that comprises a photovoltaic plant, generating the PV power P_{PV}, a charging hub with multiple EV charging points, consuming the load power P_{EV}, and a battery storage system, which can provide the power P_{B} as a buffer between generation and load. The system elements are connected and exchange power with the external grid, designated as P_{G}. The following balance equation holds:

$$P_{\mathrm{PV}} - P_{\mathrm{EV}} + P_{\mathrm{B}} = P_{\mathrm{G}} \tag{1}$$

where P_{B} is defined as negative during charging and positive during discharging of the BESS. P_{G} is assumed negative when the power is injected to the grid and positive when consumed.

The objective of this section is to present a method for modeling each element of the system in terms of power flows. In order to accurately assess the variability of the photovoltaic source, it is essential to consider both seasonal and daily fluctuations. Consequently, a minimum time horizon of one year is required for analysis. To also take into account the intermittency of both load and production, a 15-min resolution is adopted. In the following, Section 2.1 models and calculates the PV production, Section 2.2 focuses on the EV load, and Section 2.3 addresses the BESS operation with 15-min resolution for a one-year time range. In addition to analyzing power flows, it is essential to examine the price values of the energy exchanged with the external grid in order to conduct a comprehensive economic assessment. Finally, to obtain meaningful economic results from the optimization algorithm, the energy price profiles and consequently the grid energy cost model are developed in Section 2.4.

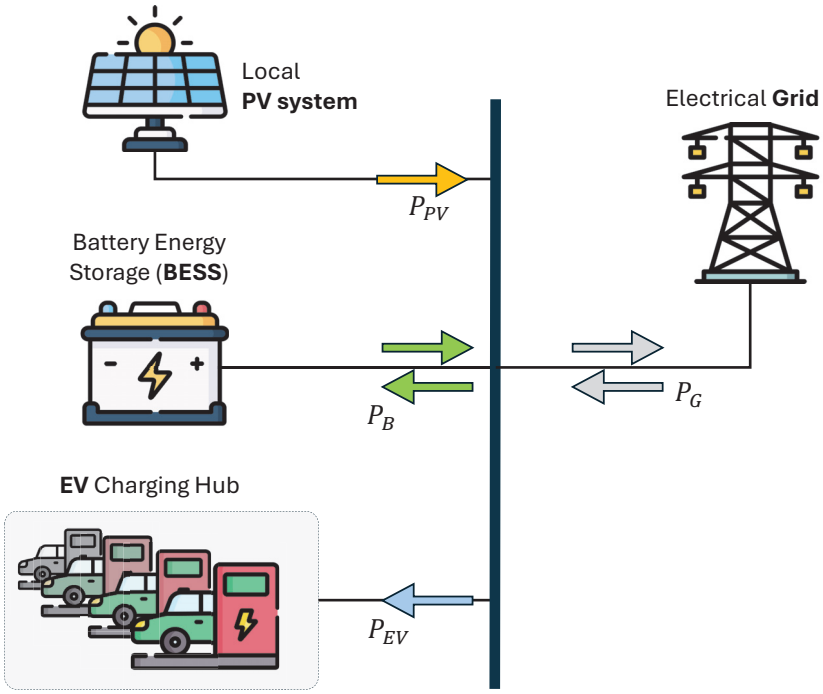

Figure 1. Reference scenario and nomenclature of the power flow for each element.

2.1. PV Power Profile Modeling

The PV power profile $P_{\mathrm{PV}}(t)$, can be calculated using the following equation:

$$P_{\mathrm{PV}}(t) = S_{\mathrm{PV}} \bar{P}_{\mathrm{PV}}(t) \tag{2}$$

where S_{PV} represents the peak power of the system, which is equivalent to the PV size in kWp. The variable $\bar{P}_{PV}(t)$ is the normalized power profile, expressed as a function of its peak power (kW/kWp). In other words, $\bar{P}_{PV}(t)$ denotes the power profile of a 1 kWp PV system. By employing Equation (2), it is possible to assess the power profile of PV plants with different sizes by varying S_{PV}, but nevertheless keeping $\bar{P}_{PV}(t)$ unchanged.

The normalized power profile can be calculated from environmental data, such as irradiance and temperature. One of the most commonly used models for calculating photovoltaic output is expressed in Equation (3) [21]:

$$\bar{P}_{PV}(t) = \frac{G(t)}{G_{STC}}[1 + \gamma(T_{cell}(t) - T_{STC})]\eta_{loss} \quad (3)$$

where $G(t)$ is the global irradiance profile (W/m^2) on the PV-array plane (inclined plane), T_{cell} is the operating temperature of the PV cell (°C), G_{STC} and T_{STC} are the irradiance and cell temperature under standard test condition, respectively, 1000 W/m^2 and 25 °C. The temperature coefficient γ represents how much the nominal power varies with respect to cell temperature, and is usually between $-0.3\%/°C$ and $-0.5\%/°C$ for many silicon photovoltaic modules. Furthermore, the η_{loss}-coefficient take into account the conversion losses from the DC to AC side of the system.

The cell temperature is related to the ambient temperature (T_{amb}) and can be estimated using the following formula:

$$T_{cell}(t) = T_{amb}(t) + \frac{G(t)}{G_{NOCT}}(T_{NOCT} - 20\,°C) \quad (4)$$

where T_{NOCT} is the Nominal Operating Cell Temperature (NOCT), which is a standard measure describing the cell temperature under irradiance of G_{NOCT} = 800 W/m^2 and ambient temperature of 20 °C. The values of both γ and T_{NOCT} can be readily derived from the module data sheet. It is worth noting that non-optimal operating conditions, such as module mismatch, partial shading, or hotspot effects, were not explicitly modeled in this work. Their influence could be represented by introducing a correction factor into Equation (3), modifying the overall PV efficiency to account for additional losses.

In order to conduct a one-year analysis with a sufficient level of resolution, data from the Photovoltaic Geographical Information System [22] are retrieved. PVGIS is a free and open-access tool that allows the assessment of photovoltaic output based on historical meteorological data. All PVGIS tools can be accessed via web APIs, and the information required for Equation (3) model can be retrieved by setting the PV system parameters, such as the location of the plant, the tilt angle of the PV arrays, the PV system losses, and so forth. Table 1 shows the setting of the main parameters used to calculate the normalized PV profile. The T_{NOCT} and γ parameters are retrieved from ref. [23], whereas the system losses are set in accordance with ref. [24].

Table 1. Setting of the PV model parameters.

Parameter	Value
Location	Bologna, Italy
Tilt angle	30°
Azimuthal orientation	South
Weather database	PVGIS-SARAH2
PV-cell technology	Crystalline Silicon
NOCT temperature (T_{NOCT})	45 °C
Temperature coeff. (γ)	$-0.45\%/°C$
Percentage system losses	14%

Finally, Figure 2 illustrates one year of the $\bar{P}_{PV}$ profile with 15-min resolution, taking into account the weather historical data from 2023 and the settings outlined in Table 1. The figure demonstrates the incorporation of both seasonal and daily power variability in the proposed PV model.

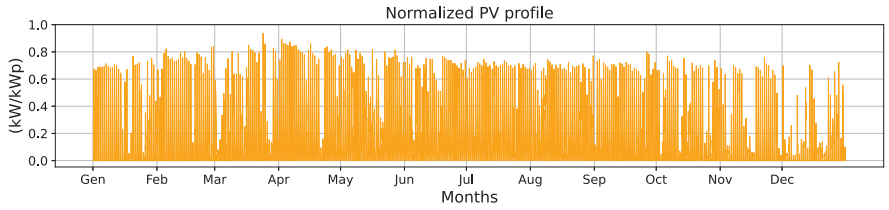

Figure 2. One-year $\bar{P}_{PV}$ power profile with 15-min resolution based on historical weather data from 2023.

2.2. EV Charging Demand Modeling

A reasonable prediction of the load profile is necessary to accurately address the sizing optimization problem. EV demand profile may depend on multiple factors such as the number of daily users and their behavior in terms of arrival, departure and parking time. The power rating of the charging infrastructure may affect the peak power and the charging session duration, as well as the characteristics of the EV models in terms of maximum charging rate. The objective of this Section is to calculate the power demand of a charging hub, designated as P_{EV}, over one-year period with a resolution of 15 min. For this purpose, the algorithm developed in ref. [15] is adapted and employed in this work. The algorithm uses a probabilistic approach to generate realistic load profiles by analyzing real-world data on vehicle arrival and departure times for various parking scenarios. These patterns are reconstructed based on probabilities to reflect typical user behavior. A similar approach is employed to estimate the initial SOC of EVs upon their arrival at the charging hub and their energy demand. Additionally, an EV battery charging behavioral model is also implemented in ref. [15] to account for the different charging characteristics of various EV models.

As reported in ref. [15], users' behavior can significantly change depending on the parking scenario. These differences in arrival and parking times are reflected in the charging hub's load profile. Starting from a data collection campaign carried out on several parking lots located in the urban area of Bologna, some of the most common urban scenarios are analyzed and described below:

- Paid public car park: in urban contexts, such as city center car parks, the distribution of arrival and departure times is more concentrated during daytime hours. Users may arrive at different times of the day, either for work activities or for leisure or shopping purposes. However, data indicate a slight increase in users' arrivals during the morning and evening peak hours. The average parking time is approximately 120 min.
- Working place car park: this scenario refers to typical parking lots in company or office areas, where usage follows a routine aligned with standard working hours. Consequently, arrival and departure time presents a well-defined pattern. Most arrivals are concentrated in the early morning hours, with the majority of departures in the late afternoon. The average parking time is about 6 h.
- Municipal car park: this scenario concerns a municipal public car park, with users arriving at different times of the day. It presents similar arrival and departure profiles to the previous city car park, with user numbers increasing during traffic peak hours. However, the data set presents a higher variance and longer parking times, with an average duration of 140 min.
- Mall car park: in this scenario, there is a high flow of users during the daytime, with a moderate increase in the evening hours. The average parking duration is shorter than in previous scenarios, around 60 min, as users tend to park for shopping or brief visits.

The input settings of the EV load demand model proposed in ref. [15] are as follows: the number of users per day (N_{EV}), i.e., the number of daily charging sessions; the car park scenario; and the maximum power rating available at the charging point (P_{CP}). It should be noted that the resulting CH load profile, given by the sum of each charging session power, can present significant changes as the input settings change. For each scenario, a trade-off value of P_{CP} is determined to ensure users have an adequate SOC at departure, while preventing oversizing of the charging infrastructure's power capacity. This value is evidently higher for scenarios with a lower average parking time. The characteristics of the charging point infrastructure are then set according to reference [15] and reported in Table 2.

The algorithm permits the calculation of EVs' load profile on a daily basis; however, the analysis proposed in this paper is on an annual basis. Consequently, a typical week is reconstructed from the daily profiles, which are then repeated to generate the annual profile. In a typical week, the number of daily users entering the parking facilities is distributed according to weekdays and weekends. On weekends, entrance data shows an increase of 4% and 51% for the paid public car park and mall car park scenarios, respectively, while a decrease of 33% is found for the municipal car park. With regard to working place car park, it is assumed that the company is closed during the weekend, and therefore no charging is recorded.

The number of daily charging sessions is determined according to the size and traffic of the car park in terms of daily entrances. Three cases are considered in this work. In the small-size case, a car park with an average of 100 users/day is considered, while 200 users/day and 400 users/day are considered in the medium- and large-size cases. The number of EV users is obtained by considering an EV penetration share of 7%. This value corresponds to the projected share of EVs in Europe in 2025, as analyzed in ref. [1]. This results in $N_{EV} = 7$, 14 and 28 charging sessions per day on a weekly average for the small-, medium- and large-case, respectively. The weekly charging load profiles for the different parking scenarios and sizes are shown in Figure 3.

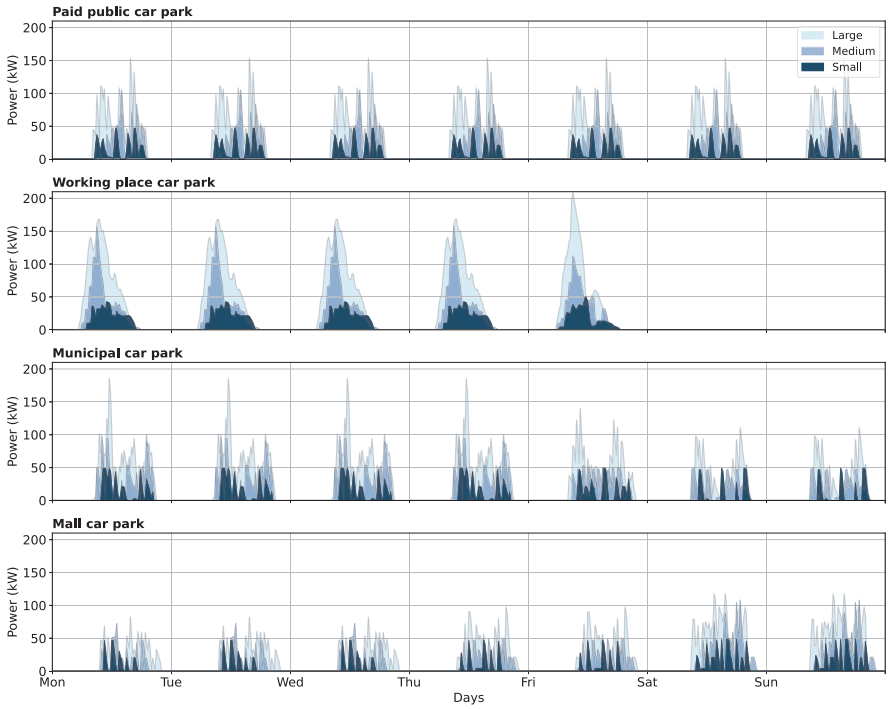

Figure 3. Weekly EV charging load profiles for different parking scenarios and lot sizes.

Table 2. Description of the reference CH scenario as a function of the car park scenario, the charging points power rating, the number of charging sessions per day, and average daily energy demand.

Car Park Scenario	Scenario	P_{CP} (kW)	N_{EV} (Daily)	Energy Demand (kWh/Day)
Paid public	small	22	7	197
	medium	22	14	393
	large	22	28	603
Working place	small	22	7	197
	medium	22	14	355
	large	22	28	661
Municipal	small	22	7	203
	medium	22	14	410
	large	22	28	602
Mall car park	small	50	7	182
	medium	50	14	417
	large	50	28	654

2.3. BESS Modeling

The BESS acts as a buffer between generation and load. When PV generation is higher than the load demand, the BESS can store excess power (charging phase); conversely, the BESS can provide energy to the load in the case of low PV power availability or higher demand (discharging phase). Considering Equation (5), the ideal BESS operation is achieved when there is no power sharing with the external grid, or, in other words, when:

$$P_B^*(t) = P_{EV}(t) - P_{PV}(t) \tag{5}$$

where P_{B}^* is the ideal battery power. However, in BESS modeling, it is essential to account for the constraints imposed by the maximum power rating of the storage system during both the charging and discharging phases, i.e., $-P_{\mathrm{B}}^{\max} \leq P_{\mathrm{B}} \leq P_{\mathrm{B}}^{\max}$. Furthermore, it is crucial to consider the limitations related to the maximum state of charge ($SOC_{\max}$) during charging and the minimum state of charge ($SOC_{\min}$) during discharging. Then Equation (5), which represents the ideal buffer operation, is modified as follows.

$$P_{\mathrm{B}} = \begin{cases} \min(P_{\mathrm{B}}^*, P_{\mathrm{B}}^{\max}) & \text{if } P_{\mathrm{B}}^* > 0 \text{ and } SOC > SOC_{\min} \\ \max(P_{\mathrm{B}}^*, -P_{\mathrm{B}}^{\max}) & \text{if } P_{\mathrm{B}}^* < 0 \text{ and } SOC < SOC_{\max} \\ 0 & \text{otherwise} \end{cases} \tag{6}$$

The maximum power rating is calculated as a function of the maximum charging rate (C_{R}) and the nominal capacity of BESS (S_{B} in kWh). C_{R} indicates the maximum charging and discharge rate (in h^{-1}) related to the nominal battery capacity. The maximum power of the system is obtained as follows: $P_{\mathrm{B}}^{\max} = C_{\mathrm{R}} S_{\mathrm{B}}$. The typical C_{R} for stationary storage applications ranges between 0.2C and 1C [25]. According to ref. [20], in this paper $C_{\mathrm{R}} = 0.5$ is assumed, which indicates that the battery can be fully charged or discharged in two hours. The usable capacity of the battery is typically limited by the manufacturer to prevent effects and damage due to overcharging and over-discharging events as described in ref. [26]. Equation (6) allows the SOC to remain within the permissible values, i.e., $SOC_{\min} = 5\%$ and $SOC_{\max} = 95\%$.

The SOC used in Equation (6) is obtained through time-step integration of the battery power, as shown in Equation (7):

$$SOC(t+1) = SOC(t) + \frac{P_B(t)\Delta t}{S_B} \tag{7}$$

where Δt is the simulation time step, set to 15 min in this study.

Finally, in order to integrate conversion losses into the BESS model, this work employs the approach proposed in ref. [27]. The losses associated with the round-trip efficiency of the battery are modeled as follows. Let P_{B} be the power measured at the DC terminals of the BESS, and η_{B} the battery efficiency during the charging or discharging phase, the power ideally measured inside the battery cell ($P_{\mathrm{B}}^{\mathrm{ins}}$) is given by the following equation.

$$\begin{cases} P_{\mathrm{B}}^{\mathrm{ins}} = \dfrac{1}{\eta_{\mathrm{B}}} P_{\mathrm{B}} & \text{if } P_{\mathrm{B}} > 0 \text{ (discharging)} \\ P_{\mathrm{B}}^{\mathrm{ins}} = \eta_{\mathrm{B}} P_{\mathrm{B}} & \text{if } P_{\mathrm{B}} < 0 \text{ (charging)} \end{cases} \tag{8}$$

Due to battery losses, the model expressed by Equation (8) results in a higher internal energy consumption during the discharge phase and a lower energy incoming during the charging phase compared to the energy measured at the battery terminals. In practice, this has an impact on the SOC trend, which demonstrates a reduction in growth during the charging phase and an increased rate of reduction during the discharging phase compared to the ideal case. In this paper, it is assumed that the battery efficiency is the same for both charging and discharging. The parameter η_{B} is derived from the battery's round-trip efficiency, designed as $\eta_{\mathrm{B-RT}}$, which measures the energy losses occurring throughout a complete charge-discharge cycle. For a stationary battery system operating at 0.5 C, the round-trip efficiency is typically around 90% [27,28]. Since the round-trip efficiency reflects the performance over a complete charge-discharge cycle, it can be assumed to be the product of the individual efficiencies of the charge and discharge processes, then efficiency used in Equation (8) is obtained from $\eta_{\mathrm{B}} = \sqrt{\eta_{\mathrm{B-RT}}}$.

BESS Degradation Model

A precise calculation of the battery's lifetime, based on its characteristics and operation, allows a more accurate assessment of the system's economic performance. During its use, the battery is subject to a reduction in its usable capacity. In general, the BESS is considered to have reached the end of its useful life when its usable capacity is reduced by 20% of its nominal value [29]. The lifetime of a BESS (y_{B}) is highly dependent on battery usage and cell technology. In this study, a $LiFePO_4$ battery storage is considered as it is one of the most widely used technologies for stationary energy storage due to its excellent chemical and thermal stability and low cost [30].

For the same load demand and generation, the size of the BESS will have a significant impact on the battery's cycling and consequently its degradation rate. For example, a smaller capacity BESS is likely to experience more frequent cycling with higher depths of discharge compared to a larger capacity system. Therefore, a battery degradation model is proposed below to incorporate BESS lifetime considerations into the sizing optimization problem. The proposed degradation model is adapted from ref. [29] and consists of two components:

$$C_{\mathrm{D}} = C_{\mathrm{D}}^{\mathrm{cal}} + C_{\mathrm{D}}^{\mathrm{cyc}} \tag{9}$$

where C_{D} is the total capacity degradation expressed as a percentage of the nominal capacity, $C_{\mathrm{D}}^{\mathrm{cal}}$ is the calendar capacity degradation and $C_{\mathrm{D}}^{\mathrm{cyc}}$ the cyclical capacity degradation.

The algorithm used to calculate the capacity degradation, and thus to estimate the BESS lifetime, is summarized in Figure 4.

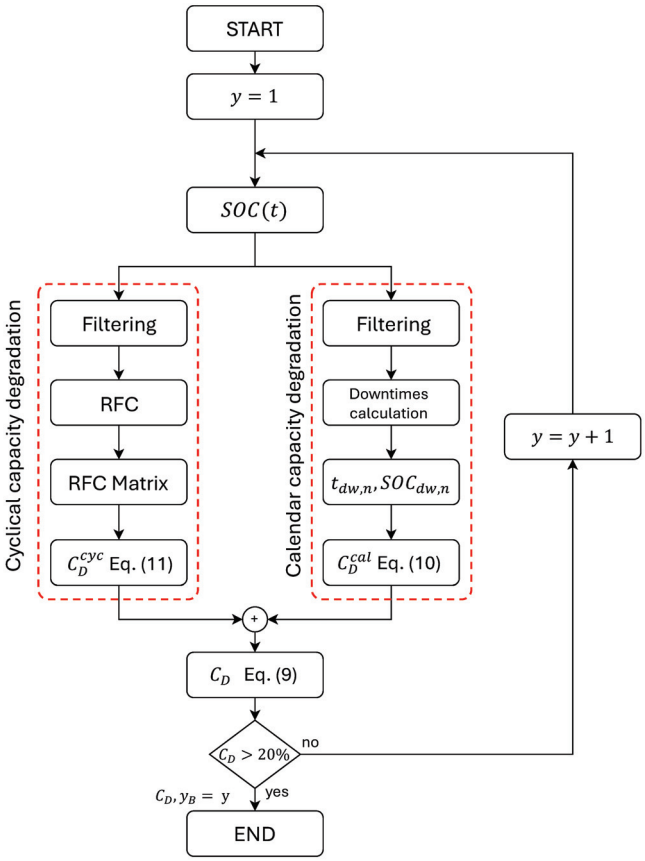

Figure 4. BESS degradation model flowchart.

Starting from the annual SOC profile obtained from the BESS model described in Section 2.3, the proposed algorithm calculates the parameters required to estimate the two degradation components. Using Equation (9), it evaluates the degradation accumulated during the y-th year. The iteration is repeated for subsequent years until the total degradation exceeds 20%. At this point, the algorithm stops and records both the level of degradation achieved and the time taken to reach it, which defines the operational lifetime of the system.

Figure 4 summarizes the 2 main branches of the degradation. The right branch shows the calculation of $C_{\mathrm{D}}^{\mathrm{cal}}$, which represents the loss of battery capacity that occurs during extended downtime. The downtime t_{dw} is defined as the time that the battery remains unused at a constant state of charge (SOC_{dw}). Calendar degradation increases with high temperatures, elevated SOC_{dw}, and extended t_{dw} durations [29]. To simplify the degradation model, a constant temperature of 25 °C is considered, as reported in ref. [29]. On the other hand, the dependence on SOC_{dw} and t_{dw} is derived via Equation (10).

$$C_{\mathrm{D}}^{\mathrm{cal}} = \sum_{n=1}^{N^{\mathrm{cal}}} K_{\mathrm{cal}} \cdot e^{0.0074 \cdot SOC_{\mathrm{dw},n}} \cdot \left(t_{\mathrm{dw},n} + t_{\mathrm{dw},n-1}^{\mathrm{eq}}\right)^{0.8} \tag{10}$$

Equation (10) allows summing the n-th calendar degradation events that occur with different SOC_{dw} and t_{dw} (expressed in months). N^{cal} represents the total number of calendar degradation events, while $K_{\mathrm{cal}} = 0.1723$ month^{-1} is a coefficient that depends on the operating temperature of the battery [31]. Since battery degradation is a non-linear process, simply adding up the capacity degradation of successive events leads to significant

discrepancies with respect to the actual degradation behavior of the battery. To overcome this limitation, this paper employs the superposition method, as proposed in ref. [32]. This method consists of considering the capacity degradation obtained in previous events (i.e., up to $n-1$) as an equivalent downtime. The equivalent downtime $t^{\mathrm{eq}}_{\mathrm{dw},n-1}$ is then added to the downtime of the n-th event in Equation (10).

The individual $SOC_{\mathrm{dw},n}$ and $t_{\mathrm{dw},n}$ values are obtained by processing the state of charge profile through two filtering steps. The first step employs a hysteresis filter that removes small variations in SOC values (less than 5%) by smoothing them to the previous value. The second step applies a binning process, discretizing the SOC values into predefined intervals, such as increments of 5%. The algorithm calculates each value of $t_{\mathrm{dw},n}$ and its relative $SOC_{\mathrm{dw},n}$, explicitly excluding instants when the SOC changes. Finally, the total $C^{\mathrm{cal}}_{\mathrm{D}}$ is obtained by Equation (10).

On the other hand, $C^{\mathrm{cyc}}_{\mathrm{D}}$ is directly related to the BESS cyclic operation, i.e., the charge and discharge phase that occurs during battery usage. A charge/discharge cycle is defined as a process in which the SOC starts from an initial value SOC_i, reaches a final value SOC_j, and returns to the same initial value SOC_i. Each cycle represents a degradation event $C^{\mathrm{cyc}}_{\mathrm{D},ij}$, whose intensity depends on the cycle depth of discharge $DOD_{ij} = |SOC_j - SOC_i|$, the average state of charge of the cycle SOC^{avr}_{ij}, and the temperature. According to ref. [32] the total cyclical capacity degradation is obtained by Equation (11):

$$C^{\mathrm{cyc}}_{\mathrm{D}} = \sum_{ij} K_{\mathrm{cyc}} \cdot e^{-0.019 \cdot SOC^{\mathrm{avr}}_{ij}} \cdot DOD^{0.716}_{ij} \cdot \left(nc_{ij} + nc^{eq}_{i-1,j-1}\right)^{0.5} \tag{11}$$

where K_{cyc} is a cyclic temperature coefficient and is equal to 0.021 considering an operating temperature of 25 °C [29]. For each pair SOC_i and SOC_j that characterizes the cycle, the total number of cycles, called nc_{ij}, is calculated. As for the calendar aging, the cyclical degradation accumulated from previous events (i.e., up to $i-1$, $j-1$) is considered by adding up an equivalent number of cycles $nc^{eq}_{i-1,j-1}$ to the current number of cycles in Equation (11).

The cyclic capacity degradation calculation is summarized in the left branch of the flowchart in Figure 4. The number of cycles nc_{ij} is obtained by the Rain-Flow Counting (RFC) method. The battery's SOC profile undergoes pre-processing before applying the RFC algorithm: an hysteresis filter removes small SOC fluctuations (<5%) to reduce noise; then a peak detector algorithm identifies maximum and minimum SOC values to mark transitions; finally, a binning process groups detected peaks into 5% SOC intervals for better cycle classification.

After this pre-processing step, the RFC method is employed. This method is generally used to calculate the number of cycles as reported in refs. [33–35]. The RFC algorithm processes four consecutive SOC points to detect cycles. If the two middle points fall between the first and last points, a valid cycle is identified. For a valid cycle, start and end SOC values, i.e., SOC_i and SOC_j, are recorded and the two middle points are removed from the SOC profile. If not valid, the next group is analyzed. The process continues until there are not enough points to form a loop.

All identified cycles are recorded in the RFC matrix, which is organized as follows: the rows identify the SOC levels at the start of the cycle (i.e., $SOC_i \in [5-95\%]$), while the columns identify the SOC levels at the end of the cycle (i.e., $SOC_j \in [5-95\%]$). Each cell of the RFC matrix indicates the number of cycles nc_{ij} between specific SOC start and end levels. Starting from the RFC matrix, it is possible to obtain the element of Equation (11) for each pair *ij*. Figure 5 provides an example of the RFC matrix, along with a graphical explanation of the method used to determine the parameters in Equation (11) for calculating cyclical capacity degradation.

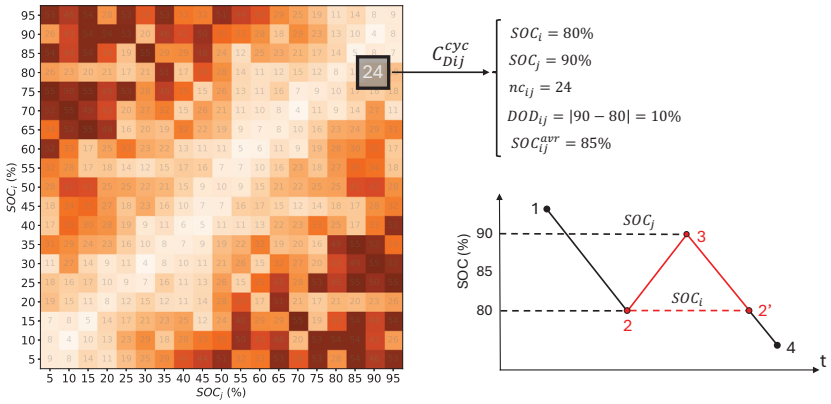

Figure 5. Example of RFC matrix and cycle parameter extraction. The color scale indicates the number of cycles ($n_{c_{ij}}$) in each matrix cell, while the red line represents an example of a charge–discharge trajectory.

It should be noted that only battery capacity degradation is considered in this study. Although the increase in internal resistance also contributes to battery aging by reducing the maximum deliverable power, previous works on $LiFePO_4$ cells have shown that when the capacity fade reaches 20% (end of life), the corresponding power fade remains below 5% [31]. Therefore, internal resistance growth was neglected to limit model complexity and computation time. However, this phenomenon can be modeled as a progressive decrease of $P_B^{\max}$, as formulated in ref. [31].

2.4. Grid Economic Exchange Modeling

In addition to the energy aspects discussed in the previous sections, this paper also addresses optimization from an economic perspective. Starting from the energy flows, it is therefore necessary to develop a model that takes into account the costs associated with the exchange of energy with the grid, including the costs of imported energy (purchased from the grid) and the revenue from injected energy (sold to the grid). Considering a one-year analysis, Equations (12) and (13) represent the calculation of the energy cost (C_G^+) and revenue (C_G^-), respectively:

$$C_G^+ = \int_{T=1\text{ year}} c_{\text{buy}}(t) \cdot P_G^+(t)\, dt \tag{12}$$

$$C_G^- = \int_{T=1\text{ year}} c_{\text{sell}}(t) \cdot P_G^-(t)\, dt \tag{13}$$

where c_{buy} and c_{sell} are the specific price of the imported and injected energy in EUR/kWh, while $P_G^+(t)$ and $P_G^-(t)$ are the profile of the grid imported and injected power, respectively.

The specific price c_{buy} is obtained from the data provided by the Italian Power Exchange—IPEX [36]. In this paper, we consider a purchase price based on the National Single Price (NSP) following Time-Of-Use (TOU) tariffs. The TOU tariffs typically have higher prices during peak hours, when demand is high and the grid is overloaded, and lower prices during off-peak hours, when demand decreases. In Italy, the energy market follows this structure by dividing the day into different price bands, such as "peak hours", "intermediate hours", and "off-peak hours". These bands correspond to specific time windows and days of the week. Additional costs, including network charges, taxes, and levies (e.g., value added tax, renewable, capacity, and environmental taxes), are included in c_{buy} according to refs. [37,38]. Fixed costs associated with contractual power were not included, as they are constant with respect to the optimization variables and thus do not affect the results.

On the other hand, the c_{sell} price depends on the adopted market mechanism. In Italy, it is generally managed by the national energy services operator, which applies either a fixed or a variable tariff depending on the market mechanism. The variable tariff is linked to the NSP for each geographical zone and follows TOU pricing. To ensure methodological generality and alignment with real market-based remuneration mechanisms, this study adopted a zonal NSP-based dynamic price.

In this paper, the annual variation of the price profiles is considered, with a 15-min resolution to match that adopted for the power profiles. Figure 6 shows the c_{buy} and c_{sell} price profiles for 2023. The annual view illustrates the monthly price variations, while a detailed weekly view highlights the daily fluctuations, showing that the purchase price follows the TOU tariff and the NSP varies on an hourly basis.

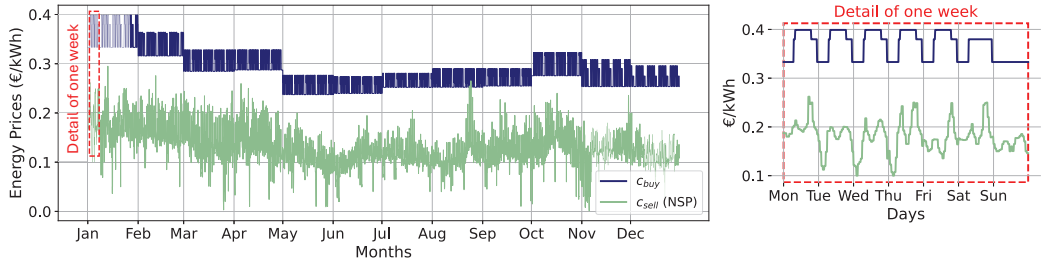

Figure 6. Annual and weekly energy price profiles.

3. PV-BESS Sizing Optimization Problem

Figure 7 shows an example of the power flow profiles of each element of the system over a one week period. A preliminary size setting of S_{PV}=100 kWp and S_{B} = 100 kWh is selected to support the EV charging load of the paid "public car park" (medium size) scenario.

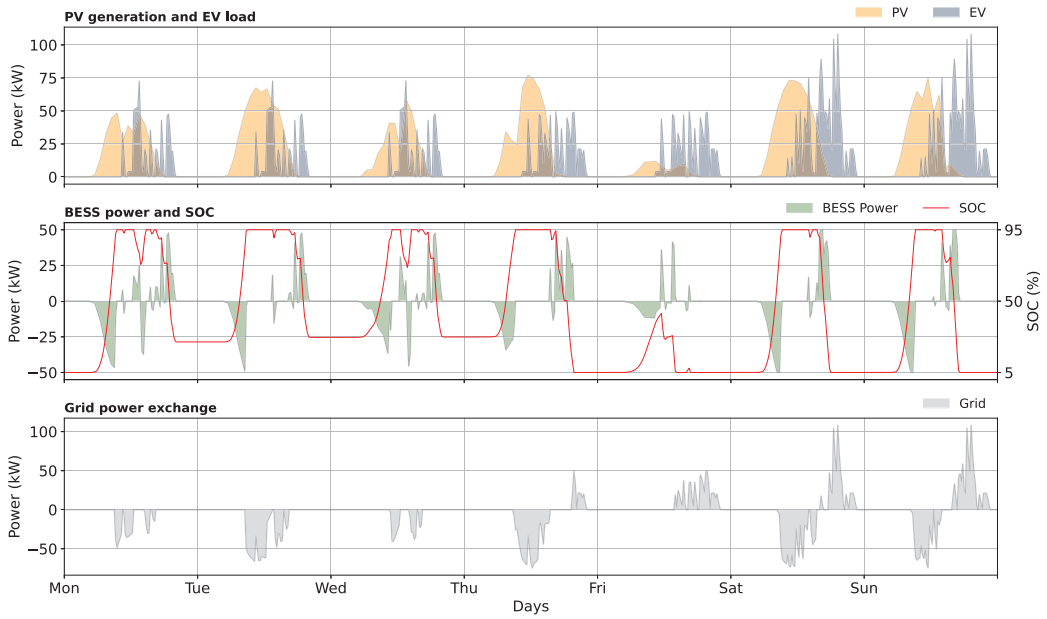

Figure 7. System power flow profiles: at the top is the PV power and the load. In the middle is the SOC and BESS power, and below is the power exchanged with the grid.

The top frame in Figure 7 shows the PV power profile in orange and the total EV load profile in blue. The output of the BESS model is shown in the middle frame: the green profile depicts the BESS power, while the red line shows the BESS SOC evolution. According to the BESS model of Equations (5) and (6), the BESS power is negative/positive during the charging/discharging phase and depends on the balance between generation

and load. The SOC profile shows that its cyclicity is highly dependent on the balance between P_{PV} and P_{EV}. Under conditions of abundant production or low demand, it can reach high values. Conversely, under conditions of low production, it can remain at low values for long periods. The parameters that affect BESS degradation, such as charge-discharge cycles and downtime periods, are highly dependent on on the PV and BESS size, highlighting therefore the need for a detailed analysis of their impact during the sizing optimization process.

Finally, the bottom frame in Figure 7 shows the power exchanged with the grid. According to Equation (1), positive values indicate power consumption (e.g., last 3 days in Figure 7), while negative values indicate power injected into the grid, i.e., when the battery cannot store the surplus of generation (e.g., first 4 days in the figure). As evident from these patterns, the sizing of the PV-BESS system has a significant impact on the exchange of power with the grid and thus on the economic performance of the system.

Based on the system model described in Section 2, it is essential to define quantitative performance parameters that not only take into account both energy and economic aspects, but also allow a direct evaluation of the system performance.

3.1. System Performance Parameters

System energy performance evaluation is based on two parameters: self-consumption (λ_{SC}) and self-sufficiency (λ_{SS}). Self-consumption is the share of the total PV-generated energy that is directly consumed locally. In other words, λ_{SC} quantifies the amount of PV energy utilized on-site rather than exported to the grid on annual basis. Self-sufficiency, on the other hand, refers to the degree to which the on-site PV generation satisfies the load energy demand. λ_{SS} indicates how much of the total energy demand is covered by the PV system. The related formulas are reported in Equations (14) and (15):

$$\lambda_{SC} = 1 - \frac{E_G^-}{E_{PV}} \tag{14}$$

$$\lambda_{SS} = 1 - \frac{E_G^+}{E_{EV}} \tag{15}$$

where E_G^+ and E_G^- are the annual energy purchased from and supplied to the grid, respectively. E_{PV} is the energy produced by the PV system and E_{EV} is the energy absorbed by the charging station on annual basis.

Self-consumption and self-sufficiency vary in the range [0, 1] and exhibit complementary behavior: $\lambda_{SC} = 1$ only if the system does not export energy to the grid, while $\lambda_{SS} = 1$ if the system does not import energy from the grid (totally grid-independent). The value of these parameters is influenced by the sizing of the system. For example, increasing PV size has a positive impact on self-sufficiency by reducing the amount of energy absorbed from the grid. However, PV-oversizing results in a higher amount of energy being injected into the grid, which ultimately reduces self-consumption. On the other hand, since BESS operations reduce grid power exchanges (both E_G^+ and E_G^-), increasing battery size results in higher values of both λ_{SC} and λ_{SS}.

The economic performance of the system is assessed through the levelized cost of energy. The LCOE (θ_{LCOE}) represents the average cost of energy incurred by the charging infrastructure operator delivering energy to EV users, over the lifetime of the system. The greater the reduction in LCOE due to the introduction of the PV-BESS system, the greater the economic benefit of the system. As defined in ref. [39], the LCOE is calculated as follows:

$$\theta_{LCOE} = \frac{\theta_{NPC}}{E_{EV}} \theta_{CRF} \tag{16}$$

The parameter θ_{CRF} in Equation (16) represent the Capital Recovery Factor—CRF that is a financial parameter used to determine the annualized cost of an investment over its lifetime. It converts the total cost of a system (EUR) into an equivalent annual payment (EUR/year) and is obtained by Equation (17):

$$\theta_{CRF} = \frac{r(1+r)^{y_{sys}}}{(1+r)^{y_{sys}} - 1} \tag{17}$$

where r is the discount rate, representing the rate used to discount future cost to their present value, and y_{sys} is the system lifetime, which is chosen equivalent to the PV system lifetime because, after a certain period, the photovoltaic components reach the end of their functional life, making it economically unfeasible to maintain the system [40].

In Equation (16), θ_{NPC} is the Net Present Cost—NPC and represents the total present value of all costs associated with the system over its lifetime, including capital and operative costs. The NPC is given by:

$$\theta_{NPC} = C_{PV} + C_B + \frac{C_G^+ - C_G^-}{\theta_{CRF}} \tag{18}$$

where C_{PV} and C_B are the PV and the BESS cost, respectively:

$$C_{PV} = C_{PV}^{CAP} + C_{PV}^{OM} \tag{19}$$

$$C_B = C_B^{CAP} + C_B^{OM} + C_B^R \tag{20}$$

The capital cost and operation & maintenance (O&M) costs are included in the PV and BESS cost. The BESS cost also takes into account the replacement cost, as BESS typically have shorter lifetimes than PV. Therefore, to accurately account for all costs incurred over the entire system lifetime, the additional costs associated with BESS replacements are included. The therm $C_G^+ - C_G^-$ represents the balance between the cost of energy purchased from the grid and the revenue from energy sold back to the grid, as calculated in Section 2.4. The θ_{NPC} of the system is thus the sum of the PV and BESS costs, plus the difference between the cost of energy purchased and the revenue from energy sold. Revenues from EV charging were not included in the optimization, as the user charging price is assumed to be constant and independent of the PV–BESS configuration.

The capital costs C_{PV}^{CAP} and C_B^{CAP} are calculated in Equations (21) and (22) considering the PV-BESS size, and their specific cost, i.e., c_{PV} in EUR/kWp and c_B in EUR/kWh, respectively, for PV and BESS:

$$C_{PV}^{CAP} = c_{PV} \cdot S_{PV} \tag{21}$$

$$C_B^{CAP} = c_B \cdot S_B \tag{22}$$

The operation and maintenance costs for both the PV and BESS systems are calculated by considering the discount rate and the system lifetime. The C_{PV}^{OM} is given by:

$$C_{PV}^{OM} = c_{PV}^{OM} S_{PV} \cdot \sum_{n=1}^{y_{sys}} \left(\frac{1}{1+r}\right)^n \tag{23}$$

where c_{PV}^{OM} is the annual O&M cost (EUR/kWp/year) of the PV plant. Similarly, the O&M cost for the BESS is calculated as:

$$C_B^{OM} = c_B^{OM} \cdot \sum_{n=1}^{y_{sys}} \left(\frac{1}{1+r}\right)^n \tag{24}$$

where $c_{\mathrm{B}}^{\mathrm{OM}}$ is the annual O&M cost of the battery system (EUR/year).

The replacement cost of the BESS is obtained by determining how many replacements are required during the system's lifetime, which is obtained by dividing the total system lifetime by the battery's lifetime y_{B}, obtained as described in the BESS Degradation Model Section, and calculating the cost of each replacement. Since the resulting number of replacements is typically not an integer, it includes both complete replacements and a fractional replacement at the end of the system's lifetime. The formula for the replacements cost is:

$$C_{\mathrm{B}}^{\mathrm{R}} = C_{\mathrm{B}}^{\mathrm{CAP}} \cdot \sum_{i=1}^{m-1} \frac{1}{(1+r)^{i \cdot y_{\mathrm{B}}}} \tag{25}$$

where m is the number of battery replacements during the system's lifetime.

The parameters relevant to the PV-BESS system's economic analysis are summarized in Table 3.

Table 3. System economic parameters and lifetime.

Parameter	Value	Reference
$c_{\mathrm{PV}}^{\mathrm{OM}}$	7.7 EUR/kWp/year	[41]
$c_{\mathrm{B}}^{\mathrm{OM}}$	60 EUR/year	[42]
c_{PV}	1100 EUR/kWp	[43]
c_B	350 EUR/kWh	[44]
r	3.4%	[45]
y	25 years	[40]

Economic performance is strongly influenced by the PV-BESS system size. Larger PV systems increase the overall system cost but help lower the expenses associated with purchasing energy from the grid. Similarly, larger BESS size raise the system's cost but increases economic independence from network, reducing system operating costs. The challenge of this work is to provide a method to optimize the performance of the system from both an energy and economic point of view.

3.2. Multi-Objective Optimization

The goal of the sizing optimization process is to determine the pair (S_{PV}, S_{BESS}) that maximizes the system performances. It is possible to consider the previous performance parameters and define two different objective functions. From the energy point of view, the information provided by the parameters λ_{SC} and λ_{SS} are included within the energy objective function, defined as follows:

$$\Lambda = \lambda_{\mathrm{SC}} \cdot \lambda_{\mathrm{SS}} \tag{26}$$

As described in Section 3.1, λ_{SC} and λ_{SS} are two parameters that range from 0 to 1 and exhibit complementary behavior with respect to system size. When analyzed individually, λ_{SC} is only indicative of system over-sizing, while λ_{SS} is only indicative of under-sizing. The objective Λ in Equation (26) also varies between 0 and 1, but only reaches high values when both λ_{SC} and λ_{SS} are high. This property allows Λ to encapsulate the performance aspects of both λ_{SC} and λ_{SS}, providing a unified measure of both over-sizing and under-sizing of the system. In other words, $\Lambda = 1$ is only achieved when the system does not export or import power to/from the grid.

On the other side, the LCOE is employed to assess the economic performance of the system. This parameter is expressed in relative terms by normalizing it with respect to

the average annual energy purchase price, $c_{\text{buy}}^{\text{av}}$. The corresponding economic objective function is defined in Equation (27):

$$\Theta = \frac{\theta_{\text{LCOE}}}{c_{\text{buy}}^{\text{av}}} \tag{27}$$

If $\Theta < 1$, it indicates that the PV-BESS system is economically advantageous, as the cost of energy is lower than the standard case, i.e., without PV-BESS, where the energy cost is equal to $c_{\text{buy}}^{\text{av}}$.

To prevent negative values of Θ, which would correspond to a gain rather than an energy cost, the selling price is set $c_{\text{sell}} = 0$. This approach avoid that the objective function may favor over-sizing the PV system to maximize revenue from energy sales, thereby deviating from the study's primary goal.

The target of the PV-BESS sizing optimization is to find the solutions (S_{PV}, S_{BESS}) that maximize Λ and minimize Θ. The multi-objective optimization (MOO) problem is described in Equation (28):

$$\begin{cases} \min\limits_{S_{\text{PV}}, S_{\text{B}}} F(S_{\text{PV}}, S_{\text{B}}) = [-\Lambda, \Theta] \\ S_{\text{PV}} \in \Omega_{\text{PV}} \\ S_{\text{B}} \in \Omega_{\text{B}} \end{cases} \tag{28}$$

In order to explore PV-BESS combination compatible with the usual car park size, the range of feasible solutions are $\Omega_{\text{PV}} \in [0, 500]$ kWp for PV and $\Omega_{\text{B}} \in [0, 500]$ kWh for BESS size.

MOO is a branch of optimization focused on solving problems that require the simultaneous optimization of multiple objectives. The two objective functions are often in conflict with each other. For example, higher values of S_{PV} and S_{B} improve Λ but increase capital costs, thereby negatively impacting Θ. As a result, there is typically no single optimal solution, but rather a set of optimal solutions. This set is known as "Pareto front" and consists of all the [S_{PV},S_B] pairs for which Θ cannot be decreased without reducing Λ, and vice versa.

MOO problems can be addressed using various algorithms to find solutions belonging to the Pareto front, identified with ε. In this work, three of the most widely adopted metaheuristic methods for MOO were considered and compared: NSGA-II, MOEA/D, and MOPSO. These algorithms were selected as they represent three distinct paradigms of multi-objective search: evolutionary selection (NSGA-II), decomposition-based optimization (MOEA/D), and swarm intelligence (MOPSO).

To perform the comparison, each algorithm underwent a preliminary parameter tuning phase to identify algorithm-specific optimal configurations. The optimization problem was then solved using each algorithm implemented in the pymoo Python library (version 0.6.1.5), with all algorithms executed under identical structural conditions (population size, number of generations, random seed management) to ensure reproducibility and fair comparison. The resulting main parameter configurations are summarized in Table 4.

A population size of 100 and 20 generations was selected as a trade-off between exploration capability and computational cost. Preliminary convergence tests confirmed that fitness stabilization was achieved after approximately 10–15 generations, with 20 generations providing a safety margin for robust convergence. Each algorithm was executed for ten independent runs using different random seeds to account for stochastic variability. The performance of each algorithm was evaluated by computing the Hypervolume (HV) indicator, which quantifies both convergence and diversity of the Pareto front. Since the problem is formulated in minimization mode as $[-\Lambda, \Theta]$, the nadir point (worst-case scenario) is

(0, 1). The reference point was set to (0, 1.1), scaling the nadir by a factor of 1.1 to ensure numerical robustness and prevent boundary effects [46]. For each algorithm, the mean and standard deviation of the HV across the ten runs were calculated, together with the average execution time.

Table 4. Parameters adopted for the three multi-objective algorithms.

Parameter	NSGA-II	MOEA/D	MOPSO
Population Size [1]	100	100	100
Number of Generations	20	20	20
Crossover Probability	0.98	0.92	-
Crossover Distribution Index	15	15	-
Mutation Probability	0.2	0.2	-
Mutation Distribution Index	20	20	-
Inertia Weight (w)	-	-	0.7
Acceleration Coefficients (c_1, c_2)	-	-	1.5, 1.5

[1] For MOEA/D, the population size corresponds to the number of reference directions.

A Kruskal–Wallis H-test was performed on the HV distributions across the three algorithms ($n = 10$ runs each, $\alpha = 0.05$). The test yielded $H = 19.42$, $p < 0.001$, indicating statistically significant differences. Pairwise Mann–Whitney U tests with Bonferroni correction ($\alpha_{\text{corrected}} = 0.0167$) revealed that NSGA-II and MOPSO achieve statistically equivalent HV values ($p = 0.734$), with mean values of 0.3552 ± 0.0002 and 0.3556 ± 0.0007, respectively. Conversely, MOEA/D exhibited significantly lower performance ($p < 0.001$ against both NSGA-II and MOPSO), with mean HV of 0.3533 ± 0.0012. Despite comparable Pareto front quality between NSGA-II and MOPSO, NSGA-II demonstrated superior stability across runs (lower standard deviation) and required 5.6% less computation time. Therefore, NSGA-II was selected as the reference algorithm for all subsequent analyses.

Having established NSGA-II as the optimal algorithm, the analysis now focuses on identifying the best design solution from the resulting Pareto front. By means of the Pareto front, it is possible to identify three significant points: $\varepsilon_\Lambda = [\Lambda^*, \Theta]$, which represents the Pareto solution with the highest energy performance Λ; $\varepsilon_\Theta = [\Lambda, \Theta^*]$, which is the Pareto solution with the best economic performance Θ. The third is the ideal point $\varepsilon^*_{\Lambda\Theta} = [\Lambda^*, \Theta^*]$, which can be obtained by the intersection of ε_Λ and ε_Θ. The ideal point is, therefore, a non-feasible solution that represents the best possible values for each objective, meaning that it achieves the highest performance for both energy and economic objective functions. However, this point cannot be realized in practice because it lies outside the feasible solution space.

Since the goal of this study is to determine the optimal size of the PV+BESS system that simultaneously maximizes energy performance and economic profitability, the optimal point between the Pareto front was chosen by finding the Pareto point that minimizes the Euclidean distances from the ideal point [47]. Euclidean distance is a geometric distance measure that quantifies the distance between two points in a multidimensional space. In the context of this study, the Euclidean distance d^* between the $\varepsilon^*_{\Lambda\Theta}$ and the closest point on the Pareto front $\varepsilon_{\Lambda\Theta}$ is calculated in Equation (29):

$$d^* = \min \sqrt{(\Lambda_j - \Lambda^*)^2 + (\Theta_j - \Theta^*)^2}, \quad j = 1, 2, \ldots, m \tag{29}$$

where Λ_j and Θ_j are the values of the objective functions for the j-th point on the Pareto front and m is the number of solution composing the Pareto front.

4. Result and Discussion

This section outlines the economic and energy benefits of integrating the PV-BESS system with EV charging infrastructure, highlighting the difference across the various locations and park sizes. Figure 8 presents the Pareto fronts for the four different parking locations under the three sizes, small, medium, and large, arranged from left to right. The points of interest on the Pareto front, such as ε_{Λ}, ε_{Θ}, $\varepsilon^{*}_{\Lambda\Theta}$, and $\varepsilon_{\Lambda\Theta}$, are highlighted in each graph. The PV-BESS sizing results and the economic and energy performances of each point of interest are also summarized in Table 5.

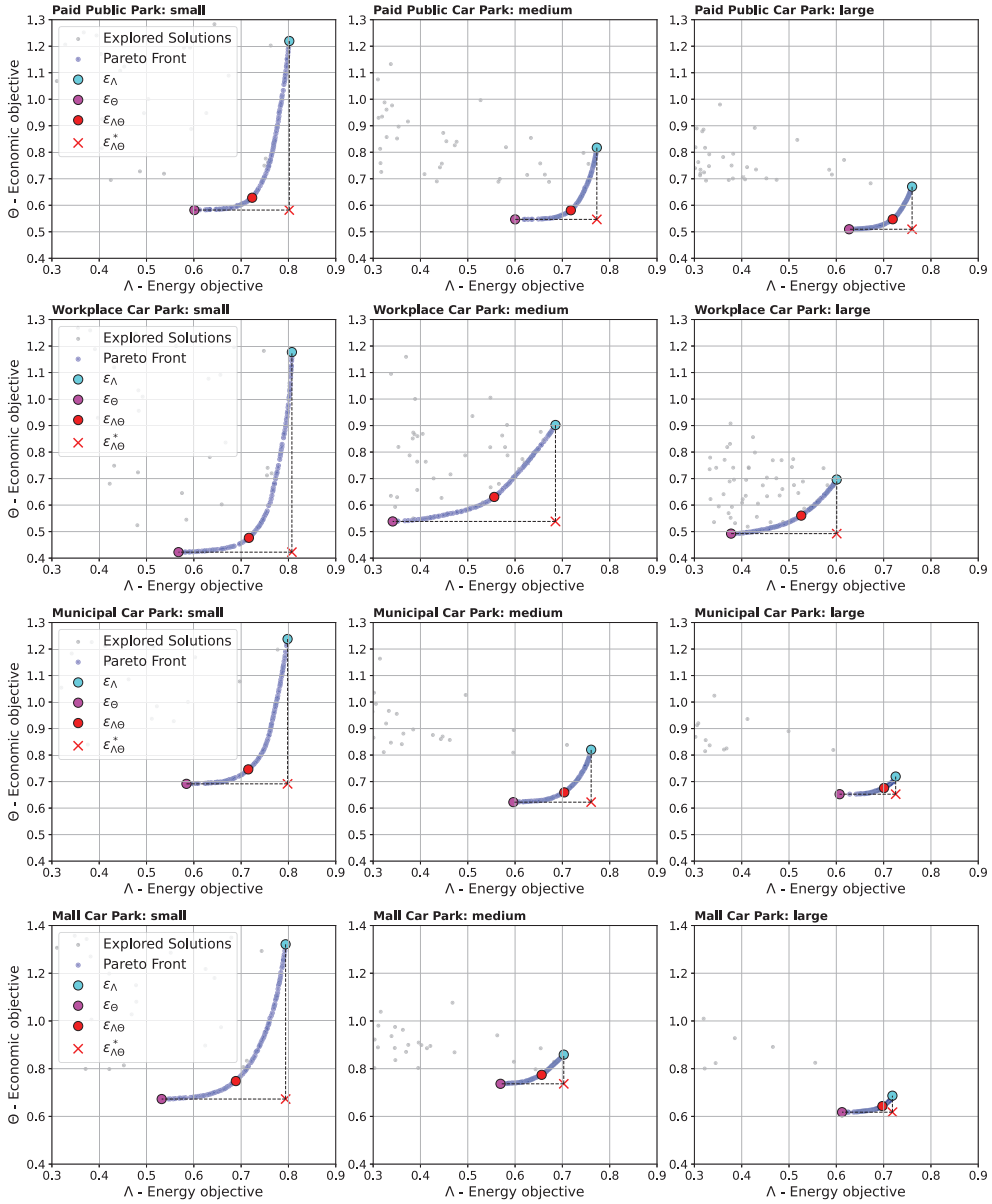

Figure 8. Pareto fronts for different car park locations and footfall scenarios: paid public car park, workplace car park, municipal car park, and mall car park.

As can be seen, the charging location, and therefore the charging power profile, have a significant impact on the energy independency and the economic effectiveness of the PV system with storage. Furthermore, the car park size also impacts the system's performance. For each scenarios, as the size of the car park increase, the spread of the Pareto front decrease. Since the same domain is considered across all scenarios, oversized PV-BESS systems in smaller car parks are economically less attractive. This is because the additional

costs associated with larger systems outweigh the benefits of reducing the share of energy absorbed from the grid. As a result, the front is vertically extended. Furthermore, since larger PV-BESS systems enhance the energy efficiency of the system, the front also extends horizontally. Conversely, larger loads within the same domain lead to a tighter Pareto front.

Table 5. Sizing and performance results for the best solution point, best economic performance point, and best energy performance point, for each location and size.

Location	Scenario	$\varepsilon_{\Lambda\Theta}$		S_{PV} (kWp)	S_B (kWh)	ε_{Θ}		S_{PV} (kWp)	S_B (kWh)	ε_{Λ}		S_{PV} (kWp)	S_B (kWh)
		Λ	Θ			Λ	Θ^*			Λ^*	Θ		
Public car park	small	0.72	0.63	49	127	0.60	0.58	59	86	0.80	1.21	49	500
	medium	0.72	0.58	95	202	0.60	0.55	115	139	0.77	0.82	93	500
	large	0.72	0.54	144	268	0.63	0.51	172	186	0.76	0.67	140	500
Workplace car park	small	0.72	0.48	45	54	0.57	0.42	60	17	0.80	1.18	46	500
	medium	0.56	0.63	110	176	0.34	0.54	164	18	0.69	0.9	93	500
	large	0.53	0.56	211	212	0.38	0.49	268	8	0.60	0.70	188	500
Municipal car park	small	0.72	0.75	52	180	0.58	0.69	62	128	0.80	1.24	51	500
	medium	0.70	0.66	100	279	0.60	0.62	123	214	0.76	0.82	100	500
	large	0.70	0.68	151	427	0.61	0.65	175	346	0.73	0.72	143	500
Mall car park	small	0.69	0.75	47	163	0.53	0.67	51	91	0.79	1.32	46	500
	medium	0.66	0.77	114	388	0.57	0.74	133	301	0.70	0.86	107	500
	large	0.70	0.64	164	423	0.61	0.62	196	356	0.72	0.69	156	500

As reported in Table 5, among the considered locations, the best energy performance result is obtained for the paid public car park. This result can be explained as, in this location, the load distribution is more concentrated during daytime hours and well-balanced throughout the day. This allows for good self-sufficiency of the system, with no excessive peak demands that would require additional energy from the grid. Furthermore, the unchanged load between weekdays and weekends, allows for a well-sized system that performs efficiently throughout the entire week, avoiding over- or under-sizing due to fluctuations in demand between weekdays and weekends. With regard to economic effectiveness, for all the considered sizes of the public car park, the chosen solution on the Pareto front $\varepsilon_{\Lambda\Theta}$ results to present an high energy cost saving, 37%, 42%, and 46% for small, medium, and large park sizes, respectively. Despite the peak load occurring in the evening, when PV power is no longer available and a larger BESS is required, there remains a substantial energy cost saving, as most of the load is concentrated during daylight hours.

The workplace car park scenario, at the $\varepsilon_{\Lambda\Theta}$ point, achieves similar economic performance, with energy cost savings of 52%, 37%, and 44% for the low, medium, and high scenarios, respectively. This is due to the alignment of the charging time slot with working hours, featuring a peak demand in the morning when PV production is available and no load during the evening. As a result, a large PV size and a very small BESS capacity are sufficient, leading to a more cost-effective system. With regard to system energy independency, the medium and large scenarios exhibit the worst results among all the considered cases. These low performances can be attributed to two factors: the sharp and sustained morning peak load and the absence of load during weekend. The morning peak, which PV generation and the small BESS capacity cannot fully cover, leading to a higher reliance on grid energy. The second factor is that during the weekend, since the load is absent, once the battery storage is full, all the energy produced by the PV system is fed into the grid, reducing the system self-consumption. However, the small car park scenario achieves good energy performance. In fact, as shown in Figure 3, the peak load in this scenario is modest, since the number of vehicles daily charged is small. In this case, the PV and BESS systems are more effective in meeting the demand, as the smaller battery is better suited to support the load, compensating for the reduced self-consumption during the weekends.

Lower economic performance is observed in the last two parking scenarios: the municipal car park and the mall car park. Regarding the municipal parking, at the $\varepsilon_{\Lambda\Theta}$ point, under the three size scenarios, the economic performance never exceeds a cost saving of 34%, while the energy performance is similar to that of the public car park. The charging hub load profile in this scenario is characterized by a high variance in parking times, including late evenings and peaks during peak traffic hours. The evening load, due to the lack of PV production, negatively impacts economic performance as it must be covered by the BESS energy supply. This requires a larger storage capacity, which increases the overall system cost, while since the BESS size required to meet the load is high, this helps to have high energy performance. Moreover, the reduction in load during the weekend, amounting to -33% compared to weekdays, slightly contributes to the reduction in energy performance. In fact, during weekdays, the higher load decreases self-sufficiency, as grid energy is required to meet demand. Conversely, during the weekend, the lower load reduces self-consumption, as the surplus energy must be injected into the grid.

Finally, in the mall car park scenario, the poorest overall performance was observed. Economic performance was the weakest among all scenarios, and energy performance was also suboptimal, surpassed only by the lower results observed in the workplace scenario. This scenario is characterized by a high flow of users during the daytime, with a moderate increase in the evening hours. In particular, the evening load increase, as observed in the municipal scenario, necessitates a larger battery capacity to supply the load required by the CH, resulting in higher system costs. Evidence of this is the fact that, for both the municipal and mall scenarios, the selected best solution on the Pareto front, $\varepsilon_{\Lambda\Theta}$, results in BESS capacities of 279 kWh and 388 kWh, respectively, which are significantly larger than those required for the first two locations. As far as energy performance is concerned, as shown in the load profile in Figure 3, there are no significant load peaks during the day. However, the reduction in energy efficiency across all scenarios can be attributed to the substantial increase in load during the weekends, i.e., 51% compared to weekdays. This increase impacts not only energy performance but also economic performance, as the higher weekend load necessitates a larger PV-BESS system to accommodate the demand, leading to increased system costs. Furthermore, during the weekdays, when the load is smaller, there is a reduction in the system's self-consumption, while at weekends, when the load is greater, self-sufficiency decreases.

The results discussed above are corroborated by the heat maps in Figure 9. The figure presents energy performance on the left and economic performance on the right, illustrating the outcomes across the optimization domain for the medium car park size scenario at the considered locations.

The energy performance heat maps clearly show that system energy independency improves as the BESS size increases, as larger systems can store and supply greater amounts of energy during operation. On the other hand, regarding the optimal PV size, similar PV sizes were obtained for all scenarios. This is because the PV size primarily depends on the energy required to meet the load, and the energy differences between the scenarios are minimal, as the same number of vehicles is considered. Consequently, the PV sizes remain comparable across scenarios, with the load profile having no significant impact in this regard. This means that, in accordance with Figure 9, the PV system with a capacity of approximately 100 kWp supply an amount of energy equivalent to that required by the charging station in the medium scenario.

As for the economic performance heat maps, the optimal PV size is consistent with that seen in the energy performance heat maps, as oversizing the PV leads to higher costs without any corresponding benefit, since the sale of surplus energy to the grid is not considered. Notably, only in the workplace scenario is the optimal PV size slightly larger

than in the others, as the peak load aligns with the peak PV production, as previously mentioned. The BESS size, however, depends on the specific load profile. The greater the deviation between the load profile and the PV production profile, the larger the battery capacity required, as observed in the municipal and mall car park scenarios.

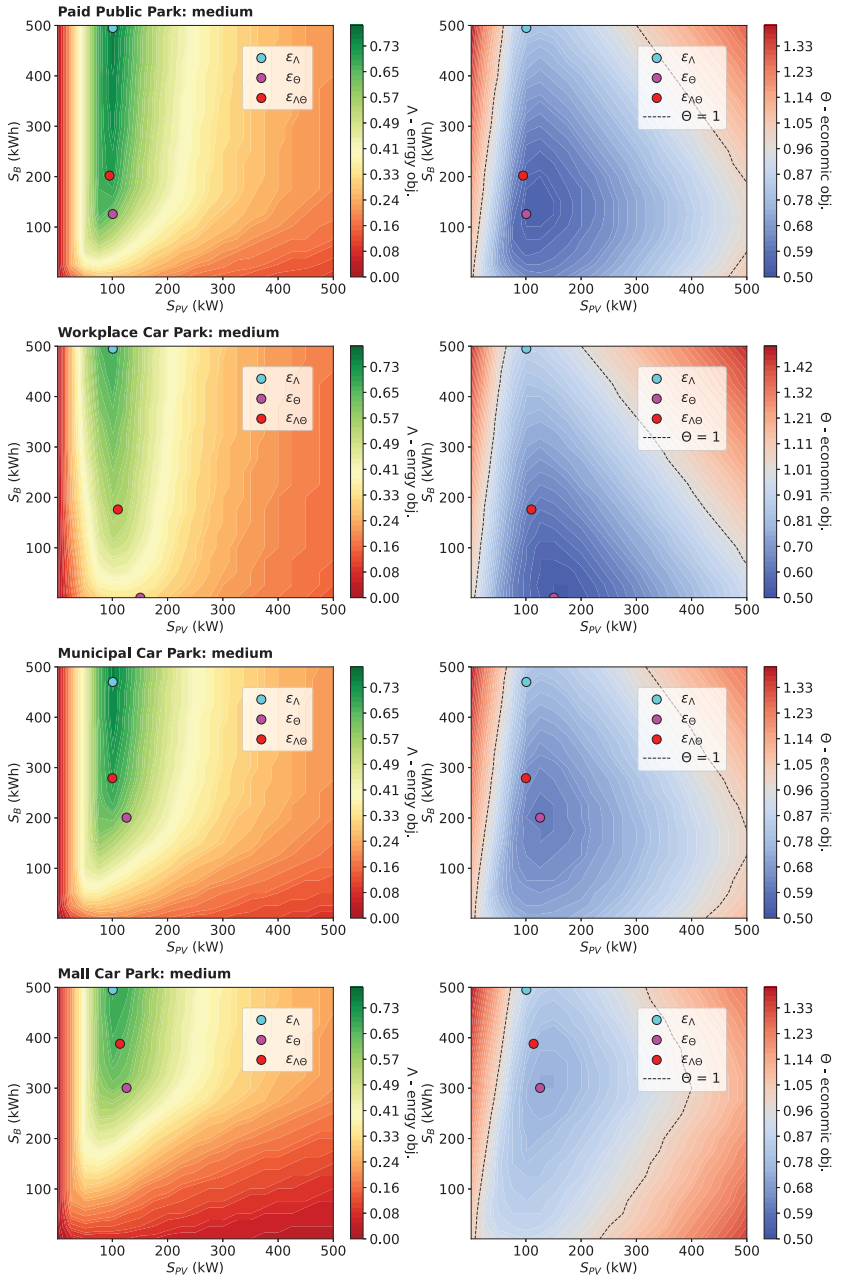

Figure 9. Heat maps showing the energy and economic performance results within the domain of the considered location for the large car park scenario.

Heat maps in Figure 9 confirm that, the overall best performance are achieved by the paid public car park. High energy performance are achieved for a wider range of BESS sizes, as indicated by the broad green area. In the economic heat map, low energy costs are achieved, while overall economic efficiency is maintained across almost the entire domain, as Θ stays below 1 in nearly all areas, indicated by the region within the dashed line. It may also be noted that, even without an energy storage, the economic effectiveness is achieved in almost the entire PV size domain.

With regard to the workplace car park, energy performance turn out to be not high as the previous location but still quite spread for greater values of BESS size. The economic performance clearly shows that, since the load profile match the PV production profile, the minimum value of the cost of energy is achieved with almost no battery storage. Moreover, Θ is below 1 for all the domain of PV when S_B is equal to 0.

In the considered domain, municipal car park location, achieved similar energy performance with respect to public car park but has lower energy performance since the BESS required is higher, as evidenced by the economic performance heat map.

Finally, the mall car park scenario demonstrates a relatively high maximum energy performance within the domain, outperforming the workplace scenario, but with a narrower range of good energy performance values, confined mainly to larger BESS sizes. This results in poor energy performance for the PV system without battery storage, highlighting once again the poor match between the PV profile and the load profile in this scenario. As a consequence, a significantly large BESS storage capacity is required, leading to higher Θ, as shown by the economic performance heat map.

The results obtained can be summarized as follows. The paid public par park achieves the best overall performance, with economic savings of up to 46%. The system is highly self-sufficient, minimizing grid reliance, and its consistent load profile throughout the week leads to efficient system sizing. The workplace car park also demonstrates excellent economic savings, up to 52%, but low energy performance, especially in medium and large scenarios due to the high peak load in the morning and the lack of load at weekends. The municipal car park has lower economic savings, never exceeding 34%, despite having similar energy performance to the public car park. This is because more battery storage is required to meet evening load demands, increasing costs and reducing performance. Finally, the mall par park shows the weakest overall performance, while it achieves good energy performance, it requires a significantly larger battery to cover evening peak loads, leading to higher costs.

5. Conclusions

This study proposed a multi-objective optimization method for the optimal sizing of PV-BESS systems to support EV charging hubs. The framework aimed to maximize both energy and economic system performance. The energy objective function, defined as the product of system self-consumption and self-sufficiency, represent the energy independency of the CH from the grid. Economic objective function, on the other hand, was defined as the LCOE, relativized to the average energy purchase price. Four distinct charging station locations, representing different urban and functional contexts, specifically, public car park, workplace car park, municipal car park, and mall car park, were analyzed to evaluate the impact of location and CH size (small, medium, and large) on system performance. A battery degradation model was implemented for realistic lifetime estimations. The resulting multi-objective problem was solved using the NSGA-II algorithm, selected after comparative testing with MOEA/D and MOPSO demonstrated its superior stability and computational efficiency while maintaining equivalent Pareto front quality.

The achieved results revealed that locations with well-aligned load distributions, such as the paid public car park, demonstrate superior overall performance due to efficient utilization of PV energy and reduced storage requirements. Specifically, for the paid public car park scenario, an average energy cost saving of 42% was obtained, while the energy independency ($\varepsilon_{\Lambda\Theta}$) was 0.72 for each CH size. Conversely, scenarios with mismatched load and generation profiles, like the mall car park, require larger battery systems to achieve comparable energy performance, with an average $\varepsilon_{\Lambda\Theta}$ of 0.68, leading to higher costs. For the mall car park scenario, in fact, the average energy cost saving obtained was 28%,

which is 33% lower compared to the paid public car park. Finally, pronounced load peaks were identified as the primary cause of the poor energy performance in the analyzed scenarios. Specifically, the workplace scenario, characterized by a significant morning load peak, achieved the lowest performance, with an average $\varepsilon_{\Lambda\Theta}$ of 0.6 across the three considered sizes. With regard to the PV-BESS system sizes among the considered scenarios, while the PV size depends more on the energy required by the specific load than on the daily load profile, the BESS size is strongly correlated with the load profile. The smallest BESS sizes were found for the paid public and workplace parking lot scenarios, with PV-BESS system sizes of 144 kWp–268 kWh and 211 kWp–212 kWh, respectively, for the large parking lot. In contrast, for the municipal and mall parking scenarios, the optimal system sizes for the large car park are 151 kWp–427 kWh and 164 kWp–423 kWh, with BESS capacities approximately double those of the previous scenarios.

These findings underscore the importance of tailored system sizing to maximize efficiency, sustainability and cost-effectiveness in EV charging infrastructures. Future developments of this work could include the implementation of Vehicle-to-Grid functionality. In such a scenario, EVs would operate as distributed energy storage units, providing bidirectional power exchange with the grid and enhancing system flexibility. This capability could reduce the required size of the stationary BESS or alter its optimal operation strategy. In addition, future work will include the modeling of the battery internal resistance growth, represented as a progressive reduction of the battery maximum deliverable power $P_B^{\max}$, to capture the effects of power fade associated with battery aging.

Author Contributions: F.M.T. contributed to conceptualization, methodology, software, validation, formal analysis, investigation, data curation, and writing—original draft. F.L.F. contributed to conceptualization, methodology, software, validation, formal analysis, investigation, data curation, writing—review and editing, and supervision. M.R. contributed to methodology, data curation, writing—review and editing, visualization, and supervision. All authors have read and agreed to the published version of the manuscript.

Funding: This work was funded by European Union under the National Recovery and Resilience Plan PNRR-Missione 4-Componente 2, Investimento 1.5 "Creazione e rafforzamento di Ecosistemi dell'innovazione, costruzione di leader territoriali di R&S" D.D. 3277 del 30 December 2021, research project "ECOSISTER-Ecosystem for Sustainable Transition in Emilia-Romagna", Code ECS00000033, CUP J33C22001240001.

Data Availability Statement: The original contributions presented in this study are included in the article material. Further inquiries can be directed to the corresponding author.

Conflicts of Interest: Author Francesco Lo Franco was employed by the company Syniergy S.r.l. The remaining authors declare that the research was conducted in the absence of any commercial or financial relationships that could be construed as a potential conflict of interest.

References

1. International Energy Agency (IEA). Global EV Data Explorer. 2024. Available online: https://www.iea.org/data-and-statistics/data-tools/global-ev-data-explorer (accessed on 30 October 2024).
2. International Energy Agency (IEA). Europe—Data and Analysis. 2024. Available online: https://www.iea.org/regions/europe (accessed on 14 January 2025).
3. Ricerca sul Sistema Energetico (RSE). Impatto Delle Infrastrutture di Ricarica Sulla Rete Elettrica di Distribuzione. 2022. Available online: https://www.rse-web.it/ (accessed on 12 December 2024).
4. The Guardian. France to Require All Large Car Parks to be Covered by Solar Panels. 2022. Available online: https://www.theguardian.com/world/2022/nov/09/france-to-require-all-large-car-parks-to-be-covered-by-solar-panels (accessed on 12 December 2024).
5. Wang, H.; Wang, J.; Piao, Z.; Meng, X.; Sun, C.; Yuan, G.; Zhu, S. The Optimal Allocation and Operation of an Energy Storage System with High Penetration Grid-Connected Photovoltaic Systems. *Sustainability* **2020**, *12*, 6154. [CrossRef]

6. Khawaja, Y.; Giaouris, D.; Patsios, H.; Dahidah, M. Optimal cost-based model for sizing grid-connected PV and battery energy system. In Proceedings of the 2017 IEEE Jordan Conference on Applied Electrical Engineering and Computing Technologies (AEECT), Aqaba, Jordan, 11–13 October 2017; pp. 1–6. [CrossRef]
7. Dai, Q.; Liu, J.; Wei, Q. Optimal Photovoltaic/Battery Energy Storage/Electric Vehicle Charging Station Design Based on Multi-Agent Particle Swarm Optimization Algorithm. *Sustainability* **2019**, *11*, 1973. [CrossRef]
8. Liu, G.; Xue, Y.; Chinthavali, M.S.; Tomsovic, K. Optimal Sizing of PV and Energy Storage in an Electric Vehicle Extreme Fast Charging Station. In Proceedings of the 2020 IEEE Power & Energy Society Innovative Smart Grid Technologies Conference (ISGT), Washington, DC, USA, 17–20 February 2020; pp. 1–5. [CrossRef]
9. Zhou, L.; Zhang, Y.; Lin, X.; Li, C.; Cai, Z.; Yang, P. Optimal Sizing of PV and BESS for a Smart Household Considering Different Price Mechanisms. *IEEE Access* **2018**, *6*, 41050–41059. [CrossRef]
10. Yan, D.; Ma, C. Optimal Sizing of A PV Based Electric Vehicle Charging Station Under Uncertainties. In Proceedings of the IECON 2019—45th Annual Conference of the IEEE Industrial Electronics Society, Lisbon, Portugal, 14–17 October 2019; Volume 1, pp. 4310–4315. [CrossRef]
11. Nafeh, A.E.S.A.; Omran, A.E.F.A.; Elkholy, A.; Yousef, H. Optimal economical sizing of a PV-battery grid-connected system for fast charging station of electric vehicles using modified snake optimization algorithm. *Results Eng.* **2024**, *21*, 101965. [CrossRef]
12. Korjani, S.; Serpi, A.; Damiano, A. A Genetic Algorithm Approach for Sizing Integrated PV-BESS Systems for Prosumers. In Proceedings of the 2020 2nd IEEE International Conference on Industrial Electronics for Sustainable Energy Systems (IESES), Cagliari, Italy, 1–3 September 2020; Volume 1, pp. 151–156. [CrossRef]
13. Kelepouris, N.S.; Nousdilis, A.I.; Bouhouras, A.S.; Christoforidis, G.C. Enhancing Self-Sufficiency in Buildings with Hybrid PV-Battery Systems and Demand Side Management: A Sizing Tool. In Proceedings of the 2021 IEEE International Conference on Environment and Electrical Engineering and 2021 IEEE Industrial and Commercial Power Systems Europe, Bari, Italy, 7–10 September 2021; pp. 1–6. [CrossRef]
14. Fang, C.; Zhao, X.; Xu, Q.; Li, Y.; Wang, H.; Feng, D.; Zhang, K.; Zhou, Y. Optimal Battery and PV Sizing of Charging Stations Considering Battery Dynamic Characteristics. In Proceedings of the 2021 Power System and Green Energy Conference (PSGEC), Shanghai, China, 20–22 August 2021; pp. 453–459. [CrossRef]
15. Lo Franco, F.; Ricco, M.; Cirimele, V.; Apicella, V.; Carambia, B.; Grandi, G. Electric Vehicle Charging Hub Power Forecasting: A Statistical and Machine Learning Based Approach. *Energies* **2023**, *16*, 2076. [CrossRef]
16. Leone, C.; Longo, M.; Fernández-Ramírez, L.M.; García-Triviño, P. Multi-Objective Optimization of PV and Energy Storage Systems for Ultra-Fast Charging Stations. *IEEE Access* **2022**, *10*, 14208–14224. [CrossRef]
17. Vermeer, W.; Mouli, G.R.C.; Bauer, P. Optimal Sizing and Control of a PV-EV-BES Charging System Including Primary Frequency Control and Component Degradation. *IEEE Open J. Ind. Electron. Soc.* **2022**, *3*, 236–251. [CrossRef]
18. Islam, M.S.; Mithulananthan, N.; Bhumkittipich, K. Feasibility of PV and battery energy storage based EV charging in different charging stations. In Proceedings of the 2016 13th International Conference on Electrical Engineering/Electronics, Computer, Telecommunications and Information Technology (ECTI-CON), Chiang Mai, Thailand, 28 June–1 July 2016; pp. 1–6. [CrossRef]
19. Alshammari, N.F.; Samy, M.M.; Barakat, S. Comprehensive Analysis of Multi-Objective Optimization Algorithms for Sustainable Hybrid Electric Vehicle Charging Systems. *Mathematics* **2023**, *11*, 1741. [CrossRef]
20. Leone, C.; Peretti, C.; Paris, A.; Longo, M. Photovoltaic and battery systems sizing optimization for ultra-fast charging station integration. *J. Energy Storage* **2022**, *52*, 104995. [CrossRef]
21. Abe, C.F.; Dias, J.B.; Notton, G.; Poggi, P. Computing Solar Irradiance and Average Temperature of Photovoltaic Modules from the Maximum Power Point Coordinates. *IEEE J. Photovolt.* **2020**, *10*, 655–663. [CrossRef]
22. Huld, T.; Müller, R.; Gambardella, A. A new solar radiation database for estimating PV performance in Europe and Africa. *Sol. Energy* **2012**, *86*, 1803–1815. [CrossRef]
23. Sun, V.; Asanakham, A.; Deethayat, T.; Kiatsiriroat, T. Evaluation of nominal operating cell temperature (NOCT) of glazed photovoltaic thermal module. *Case Stud. Therm. Eng.* **2021**, *28*, 101361. [CrossRef]
24. Bortolini, M.; Gamberi, M.; Graziani, A. Technical and economic design of photovoltaic and battery energy storage system. *Energy Convers. Manag.* **2014**, *86*, 81–92. [CrossRef]
25. Raszmann, E.; Baker, K.; Shi, Y.; Christensen, D. Modeling stationary lithium-ion batteries for optimization and predictive control. In Proceedings of the 2017 IEEE Power and Energy Conference at Illinois (PECI), Champaign, IL, USA, 23–24 February 2017; pp. 1–7. [CrossRef]
26. Akeyo, O.M.; Rallabandi, V.; Jewell, N.; Patrick, A.; Ionel, D.M. Parameter Identification for Cells, Modules, Racks, and Battery for Utility-Scale Energy Storage Systems. *IEEE Access* **2020**, *8*, 215817–215826. [CrossRef]
27. Lo Franco, F.; Morandi, A.; Raboni, P.; Grandi, G. Efficiency comparison of DC and AC coupling solutions for large-scale PV+BESS power plants. *Energies* **2021**, *14*, 4823. [CrossRef]

28. Noyanbayev, N.; Forsyth, A.; Feehally, T. Efficiency analysis for a grid-connected battery energy storage system. *Mater. Today Proc.* **2018**, *5*, 22811–22818. [CrossRef]
29. Stroe, D.I.; Swierczynski, M.; Stroe, A.I.; Teodorescu, R.; Laerke, R.; Kjaer, P.C. Degradation behaviour of Lithium-ion batteries based on field measured frequency regulation mission profile. In Proceedings of the 2015 IEEE Energy Conversion Congress and Exposition (ECCE), Montreal, QC, Canada, 20–24 September 2015; pp. 14–21. [CrossRef]
30. Wang, J.; Liu, P.; Hicks-Garner, J.; Sherman, E.; Soukiazian, S.; Verbrugge, M.; Tataria, H.; Musser, J.; Finamore, P. Cycle-life model for graphite-LiFePO4 cells. *J. Power Sources* **2011**, *196*, 3942–3948. [CrossRef]
31. Stroe, D.I.; Świerczyński, M.; Stan, A.I.; Teodorescu, R.; Andreasen, S.J. Accelerated Lifetime Testing Methodology for Lifetime Estimation of Lithium-Ion Batteries Used in Augmented Wind Power Plants. *IEEE Trans. Ind. Appl.* **2014**, *50*, 4006–4017. [CrossRef]
32. Wu, C.H.; Jhan, J.Z.; Ko, C.H.; Kuo, C.C. Evaluating and Analyzing the Degradation of a Battery Energy Storage System Based on Frequency Regulation Strategies. *Appl. Sci.* **2022**, *12*, 6111. [CrossRef]
33. Akpinar, K.N.; Gundogdu, B.; Ozgonenel, O. A novel cycle counting perspective for energy management of grid integrated battery energy storage systems. *Energy Rep.* **2023**, *9*, 123–131. [CrossRef]
34. Alam, M.J.E.; Saha, T.K. Cycle-life degradation assessment of Battery Energy Storage Systems caused by solar PV variability. In Proceedings of the 2016 IEEE Power and Energy Society General Meeting (PESGM), Boston, MA, USA, 17–21 July 2016; pp. 1–5. [CrossRef]
35. Chen, Y.; Ni, J.; Li, H.; Yang, F.; Yin, G. Enhanced Research on the Determination of Aging Degree in Embedded Energy Storage Configurations Utilizing the Rain Flow Counting Method. In Proceedings of the 2024 43rd Chinese Control Conference (CCC), Kunming, China, 28–31 July 2024; pp. 2160–2164. [CrossRef]
36. Gestore dei Mercati Energetici. GME Profile—Italian Electricity Market Operator. 2024. Available online: https://www.mercatoelettrico.org/en-us/Home/GME/GMEProfile (accessed on 3 December 2024).
37. Eurostat. Electricity Prices for Household Consumers—NRG_PC_204. 2024. Available online: https://ec.europa.eu/eurostat/databrowser/view/nrg_pc_204/default/table?lang=en (accessed on 14 October 2024).
38. ARERA—Autorità di Regolazione per Energia Reti e Ambiente. Relazione Annuale Sullo Stato Dei Servizi e Sull'Attività Svolta. 2024. Available online: https://www.arera.it/fileadmin/allegati/relaz_ann/24/RA24_vol1.pdf (accessed on 16 December 2024).
39. Sun, B. A multi-objective optimization model for fast electric vehicle charging stations with wind, PV power and energy storage. *J. Clean. Prod.* **2021**, *288*, 125564. [CrossRef]
40. Khezri, R.; Mahmoudi, A.; Haque, M.H. A Demand Side Management Approach For Optimal Sizing of Standalone Renewable-Battery Systems. *IEEE Trans. Sustain. Energy* **2021**, *12*, 2184–2194. [CrossRef]
41. NREL. *Best Practices for Operation and Maintenance of Photovoltaic and Energy Storage Systems*, 3rd ed.; U.S. Department of Energy (DOE): Golden, CO, USA, 2019. Available online: https://www.nrel.gov/docs/fy19osti/73822.pdf (accessed on 14 October 2024).
42. Brinsmead, T.; Graham, P.; Hayward, J.; Ratnam, E.; Reedman, L. *Future Energy Storage Trends: An Assessment of the Economic Viability, Potential Uptake, and Impacts of Electrical Energy Storage on the NEM 2015–2035*; Technical Report; CSIRO: Melbourne, Australia, 2015; Report Prepared for the Australian Energy Market Commission (AEMC).
43. Fall, S.; Dreves, H. *U.S. Solar Photovoltaic System and Energy Storage Cost Benchmarks, with Minimum Sustainable Price Analysis: Q1 2023*; Technical Report; National Renewable Energy Laboratory (NREL): Golden, CO, USA, 2023.
44. Bielewski, M.; Pfrang, A.; Bobba, S.; Kronberga, A.; Georgakaki, A.; Letout, S.; Kuokkanen, A.; Mountraki, A.; Ince, E.; Shtjefni, D.; et al. *Clean Energy Technology Observatory: Batteries for Energy Storage in the European Union—2022 Status Report on Technology Development, Trends, Value Chains and Markets*; Publications Office of the European Union: Luxembourg, 2022; JRC130724. [CrossRef]
45. Trading Economics. Euro Area Interest Rate. 2024. Available online: https://tradingeconomics.com/euro-area/interest-rate (accessed on 4 December 2024).
46. Ishibuchi, H.; Imada, R.; Setoguchi, Y.; Nojima, Y. Reference point specification in hypervolume calculation for fair comparison and efficient search. In Proceedings of the 2017 Genetic and Evolutionary Computation Conference (GECCO'17), Berlin, Germany, 15–19 July 2017; pp. 585–592.
47. Chen, W.; Hu, Z.; Gao, X.; Liu, Y. Simulation and Multi-Objective Optimization of Three-Column Double-Effect Methanol Distillation by NSGA-III Algorithm. *Processes* **2023**, *11*, 1515. [CrossRef]

Disclaimer/Publisher's Note: The statements, opinions and data contained in all publications are solely those of the individual author(s) and contributor(s) and not of MDPI and/or the editor(s). MDPI and/or the editor(s) disclaim responsibility for any injury to people or property resulting from any ideas, methods, instructions or products referred to in the content.

batteries

MDPI

Article

Hybrid Deep Learning Approach for Fractional-Order Model Parameter Identification of Lithium-Ion Batteries

Maharani Putri [1], Dat Nguyen Khanh [2], Kun-Che Ho [2], Shun-Chung Wang [3] and Yi-Hua Liu [1,*]

[1] Department of Electrical Engineering, National Taiwan University of Science and Technology, Taipei 106335, Taiwan; d11307803@mail.ntust.edu.tw
[2] Department of Automation Engineering, National Formosa University, Yunlin 632301, Taiwan; 11457146@nfu.edu.tw (D.N.K.)
[3] Department of Marine Engineering, National Taiwan Ocean University, Keelung 20224, Taiwan; scwang@mail.ntou.edu.tw
* Correspondence: yhliu@mail.ntust.edu.tw

Abstract

Fractional-order models (FOMs) have been recognized as superior tools for capturing the complex electrochemical dynamics of lithium-ion batteries, outperforming integer-order models in accuracy, robustness, and adaptability. Parameter identification (PI) is essential for FOMs, as its accuracy directly affects the model's ability to predict battery behavior and estimate critical states such as state of charge (SOC) and state of health (SOH). In this study, a hybrid deep learning approach has been introduced for FOM PI, representing the first application of deep learning in this domain. A simulation platform was developed to generate datasets using Sobol and Monte Carlo sampling methods. Five deep learning models were constructed: long short-term memory (LSTM), gated recurrent unit (GRU), one-dimensional convolutional neural network (1DCNN), and hybrid models combining 1DCNN with LSTM and GRU. Hyperparameters were optimized using Optuna, and enhancements such as Huber loss for robustness to outliers, stochastic weight averaging, and exponential moving average for training stability were incorporated. The primary contribution lies in the hybrid architectures, which integrate convolutional feature extraction with recurrent temporal modeling, outperforming standalone models. On a test set of 1000 samples, the improved 1DCNN + GRU model achieved an overall root mean square error (RMSE) of 0.2223 and a mean absolute percentage error (MAPE) of 0.27%, representing nearly a 50% reduction in RMSE compared to its baseline. This performance surpasses that of the improved LSTM model, which yielded a MAPE of 9.50%, as evidenced by tighter scatter plot alignments along the diagonal and reduced error dispersion in box plots. Terminal voltage prediction was validated with an average RMSE of 0.002059 and mean absolute error (MAE) of 0.001387, demonstrating high-fidelity dynamic reconstruction. By advancing data-driven PI, this framework is well-positioned to enable real-time integration into battery management systems.

Keywords: fractional-order model; lithium-ion battery; parameter identification; deep learning hybrids; battery management system

1. Introduction

1.1. Literature Review

Fractional-order models (FOMs) have emerged as a powerful tool for accurately capturing the complex electrochemical dynamics of lithium-ion batteries, offering significant

improvements over traditional integer-order models in terms of accuracy, robustness, and adaptability to varying operating conditions [1–3]. Parameter identification (PI) is a critical step in leveraging the full potential of FOMs, as it directly impacts the model's ability to predict battery behavior, estimate state of charge (SOC), and assess state of health (SOH) [4,5]. Accurate PI is crucial for the deployment of FOMs in battery management systems (BMS) and hybrid energy storage systems [6,7]. Reliable model parameters are preconditions for high-precision state estimation, such as State of Charge (SOC) [8]. The core challenge in identifying FOM parameters lies in the inherent nonlinearity introduced by the fractional order, which distinguishes them from integer-order models (IOMs). The model parameters and the fractional order are highly sensitive and time-varying, depending on numerous factors such as SOC, temperature, SOH, and load.

FOM parameter identification methods are generally categorized by their operational domain (frequency vs. time) and implementation style (offline vs. online/recursive). Offline and global optimization methods are particularly favored for identifying parameters in complex, non-convex problems due to their robust global search capabilities, which help avoid convergence to local minima. Among the intelligent optimization algorithms employed, particle swarm optimization (PSO) is widely used, often enhanced through variants such as hybrid multi-swarm PSO [9] or by incorporating chaos theory to refine local search [10]. Further improvements include adaptive fractional order PSO, which dynamically adjusts a particle's inertia weight based on its proximity to the global optimum [11]. Coevolutionary PSO (CPSO) has also been applied to synchronously identify both the parameters and the order-values of FOMs [12,13]. Genetic algorithm (GA) and its hybrid with PSO are also utilized for the simultaneous identification of model coefficients and differentiation orders [9,14,15]. For instance, the hybrid genetic–fractional beetle swarm optimization method, which synergizes GA with fractional beetle swarm optimization, has demonstrated superior accuracy compared to individual algorithms [16]. Additionally, variants of differential evolution (DE), such as the neighborhood-based multi-strategy and mean factor DE algorithm, are designed to enhance population diversity and convergence performance [17]. Beyond these, the Runge–Kutta optimizer (RUN) is also utilized, leveraging its fast convergence speed and high precision for extracting FOM parameters from either electrochemical impedance spectroscopy (EIS) or time-domain data [18].

For real-time applications requiring rapid parameter tracking under varying operating conditions, online and adaptive methods are essential. The forgetting factor recursive least squares (FFRLS) algorithm is commonly employed for the fast online identification of linear model parameters when the fractional order is predetermined [19,20], utilizing discrete representations of the fractional derivative such as the Grünwald–Letnikov definition [6,15,21,22]. To address the simultaneous identification of all parameters including the fractional order α, multi-time scale frameworks have been proposed. In such frameworks, α is updated periodically on a slow time scale using global optimization methods with low computational burden, while remaining parameters are updated frequently via FFRLS on a fast time scale. Synergistic approaches, such as the beetle antennae search and recursive least squares (BAS-RLS), iteratively determine α using BAS while RLS estimates linear parameters [5]. Variable-order recursive methods repeatedly apply RLS with different fractional orders to continuously correct approximation errors and converge toward the optimal dynamic order [20]. Kalman Filter-based integration, including the adaptive extended Kalman filter (AEKF) and adaptive fractional-order unscented particle filter, simultaneously estimates state-of-charge, state-of-health, and model parameters by treating them as part of an extended state vector [23,24]. Gradient Descent variants, such as weighted gradient descent and weighted forgetting factor gradient descent, are also utilized for online identification of both parameters and fractional orders, incorporating weighting factors

inspired by particle filter innovations to enhance precision and convergence speed [22]. Multi-domain identification strategies combine optimization in both time and frequency domains, constructing a unified objective function to achieve parameter sets that satisfy both impedance characteristics and dynamic response simultaneously. Algorithms such as GA-PSO are typically employed for this multi-domain optimization [15]. Furthermore, data-driven techniques like transfer learning combined with back propagation neural networks (BPNN) have been applied to accurately identify physics-based FOM parameters across the battery's entire life cycle, demonstrating effectiveness even under accelerated aging conditions [25]. Table 1 summarizes the advantages and disadvantages of the PI methods for FOM.

Table 1. Comparison of various parameter identification methods.

	Category	Typical Methods/Algorithms	Advantages	Disadvantages
I.	Offline Global Optimization	PSO, GA, DE, RUN, CPSO	Guaranteed ability to search for the global optimum solution, essential for finding the inherently nonlinear fractional order (α). High resulting model accuracy (low RMSE/MAE).	High computational complexity and expense, unsuitable for real-time/on-board applications due to batch processing requirement.
II.	Online Recursive (Decoupled/ Fixed Order)	RLS, FFRLS, AEKF	Low computational load, fast parameter updates suitable for real-time/microprocessor implementation. Effective for tracking linear parameters.	Requires α to be fixed or determined separately, which may lead to parameter estimation errors and loss of physical meaning.
III.	Online Adaptive	BAS-RLS	Realizes simultaneous full-parameter and order identification online, capturing dynamic changes in α. Provides highly accurate terminal voltage prediction.	Increased computational burden compared to fixed-order RLS methods, often requiring complex software implementation (e.g., G-L definition).
IV.	Multi-Domain and Data-Driven	GA + PSO, Transfer Learning + BPNN	Improves robustness by constraining parameters across both frequency (EIS) and time (dynamic) domains. Data-driven methods facilitate parameter tracking across the entire aging lifecycle.	Requires extensive experimental data collection (both EIS and time-domain). Data-driven methods require a large training dataset for initial learning.

On the other hand, machine learning and deep learning (DL) are also applied to the parameter identification of equivalent circuit models of lithium-ion batteries as well as other complex systems. Techniques including long short-term memory (LSTM) networks, convolutional neural networks (CNNs), and hybrid models (e.g., CNN–LSTM) have demonstrated the capability to accurately estimate time-varying or uncertain parameters by extracting temporal and spatial features from measurement data, often outperforming traditional methods in terms of robustness and accuracy [26,27]. In scientific and engineering contexts, DL architectures are increasingly applied to inverse problems and PI in partial differential equations (PDEs), offering flexible solutions for both direct and indirect measurement scenarios [28,29]. Qiang You et al. present a machine learning approach to accurately identify parameters of the 11-dimensional adapted randles equivalent cir-

cuit model from EIS data, overcoming the high-dimensionality challenge by reducing the model into two low-dimensional forms and applying a Euclidean distance-based pre-classification to select optimal training data for Gaussian process regression [30]. In [31], a neural network is developed to estimate key physics-based electrochemical properties from equivalent circuit model (ECM) parameters, achieving prediction errors below 1% for electrolyte transport properties in nearly all cases. Hanjing Fu et al. present a novel physics-informed neural network (PINN) model that integrates an ECM within a recurrent neural network (RNN) framework for lithium-ion battery modeling and SOH estimation, achieving high accuracy with SOH errors below 2% [32]. Zeyang Geng et al. introduce a new implementation of Pseudo-Two-Dimensional (P2D) model using a transmission line circuit structure combined with the finite difference method, effectively bridging physics-based and equivalent circuit models to deliver precise results without relying on empirical fitting [33]. However, the application of DL to PI remains relatively underexplored in certain domains. For instance, Junfu Li et al. [34] developed a DL method using CNNs for online PI in Lithium-ion batteries; however, the inputs to their model were preprocessed features rather than raw data, and the electrochemical model employed is relatively complex and not well-suited for BMS applications. Zichen Du and Renhao Lu review the use of physics-informed neural networks (PINNs) for efficient thermal management in electronics and battery systems, highlighting their speed and accuracy compared to traditional methods. It discusses recent advancements, challenges, and future research directions for integrating PINNs with advanced technologies [35]. In previous work, the authors proposed a DL approach for PI of a 2RC ECM [36]. To the best of the authors' knowledge, no study has yet applied DL to PI of a FOM. Therefore, this paper introduces several DL models to estimate the parameters of FOMs, aiming to validate their feasibility and effectiveness in this emerging area.

1.2. Theoretical Backgrounds

The methodologies employed in this study encompass various deep learning techniques and their improvement methods. To facilitate understanding, the theoretical foundations and implementation principles of each method—spanning LSTM, gated recurrent unit (GRU), and one-dimensional convolutional neural network (1DCNN)—as well as improvement techniques including the Huber loss function, stochastic weight averaging (SWA), and exponential moving average (EMA), are introduced as follows.

1.2.1. LSTM and GRU [37]

LSTM and GRU were employed as advanced recurrent neural network architectures to handle sequential data, leveraging their ability to capture long-term dependencies. The LSTM cell diagram revealed a structure with three gates as shown in Figure 1a: the forget gate f_t, input gate i_t, and output gate o_t, alongside a cell state C_t and hidden state h_t. Mathematically, the LSTM operations were defined as follows: the forget gate output was $f_t = \sigma\left(W_f \cdot [h_{t-1}, x_t] + b_f\right)$, the input gate output was $i_t = \sigma(W_i \cdot [h_{t-1}, x_t] + b_i)$, the cell candidate was $\widetilde{C}_t = tanh(W_c \cdot [h_{t-1}, x_t] + b_c)$, the cell state update was $C_t = f_t \cdot C_{t-1} + i_t \cdot \widetilde{C}_t$, and the hidden state was $h_t = o_t \cdot tanh(C_t)$ with $o_t = \sigma(W_o \cdot [h_{t-1}, x_t] + b_o)$. This allowed LSTM to selectively remember or forget information over time, making it suitable for the time-series problem where long-term patterns were critical. The GRU cell diagram shown in Figure 1b simplified the architecture with two gates: the reset gate r_t and update gate z_t, merging the forget and input gates into a single update mechanism. The GRU equations were $r_t = \sigma(W_r \cdot [h_{t-1}, x_t] + b_r)$, $z_t = \sigma(W_z \cdot [h_{t-1}, x_t] + b_z)$, the candidate hidden state was $\widetilde{h}_t = tanh(W \cdot [r_t \cdot h_{t-1}, x_t] + b)$, and the hidden state update was $h_t = (1 - z_t) \cdot h_{t-1} + z_t \cdot \widetilde{h}_t$. This reduction in complexity improved computational efficiency while retaining the ability

to model dependencies, which was advantageous for the problem. Both LSTM and GRU models were suitable for this problem because of their intrinsic ability to model long-range dependencies, a requirement directly analogous to the memory effect observed in lithium-ion battery dynamics. The battery's voltage response is governed by its entire historical usage, an enduring non-local effect that standard RNNs could not capture due to the vanishing gradient. By regulating the information flow through their respective gating mechanisms, LSTM and GRU were enabled to maintain a persistent internal state (memory) over extended time steps. This effectively allowed the models to learn the complex, nonlinear patterns within the sequential battery data and implicitly capture the same long-memory behavior that was explicitly represented by the fractional-order elements (like CPE and Warburg) in the analytical FOMs.

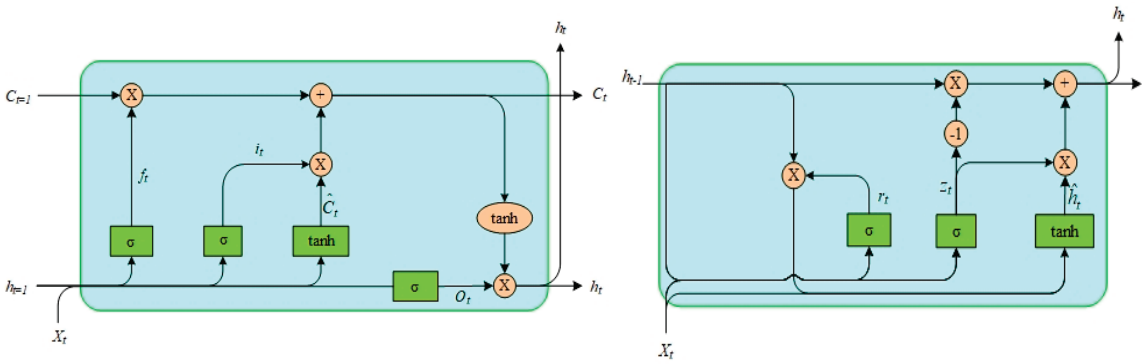

(**a**) (**b**)

Figure 1. LSTM and GRUs (**a**) LSTM cell (**b**) GRU cell.

1.2.2. DCNN [38]

The 1DCNN was utilized as an effective architecture for processing the sequential time-series data from the battery. Unlike 2D CNNs, which slide filters across two spatial dimensions, the 1DCNN employed filters that were moved exclusively across the single time dimension of the input vector (the "Input Signal"). This design allowed the network to automatically extract crucial features regardless of their position in the sequence. As illustrated in Figure 2, the fundamental operation of a 1DCNN is the convolution performed in layers like 'Conv1D Layer'. In this process, a small filter (kernel), K, was applied to a localized segment of the input sequence, X, at time step t to produce an element in the output feature map, y_t. This operation was mathematically defined by:

$$y_t = f\left(\sum_{i=0}^{N-1} K_i \cdot X_{t+i} + b\right) \quad (1)$$

where N is the kernel size, b is the bias, and f is the nonlinear activation function. This filter was swept across the entire input sequence, generating a feature map that highlighted specific temporal patterns. Following the convolutional layer, a Max Pooling 1D layer was typically applied to reduce the dimensionality of the feature maps, thereby decreasing computational load and making the model more robust to minor temporal shifts. The resulting high-level feature maps were then flattened and passed to a fully connected layer (FC Layer) for the final prediction.

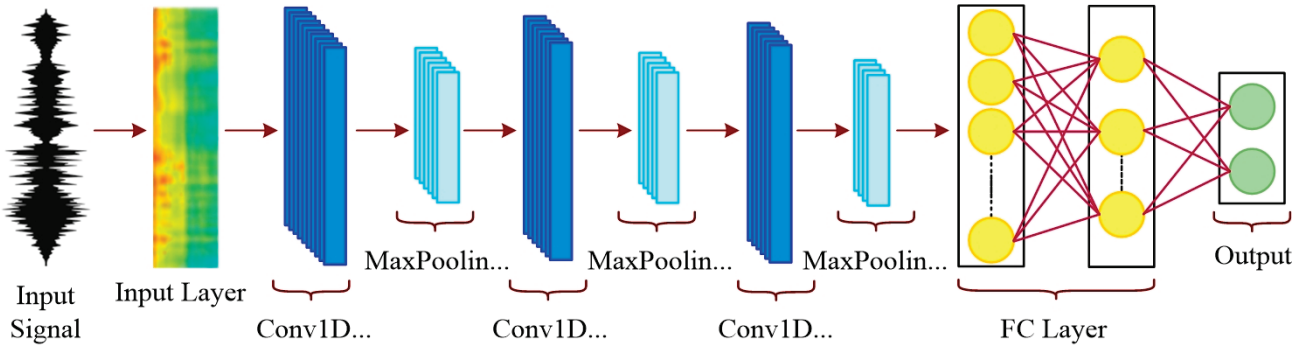

Figure 2. Block diagram of the 1DCNN.

The 1DCNN was employed for this problem because of its efficacy in processing time-series data. The convolutional filters were adept at automatically identifying local temporal features within the sequences, such as sharp current pulses or rapid voltage transients, which are crucial signatures of internal battery kinetics (e.g., Ohmic and charge-transfer resistances). Since the filters were shared across the entire length of the sequence, the model was made translationally invariant, meaning it could detect a specific transient feature regardless of where it appeared in the operating cycle. Furthermore, the 1DCNN generally had a lower computational cost for feature extraction compared to recurrent models, and it demonstrated superior capability in extracting the essential, localized features from the input sequences, a factor which subsequently justified its incorporation into the hybrid architectures to enhance overall predictive power.

1.2.3. Improvement Strategies

Two improvement strategies, the adoption of the Huber loss function [39] and the implementation of SWA [40] and EMA [41], are incorporated to further enhance the robustness and generalization performance of the proposed deep learning models. Next, the theoretical basis of these technologies will be introduced.

The Huber loss function is a robust regression metric that combines the squared error for small residuals and the absolute error for large ones, defined as

$$\mathrm{L}_\delta(y,\hat{y}) = \begin{cases} \frac{1}{2}(y-\hat{y})^2, & if|y-\hat{y}| \le \delta \\ \delta(|y-\hat{y}| - \frac{1}{2}\delta), & otherwise \end{cases} \tag{2}$$

where d is a tuning parameter. This formulation mitigates the influence of outliers compared to mean squared error while retaining sensitivity to smaller errors.

SWA is a training technique that improves generalization by averaging the weights of a model visited during the later stages of stochastic gradient descent optimization, resulting in a flatter minimum in the loss landscape. Mathematically, the averaged weights are computed as

$$\theta_{\mathrm{SWA}} = \frac{1}{N}\sum_{i=1}^{N}\theta_i \tag{3}$$

where θ_i denotes the model weights at the ith checkpoint and N is the total number of checkpoints used for averaging. By averaging these parameters, SWA effectively shifts the final solution toward the center of a wider and flatter region in the loss landscape. This property reduces the model's sensitivity to local fluctuations and improves its generalization capability under varying data distributions. In practice, SWA was applied during the last 20–30% of training epochs, allowing the optimizer to converge to a stable region before averaging began.

EMA keeps a running (exponentially decaying) average of past parameter values, giving recent weights the highest influence and producing a smoother, more stable parameter estimate. The update rule for EMA is defined as

$$\theta_{\text{EMA}}^{(t)} = \beta \cdot \theta_{\text{EMA}}^{(t-1)} + (1-\beta) \cdot \theta^{(t)} \tag{4}$$

where $\theta^{(t)}$ represents the current model weights and $\beta \in [0.999, 0.9995]$ is the exponential decay factor controlling the smoothing strength. EMA acts as a low-pass filter, damping high-frequency noise caused by stochastic gradient variations, thus ensuring a smoother and more stable convergence trajectory. By combining both techniques during the final fine-tuning stage, the model benefits from the complementary effects of discrete checkpoint averaging (SWA) and continuous weight smoothing (EMA).

1.3. Contributions of the Proposed Method

In this study, a simulation platform for the FOM of lithium-ion batteries is first established. The platform is used to generate training and testing datasets through two different sampling strategies: Sobol sampling and Monte Carlo sampling. Subsequently, this work addresses the PI problem of the FOM by developing three DL-based identification frameworks, namely LSTM, GRU, and 1DCNN. The hyperparameters and architectures of these models are optimized using Optuna (version 4.5.0), and their performances are systematically compared. In general, DL models generally exhibit superior representation and generalization capabilities compared to traditional methods, as they learn nonlinear relationships directly from data without necessitating explicit mathematical modeling or manual feature extraction. In contrast, optimization-based techniques such as PSO, GA, or RLS rely on iterative search procedures and often incur substantial computational costs, particularly for high-dimensional or fractional-order systems. Moreover, the trained hybrid deep network enables parameter identification through a single forward pass, significantly reducing inference time while maintaining competitive or enhanced accuracy. The hybrid CNN-GRU framework presents a clear advantage over conventional feature-based machine learning approaches by obviating the need for manual feature engineering and selection. Traditional methods, including tree-based models and support vector machines, rely heavily on domain expertise to extract and predefine salient input features, whereas the deep learning architecture autonomously learns hierarchical and temporal features directly from raw data. This data-driven approach not only mitigates human bias but also facilitates the discovery of complex nonlinear patterns that may be overlooked by manual processes, resulting in a more robust and generalizable model for identifying intricate system parameters. The neuro-physical approach, which incorporates physical laws as constraints within neural network architectures, can indeed be extended from traditional ECMs to FOMs to enhance physical consistency. However, the proposed hybrid deep learning method fundamentally differs by adopting a data-centric rather than a physics-informed strategy. While neuro-physical methods require explicit and accurate prior knowledge of governing equations, our approach exploits the representational capacity of deep learning to implicitly capture complex dynamics directly from data. This confers a significant advantage for FOMs, where governing fractional-order operators are often computationally intensive or where the underlying physical processes are not fully characterized, thereby offering greater flexibility and the potential to uncover unmodeled dynamics.

In this study, two hybrid architectures—1DCNN + LSTM and 1DCNN + GRU—are proposed to enhance the identification accuracy by leveraging both temporal dependency learning and feature extraction capabilities. Finally, two improvement strategies are introduced to further enhance the performance and generalization ability of the DL models: (1) adopting the Huber loss function to achieve a balance between robustness and

sensitivity to outliers, and (2) SWA, and EMA have been applied to improve robustness and training stability. Performance on a 1000-sample test set has been evaluated using root mean square error (RMSE) and mean absolute percentage error (MAPE), with scatter plots, box plots, and heatmaps utilized to assess accuracy for parameters. The improved 1DCNN + GRU model has been identified as the top performer, achieving an RMSE of 0.2223 and MAPE of 0.27%. Terminal voltage prediction has also been validated, yielding an average RMSE of 0.002059 and mean absolute error (MAE) of 0.001387, thereby confirming the models' ability to reconstruct dynamic battery behavior with high fidelity. This study employs a data-driven framework where DL models are trained on simulated synthetic data. Once trained, these models can be directly deployed onto a digital signal controller for real-time, online parameter identification. The main contributions of this paper are listed as follows:

- DL has been applied innovatively to FOM PI problem for lithium-ion batteries, addressing gaps where traditional methods like PSO or RLS are constrained by computational demands or inability to manage nonlinear fractional orders in real-time.
- Hybrid architectures have been introduced, combining convolutional local feature extraction with recurrent temporal modeling, resulting in superior performance; for example, the improved 1DCNN + GRU reduces overall RMSE by nearly 50% from baseline (0.4386 to 0.2223) and achieves MAPE of 0.27%, outperforming the improved LSTM's 9.50% MAPE.
- A simulation platform has been established for dataset generation via Sobol and Monte Carlo strategies, providing diverse and representative data without reliance on physical experiments, thus facilitating scalable training; hyperparameters have been optimized using Optuna to ensure comparative fairness.
- Two enhancement strategies have been proposed: Huber loss for balancing robustness against outliers and sensitivity, and SWA with EMA for training stabilization, leading to up to 31-fold RMSE improvements in hybrids (e.g., 1DCNN + LSTM from 4.658 to 0.268); these are reflected in heatmaps showing consistent low errors across parameters.
- Terminal voltage prediction has been validated with average RMSE of 0.002059 and MAE of 0.001387, enabling high-fidelity reconstruction of battery dynamics and advancing practical applications in BMS by supporting adaptive PI under varying conditions.

2. Fractional-Order Model of Lithium-Ion Batteries

2.1. Brief Description of Fractional-Order Model

An FOM of a lithium-ion battery is an evolution of traditional modeling techniques that leverages fractional calculus (differentiation and integration to a non-integer order) to more accurately describe the complex, non-ideal dynamics within the cell. Instead of relying only on ideal integer-order components like pure resistors and capacitors, the FOM introduces elements that capture the distributed and dispersive nature of electrochemical processes. The model's key components, which replace or enhance those in standard ECM, include the constant phase element (CPE) and the fractional-order Warburg element. The CPE is used to model non-ideal capacitance, particularly the double-layer capacitance at electrode-electrolyte interfaces. In a real battery, the electrode surface is not perfectly smooth; its roughness and porosity cause a distribution of relaxation times. An ideal capacitor has an impedance with a phase angle of -90°, while a resistor has a phase of 0°. The CPE's impedance shown in Equation (5) has a constant phase angle between 0° and -90°

$$Z_{\mathrm{CPE}}(\omega) = \frac{1}{Q(j\omega)^{\alpha}}$$

$$Z_{\mathrm{Re}} = \frac{1}{Q\omega^{\alpha}} cos\left(\frac{\alpha\pi}{2}\right), Z_{\mathrm{Im}} = -\frac{1}{Q\omega^{\alpha}} sin\left(\frac{\alpha\pi}{2}\right), 0 < \alpha < 1 \quad (5)$$

where Z_{CPE} is the impedance of the CPE, Q is the CPE coefficient determining magnitude. α is the fractional order ($0 < \alpha < 1$): $\alpha = 1$ yields a pure capacitor, $\alpha = 0$ yields a pure resistor. ω is the angular frequency. j denotes the imaginary unit. The impedance comprises real (Z_{Re}) and imaginary (Z_{Im}) parts, representing resistive and capacitive contributions, respectively.

The fractional-order Warburg element models the diffusion of lithium ions within the solid electrode particles and the electrolyte. In a conventional analysis, the Warburg element for semi-infinite diffusion is an impedance as shown in Equation (6)

$$Z_W(\omega) = \frac{1}{W(j\omega)^{\alpha}}, \alpha = 0.5 \quad (6)$$

which corresponds to a fractional order of $\alpha = 0.5$ and appears as a 45° line on a Nyquist plot. In lithium-ion batteries, a finite-length Warburg element is typically used to represent diffusion within a bounded volume (e.g., electrode particles).

The primary advantage of FOMs over ECM is significantly higher accuracy with comparable or even fewer fitting parameters. ECMs, like the common RC models, often require a high number of RC pairs to accurately match experimental data, particularly EIS plots, which is computationally expensive and makes parameter identification challenging [42]. FOMs achieve high fidelity by capturing the frequency-dependent behavior using elements with non-integer orders, which inherently accounts for the distributed parameters resulting from non-uniform electrode structure. Compared to electrochemical models (EChMs) such as the pseudo two-dimensional model, the FOM offers a compelling trade-off between physical meaning and computational efficiency. EChMs are based on coupled PDEs and are highly accurate, but they are computationally intensive, making them unsuitable for real-time applications in a BMS. The FOM, by replacing complex diffusion and surface dynamics with fractional-order ODEs, maintains a strong link to the underlying physics while being fast enough for real-time control and state estimation. This superior balance is why FOMs are becoming an increasingly popular choice for advanced battery management.

2.2. FOM Utilized in This Study

In fractional models, circuits combine R, CPE, and Warburg in series/parallel to simulate battery voltage response under various loads. The primary objective of this paper is to validate the feasibility of identifying FOM parameters using voltage response time-series data from batteries. To achieve this, the R(RQ)W model as shown in Figure 3 is selected to represent the lithium battery. This model structure consists of a resistor (R_0) in series with a parallel combination of another resistor (R_1) and a constant phase element (CPE_1), which is then in series with a Warburg element (W). The R(RQ)W model is chosen for its effectiveness in capturing key battery dynamics. The R(RQ) segment effectively describes the charge transfer and double-layer effects, while the series Warburg element is crucial for modeling the solid-state diffusion processes within the battery. This combination provides a compact yet accurate representation, making it highly suitable for FOM parameter identification from time-domain voltage data. The impedance expression of the FOM used in this paper is given in Equation (7).

$$Z(s) = R_i + \frac{R_1 \frac{1}{s^{\alpha} Q_1}}{R_1 + \frac{1}{s^{\alpha} Q_1}} + \frac{1}{s^{\beta} W}, 0 < \alpha < 1, \beta = 0.5 \quad (7)$$

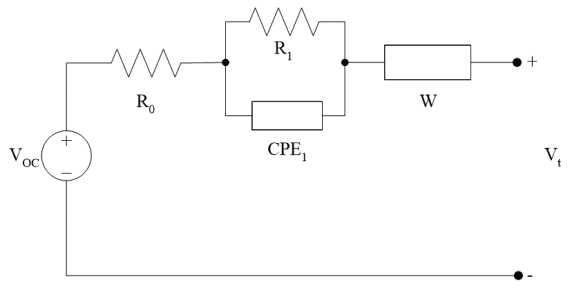

Figure 3. The utilized FOM.

The model used in this paper is a fractional-order version of the popular Partnership for a New Generation of Vehicles (PNGV) model. The PNGV model accurately simulates battery behavior under dynamic loads, offering simplicity and good fit for hybrid vehicle applications. Converting it to a fractional-order representation enhances precision by better capturing nonlinear dynamics and memory effects, improving accuracy in modeling complex electrochemical processes with fewer parameters [43].

2.3. Time Domain Voltage Response of the Utilized FOM

Fractional calculus can be solved using methods like Grünwald-Letnikov (GL), Riemann-Liouville (RL), or Caputo. GL approximates fractional derivatives via discrete differences, suitable for numerical computations [44]. RL defines fractional integrals and derivatives through convolution, effective for analytical solutions. Caputo reformulates derivatives to handle initial conditions better, ideal for physical systems. GL method is often chosen for its straightforward numerical implementation and accuracy in discretizing fractional operators, especially in simulations. The R(RQ)W equivalent circuit is described by the following continuous-time state equations, with I(t) as the input current and $x(t) = \begin{bmatrix} V_1(t) \\ V_2(t) \end{bmatrix}$ as the state vector:

$$\begin{cases} \mathbf{D}^{\alpha} V_1(t) = -\frac{1}{R_1 Q_1} V_1(t) + \frac{1}{Q_1} I(t) \\ \mathbf{D}^{\beta} V_2(t) = \frac{1}{W} I(t) \end{cases} \tag{8}$$

Here, D^a is the fractional derivative operator, a is the order of the CPE (Q), β is the order of the Warburg element (W) (typically β = 0.5), R_1Q_1 is the time constant of the RQ branch, respectively. For brevity, let $a_1 = -\frac{1}{R_1Q_1}, b_1 = \frac{1}{Q_1}, a_2 = 0$, and $b_2 = \frac{1}{W}$.

The GL approximation is the core tool for discretization, as it transforms the fractional derivative at time $t_k = k\Delta t$ into a discrete, weighted sum that inherently captures the system's long memory effect

$$\mathrm{D}^{\alpha} x(t_k) \approx \frac{1}{\Delta t^{\alpha}} \sum_{j=0}^{k} c_j^{(\alpha)} x_{k-j} \tag{9}$$

where Δt is the sampling time, and $c_j^{(\alpha)}$ are the GL coefficients, calculated recursively by $c_0^{(\alpha)} = 1$ and $c_j^{(\alpha)} = \left(1 - \frac{\alpha+1}{j}\right) c_{j-1}^{(\alpha)}$ for $j \geq 1$.

Applying the GL approximation to the state equations and solving for the state at the next time step, $V_{i,k+1}$, leads directly to the discrete state-space form. Use $j = 0$ for

the current state $V_{i,k+1}$ and move the memory terms (where $j \geq 1$) to the right side of the equation. The resulting discrete state-space equation for the ith state is:

$$V_{i,k+1} = \underbrace{\frac{-Q_1^{(\alpha_i)}}{1 - a_i \Delta t^{\alpha_i}}}_{\widetilde{A}_{i,i}} V_{i,k} + \underbrace{\frac{b_i \Delta t^{\alpha_i}}{1 - a_i \Delta t^{\alpha_i}}}_{\widetilde{B}_i} I_{k+1} + \underbrace{\frac{-1}{1 - a_i \Delta t^{\alpha_i}} \sum_{j=2}^{k+1} c_j^{(\alpha_i)} V_{i,k+1-j}}_{\widetilde{\Gamma}_{i,k}} \tag{10}$$

In the standard discrete state-space form, $\mathbf{x}_{k+1} = \mathbf{A}\mathbf{x}_k + \mathbf{B}u_{k+1} + \mathbf{\Gamma}_k$:

$$\mathbf{x}_{k+1} = \begin{bmatrix} V_{1,k+1} \\ V_{2,k+1} \end{bmatrix} = \underbrace{\begin{bmatrix} A_{11} & 0 \\ 0 & A_{22} \end{bmatrix}}_{\mathbf{A}} \begin{bmatrix} V_{1,k} \\ V_{2,k} \end{bmatrix} + \underbrace{\begin{bmatrix} B_1 \\ B_2 \end{bmatrix}}_{\mathbf{B}} I_{k+1} + \underbrace{\begin{bmatrix} \Gamma_{1,k} \\ \Gamma_{2,k} \end{bmatrix}}_{\mathbf{\Gamma}_k} \tag{11}$$

The output equation for the terminal voltage $V_{t,k}$ is the sum of the open-circuit voltage $V_{oc,k}$, the ohmic drop, and the polarization voltages:

$$V_{t,k} = V_{oc,k} + V_{1,k} + V_{2,k} + R_0 I_k \;\Rightarrow\; V_{t,k} = V_{oc,k} + \underbrace{[11]}_{\mathbf{C}} \mathbf{x}_k + \underbrace{R_0}_{\mathbf{D}} I_k \tag{12}$$

This model is a concise Fractional-Order State-Space representation. The matrices A and B capture the immediate dynamics, while the crucial memory vector Γ_k (the long summation of past states weighted by GL coefficients) captures the long-term history dependence inherent to fractional-order systems, making the model highly accurate for real battery dynamics.

3. Description of the Proposed Parameter Identification Method

3.1. Description of the Generation of the Dataset

This study validates the feasibility of identifying FOM parameters from battery voltage response data, adopting the R(RQ)W model for its ability to capture key dynamics such as charge transfer and solid-state diffusion. A custom simulation platform was developed to generate the training dataset, which comprises 2048 samples. Each sample consists of a voltage response as input and the corresponding FOM parameters as labels. The simulation was configured with a duration of 0–30 s and a time step of 0.01 s. A single current pulse of 1.0 A, applied from t = 10 s to t = 20 s, served as the excitation signal across all simulations. The FOM parameters were sampled around normalized baseline values, experimentally obtained from a real battery at 50% state of charge (SOC). To account for parameter variations across the full SOC range (0–100%), each parameter—except the fractional order α—was varied within $\pm 20\%$ of its baseline. This range ensures broad coverage of realistic battery conditions. The resultant ranges for the key circuit elements were: the Ohmic Resistance R_0 spanned $[0.0174, 0.0260]\Omega$; the Charge-Transfer Resistance R_1 was defined between $[0.0080, 0.0120]\Omega$; the coefficient for the Constant Phase Element Q_1 ranged from $[82.85, 124.28]$ $\mathrm{F{\cdot}S^{(\alpha-1)}}$; and the Warburg Coefficient W covered $[253.26, 379.90]\Omega{\cdot}\mathrm{s}^{-0.5}$. The fractional order (α), which characterizes the behavior of the constant phase element, was independently sampled within the range of 0.5 to 1.0, encompassing the physical spectrum from pure diffusion to pure capacitance.

This study utilized Sobol sampling to generate 2048 parameter sets for simulating FOM voltage responses, leveraging Sobol sequences' ability to uniformly cover multidimensional spaces more effectively than random sampling. These sequences are deterministic, constructed using number theory and primitive polynomials modulo 2, and employ bitwise XOR operations with carefully chosen direction numbers to minimize clustering and

gaps [45]. While the full algorithm is complex, the value of the $n - t_h$ point in the sequence for the $j - t_h$ dimension can be conceptualized as:

$$x_n^{(j)} = i_1 v_1^{(j)} \oplus i_2 v_2^{(j)} \oplus \ldots \tag{13}$$

where i_k are the binary digits of n, $v_k^{(j)}$ are carefully chosen direction numbers for the $n - t_h$ dimension, and $\oplus$ is the bitwise XOR operation.

This quasi-Monte Carlo (MC) technique ensures space-filling sampling even in high-dimensional parameter spaces, leading to faster convergence in integration and sampling tasks. The approach is particularly suited for identifying parameters in complex electrochemical systems like batteries, where parameters are nonlinear and time-dependent. By providing comprehensive and uniform coverage of the parameter space, Sobol sampling enables training algorithms to better capture diverse dynamic behaviors and parameter correlations, thereby enhancing the accuracy and robustness of parameter identification.

The generalization capability of DL models is evaluated by ensuring that the test dataset differs from the training data, thereby allowing performance to be assessed on unseen inputs. In this study, 1000 independent samples are generated as test data using the Monte Carlo method, with parameter bounds aligned to those employed in the Sobol sequence to maintain consistency in the sampling space. The MC method is utilized to approximate integrals or distributions through random sampling, mathematically expressed as

$$\hat{I} = \frac{1}{N} \sum_{i=1}^{N} f(x_i) \tag{14}$$

where x_i are randomly drawn from a uniform distribution over the domain, and N is the number of samples. This approach is considered suitable for test data generation, as diverse and unbiased samples are produced that mimic real-world variability, thereby enhancing the robustness evaluation of the model without requiring structured quasi-random sequences. Figure 4 Illustrates the training and test dataset used in this paper.

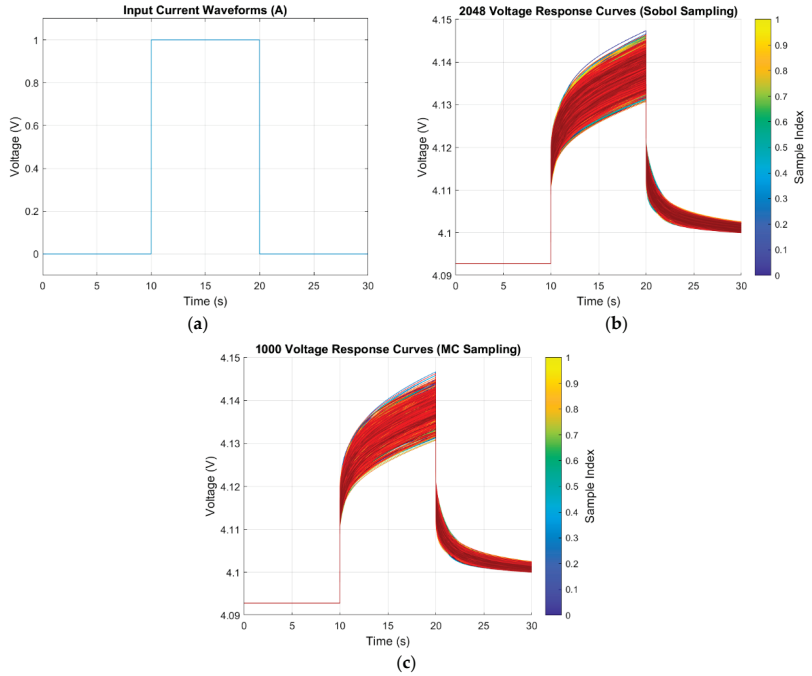

Figure 4. Illustration of the training and test data used in this paper. (**a**) Input current profile. (**b**) Voltage responses generated by the Sobol sampling method. (**c**) Voltage responses generated by the MC sampling method.

3.2. The Proposed DL Parameter Identification Models

Due to the time-series nature of the data, LSTM, GRU, and 1DCNN are adopted as baseline models, while vanilla RNNs are excluded because of their susceptibility to vanishing gradients, which hinder the learning of long-term dependencies. LSTM and GRU are chosen for their gating mechanisms that effectively capture long-term dependencies; LSTM is well-suited for complex sequences, whereas GRU offers greater computational efficiency. Additionally, 1DCNN is included for its superior ability to extract local temporal patterns, often outperforming RNN variants in this regard. To leverage complementary strengths, hybrid architectures combining 1DCNN with LSTM and 1DCNN with GRU are further explored. As illustrated in Figure 5 (using 1DCNN + LSTM as an example), these models utilize a two-stage design: multiple Conv1D layers with MaxPooling1D first extract hierarchical local features from the raw time-series input. These features are then passed to LSTM or GRU layers for sequential modeling, followed by a fully connected output layer. Mathematically, the CNN stage extracted features via convolution, $y[i] = \sum_m x[i-m] \cdot w[m] + b$ with ReLU activation $y[i] = \max(0, y[i])$ and max-pooling $p[j] = \max_{k \in [j \cdot s, (j+1) \cdot s)} y[k]$, where x was the input, w the filter, b bias, and s stride. The LSTM stage then processed these features with equations like forget gate $f_t = \sigma(W_f[h_{t-1}, x_t] + b_f)$, cell update $C_t = f_t \cdot C_{t-1} + i_t \cdot \tanh(W_C[h_{t-1}, x_t] + b_C)$, and hidden state $h_t = o_t \cdot \tanh(C_t)$, integrating temporal dependencies.

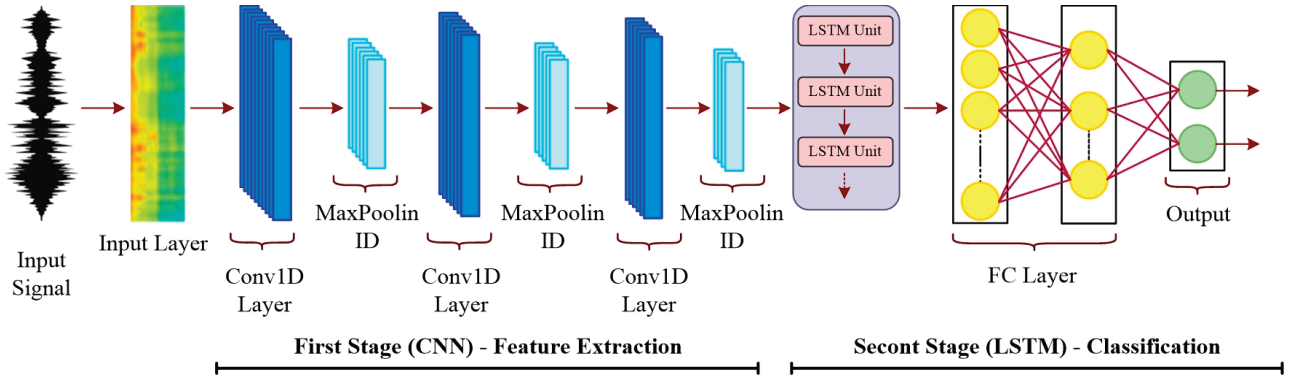

Figure 5. Block diagram of the 1DCNN + LSTM.

These hybrid models were suitable for the time-series problem because they combined 1DCNN's efficient local feature extraction with LSTM/GRU's capability to model long-term dependencies, enhancing overall performance. The 1DCNN component excelled in detecting short-term patterns in sequential data, often outperforming standalone LSTM and GRU, prompting the hypothesis that stacking it as a preprocessor could yield synergistic improvements. This approach mitigated vanishing gradient issues in pure recurrent models while maintaining robustness for complex electrochemical simulations, aligning with the dataset's temporal and dynamic characteristics.

3.3. Improving Performance by Introducing HuberLoss and SWA/EMA

To enhance the regression accuracy and improve the model's robustness against noisy measurements or outlier samples, the conventional mean squared error (MSE) loss was modified into a hybrid loss function. The proposed loss combines the sensitivity of MSE to small errors with the robustness of the Huber (smooth L1) loss, controlled by a tunable coefficient α:

$$\mathcal{L}_{\text{hybrid}} = \text{MSE} + \alpha_h \cdot \text{HuberLoss} \tag{15}$$

Here, $\alpha_h \in [0, 1]$ adjusts the contribution of the Huber term. When $a_h = 0$, the function reduces to pure MSE; when $a_h > 1$, the loss penalizes large residuals less aggressively,

reducing the impact of sporadic measurement noise or transient mismatches in the wireless power transfer data. When Huber loss is incorporated, a_h is treated as a tunable parameter and optimized using Optuna.

After the main training phase, the obtained models were further refined using a combination of SWA and EMA to enhance the model's stability, generalization, and robustness. SWA operates by maintaining an arithmetic average of model parameters over several checkpoints collected during the final fine-tuning epochs. The resulting models demonstrated smoother validation curves, lower RMSE and MAPE values, and reduced sensitivity to initialization or data imbalance. This improvement was particularly significant for recurrent and hybrid architectures, whose optimization landscapes are highly non-convex and prone to oscillations.

4. Simulation and Experimental Results

Following the introduction of the FOM for lithium-ion batteries in Section 2 and the detailed presentation of the five proposed models—LSTM, GRU, 1DCNN, 1DCNN + LSTM, and 1DCNN + GRU—in Section 3, this section evaluates the performance of these methods in identifying FOM parameters (R_0, R_1, Q_1, α, and W) on a test dataset comprising 1000 samples. Performance assessment utilizes RMSE and MAPE as key metrics, providing quantitative insights into PI accuracy and model generalization. RMSE is a measure of the magnitude of the error between predicted and actual values. It is the square root of the average of the squared differences, giving a relatively high weight to large errors. This makes it particularly useful when large errors are undesirable. The equation for RMSE is:

$$\text{RMSE} = \sqrt{\frac{1}{N}\sum_{i=1}^{N}(y_i - \hat{y}_i)^2} \tag{16}$$

where N is the total number of data points, y_i is the actual (true) value for the $i - t_h$ data point, and $\hat{y}_i$ is the predicted (estimated) value for the $i - t_h$ data point.

MAPE expresses the accuracy as a percentage of the error. It calculates the average of the absolute percentage differences between predicted and actual values. It is easily interpretable but can be problematic if the actual values are close to zero, as it can lead to infinite or extremely large percentages. The equation for MAPE is:

$$\text{MAPE} = \frac{100\%}{N}\sum_{i=1}^{N}\left|\frac{y_i - \hat{y}_i}{y_i}\right| \tag{17}$$

where the variables are the same as defined for RMSE. The result is a percentage value.

To ensure an optimal and robust identification process, the hyperparameters of the optimization algorithm were systematically tuned using the Optuna framework [46]. The resulting optimal hyperparameters for each of the five models are summarized in Table 2. These configurations were consistently applied in all subsequent experiments to maintain a fair basis for comparison.

The hyperparameters detailed in Table 2 can be categorized as follows. Architectural parameters define the model's structure; these include n_channels_1 and n_channels_2, which specify the number of convolutional filters in the first and second layers, and kernel_size_1 and kernel_size_2, which determine the size of these convolutional filters. For the recurrent models, gru_hidden_units/lstm_hidden_units and gru_layers/lstm_layers set the number of hidden units and the stack count of the GRU or LSTM layers, respectively, while the gru_bidirectional/lstm_bidirectional flag indicates the use of a bidirectional architecture. The fc_units/fcl_units parameter controls the size of the fully connected

layer. Regularization parameters are crucial for preventing overfitting and include various dropout rates applied to convolutional, recurrent, and fully connected layers, as well as weight_decay for L2 regularization. Finally, training parameters govern the optimization process, encompassing the learning rate (lr), batch_size, the type of activation function (e.g., GELU, ReLU), and the alpha parameter for the negative slope of the Leaky ReLU activation. Regarding the training procedure, all models were trained end-to-end using the AdamW optimizer to minimize the MSE loss function. To ensure robust training and prevent overfitting, an early stopping mechanism is employed with a patience of 50 epochs, monitoring the validation loss, and set a maximum training duration of 500 epochs. The optimal set of hyperparameters for each model architecture, as reported in Table 2, was determined through an extensive search of 100 trials per model using the Optuna library.

Table 2. Optimal hyperparameters for the proposed method as determined by Optuna for each of the five models.

Hyperparameters	**IDCNN_FCN**	**IDCNN_GRU**	**IDCNN_LSTM**
n_channels_1	160	192	224
n_channels_2	32	288	384
kernel_size_1	3	5	3
kernel_size_2	7	5	5
fc_units	192	64	256
dropout	0.2	0.1	0.2
activation	gelu	gelu	relu
lr	0.0002	0.0007	0.001
batch_size	8	16	16
weight_decay	0.00008	0.000001	0.00005
alpha	0.2	0.2	0.4
Hyperparameters	GRU_FCN	Hyperparameters	LSTM
gru_hidden_units	320	lstm_hidden_units	320
gru_layers	1	lstm_layers	1
gru_bidirectional	TRUE	lstm_bidirectional	TRUE
gru_dropout	0.02	lstm_dropout	0.3
fc1_units	160	fc_dropout	0.3
fc_dropout	0.3	lr	0.0005
activation	gelu	batch_size	16
lr	0.0001	weight_decay	0.00008
batch_size	64	alpha	0.4
weight_decay	0.000007		
alpha	0.4		

The core of the evaluation lies in the identification accuracy of the fundamental model parameters: the ohmic resistance (R_0), the charge transfer resistance (R_1), the constant phase element (Q_1), the fractional-order derivative (α), and the Warburg impedance element (W). Figure 6 presents a comprehensive visual assessment of the estimation accuracy for five distinct models, each with a baseline and an improved variant. The scatter plots, which correlate estimated values with their ground truth counterparts over 1,000 test samples, reveal several key insights. Ideal estimation would place all data points directly on the diagonal identity line, indicating a perfect match. Overall, the improved versions of the models demonstrate a clear enhancement in estimation accuracy, as evidenced by the tighter clustering of data points along the diagonal reference line. Among the five examined parameters (R_0, R_1, Q_1, α, and W), the resistive parameters R_0 and W are generally easier to identify, with all models exhibiting near-perfect linear correlations between predicted and true values for the improved versions—except for the LSTM model. For the capacitive parameter

(Q_1) and the fractional order (α), larger deviations are observed, particularly in the baseline models, suggesting higher sensitivity to model architecture and data representation. The pure recurrent architectures (LSTM and GRU) show relatively greater dispersion in these parameters, indicating difficulties in capturing the nonlinear fractional-order dynamics solely through temporal dependencies. In contrast, models incorporating convolutional layers (1DCNN, 1DCNN + LSTM, and 1DCNN + GRU) achieve substantially improved alignment with the ground truth, demonstrating the advantage of spatiotemporal feature extraction. The improved versions of all hybrid models, especially 1DCNN + GRU, exhibit the most consistent performance across all parameters, with minimal bias and scatter. These results highlight that convolutional–recurrent fusion enhances parameter identifiability by leveraging both local feature extraction and temporal correlation learning. Additionally, R1 appears moderately difficult to estimate, though the improved hybrid models maintain high predictive fidelity. Overall, the results confirm that the proposed improvements effectively enhance robustness and accuracy in parameter estimation for fractional-order lithium-ion battery models.

Figure 7 presents the estimation error distributions for all models across the five parameters, providing a quantitative complement to the scatter plots shown in Figure 6. Overall, the improved models consistently exhibit narrower interquartile ranges and smaller median deviations, confirming that the proposed enhancements effectively reduce estimation variance and bias. The 1DCNN-based hybrid models, particularly the 1DCNN + GRU (Improved) model, achieve the lowest error dispersion across all parameters, demonstrating superior robustness and generalization. Comparing architectures, the convolution–recurrent hybrids outperform both pure CNN and pure RNN models, highlighting the advantage of integrating local feature extraction with temporal modeling. These findings align with the scatter plot results, collectively confirming that the improved hybrid frameworks yield more accurate and stable parameter identification across all fractional-order components of the lithium-ion battery model. Figure 8 presents heatmaps of the RMSE and MAPE, offering a definitive quantitative summary of model performance that strongly aligns with the preceding visual analyses from the scatter and box plots. The results provide unambiguous numerical evidence supporting the key conclusions about the efficacy of the model improvements, the performance ranking of the architectures, and the relative difficulty of parameter identification. The most prominent finding is the substantial performance gap between the baseline and improved models. The baseline variants are universally characterized by high error metrics, visualized as bright yellow and green hues, with MAPE often exceeding 9%. In stark contrast, the improved models consistently display dark purple and blue hues, representing dramatically lower errors. This confirms the overwhelming effectiveness of the proposed improvements in enhancing model accuracy and reliability. Furthermore, the heatmaps reaffirm the parameter identification hierarchy. For the majority of the improved models, the fractional-order exponent α_1 consistently yielded the highest MAPE values. This observation confirms that α is the most difficult parameter to identify with precision, while R_0 is identified with the highest fidelity.

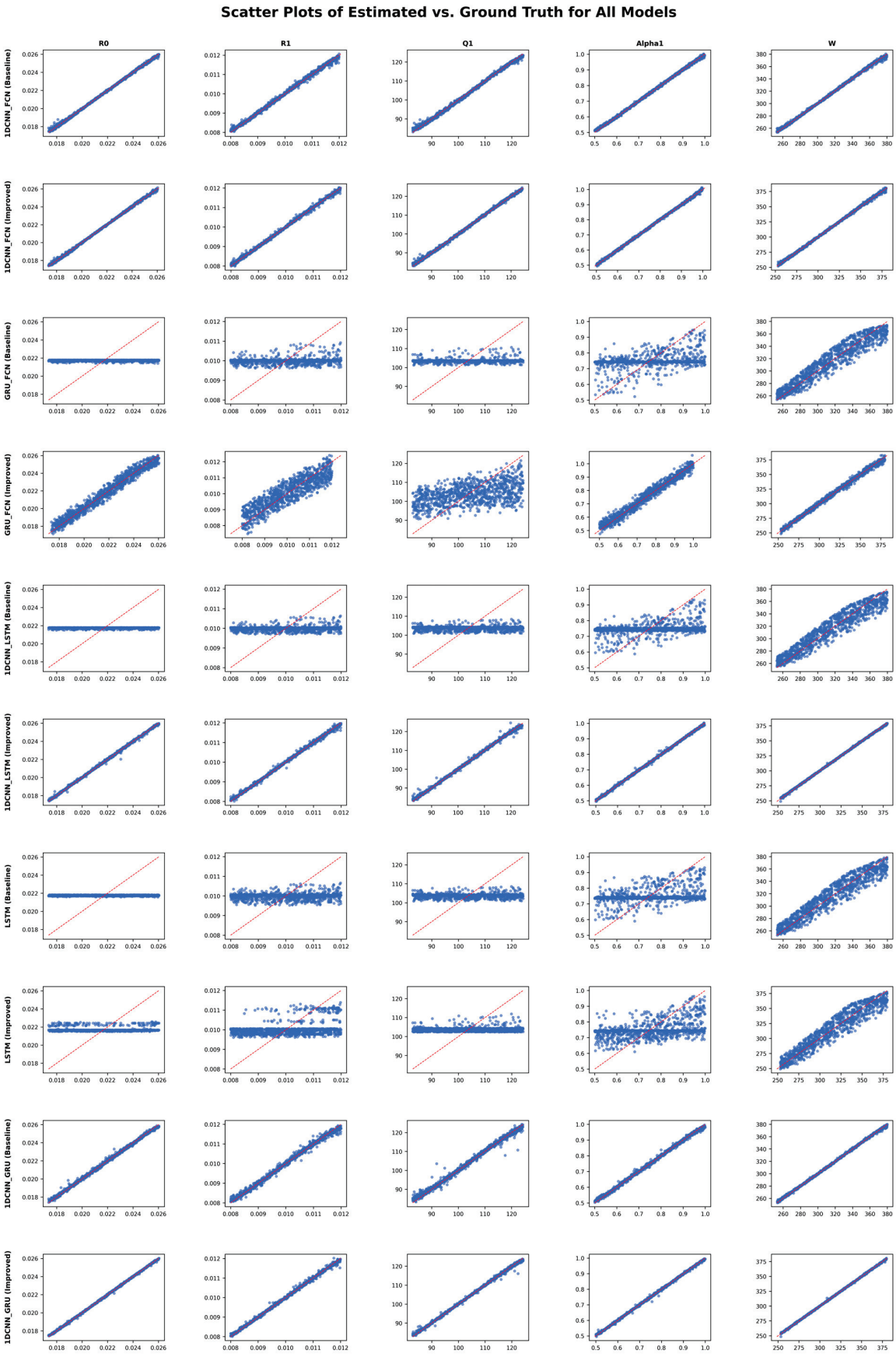

Figure 6. Scatter Plots of Estimated vs. Ground-Truth Parameter Values for All Model Variants.

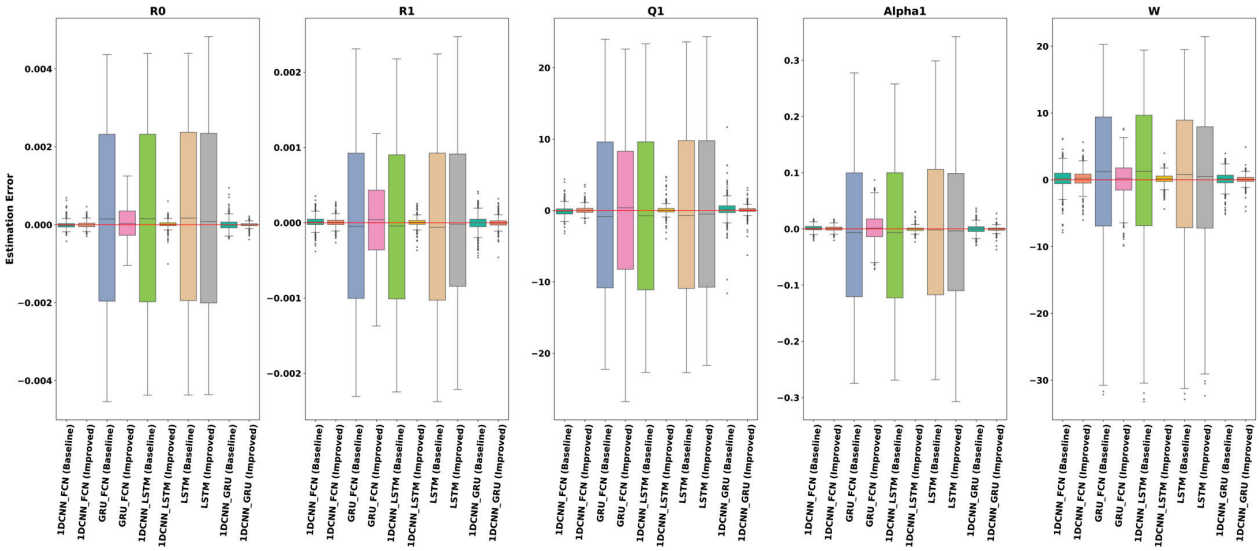

Figure 7. Box plots of parameter estimation errors for R_0, R_1, Q_1, α, and W for each model.

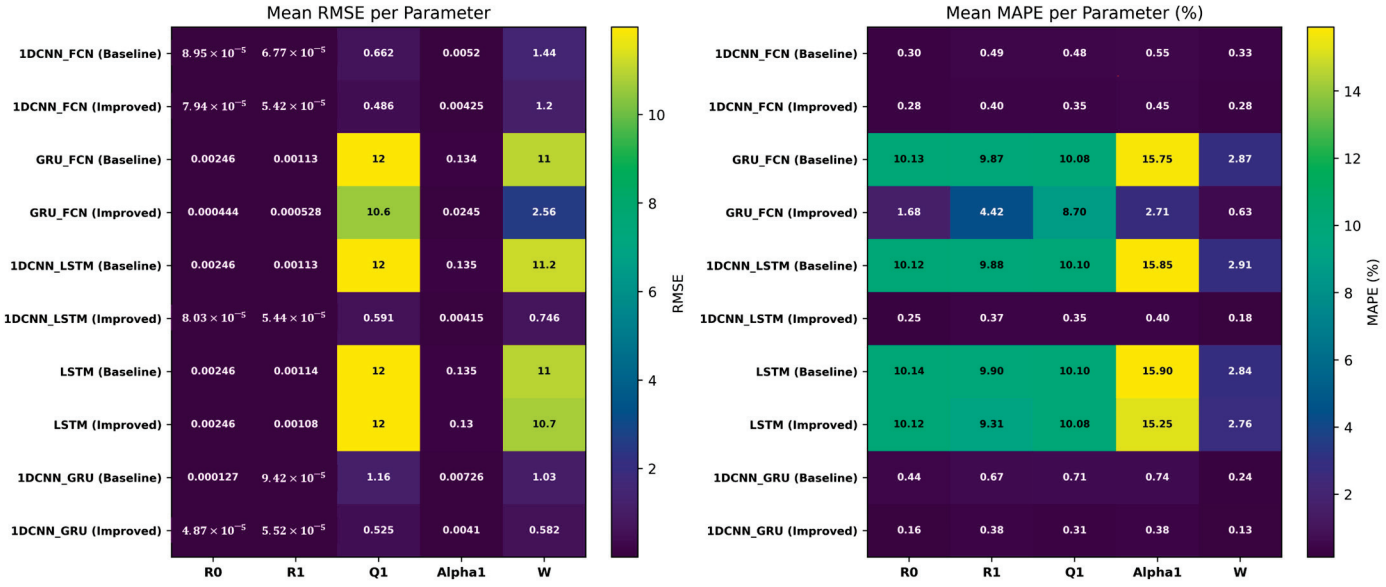

Figure 8. Heatmap of the mean parameter estimation errors across all 10 models.

The efficacy of the proposed FOM parameter identification methods was evaluated on a test set of 1000 samples, with the overall results summarized in Table 3. For each of the ten model variants—baseline and improved versions of LSTM, GRU, 1DCNN-FCN, 1DCNN-LSTM, and 1DCNN-GRU—the overall RMSE and MAPE values were computed as the mean of the respective errors across all five model parameters. These numerical results establish a definitive performance hierarchy, reinforcing conclusions drawn from prior graphical analyses and quantifying the impact of the proposed improvements. The improved versions consistently outperformed their baseline counterparts, with hybrid architectures—particularly those incorporating 1D convolutional layers—forming the top tier of accuracy. A clear stratification emerged among the models, with 1DCNN_GRU, 1DCNN_LSTM, and standalone 1DCNN leading in performance. The 1DCNN_GRU (Improved) model was the top performer, achieving an RMSE of 0.2223 and a MAPE of 0.27%, representing nearly a 50% reduction in RMSE compared to its baseline version. Similarly, the 1DCNN_LSTM (Improved) variant exhibited dramatic improvement, reducing RMSE from 4.658 to 0.268 and MAPE from 9.77% to 0.31%, reflecting a performance increase of

over 31-fold. This underscores a powerful synergistic effect between convolutional feature extraction and recurrent layers, enhanced by the improved framework. In contrast, standalone recurrent models lagged significantly. The improved GRU model recorded a MAPE of 3.63%, while the improved LSTM model had a high MAPE of 9.50%, showing only a marginal reduction from 9.77%. This minimal improvement suggests that the standalone LSTM architecture is fundamentally ill-suited for this task, as the enhanced techniques could not fully mitigate its inherent limitations. The magnitude of improvement from baseline to improved versions varied across models, with hybrid architectures exhibiting the most substantial gains. For instance, 1DCNN_FCN (Improved) showed solid progress, though it remained mid-tier among hybrids with a reduced RMSE. Meanwhile, GRU_FCN (Improved) halved its RMSE to 2.639 but still trailed the top performers. The standalone LSTM and GRU_FCN models exhibited more modest enhancements, with LSTM (Improved) reducing RMSE from 4.615 to 4.563, indicating limited responsiveness to the applied improvements. These results highlight the advantage of integrating convolutional layers with recurrent units, which effectively capture both spatial and temporal features critical for parameter estimation in this context. Ranking the models, 1DCNN_GRU (Improved) and 1DCNN_LSTM (Improved) led, followed by 1DCNN_FCN (Improved), with GRU_FCN (Improved) and LSTM (Improved) trailing significantly. The superior performance of hybrid models can be attributed to the complementary strengths of 1DCNN's local feature extraction and the temporal modeling capabilities of LSTM or GRU, amplified by the proposed enhancements. The inclusion of Huber loss likely improved robustness to outliers, while SWA and EMA enhanced generalization, with their combined effect yielding the most substantial accuracy gains. This analysis affirms that the 1DCNN-GRU architecture, optimized with both techniques, provides the most accurate and robust solution for parameter identification in the FOM, as substantiated by the comprehensive metrics in Table 3.

Table 3. Aggregated RMSE and MAPE for Parameter Estimation Across the 10 Model Variants.

Model	RMSE	MAPE (%)
1DCNN_FCN (Baseline)	0.42088	0.42993
1DCNN_FCN (Improved)	0.33886	0.35212
GRU_FCN (Baseline)	4.62582	9.73964
GRU_FCN (Improved)	2.63896	3.62933
1DCNN_LSTM (Baseline)	4.65831	9.77203
1DCNN_LSTM (Improved)	0.26827	0.31004
LSTM (Baseline)	4.61500	9.77574
LSTM (Improved)	4.56344	9.50254
1DCNN_GRU (Baseline)	0.43863	0.56150
1DCNN_GRU (Improved)	0.22232	0.27387

Accurate parameter estimation is essential; however, the ultimate validation of the identified model lies in its ability to precisely predict the battery's terminal voltage. The parameters obtained from the test set were subsequently substituted into the realized FOM simulation platform to generate simulated voltage responses. The best-performing 1DCNN_GRU model achieves average RMSE and MAE values of 0.002059 and 0.001387, respectively, across 1000 test data points, further validating the accuracy of the proposed method. Figure 9 presents the simulated voltage responses alongside the ground truth for three randomly selected test samples. In every model and case, the simulated waveforms exhibit an exceptionally close overlap with the actual voltage profiles. This excellent visual agreement, quantitatively supported by consistently low RMSE and MAE values dis-

played on each plot, confirms that all improved models effectively leverage their estimated parameters to accurately reconstruct the battery's dynamic behavior with high fidelity.

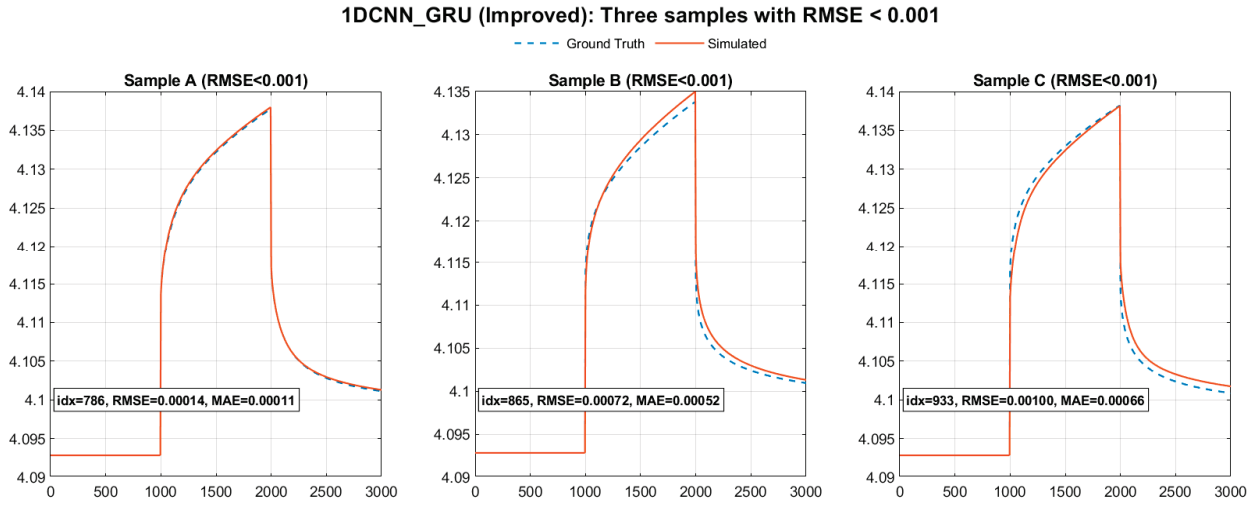

Figure 9. Comparison of Simulated Voltage Responses (from Estimated Parameters) vs. Ground-Truth Responses for Representative Test Samples.

To simulate real-world measurement conditions, synthetic voltage waveforms were corrupted with noise to assess the robustness of the proposed deep learning methods. Considering that the voltage measurement accuracy of typical commercial battery cyclers is generally lower than 0.1% full scale, three noise levels0.05%, 0.1%, and 0.2% of the signal amplitude—were tested, representing optimistic, typical, and worst-case scenarios, respectively. Table 4 presents the RMSE and MAPE of the three top-performing models under these noise conditions, while Figure 10 shows the scatter plots of the parameter identification results across varying noise intensities. Based on the results presented in Table 4 and Figure 10, the robustness of the three improved models against simulated measurement noise was evaluated. The 1DCNN_GRU (Improved) model demonstrates superior noise immunity, maintaining relatively stable RMSE and MAPE values even at a 0.2% noise level (RMSE: 0.726, MAPE: 0.633%). Its performance degradation is the most gradual among the three, indicating a strong ability to learn robust features from noisy inputs. In contrast, the 1DCNN_LSTM (Improved) model exhibits significant sensitivity to noise. While its performance is excellent with clean data, its RMSE and MAPE deteriorate dramatically with increasing noise, surging to 3.452 and 3.722%, respectively, at the 0.2% noise level, which suggests potential overfitting to the clean training data or instability in its temporal processing under perturbation. The 1DCNN_FCN (Improved) model shows moderate and consistent robustness. Its error metrics increase only slightly across the tested noise levels, reflecting a stable architecture less affected by minor input variations. This analysis confirms that the 1DCNN_GRU model possesses the most reliable anti-interference capability, making it the most suitable candidate for deployment in real-world scenarios where sensor data is often contaminated with noise. The varying degrees of robustness highlight the critical impact of the recurrent layer's architecture on model stability.

Table 4. Performance Of The 3 Best Performing Models Under Different Levels of Noise.

Model	Noise Level	RMSE	MAPE (%)
1DCNN_FCN (Improved)	0.05%	0.33889	0.35359
RMSE (noise = 0): 0.33886	0.1%	0.34105	0.35675
MAPE (noise = 0): 0.35212	0.2%	0.35482	0.36861

Table 4. *Cont.*

Model	Noise Level	RMSE	MAPE (%)
1DCNN_LSTM (Improved)	0.05%	0.73823	0.75877
RMSE (noise = 0): 0.26827	0.1%	1.89417	1.90011
MAPE (noise = 0): 0.31004	0.2%	3.45218	3.72231
1DCNN_GRU (Improved)	0.05%	0.25453	0.30438
RMSE (noise = 0): 0.22232	0.1%	0.38005	0.37900
MAPE (noise = 0): 0.27387	0.2%	0.72605	0.63324

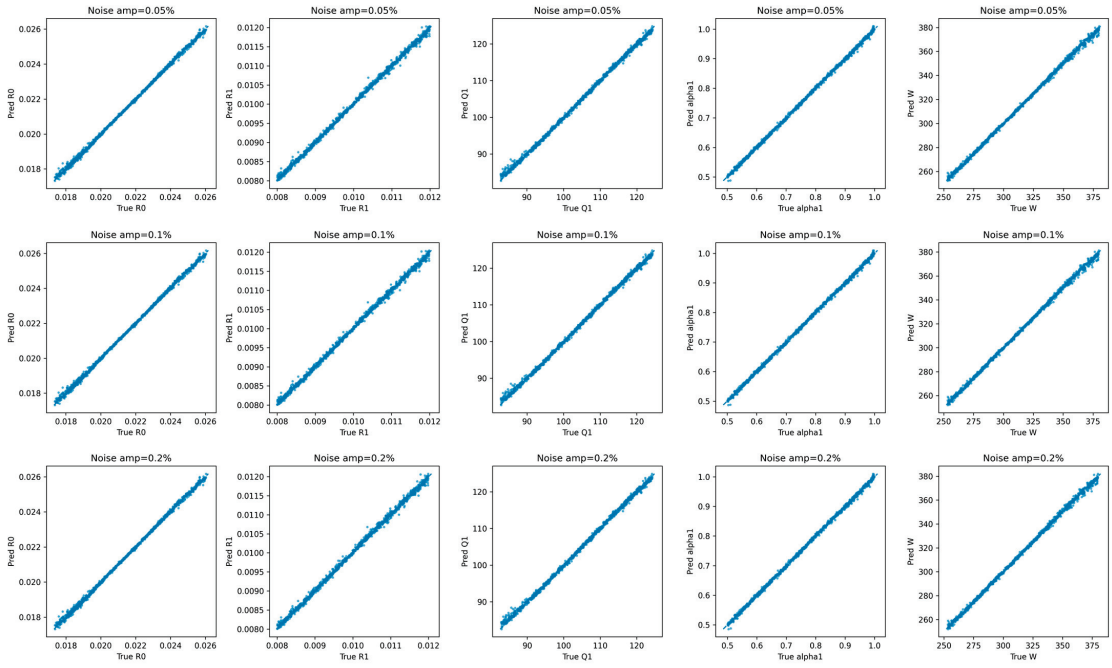

(**a**)

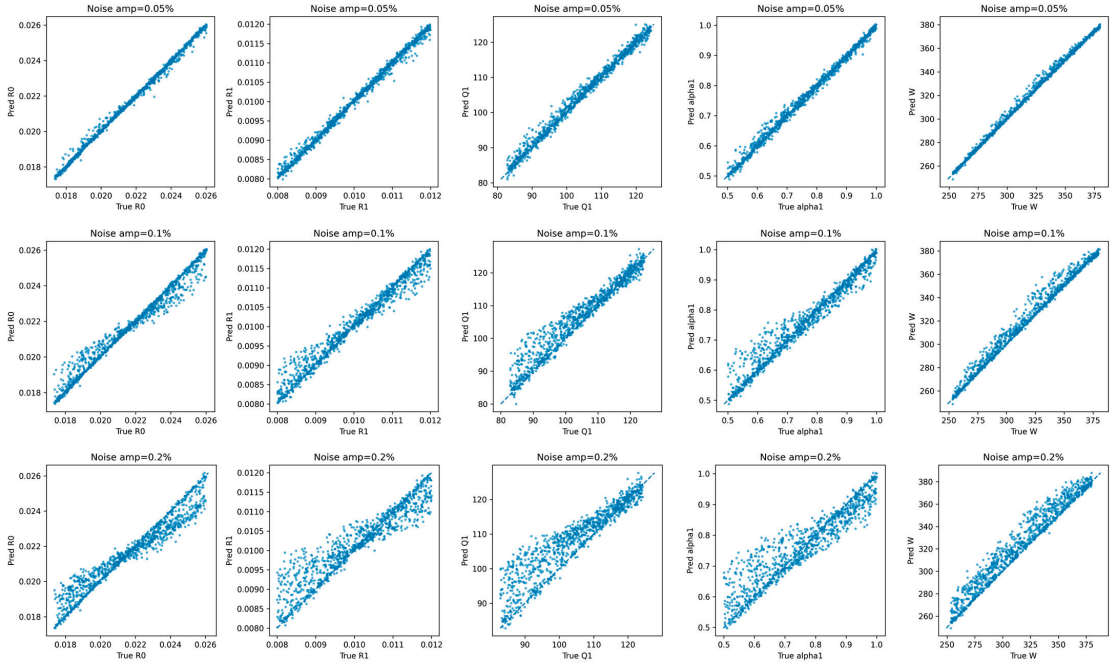

(**b**)

Figure 10. *Cont.*

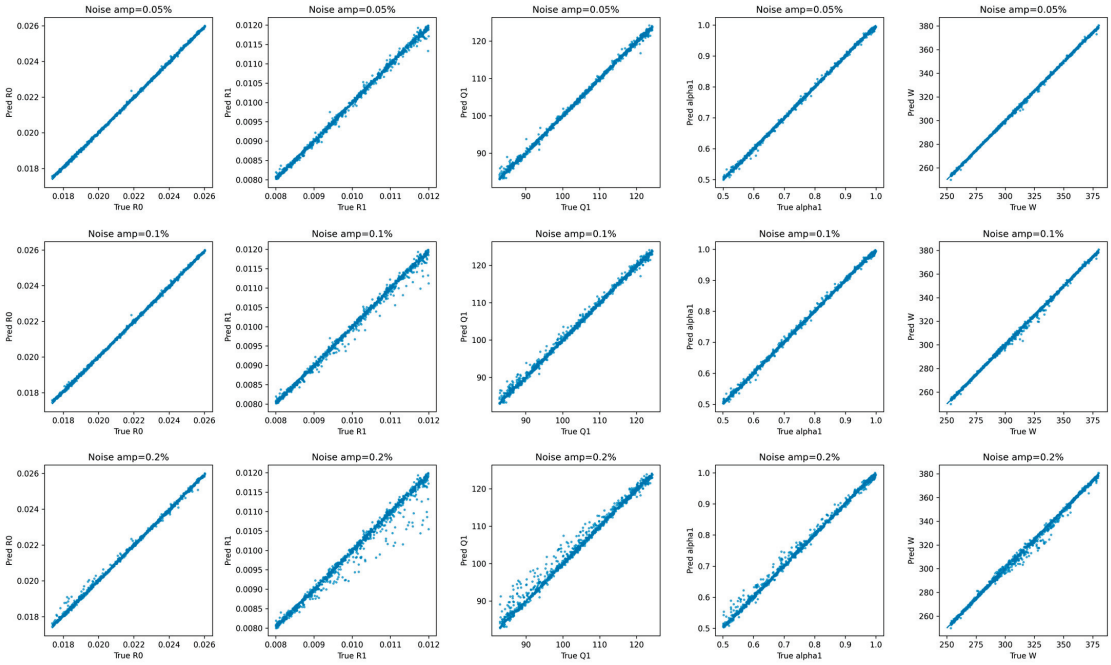

(**c**)

Figure 10. Scatter Plots of Three Best Performing Models Under Different Noise Levels (**a**) 1DCNN_FCN (improved) (**b**) 1DCNN_LSTM (improved) (**c**) 1DCNN_GRU (improved).

5. Conclusions

This study demonstrates the effectiveness of a hybrid deep learning framework for identifying parameters in fractional-order models of lithium-ion batteries, addressing limitations in accuracy and adaptability. By integrating convolutional and recurrent neural network layers, the proposed approach enhances feature extraction and captures temporal dependencies, pioneering the application of deep learning to fractional-order model parameter identification. A simulation platform was employed to generate diverse datasets, while the Optuna framework was utilized for hyperparameter optimization. To improve robustness, techniques such as Huber loss, stochastic weight averaging, and exponential moving averaging were incorporated to mitigate the effects of outliers and ensure stable convergence. The contributions are supported by quantitative results on a 1,000-sample test set. The improved 1DCNN–GRU model achieved an overall RMSE of 0.2223 and MAPE of 0.27%, outperforming baseline models by up to 50% in RMSE (e.g., reduced from 0.4386) and surpassing other hybrid models such as 1DCNN–LSTM (MAPE 0.31%). In contrast, standalone recurrent models, including the improved LSTM, exhibited significantly higher errors, with a MAPE of 9.50%. Scatter plots confirmed low estimation bias for the fractional-order coefficient α, while box plots indicated narrower interquartile ranges across parameters. Heatmaps further illustrated the hierarchy of estimation difficulty, identifying α as the most challenging parameter—yet it was estimated with a MAPE below 1% in the top-performing models. Resistive components (R_0, W) were predicted with near-ideal accuracy, while parameters Q_1 and R_1 showed reduced variance. Terminal voltage reconstruction achieved an average RMSE of 0.002059 and MAE of 0.001387, confirming close alignment with the reference waveform and underscoring the practical reliability of the proposed method. This work establishes hybrid deep learning as a pivotal advancement in electrochemical modeling, successfully balancing high precision with computational efficiency.

Although noise has been deliberately introduced into synthetic voltage waveforms to approximate real-world conditions, the robustness of the proposed models under such

perturbations varies significantly. While the 1DCNN_GRU model demonstrates exceptional noise immunity with minimal performance degradation, the 1DCNN_LSTM model exhibits considerable sensitivity, with error metrics increasing sharply at higher noise levels. This indicates that while some architectures show satisfactory resilience, others may be less reliable. Furthermore, using actual measured waveforms as inputs presents challenges beyond synthetic noise, including sensor drift, environmental interference, and non-stationary disturbances, which are likely to pose greater difficulties. Future work will therefore focus on in-depth investigations in this area to further bridge the gap between simulated tests and real-world deployment, with a specific emphasis on enhancing model generalization against a broader spectrum of real-world imperfections.

Author Contributions: Conceptualization, K.-C.H. and M.P.; methodology, M.P., Y.-H.L. and S.-C.W.; software, D.N.K.; validation, D.N.K. and K.-C.H.; formal analysis, M.P., K.-C.H. and S.-C.W.; investigation, M.P. and D.N.K.; data curation, D.N.K.; writing—original draft, M.P. and D.N.K.; writing—review & editing, S.-C.W. and K.-C.H.; visualization, D.N.K.; supervision, Y.-H.L. and K.-C.H. All authors have read and agreed to the published version of the manuscript.

Funding: This research received no external funding.

Data Availability Statement: The data presented in this study are available on request from the corresponding author due to privacy reasons.

Conflicts of Interest: The authors declare no conflicts of interest.

References

1. Wei, X.; Wu, L.; Liu, C.; Si, Z.; Shu, X.; Li, H. Comparative Evaluation of Fractional-Order Models for Lithium-Ion Batteries Response to Novel Drive Cycle Dataset. *Fractal Fract.* **2025**, *9*, 429. [CrossRef]
2. Model, F.; Guha, A.; Routh, B.; Velivela, N.P. Adaptive Extended Kalman Filtering Based State-of-Charge and Voltage Estimation of a Lithium-Ion Battery Using a. *IEEE Sens. J.* **2024**, *24*, 26225–26234. [CrossRef]
3. Zhang, X.; Li, X.; Yang, K.; Wang, Z. Lithium-Ion Battery Modeling and State of Charge Prediction Based on Fractional-Order Calculus. *Mathematics* **2023**, *11*, 3401. [CrossRef]
4. Chen, L.; Yu, W.; Cheng, G.; Wang, J. State-of-charge estimation of lithium-ion batteries based on fractional-order modeling and adaptive square-root cubature Kalman filter Hybrid Electric vehicle. *Energy* **2023**, *271*, 127007. [CrossRef]
5. Wang, J.; Yu, W.; Cheng, G.; Chen, L. Identification of fractional-order equivalent circuit model of lithium-ion battery for improving estimation of state of charge. *J. Energy Storage* **2023**, *70*, 108043. [CrossRef]
6. Wang, Y.; Li, M.; Chen, Z. Experimental study of fractional-order models for lithium-ion battery and ultra-capacitor: Modeling, system identification, and validation. *Appl. Energy* **2020**, *278*, 115736. [CrossRef]
7. Hu, M.; Li, Y.; Li, S.; Fu, C.; Qin, D.; Li, Z. Lithium-ion battery modeling and parameter identification based on fractional theory. *Energy* **2018**, *165*, 153–163. [CrossRef]
8. Liu, Z.; Qiu, Y.; Yang, C.; Feng, J.; Jing, B. A Parameter Identification Method for Lithium-Ion Batteries Using Simplified Impedance Model and Fractional Order Kalman Filter. *J. Electr. Eng. Technol.* **2022**, *17*, 197–208. [CrossRef]
9. Wang, B.; Li, S.E.; Peng, H.; Liu, Z. Fractional-order modeling and parameter identification for lithium-ion batteries. *J. Power Sources* **2015**, *293*, 151–161. [CrossRef]
10. Wang, Y.; Gao, G.; Li, X.; Chen, Z. A fractional-order model-based state estimation approach for lithium-ion battery and ultra-capacitor hybrid power source system considering load trajectory. *J. Power Sources* **2020**, *449*, 227543. [CrossRef]
11. Chen, L.Y.L.; Guo, W.; Lopes, A.M.; Wu, R.; Li, P. *State-of-Charge Estimation for Lithium-Ion Batteries Based on Incommensurate Fractional-Order Observer*; Elsevier B.V: Amsterdam, The Netherlands, 2023; pp. 1–21. [CrossRef]
12. Mao, S.; Lu, Z.; Zhang, Z.; Lv, B.; Sun, Z.; Huai, R.; Chang, L.; Li, H. Parameter identification method for the variable order fractional-order equivalent model of lithium-ion battery. *J. Energy Storage* **2023**, *57*, 106273. [CrossRef]
13. Yu, Z.; Huai, R.; Li, H. CPSO-Based Parameter-Identification Method for the Fractional-Order Modeling of Lithium-Ion Batteries. *IEEE Trans. Power Electron.* **2021**, *36*, 11109–11123. [CrossRef]
14. Tian, J.; Xiong, R.; Shen, W.; Wang, J.; Yang, R. Online simultaneous identification of parameters and order of a fractional order battery model. *J. Clean. Prod.* **2020**, *247*, 119147. [CrossRef]
15. Zhang, L.; Wang, X.; Chen, M.; Yu, F.; Li, M. A fractional-order model of lithium-ion batteries and multi-domain parameter identification method. *J. Energy Storage* **2022**, *50*, 104595. [CrossRef]

16. Guo, P.; Wu, X.; Lopes, A.M.; Cheng, A.; Xu, Y.; Chen, L. Parameter Identification for Lithium-Ion Battery Based on Hybrid Genetic–Fractional Beetle Swarm Optimization Method. *Mathematics* **2022**, *10*, 3056. [CrossRef]
17. Yu, K.; Zhang, K.; Zhong, Y.; Yang, D.; Liang, J. Fractional-order modeling and parameter estimation of lithium-ion battery via multi-strategy and mean factor differential evolution. *Meas. J. Int. Meas. Confed.* **2025**, *246*, 116721. [CrossRef]
18. Wang, Y.; Zhao, G. A comparative study of fractional-order models for lithium-ion batteries using Runge Kutta optimizer and electrochemical impedance spectroscopy. *Control Eng. Pract.* **2023**, *133*, 105451. [CrossRef]
19. Wu, S.; Zhang, S.; Li, H.; Cao, G.; Hu, Z.; Yu, Y.; Zhang, X. A totally coupled multi time-scale framework containing full parameters online identification and SOC real-time estimation of lithium-ion battery based on a fractional order model. *J. Energy Storage* **2023**, *73*, 109012. [CrossRef]
20. Sun, X.; Ji, J.; Ren, B.; Chen, G.; Zhang, Q. A novel online identification algorithm of lithium-ion battery parameters and model order based on a fractional order model. *IET Renew. Power Gener.* **2021**, *15*, 2396–2408. [CrossRef]
21. Liu, C.Y.Z.; Qiu, Y.; Feng, J.; Chen, S. A Simplified Fractional Order Modeling and Parameter Identification for Lithium-Ion Batteries. *J. Electrochem. Energy Convers. Storage* **2022**, *19*, 8. [CrossRef]
22. Hu, Y.J.C.; Liu, H. Parameter and order estimation algorithms and convergence analysis for lithium-ion batteries. *Int. J. Robust Nonlinear Control.* **2023**, *33*, 11411–11433. [CrossRef]
23. Chen, L.; Wang, S.; Jiang, H.; Fernandez, C.; Xiong, X. A novel combined estimation method of online full-parameter identification and adaptive unscented particle filter for Li-ion batteries SOC based on fractional-order modeling. *Int. J. Energy Res.* **2021**, *45*, 15481–15494. [CrossRef]
24. Xu, J.; Zhen, A.; Cai, Z.; Wang, P.; Gao, K.; Jiang, D. State of Health Diagnosis and Remaining Useful Life Prediction of Lithium-Ion Batteries Based on Multi-Feature Data and Mechanism Fusion. *IEEE Access* **2021**, *9*, 85431–85441. [CrossRef]
25. Guo, D.; Yang, G.; Han, X.; Feng, X.; Lu, L.; Ouyang, M. Parameter identification of fractional-order model with transfer learning for aging lithium-ion batteries. *Int. J. Energy Res.* **2021**, *45*, 12825–12837. [CrossRef]
26. Wang, S.; Shao, X.; Yang, L.; Liu, N. Deep Learning Aided Dynamic Parameter Identification of 6-DOF Robot Manipulators. *IEEE Access* **2020**, *8*, 138102–138116. [CrossRef]
27. Fan, R.; Huang, R.; Wang, S.; Zhao, J. Wavelet and Deep-Learning-Based Approach for Generation System Problematic Parameters Identification and Calibration. *IEEE Trans. Power Syst.* **2023**, *38*, 3787–3798. [CrossRef]
28. Yue, X.; Jing, X.; Liu, X.; Li, Y.; Xu, Y. Parameter identification of dynamical systems based on short-term prediction by the generalized cell mapping method with deep learning. *Nonlinear Dyn.* **2025**, *113*, 4031–4044. [CrossRef]
29. Tanyu, D.N.; Ning, J.; Freudenberg, T.; Heilenkötter, N.; Rademacher, A.; Iben, U.; Maass, P. Deep learning methods for partial differential equations and related parameter identification problems. *Inverse Probl.* **2023**, *39*, 103001. [CrossRef]
30. You, Q.; Zhang, Y.; Xiong, R.; Ruan, H. Machine Learning-Based in situ identification of the High-Dimensional Parameter space for an equivalent circuit model. *J. Electrochem. Soc.* **2025**, *172*, 020518. [CrossRef]
31. Nicodemo, N.; Di Rienzo, R.; Lagnoni, M.; Bertei, A.; Baronti, F. Estimation of lithium-ion battery electrochemical properties from equivalent circuit model parameters using machine learning. *J. Energy Storage* **2024**, *99*, 113257. [CrossRef]
32. Fu, H.; Liu, Z.; Cui, K.; Du, Q.; Wang, J.; Shi, D. Physics-Informed neural Network for spacecraft Lithium-Ion battery modeling and health diagnosis. *IEEE/ASME Trans. Mechatron.* **2024**, *29*, 3546–3555. [CrossRef]
33. Geng, Z.; Wang, S.; Lacey, M.J.; Brandell, D.; Thiringer, T. Bridging physics-based and equivalent circuit models for lithium-ion batteries. *Electrochimica Acta* **2021**, *372*, 137829. [CrossRef]
34. Li, J.; Li, X.; Yuan, X.; Zhang, Y. Deep learning method for online parameter identification of lithium-ion batteries using electrochemical synthetic data. *Energy Storage Mater.* **2024**, *72*, 103697. [CrossRef]
35. Du, Z.; Lu, R. Physics-Informed Neural Networks for Advanced Thermal Management in Electronics and Battery Systems: A Review of Recent Developments and Future Prospects. *Batteries* **2025**, *11*, 204. [CrossRef]
36. Ho, K.C.; Khanh, D.N.; Hsueh, Y.F.; Wang, S.C.; Liu, Y.H. Deep Learning Approach for Equivalent Circuit Model Parameter Identification of Lithium-Ion Batteries. *Electronics* **2025**, *14*, 2201. [CrossRef]
37. Abumohsen, M.; Owda, A.Y.; Owda, M. Electrical Load Forecasting Using LSTM, GRU, and RNN Algorithms. *Energies* **2023**, *16*, 2283. [CrossRef]
38. Makhloughi, F. Artificial intelligence-based non- invasive bilirubin prediction for neonatal jaundice using 1D convolutional neural network. *Sci. Rep.* **2025**, *15*, 11571. [CrossRef] [PubMed]
39. Huang, S. Robust learning of Huber loss under weak conditional moment. *Neurocomputing* **2022**, *507*, 191–198. [CrossRef]
40. Yang, L.; Wang, Y.; Yang, X.; Zheng, C. Stochastic weight averaging enhanced temporal convolution network for EEG-based emotion recognition. *Biomed. Signal Process. Control* **2023**, *83*, 104661. [CrossRef]
41. Morales-Brotons, D.; Vogels, T.; Hendrikx, H. Exponential Moving Average of Weights in Deep Learning: Dynamics and Benefits. *Trans. Mach. Learn. Res.* **2024**, *2024*, 1–27.
42. Wu, Y.; Balasingam, B. A Comparison of Battery Equivalent Circuit Model Parameter Extraction Approaches Based on Electrochemical Impedance Spectroscopy. *Batteries* **2024**, *10*, 400. [CrossRef]

43. Liu, C.; Liu, W.; Wang, L.; Hu, G.; Ma, L.; Ren, B. A new method of modeling and state of charge estimation of the battery. *J. Power Sources* **2016**, *320*, 1–12. [CrossRef]
44. Li, F.; Zeng, C. *Numerical Methods Fractional Calculus for*; CRC Press: Boca Raton, FL, USA; Taylor & Francis Group: Oxfordshire, UK, 2015.
45. Aygun, S.; Member, S.; Najafi, M.H.; Member, S.; Hyperdimensional, A. Sobol Sequence Optimization for Hardware-Efficient Vector Symbolic Architectures. *IEEE Trans. Comput. Des. Integr. Circuits Syst.* **2025**, *44*, 937–950. [CrossRef]
46. Akiba, T.; Sano, S.; Yanase, T.; Ohta, T.; Koyama, M. Optuna: A Next-generation Hyperparameter Optimization Framework. In Proceedings of the 25th ACM SIGKDD International Conference on Knowledge Discovery & Data Mining, Anchorage, AK, USA, 4–8 August 2019; pp. 2623–2631. [CrossRef]

Disclaimer/Publisher's Note: The statements, opinions and data contained in all publications are solely those of the individual author(s) and contributor(s) and not of MDPI and/or the editor(s). MDPI and/or the editor(s) disclaim responsibility for any injury to people or property resulting from any ideas, methods, instructions or products referred to in the content.

batteries

MDPI

Article

State of Health Estimation of Lithium Cobalt Oxide Batteries Based on ARX Identification Across Different Temperatures

Simone Barcellona [1,*], Mattia Ribera [2], Emanuele Fedele [2], Pasquale Franzese [2], Luigi Piegari [1], Lorenzo Codecasa [1] and Diego Iannuzzi [2]

[1] Department of Electronics, Information and Bionengineering (DEIB), Politecnico di Milano, I-20133 Milan, Italy; luigi.piegari@polimi.it (L.P.); lorenzo.codecasa@polimi.it (L.C.)
[2] Department of Electrical Engineering and Information Technology (DIETI), Università degli Studi di Napoli Federico II, I-80125 Naples, Italy; mattia.ribera@unina.it (M.R.); emanuele.fedele@unina.it (E.F.); pasquale.franzese@unina.it (P.F.); iandiego@unina.it (D.I.)
* Correspondence: simone.barcellona@polimi.it

Abstract

Lithium-ion batteries (LiBs) undergo degradation influenced by storage and cycling conditions. Accurate state of health (SOH) assessment is crucial for predicting battery aging, which is generally marked by a decline in capacity (energy fade) or an increase in internal resistance (power fade). This study investigates the impulse response (IR) technique for assessing the SOH of lithium cobalt oxide batteries, addressing both capacity fade and rising internal resistance. The IR method relies on a predefined dataset that records the voltage response of the LiB to pulse current inputs across various states of charge (SOC), temperatures, and aging conditions to train a series of linear auto-regressive exogenous (ARX) models. This dataset is then used as a look-up table for subsequent SOH estimation under new operating conditions. The results demonstrate that the method can capture trends in capacity fade and resistance increase only when multiple battery temperatures are incorporated into the look-up table. In contrast, estimations based on ARX models trained at a single fixed temperature fail to provide reliable predictions of battery SOH.

Keywords: lithium-ion batteries; cycle aging; impulse response method; state of health estimation

1. Introduction

Among rechargeable batteries, lithium-ion batteries (LiBs) are the most widely employed in various applications, ranging from small electronic devices (such as smartphones, laptops, and medical tools) to larger systems such as electric vehicles (EVs) [1]. Moreover, they are used as energy storage systems to support renewable energy sources and to supply power to EV charging stations [2–4]. The reasons for their widespread use lie in their high energy and power density, high efficiency, and relatively long lifetime. Furthermore, their low self-discharge rate and lack of memory effect add additional advantages to these batteries [5]. Nevertheless, the term *lithium-ion battery* is a general designation that refers to a variety of chemistries, typically classified according to the cathode material used. These, which use carbon-based anodes, include lithium iron phosphate (LFP), lithium manganese oxide (LMO), lithium cobalt oxide (LCO), lithium nickel manganese cobalt oxide (NMC), and lithium nickel cobalt aluminum oxide (NCA) [6]. Actually, each type of LiB has its own advantages and drawbacks, and the best choice is made according to the specific application [7].

In this work, LCO cells were selected as a model system because their layered cobalt-oxide structure, combined with a carbon-based anode, is similar to widely used transportation-relevant chemistries such as NMC and NCA. Although these chemistries differ in energy density, thermal stability, lifespan, and cost, they share similar open circuit voltage (OCV) profiles and common aging mechanisms, such as solid electrolyte interface (SEI) growth and lithium plating at the anode [8]. Therefore, in our opinion, this makes LCO a representative platform for evaluating the proposed estimation method. Although materials with different structures, such as LFP, may show distinct thermal and electrochemical responses, the proposed approach can be readily extended.

LiBs degrade both during use (cycle aging) and while not in use (calendar aging). The mechanism and rate of degradation depend on several factors, such as temperature, state of charge (SOC), current rate, and voltage limits. The consequences of degradation result in energy and power fade [9]. Specifically, the former is due to a decrease in capacity, while the latter is caused by an increase in internal resistance.

On the other hand, it is possible to reduce the aging rate and increase both efficiency and lifespan by properly using and storing LiBs, i.e., operating them within safe limits, avoiding overcharging or over-discharging, preventing extreme temperatures, and storing them at optimal SOC levels and temperatures. To achieve this, many algorithms have been proposed and implemented in battery management systems (BMSs) to estimate key parameters such as SOC and state of health (SOH) [10–12]. Typically, SOH is quantified in terms of capacity fade or internal resistance increase, and continuous estimation of these parameters can be used to predict the remaining useful life [13,14]. In the literature, it is possible to find various SOH estimation methods that can be divided into non-model- and model-based approaches.

The non-model-based methods are typically more straightforward, as they depend primarily on experimental measurements. A basic technique known as Coulomb counting for determining the actual battery capacity involves performing a full charge–discharge cycle during which the current is integrated. However, in applications such as EVs, only the charging phase can typically be controlled, making this method often impractical. In [15], the researchers examined the relationship between cycle aging and two key indicators: incremental capacity (IC) and differential voltage (DV). However, these methods are time-consuming and may not be practical, as calculating IC or DV requires knowledge of the relationship between OCV and SOC, which must be estimated in non-model-based approaches. This can be achieved by acquiring many experimental OCV values when the battery is at rest, after a sufficient relaxation period that allows the terminal voltage to reach equilibrium with the OCV. In [16–18], the authors attempted to overcome this drawback by reconstructing the entire OCV curve using only partial segments of the curve. This was achieved either through analytical correlations based on monotonicity and shape or by employing various machine learning regression methods. Nevertheless, collecting even these fragments can be time-consuming and requires offline measurements. Another non–model-based technique involves measuring the battery's internal resistance, using pulse testing and related methods, which demonstrates high sensitivity in detecting the pronounced increase in internal resistance that occurs with aging [19].

On the other hand, model-based methods can be physical-based (white-box), data-driven (black-box), or a hybrid of both (grey-box) [14,20].

Specifically, a physics-based approach allows modeling of the aging mechanisms occurring within the battery and enables estimation of the SOH or of electrical parameters related to it. This approach relies on electrochemical models governed by complex partial differential equations. Based on porous electrode theory and electrochemical kinetics, such models identify internal parameters that represent the battery dynamic aging and

https://doi.org/10.3390/batteries12010002

degradation processes, thereby facilitating SOH estimation and prediction [21–23]. These methods can be very accurate but demand high computational burden, making it difficult to implement them in real-time on BMSs.

On the other hand, data-driven methods are based on the collection, analysis, and fitting of experimental or historical data and can be used to parameterize regression models derived from input–output relationships. They include various fitting techniques and can be divided into classical statistical data methods, filtering methods, and artificial intelligence–based methods [24]. The first category includes numerous analytical models based on linear and nonlinear regression methods, Gaussian process regression, and Wiener process regression [25,26], as well as time-series methods such as auto-regressive with exogenous input (ARX) and auto-regressive moving average with exogenous input (ARMAX) [27–30]. Among the filtering methods are the Kalman filter (KF), extended Kalman filter (EKF), unscented Kalman filter (UKF), and particle filter (PF) [31–36]. Finally, the emerging artificial intelligence methods primarily include various machine learning (ML) [37–47], and deep learning (DL) techniques [48–58].

Grey-box models can represent a trade-off between the two approaches. Among them, equivalent electric circuit (EEC) models are usually considered grey-box because their components can be associated with physical meaning, yet the modeling of their parameters is often based on experimental data obtained through specific measurement techniques. Depending on the target accuracy and desired level of detail, EECs can range from simpler models—comprising only the OCV and total internal resistance—to more complex ones composed of several parallel RC branches that capture the battery dynamic behavior [59–62]. In general, the parametrization of these models can be performed either in the frequency domain or in the time domain. Among the frequency-domain techniques, electrochemical impedance spectroscopy is the most commonly used. Time-domain techniques, on the other hand, mainly include constant charging/discharging tests—such as the galvanostatic intermittent titration technique—and current-pulse-based methods, including hybrid pulse power characterization (HPPC) and impulse response (IR) tests [63,64]. Furthermore, these measurements can be carried out either offline or online. Offline characterization relies on dedicated experimental tests designed to determine how model parameters vary as a function of factors such as voltage, temperature, and aging. Online parameter estimation, instead, is performed during real-time battery operation using identification algorithms [65], which are primarily based on least squares (LS) methods [66–68] and nonlinear filtering techniques such as KF, EKF, UKF, and PF [69,70]. A detailed comparison of these techniques is provided in [71].

Focusing on time-domain techniques for EEC model parameter identification, the IR approach was initially proposed in [72] for the online estimation of SOC and was later extended to estimate capacity and power degradation in [73,74]. In these studies, the IR method—implemented using the LS algorithm—was first used offline to identify various EEC–ARX linear models describing the battery's electrical behavior, with the extracted parameters stored in look-up tables (LUTs). The method was then applied online to estimate the actual SOC, capacity fade, or power fade by comparing the measured terminal-voltage response to that predicted by each ARX model in the LUT database and selecting the impulse response that yields the minimum error between measured and computed voltages. Specifically, the ARX model corresponds to a discrete-time Thevenin equivalent circuit representation of the battery, where the number of parallel RC networks in the circuit defines the order of the ARX model [65]. The fundamental concept behind the IR method is to train and parameterize a distinct ARX model for each specific aging and operating condition of the battery, such as SOC and temperature, which can then be used for real-time SOC and SOH estimation.

https://doi.org/10.3390/batteries12010002

On the other hand, traditional EEC models with filtering-based parameter tracking, although highly accurate, are mathematically complex and labor-intensive, making their practical implementation challenging. They require repeated re-identification and often suffer from convergence issues as the battery ages [73]. In contrast, the EEC–ARX model derived from the IR method, with parameters stored in LUTs, provides a direct data-driven mapping. The resulting LUTs are computationally lightweight and can be easily updated with minimal experimental data, without requiring full re-identification of the parameters' analytical expressions, as is necessary in traditional EEC models where parameter dependencies are expressed as functions of SOC, temperature, and aging. Finally, compared to ML approaches, the IR + ARX framework is simpler in terms of model training. All of this motivates the use of the IR + ARX framework as an efficient solution for parameter estimation.

In a previous work [75], the IR method was employed to estimate the SOH in terms of capacity fade for an LCO battery that underwent cyclic charging and discharging at a constant current and temperature until it aged. At specific cycle aging intervals, the voltage responses of the battery to brief current pulses at different SOC and temperature levels were recorded and used in the ARX least-squares parameterization routine [76]. This process generated a set of ARX models, which were then used to create a data map serving as a ground-truth knowledge base for SOH estimation under various conditions of SOC and cycling level. The estimation was based on the best-fit principle, where the trained model that most accurately matched the actual data collected from the battery was considered to represent its most likely SOC and SOH.

On the other hand, to accurately estimate the SOH of a battery, it is essential to recognize that although temperature contributes to irreversible aging, it also exerts a reversible influence on battery performance, as reported in [77,78]. Several studies have shown that battery capacity depends on temperature [79–82]. Therefore, in addition to considering cycle aging at a fixed temperature, the reversible effect of temperature on battery capacity must also be taken into account. In [83], the authors developed an ARX model that incorporates battery temperature into the OCV–SOC LUT relationship. However, the incorporation of temperature into ARX-based battery modeling for SOH estimation has not been reported in the literature, and the impact of temperature variations on the estimation accuracy of this method remains unclear and unexplored.

In light of the above, the main novelty of this study compared to [75] lies in extending the IR method, as proposed in that work, to account for the reversible effect of battery temperature on SOH estimation in terms of capacity fade, based on an extensive experimental campaign conducted on the same type of LiB used in [75]. Moreover, SOH estimation in terms of power fade, through the estimation of internal resistance increase, is also developed. The results indicate that the IR method can successfully track trends in capacity deterioration and resistance increase only when various battery temperatures are incorporated into the LUTs built from trained ARX models. In this sense, explicit inclusion of temperature as an exogenous factor during ARX model training is crucial to obtain reliable estimation results from the IR method.

2. Battery Modeling

2.1. Battery Electrical Dynamics

The use of EEC to model battery cells is a well-established approach that effectively balances accuracy with complexity in capturing internal system dynamics. Figure 1 shows the typical EEC battery model together with the nomenclature used throughout this work. The circuit is characterized by the OCV, which represents the output voltage when the battery is at equilibrium; a series resistance R_0 that models the ohmic components of the LiB, such as the current collector, electrolyte, and electrodes; and several parallel RC branches,

https://doi.org/10.3390/batteries12010002

R_iC_i, that represent the dynamic behavior of the battery related to the SEI, charge-transfer chemical reactions, and lithium-ion diffusion. These components capture the transient and steady-state voltage responses observed during charging and discharging.

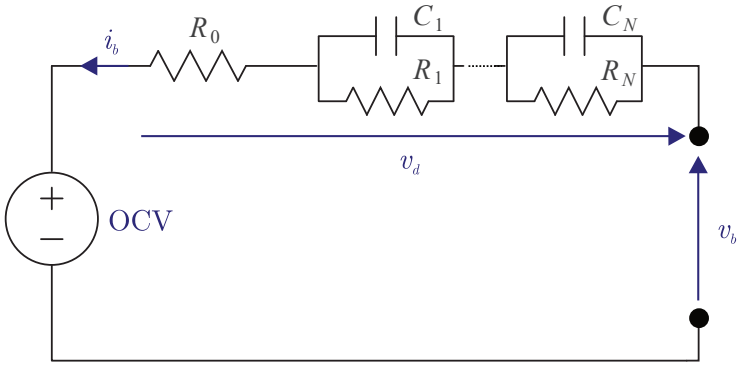

Figure 1. Battery equivalent circuit model.

The battery terminal voltage, v_b, is expressed as:

$$v_b = \mathrm{OCV}(Q, \mathrm{SOC}, T) + v_d(Q, \mathrm{SOC}, T, i_b) \tag{1}$$

that is, the battery terminal voltage is divided into two fundamental components: a static OCV, which can be considered independent on the battery current, i_b, over a short-time duration, and a dynamic voltage response, v_d. Both the static OCV and dynamic voltage response of the battery depend on the actual SOC, temperature, T, and cycling level, Q. The latter is associated with cycle aging and is quantified by the total charge transferred to and from the battery:

$$Q(t) = \int_0^t |i_b(\tau)| d\tau. \tag{2}$$

In this work, the SOH is quantified in terms of both capacity fade and power fade, as follows:

$$\mathrm{SOH_C}(T) = \frac{C_a(T)}{C_i(T)} \tag{3}$$

$$\mathrm{SOH_R}(SOC, T) = \frac{R_i(SOC, T)}{R_a(SOC, T)} \tag{4}$$

where $C_a(T)$ and $C_i(T)$ denote the actual and initial capacities of the battery at a given temperature, respectively. Similarly, $R_a(SOC, T)$ and $R_i(SOC, T)$ denote the actual and initial internal resistances of the battery at specified SOC levels at different temperatures.

The mapping of the dynamic voltage response to current steps under different SOC, Q, and T conditions represents the core of the ARX-based SOH estimation method presented in this work.

2.2. Black-Box ARX Modeling

The ARX modeling offers flexibility in adjusting model orders to suit specific requirements, making it a versatile approach for battery modeling. Specifically, the dynamic voltage response to charge or discharge currents can be associated with a linear time invariant (LTI) system, where the input is the battery current and the output is the dynamic voltage. The discrete-time ARX representation of such system is:

$$A(z^{-1})v_d(k) = B(z^{-1})i_b(k) \tag{5}$$

https://doi.org/10.3390/batteries12010002

where the auto-regressive and exogenous polynomial operators are:

$$A(z^{-1}) = 1 + a_1 z^{-1} + ... + a_n z^{-n} \tag{6}$$

$$B(z^{-1}) = b_0 + b_1 z^{-1} + ... + b_m z^{-m}. \tag{7}$$

Clearly, the auto-regressive part captures past voltage behavior whereas the exogenous part predicts future responses based on actual and past current values.

The ARX representation of the battery employs a black-box approach, meaning it is not tied to any specific physical model of the battery. Instead, it uses a simplified LTI approximation of the system dynamics, where the battery behavior at a given Q, SOC, and T condition is completely described by the coefficients in polynomials $A(z^{-1})$ and $B(z^{-1})$ of the corresponding ARX model parametrization. This is the core concept behind the ARX-based SOH estimation approach discussed in this work.

For an accurate representation of the battery dynamics, selecting the correct polynomial orders is essential. Following a pure black-box approach, n and m can be set according to best-fitting criteria and based on whiteness analysis of model residuals. Alternatively, ARX orders can be inferred from the complexity of an underlying EEC model that is considered to reasonably approximate battery behavior.

2.3. Relation with EEC Model

The EEC and ARX representations are mathematically equivalent descriptions of the same LTI dynamic response between the battery current, i_b, and the dynamic voltage, v_d. The EEC model leads to a continuous-time transfer function composed of N parallel RC branches, whose discrete-time counterpart corresponds to an ARX model of order ($n = N$, $m = N$). In other words, while the EEC formulation provides physical interpretation, the ARX approach enables the construction of a comprehensive database of polynomial operators $A(z^{-1})$ and $B(z^{-1})$, where each RC branch maps to one pair of ARX poles and zeros.

The continuous-time transfer function from $i_b(t)$ to $v_d(t)$ of an EEC model with N parallel RC branches is:

$$\frac{V_d(s)}{I_b(s)} = G(s) = R_0 + \sum_{i=1}^{N} \frac{R_i}{1 + sR_iC_i}. \tag{8}$$

Discretization of the continuous-time model with sample time T_s by means of bilinear transform yields:

$$\frac{V_d(z)}{I_b(z)} = G(z^{-1}) = \frac{B(z^{-1})}{A(z^{-1})}. \tag{9}$$

For instance, the following relations exist between EEC parameters and ARX polynomial coefficients when only one parallel RC branch is considered:

$$b_0 = \frac{(R_0 + R_1)T_s + 2C_1R_0R_1}{T_s + 2C_1R_1} \tag{10}$$

$$b_1 = \frac{(R_0 + R_1)T_s - 2C_1R_0R_1}{T_s + 2C_1R_1} \tag{11}$$

$$a_1 = \frac{T_s - 2C_1R_1}{T_s + 2C_1R_1}. \tag{12}$$

On the other hand, additional analytical or numerical comparisons were not conducted or included, as the resulting equations would be prohibitively lengthy.

Hence, under this EEC-based approach, the ARX orders are inherently determined by the order of the underlying battery EEC model being considered. The advantage of

https://doi.org/10.3390/batteries12010002

this EEC-derived ARX formulation is that the ARX parametrization obtained from best-fit criteria can be directly used to estimate the battery's internal resistance. Considering the same example of an EEC model with a single parallel RC branch, the dc resistance of the battery can be defined as follows:

$$R_{dc} = R_0 + R_1 = -\frac{(b_0 - b_1)}{(a_1 - 1)} - 2\frac{(b_1 - a_1 b_0)}{(a_1^2 - 1)}. \quad (13)$$

Since battery resistance is closely correlated with power fade, the ARX model can be used to flexibly estimate the progressive increase in resistance, providing an additional source of information for SOH estimation.

ARX modeling can be employed to build a large database of polynomial operators $A(z^{-1})$ and $B(z^{-1})$, each one corresponding to the dynamic voltage response to a step current under a specific Q, SOC, and T condition. This database can be arranged in the form of LUTs, which serve as the knowledge base that is subsequently used for actual SOH estimation.

2.4. Creation of LUT Database

First, the battery terminal voltage response to a given input current profile is sampled under specific conditions of Q, SOC, and T. The collected samples $v_b(k)$ and $i_b(k)$ correspond to the *training set* for this specific operating condition. Based on this training set, the corresponding ARX model coefficients must be obtained. To this aim, parameter-estimation routines available from the MATLAB R2024b System Identification Toolbox were employed. The procedure aims at finding the ARX parametrization that best fits the training data, i.e., that yields the lowest error between the measured response and the model output. It is worth remarking that, as dictated by (1), the battery terminal voltage results from the combination of the OCV and dynamic voltage drop. As such, it is a two-input dynamic system, with the OCV acting as first input and the battery current as second input. However, ARX modeling inherently applies to single-input systems. Therefore, before being fed to the parameter-estimation routine, the OCV is removed from the collected battery terminal voltage, $v_b(k)$, to obtain an indirect measurement of the actual dynamic voltage, $v_d(k)$. In each training-set condition, the OCV is obtained by sampling the battery voltage after a relaxation time of sufficient duration, after which the training-set current profile begins. The overall procedure for creating the LUT database under different Q, SOC, and T conditions is shown in Figure 2.

2.5. SOH Estimation

The SOH estimation method involves comparing the battery terminal voltage response obtained from a new current profile with the voltage response obtained from each of the ARX models stored in the LUT database. These predicted responses are obtained by summing the OCVs and the dynamic voltages obtained from the ARX models. In this work, the actual battery SOC was evaluated by Coulomb counting, while the temperature was measured by a dedicated sensor. Therefore, the comparison between measured and predicted voltages is one-dimensional, i.e., it is done only inside the LUT corresponding to the measured temperature, T, and along the column of the estimated SOC.

The actual estimation is based on the goodness of fit (GoF) of each polled ARX model, where:

$$\mathrm{GoF} = 1 - \frac{1}{N_s}\sum_{k=1}^{N_s}\left(\frac{v_b(k) - \hat{v}_b(k)}{v_b(k)}\right)^2 \quad (14)$$

and $v_b(k)$ and $\hat{v}_b(k)$ are the measured and predicted battery voltage responses, respectively. Specifically, the model exhibiting the highest GoF is considered to provide the closest

https://doi.org/10.3390/batteries12010002

representation of the actual SOH. Accordingly, both SOH_C and SOH_R are estimated based on this best-fitting ARX model instance. Specifically, SOH_R, which reflects the increase in internal resistance, is determined from the dc resistance derived from the optimal ARX model using (13). The LUT-based SOH estimation procedure is illustrated in Figure 3.

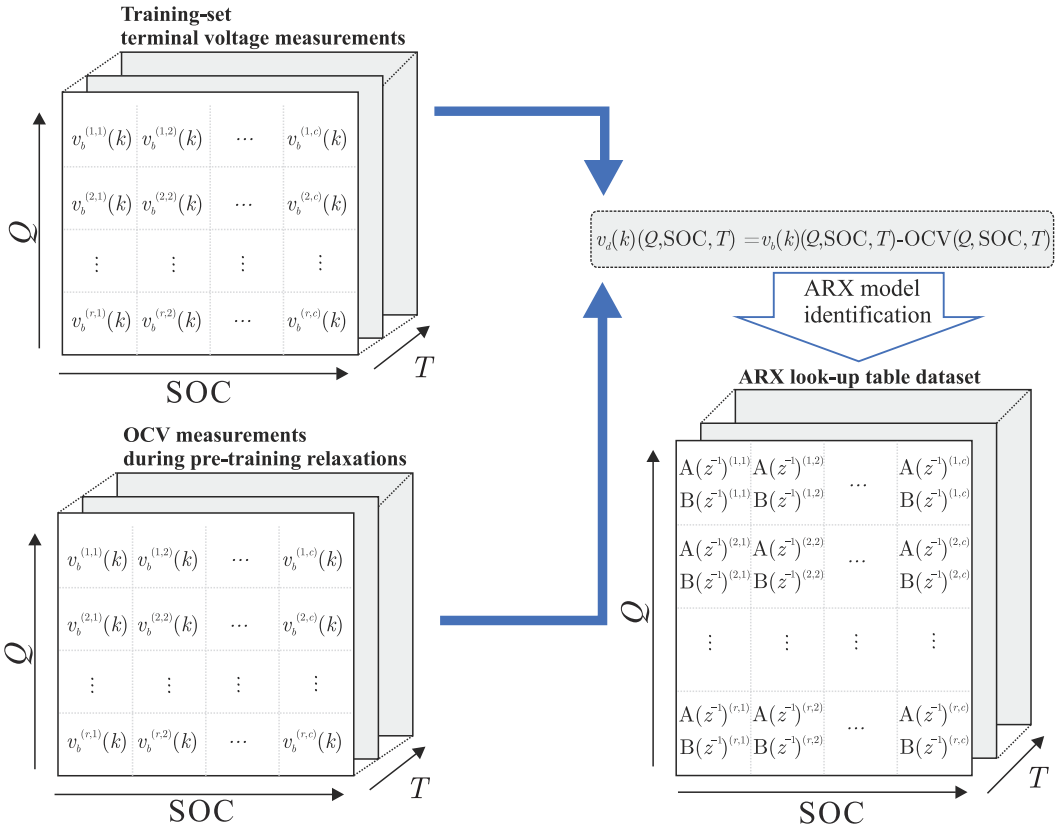

Figure 2. Procedure for the creation of the LUT database for ARX models obtained at different Q, SOC, and T conditions.

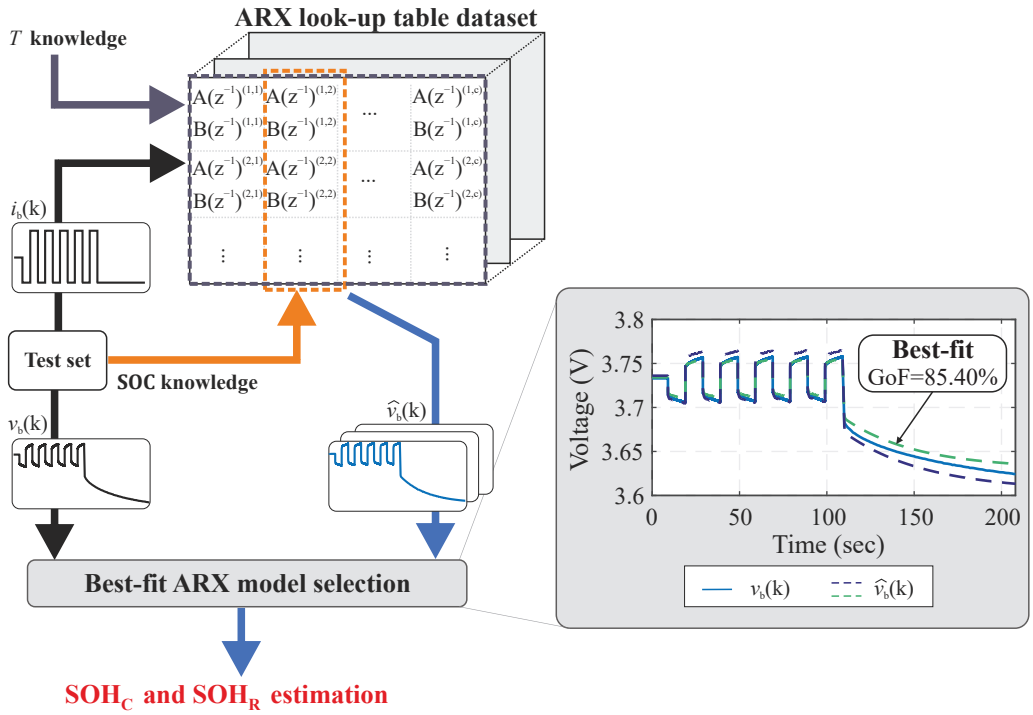

Figure 3. Procedure for ARX LUT-based SOH estimation.

3. Experimental Setup and Test Procedure

3.1. Experimental Setup

The investigation was carried out using an LCO battery cell manufactured by General Electronics Battery Co., Ltd., (Shenzhen, China) specifically the 8773160K pouch cell with a nominal capacity of 10 Ah and an operating voltage range from 2.75 V to 4.2 V. Figure 4 shows the experimental setup, which consists of a potentiostat (SP-150) paired with a 100 A booster (VMP3B-100), both provided by Biologic Science Instrument (Seyssinet-Pariset, France). The potentiostat was connected to a PC via an Ethernet cable running EC-lab software (v11.34), enabling precise control and monitoring. The LiB under test was directly connected to the 100 A booster.

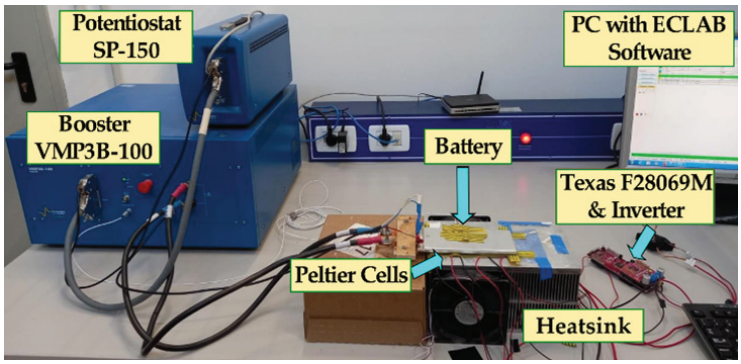

Figure 4. Experimental setup [2].

To ensure consistent and uniform temperature control during testing, three Peltier cells (TEC1-12706 12 V, 6 A) were used instead of a climatic chamber. Moreover, these cells helped mitigate the self-heating effect observed during high charging/discharging currents above 1C. The Peltier elements were positioned between the tested LiB and a heatsink equipped with two fans. Specifically, one face of the Peltier cells was in contact with the heat sink, while the other face was in contact with the bottom side of the tested LiB, with the opposite side of the battery exposed to ambient air.

The battery temperature was monitored and controlled to the reference value using a Pt100 probe (Class B) positioned on the top side of the LiB. The measured temperature was sent as input to a control board (F28069M) from Texas Instruments, where a proportional-integral controller was implemented to drive a converter (BOOSTXL-DRV8323RX), also from Texas Instruments. This setup regulated the Peltier cells to maintain a stable battery temperature throughout the aging cycles and characterization tests.

Even though temperature control was applied only to the bottom of the battery and measurements were taken at the center of the top side, the thin profile of the cell resulted in a minimal temperature gradient across it, as reported in [84], allowing this gradient to be neglected.

3.2. Aging and Test Procedure

The experimental procedure was divided into two distinct phases: the IR phase and the aging cycle phase. The IR phase was carried out initially and then repeated after each aging cycle to evaluate changes in the battery voltage response.

The IR phase was conducted at various fixed battery temperatures and under different SOC and cycling conditions. Specifically, eight temperatures (20 °C, 22.5 °C, 25 °C, 27.5 °C, 30 °C, 35 °C, 40 °C, and 45 °C) were tested, along with five SOC levels (100%, 75%, 50%, and 25% of the nominal capacity) and three cycling levels represented by $Q = 0,\ 10,\ 15$ kAh.

At a fixed temperature and cycling level, the battery was subjected to the HPPC procedure, for which it was initially charged to 100% of SOC using a constant current-

https://doi.org/10.3390/batteries12010002

constant voltage (CC–CV) protocol. Specifically, the CC stage was carried out at 1C until the cut-off voltage was reached, followed by the CV stage at 4.2 V until the current decreased to 0.01C. After charging, the battery was allowed to rest for one hour to stabilize. The IR test was then performed, consisting of five consecutive 0.4C charge/discharge current pulses, each lasting 10 s. This procedure was repeated at SOC levels of 75%, 50%, and 25%. A representative plot of the battery terminal voltage and current profiles during the IR test is shown in Figure 5a. This procedure was repeated across the various temperatures and cycling levels.

The aging cycle phase was performed maintaining a constant temperature of 30 °C. To accelerate the aging process, a charging and discharging current of 5C was initially used. However, once the battery reached a cycling level of 10 kAh, the current was lowered to 4C to reduce the effects of high-frequency aging [85]. During these cycles, two constraints were enforced: the SOC was limited to a range of 20–80%, and the battery terminal voltage was restricted between 3.45 V and 4.05 V. It is worth mentioning that, if the voltage limits were reached before hitting the SOC boundaries, the exchanged charge in a single cycle would be less than 6 Ah. Nevertheless, previous studies [86] have shown that battery aging is primarily influenced by the total moved charge rather than the specific charge/discharge profile. Additionally, findings from [84] confirm that, when SOC is confined between 20–80% and the battery operates at a controlled temperature, the current rate does not significantly affect aging. As a result, reducing the current from 5C to 4C is not expected to impact the cycle aging behavior. An example of the battery terminal voltage and current profiles during this stage is presented in Figure 5b.

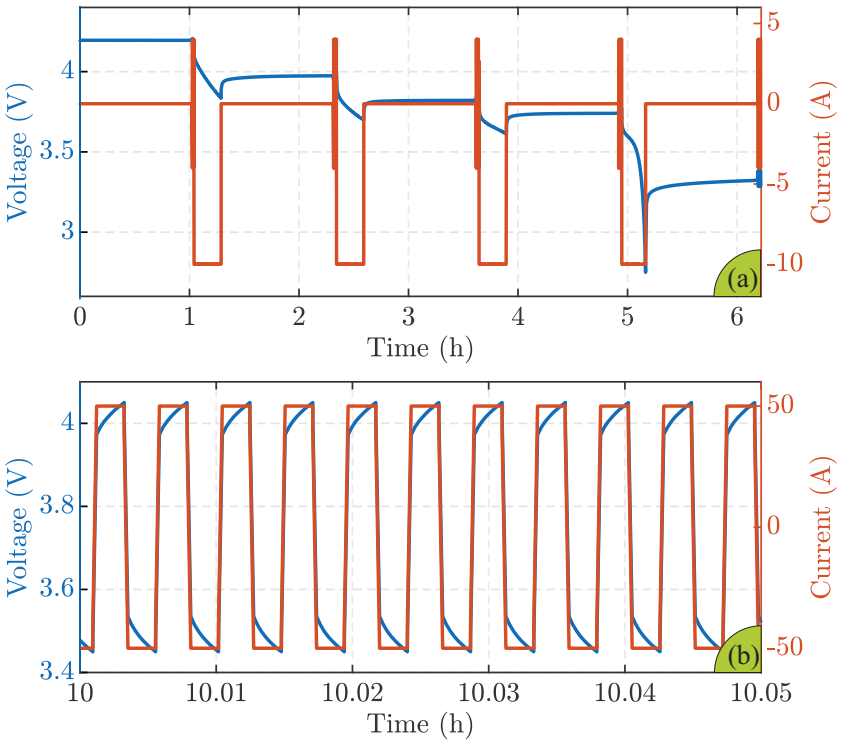

Figure 5. Voltage and current of the battery during: (**a**) IR phase, (**b**) aging cycle phase.

3.3. Training and Validation Data

Figure 6 shows one of the acquisition windows available for each SOC level within the HPPC procedure described in Section 3.2.

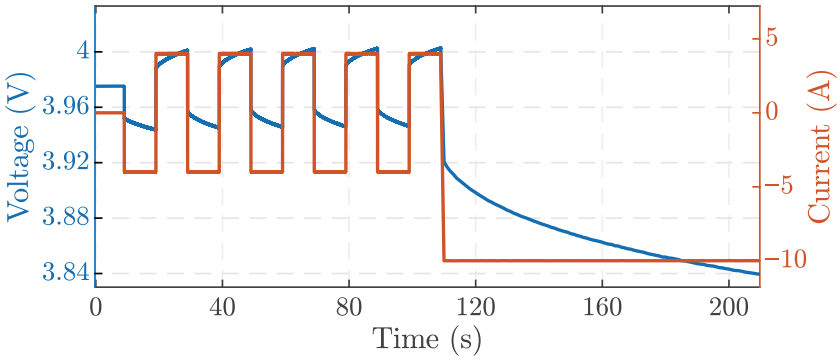

Figure 6. Typical current and voltage window used for ARX model training.

This window contains the input and output signals—respectively the current and voltage—of the LiB under test, and it is used both for the ARX model identification and the validation during the estimation procedure. Referring to the EEC model, this window captures the IR dynamics, which highlights the behavior of the fastest parallel RC branch (i.e., that with the shortest time constant). In addition, it includes the initial part of a partial discharge at 25% of SOC lasting approximately 100 s, which is useful for acquiring information associated with the slower parallel RC branch (with a longer time constant). The voltage value before the start of the current pulse train was assumed to represent the OCV corresponding to the same LiB temperature, SOC, and cycling level of the ARX model. The duration of the partial discharge phase (100 s) was chosen based on the assumption that the SOC remains nearly constant within this acquisition window. This condition allows the resulting ARX model to be reliably associated with a single SOC level, avoiding ambiguity due to SOC varying.

4. Experimental Results

4.1. Model Order Selection for ARX Identification

The selection of the polynomial order is a key aspect in ARX-based identification of the EEC, as it directly influences the model capability to reproduce both the steady-state behavior and the transient voltage dynamics. To investigate the effect of increasing model complexity, ARX structures with orders ranging from 1 to 4 were identified and compared.

Figure 7 illustrates a representative example of this evaluation, where the identified models are benchmarked in terms of their GoF. The dataset used in this comparison corresponds to the operating condition $\mathrm{SoH}_c = 1$, $\mathrm{SoC} = 75\%$, and $T = 22\ ^\circ\mathrm{C}$. Although the global view over the entire identification window provides an indication of the overall accuracy, it does not allow a clear assessment of model performance in the transient regions, where the contribution of the RC dynamics is more pronounced.

A more detailed inspection of the transient response is provided in Figure 8, where a zoomed view highlights the differences among the identified models. In this region, ARX structures with an order higher than two exhibit a substantially improved capability to track the measured voltage dynamics, effectively capturing the rapid variations associated with the EEC behavior. Among these, the order-3 model achieves an excellent compromise: it closely follows the experimental transient response with an accuracy comparable to the order-4 structure, while avoiding unnecessary growth in model complexity.

Based on these considerations, the ARX model of order 3 was selected as the most appropriate trade-off between accuracy and compactness, ensuring an effective representation of the EEC dynamics without unnecessary parameter inflation.

https://doi.org/10.3390/batteries12010002

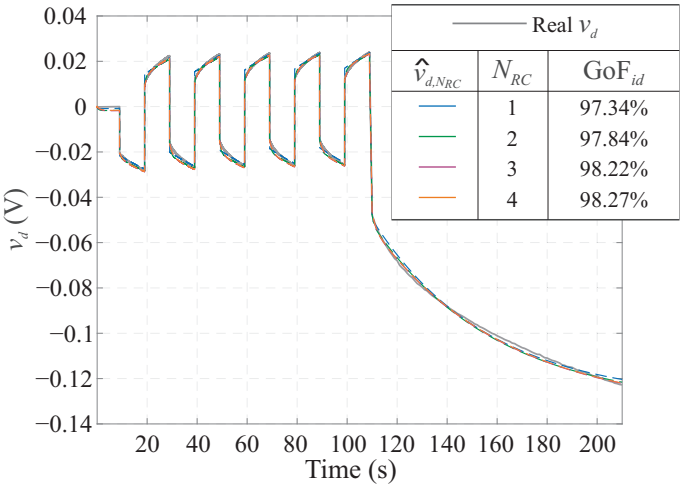

Figure 7. Global comparison of ARX models of order 1 to 4 at SoH$_c$ = 1, SoC = 75%, and T = 22 °C. The GoF is computed over the full identification window.

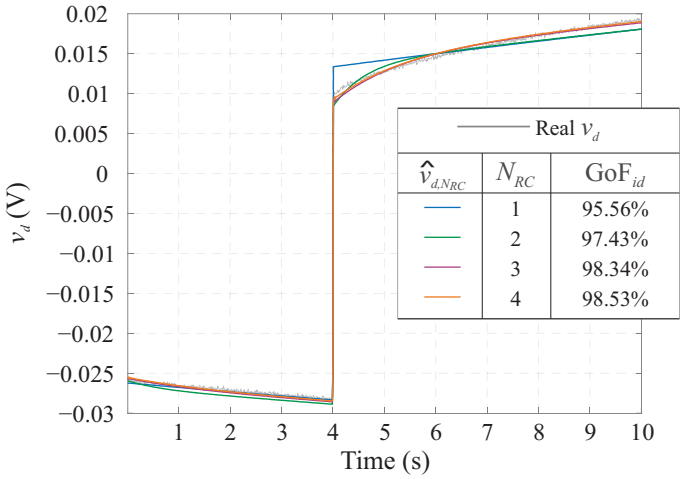

Figure 8. Zoomed view of the transient response used to compare ARX models with different polynomial orders.

4.2. Comparison of Estimation Results

Based on the cycling routine described in Section 3.2, the voltage response of the battery under test was measured across different Q, SOC, and T conditions. To evaluate the effectiveness of the estimation method, an ARX-based LUT was constructed incorporating parameters from both the beginning of life and after a moved charge, Q, of 15 kAh, across all SOC levels.

To assess the accuracy of the capacity and power fade estimation under varying temperature conditions, the method was evaluated in two configurations: a 2D LUT, using ARX models corresponding to a fixed reference temperature of 25 °C, and a 3D LUT, composed of multiple ARX models, each associated with a specific battery temperature. The objective is to demonstrate how the inclusion of temperature in the model enhances the reliability of SOH estimation.

The battery responses at intermediate cycling levels, for all available SOC and temperature values, were used as a validation dataset. Specifically, the SOH$_C$ estimation was performed quantitatively using the experimental battery capacity measured through Coulomb counting, while the SOH$_R$ estimation was carried out qualitatively to enable the correct interpretation of the dc resistance (defined as the sum of the resistance terms in the EEC model) as a monotonic indicator of power fade.

https://doi.org/10.3390/batteries12010002

The results of SOH_C estimation are presented in Figures 9 and 10, where each subplot compares the validation capacity to the corresponding characterization values at different temperatures. The *x*-axis represents the cycling levels, while the colored arrows illustrate the matching of SOH_C values for various SOC levels. The black dashed segments represent the SOH_C derived from validation data, while the green and purple dashed horizontal lines represent the SOH_C values from the characterization model.

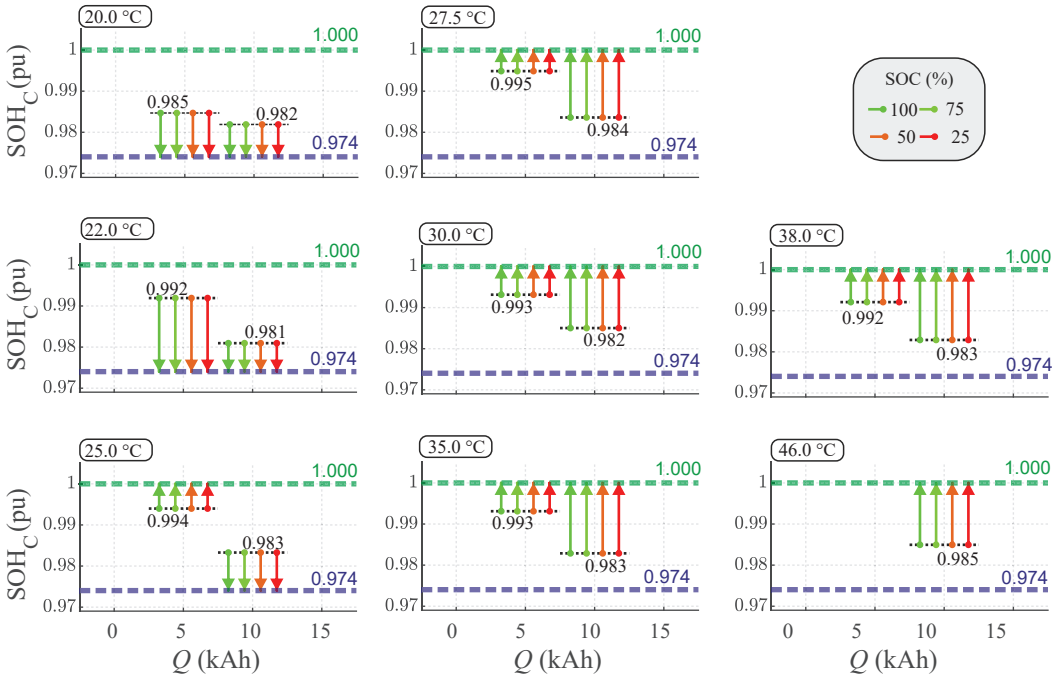

Figure 9. Results of the SOH_C estimation procedure across different temperatures using an ARX LUT that neglects for temperature variation.

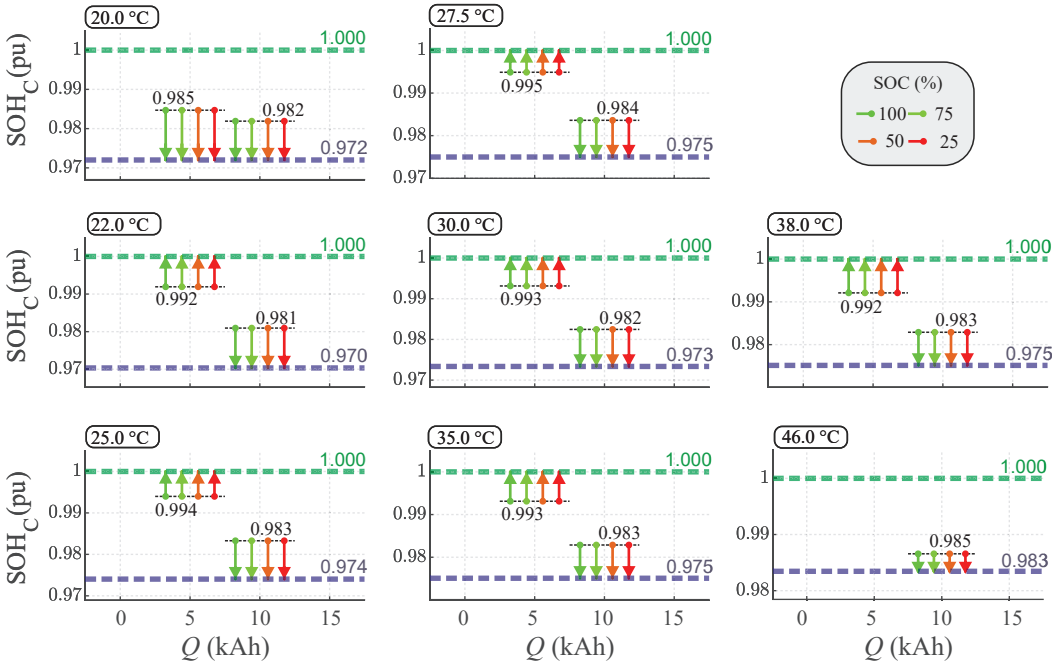

Figure 10. Results of the SOH_C estimation procedure across different temperatures using an ARX LUT that accounts for temperature variation.

The relative SOH_C was formulated with respect to the maximum capacity observed at the beginning of life for each temperature. This normalization allows a direct comparison of

degradation trends at different thermal conditions, emphasizing the impact of temperature on capacity fade.

In Figure 9, where the temperature effect is not considered, the results show that for all temperatures—except for 25 °C, which is used for training—the fixed-temperature model associates the same capacity value (i.e., a single Q level) for all intermediate validation points. This leads to a lack of resolution in capturing the actual degradation trend, making it impossible to identify the capacity fade occurring during cycling. In other words, the model fails to reflect the gradual loss of capacity at different SOC levels and temperatures, resulting in an inaccurate SOH_C estimation. In contrast, Figure 10, which includes the effect of temperature in the ARX model, shows a more detailed and progressive association of SOH_C values for all available temperatures. Here, the SOH_C estimation more clearly reflects the capacity fade over cycling levels, offering a much better fit to the actual battery behavior. This confirms that including temperature dependency in the characterization model is critical for accurately capturing the capacity degradation dynamics.

Figures 11 and 12 show the results of SOH_R estimation procedure.

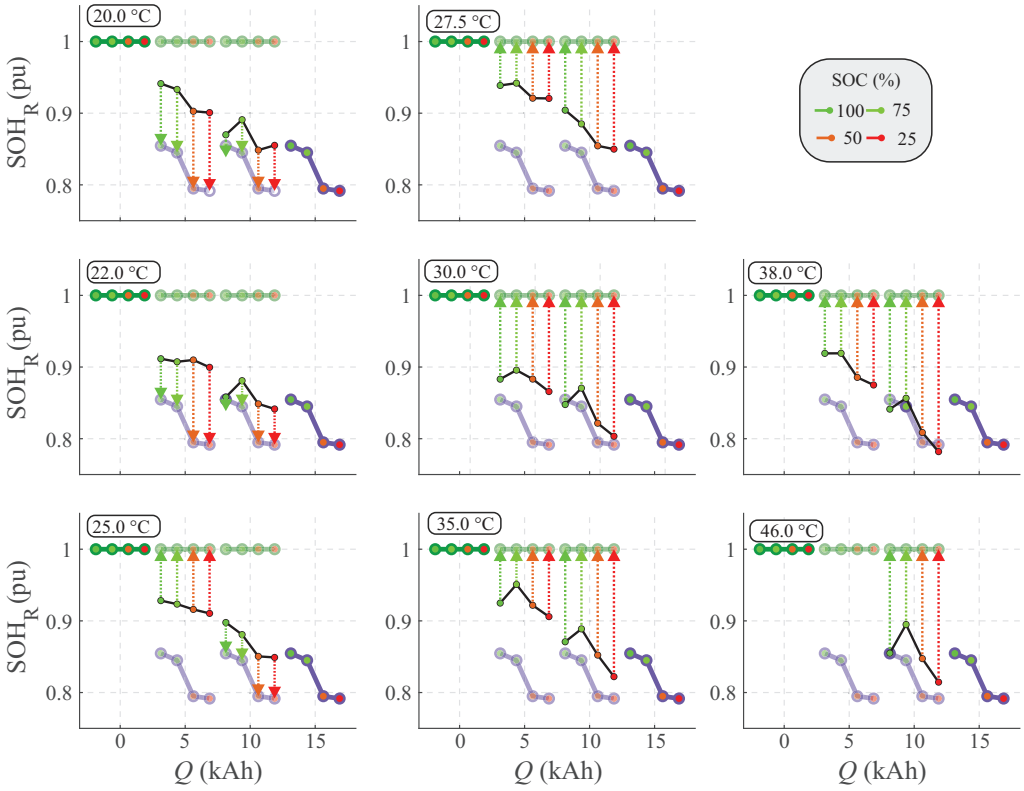

Figure 11. Results of the SOH_R estimation procedure at different temperatures neglecting temperature effect.

In this case, the dc resistance values are normalized with respect to the initial dc resistance identified at each SOC level and temperature. Specifically, for SOC levels of 25%, 50 %, 75%, and 100%, the resistance value at the beginning of life is set as the reference (1.0) and is represented by green markers. The resistance values after a moved charge of 15 kAh—used to build the additional ARX models—indicate the increase in resistance relative to the beginning of life and are represented by purple markers. As shown in the plots, each curve starts from a normalized value of 1.0 and evolves with cycling, indicating the degradation effect at each SOC.

https://doi.org/10.3390/batteries12010002

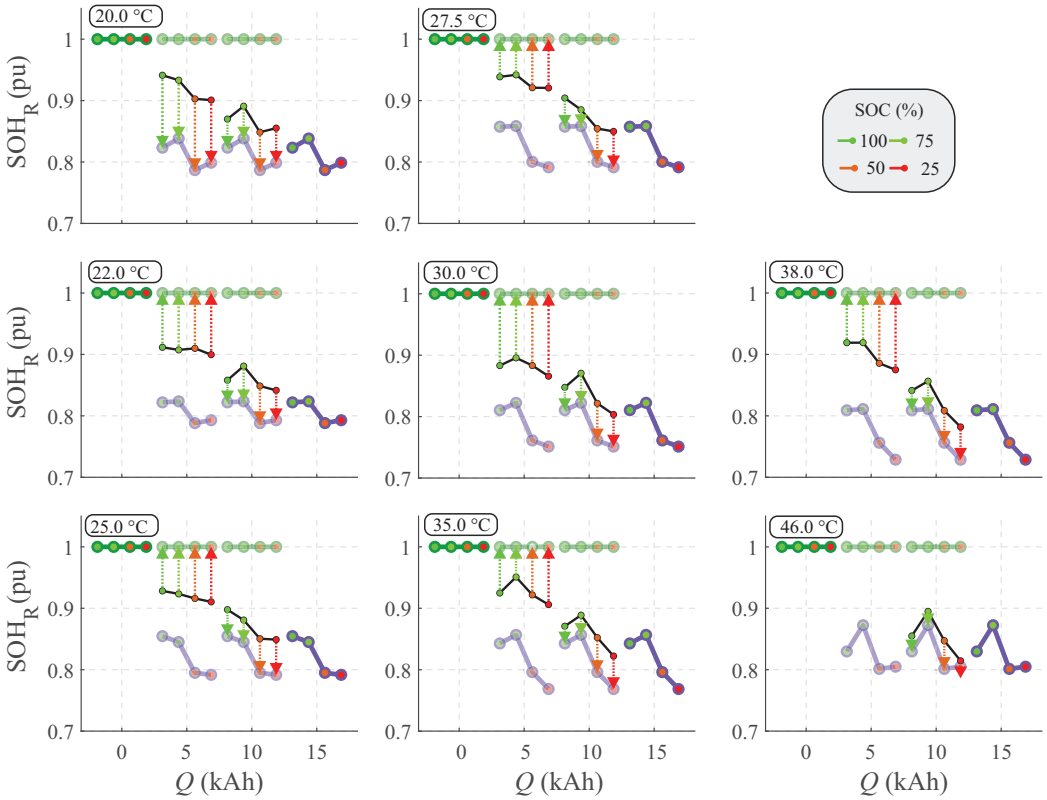

Figure 12. Results of the SOH_R estimation procedure at different temperatures considering temperature variation.

The focus is on validation cycles for $Q = 5$ kAh and $Q = 10$ kAh, where ARX modeling is used to estimate SOH_R for each SOC and temperature condition, represented by black lines. For each estimation procedure, the shaded-color markers indicate the set of the possible resistance values that could be associated with the estimation, depending on the characterization approach: In Figure 11, the ARX 2D LUT contains the models at a single reference temperature (25 °C); in Figure 12, the ARX 3D LUT is defined across all available temperatures.

The associations made by the estimation algorithm demonstrate that only when multiple temperatures are used in the LUT, the method is able to clearly capture the incremental resistance phenomena for the intermediate cycling levels used for validation. Conversely, when only a single temperature is considered (see Figure 11), the algorithm fails to reflect the actual increase in resistance across different SOC and temperature conditions. Therefore, for accurate power fade estimation, it is again demonstrated that temperature-dependent characterization is essential. The 3D LUT ARX-based model significantly improves estimation quality and sensitivity to real aging effects, confirming the critical role of temperature in battery performance modeling.

A comparison between Figures 10 and 12 reveals a strong correlation between the accuracy of capacity-fade and power-fade estimations. In particular, the 3D-LUT ARX algorithm consistently provides accurate predictions for both health indices, and no cases are observed in which only one of the two indices is correctly estimated. This consistency stems from the parametric structure of the algorithm and from the close relationship between the ARX model and the EEC representation. For each training dataset provided to the algorithm, the ARX model coefficients are identified so as to maximize the GoF of the measured time-domain battery response. As a result, these coefficients encode how the gradual capacity loss induced by aging influences the dynamic behavior of the battery. Moreover, the ARX parameters are uniquely related to the physical parameters of the

https://doi.org/10.3390/batteries12010002

underlying EEC model, in which the internal resistance plays a major role. Consequently, the best-GoF criterion leads to the most accurate capacity-fade estimation and, as a by-product, also yields an accurate characterization of the increase in internal resistance and thus of the associated power fade.

5. Conclusions

This work provided an investigation of the IR technique for assessing the SOH of an LCO battery, addressing both capacity and power fade under different temperature and SOC levels. As prescribed by the IR method, ARX models of the battery based on the impulse response were trained under various battery temperatures, SOC, and cycling conditions. The trained models were employed to estimate battery capacity fade and dc internal resistance increase under new operational conditions. In particular, the impact of temperature on estimation accuracy was evaluated by comparing results from a temperature-informed ARX model database against those from models trained at a constant temperature.

The results demonstrate that temperature has a significant impact on the accuracy of the IR-based estimation method. Specifically, the method was able to capture trends in capacity degradation and resistance increase across cycling levels between 0 and 15 kAh, and SOC levels between 25% and 100% only when temperatures between 20 °C and 46 °C were incorporated into the ARX model database. Outside these limits, however, extrapolation of the LUT can lead to inaccurate results. In contrast, a single-temperature ARX database failed to provide a clear estimation of these aging trends. Therefore, the temperature-aware ARX database markedly enhances the accuracy and sensitivity of the IR estimation routine to temperature variations, confirming the critical role of temperature in battery SOH estimation through IR characterization.

Moreover, the proposed procedure can be easily implemented in real-time BMS to effectively monitor battery SOH and regulate it by adjusting or limiting the actual maximum current based on the estimated SOH_C and SOH_R.

Although the results are promising, the proposed method has several important limitations. Some of these relate to its generalization to other batteries. First, the estimation method may fail if the training and test phases are performed on different cells due to manufacturing variations and calendar aging. Moreover, while the LUT is intrinsically compatible with modular use, the transition from a controlled single-cell environment to a multi-cell pack introduces additional challenges, including cell dispersion, thermal gradients, and cell-balancing strategies. Temperature measurement and management are also affected by the cell form factor, meaning that incorporating temperature into the method may lead to different performance levels for pouch, prismatic, and cylindrical cells.

Additional challenges may arise when scaling the LUT approach. As the number of conditioning variables increases, the LUT can grow exponentially, significantly increasing memory requirements for embedded systems. Furthermore, the implementation must ensure consistency across a large population of cells.

In future work, the proposed procedure could be extended to include a wider range of temperatures—particularly low-temperature conditions—as well as broader cycling ranges. The analysis could also be expanded and validated on different battery chemistries, such as LFP or LMO, and across different cell geometries.

Author Contributions: Conceptualization, S.B., M.R., E.F. and P.F.; methodology, S.B., M.R., E.F. and P.F.; validation, S.B., M.R., E.F. and P.F.; formal analysis, S.B., M.R., E.F. and P.F.; writing—original draft preparation, S.B., M.R., E.F. and P.F.; writing—review and editing, S.B., M.R., E.F., P.F., L.C., D.I. and L.P.; supervision, L.C., D.I. and L.P. All authors have read and agreed to the published version of the manuscript.

Funding: This research received no external funding.

Data Availability Statement: The datasets presented in this article are not readily available because the data are part of an ongoing study.

Conflicts of Interest: The authors declare no conflicts of interest.

References

1. Hannan, M.; Wali, S.; Ker, P.; Rahman, M.A.; Mansor, M.; Ramachandaramurthy, V.; Muttaqi, K.; Mahlia, T.; Dong, Z. Battery energy-storage system: A review of technologies, optimization objectives, constraints, approaches, and outstanding issues. *J. Energy Storage* **2021**, *42*, 103023. [CrossRef]
2. Barresi, M.; Ferri, E.; Piegari, L. A Fast Charging Station for Electric Vehicles with 400-V/800-V Charging Ports and Second-Life Batteries. In Proceedings of the 2023 IEEE 17th International Conference on Compatibility, Power Electronics and Power Engineering (CPE-POWERENG), Tallinn, Estonia, 14–16 June 2023; pp. 1–8. [CrossRef]
3. Barresi, M.; Colnago, S.; Ferri, E. Sizing and Energy Management Strategy of a Hybrid Energy Storage System for EVs. In Proceedings of the 2022 IEEE Vehicle Power and Propulsion Conference (VPPC), Merced, CA, USA, 1–4 November 2022; pp. 1–6. [CrossRef]
4. Barresi, M.; Ferri, E.; Piegari, L. An MV-Connected Ultra-Fast Charging Station Based on MMC and Dual Active Bridge with Multiple dc Buses. *Energies* **2023**, *16*, 3960. [CrossRef]
5. Vishnumurthy, K.; Girish, K. A comprehensive review of battery technology for E-mobility. *J. Indian Chem. Soc.* **2021**, *98*, 100173. [CrossRef]
6. Kim, H.J.; Krishna, T.; Zeb, K.; Rajangam, V.; Gopi, C.V.V.M.; Sambasivam, S.; Raghavendra, K.V.G.; Obaidat, I.M. A Comprehensive Review of Li-Ion Battery Materials and Their Recycling Techniques. *Electronics* **2020**, *9*, 1161. [CrossRef]
7. Nitta, N.; Wu, F.; Lee, J.T.; Yushin, G. Li-ion battery materials: Present and future. *Mater. Today* **2015**, *18*, 252–264. [CrossRef]
8. Geisbauer, C.; Wöhrl, K.; Koch, D.; Wilhelm, G.; Schneider, G.; Schweiger, H.G. Comparative Study on the Calendar Aging Behavior of Six Different Lithium-Ion Cell Chemistries in Terms of Parameter Variation. *Energies* **2021**, *14*, 3358. [CrossRef]
9. Belt, J.R.; Ho, C.D.; Motloch, C.G.; Miller, T.J.; Duong, T.Q. A capacity and power fade study of Li-ion cells during life cycle testing. *J. Power Sources* **2003**, *123*, 241–246. [CrossRef]
10. Misyris, G.S.; Doukas, D.I.; Papadopoulos, T.A.; Labridis, D.P.; Agelidis, V.G. State-of-Charge Estimation for Li-Ion Batteries: A More Accurate Hybrid Approach. *IEEE Trans. Energy Convers.* **2019**, *34*, 109–119. [CrossRef]
11. Stroe, D.I.; Schaltz, E. Lithium-Ion Battery State-of-Health Estimation Using the Incremental Capacity Analysis Technique. *IEEE Trans. Ind. Appl.* **2020**, *56*, 678–685. [CrossRef]
12. Zhao, G.; Wang, X.; Negnevitsky, M. Connecting battery technologies for electric vehicles from battery materials to management. *iScience* **2022**, *25*, 103744. [CrossRef]
13. Gou, B.; Xu, Y.; Feng, X. State-of-Health Estimation and Remaining-Useful-Life Prediction for Lithium-Ion Battery Using a Hybrid Data-Driven Method. *IEEE Trans. Veh. Technol.* **2020**, *69*, 10854–10867. [CrossRef]
14. Ecker, M.; Gerschler, J.B.; Vogel, J.; Käbitz, S.; Hust, F.; Dechent, P.; Sauer, D.U. Development of a lifetime prediction model for lithium-ion batteries based on extended accelerated aging test data. *J. Power Sources* **2012**, *215*, 248–257. [CrossRef]
15. Zheng, L.; Zhu, J.; Lu, D.D.C.; Wang, G.; He, T. Incremental capacity analysis and differential voltage analysis based state of charge and capacity estimation for lithium-ion batteries. *Energy* **2018**, *150*, 759–769. [CrossRef]
16. Xu, X.; Xu, Z.; Wang, T.; Xu, J.; Pei, L. Open-circuit voltage curve reconstruction for degrading lithium-ion batteries utilizing discrete curve fragments from an online dataset. *J. Energy Storage* **2022**, *56*, 106003. [CrossRef]
17. Sun, J.; Tang, Y.; Ye, J.; Jiang, T.; Chen, S.; Qiu, S. A novel capacity and initial discharge electric quantity estimation method for LiFePO4 battery pack based on OCV curve partial reconstruction. *Energy* **2022**, *243*, 122882. [CrossRef]
18. Siva Suriya Narayanan, S.; Thangavel, S. Machine learning-based model development for battery state of charge–open circuit voltage relationship using regression techniques. *J. Energy Storage* **2022**, *49*, 104098. [CrossRef]
19. Grandjean, T.R.B.; Groenewald, J.; McGordon, A.; Widanage, W.D.; Marco, J. Accelerated Internal Resistance Measurements of Lithium-Ion Cells to Support Future End-of-Life Strategies for Electric Vehicles. *Batteries* **2018**, *4*, 49. [CrossRef]
20. He, H.; Xiong, R.; Zhang, X.; Sun, F.; Fan, J. State-of-Charge Estimation of the Lithium-Ion Battery Using an Adaptive Extended Kalman Filter Based on an Improved Thevenin Model. *IEEE Trans. Veh. Technol.* **2011**, *60*, 1461–1469. [CrossRef]
21. Wang, Y.; Tian, J.; Sun, Z.; Wang, L.; Xu, R.; Li, M.; Chen, Z. A comprehensive review of battery modeling and state estimation approaches for advanced battery management systems. *Renew. Sustain. Energy Rev.* **2020**, *131*, 110015. [CrossRef]
22. Zhang, Q.; Wang, D.; Yang, B.; Cui, X.; Li, X. Electrochemical model of lithium-ion battery for wide frequency range applications. *Electrochim. Acta* **2020**, *343*, 136094. [CrossRef]
23. Lee, J.L.; Chemistruck, A.; Plett, G.L. One-dimensional physics-based reduced-order model of lithium-ion dynamics. *J. Power Sources* **2012**, *220*, 430–448. [CrossRef]

24. Wu, L.; Fu, X.; Guan, Y. Review of the Remaining Useful Life Prognostics of Vehicle Lithium-Ion Batteries Using Data-Driven Methodologies. *Appl. Sci.* **2016**, *6*, 166. [CrossRef]
25. Liu, D.; Pang, J.; Zhou, J.; Peng, Y.; Pecht, M. Prognostics for state of health estimation of lithium-ion batteries based on combination Gaussian process functional regression. *Microelectron. Reliab.* **2013**, *53*, 832–839. [CrossRef]
26. Tang, S.; Yu, C.; Wang, X.; Guo, X.; Si, X. Remaining Useful Life Prediction of Lithium-Ion Batteries Based on the Wiener Process with Measurement Error. *Energies* **2014**, *7*, 520–547. [CrossRef]
27. Yu, S.; Wang, J.; Cao, Y.; Yi, Y.; Li, C.; Li, B. WRLS-ARMAX-Based Parameter Identification for System Frequency Response Model with Battery Energy Storage System. In Proceedings of the 2025 IEEE International Conference on Power and Integrated Energy Systems (ICPIES), Haikou, China, 7–9 April 2025; pp. 378–382. [CrossRef]
28. Jiao, R.H.; Ma, X.; Li, L.; Xiao, J.P. Battery Remaining Useful Life Prediction Based on a Combination of ARMA and Degradation Model. In Proceedings of the 2022 13th International Conference on Reliability, Maintainability, and Safety (ICRMS), Kowloon, Hong Kong, China, 21–24 August 2022; pp. 115–119. [CrossRef]
29. Kim, S.; Lee, P.Y.; Lee, M.; Kim, J.; Na, W. Improved State-of-health prediction based on auto-regressive integrated moving average with exogenous variables model in overcoming battery degradation-dependent internal parameter variation. *J. Energy Storage* **2022**, *46*, 103888. [CrossRef]
30. Shen, S.; Ci, S.; Zhang, K.; Liang, X. Lifecycle Prediction of Second Use Electric Vehicle Batteries Based on ARIMA Model. In Proceedings of the 2019 IEEE Globecom Workshops (GC Wkshps), Waikoloa, HI, USA, 9–13 December 2019; pp. 1–6. [CrossRef]
31. Wang, S.; Shang, L.; Li, Z.; Deng, H.; Ma, Y. Lithium-ion Battery Security Guaranteeing Method Study Based on the State of Charge Estimation. *Int. J. Electrochem. Sci.* **2015**, *10*, 5130–5151. [CrossRef]
32. Sepasi, S.; Ghorbani, R.; Liaw, B.Y. Inline state of health estimation of lithium-ion batteries using state of charge calculation. *J. Power Sources* **2015**, *299*, 246–254. [CrossRef]
33. He, W.; Williard, N.; Chen, C.; Pecht, M. State of charge estimation for electric vehicle batteries using unscented kalman filtering. *Microelectron. Reliab.* **2013**, *53*, 840–847. [CrossRef]
34. Zheng, X.; Fang, H. An integrated unscented kalman filter and relevance vector regression approach for lithium-ion battery remaining useful life and short-term capacity prediction. *Reliab. Eng. Syst. Saf.* **2015**, *144*, 74–82. [CrossRef]
35. Walker, E.; Rayman, S.; White, R.E. Comparison of a particle filter and other state estimation methods for prognostics of lithium-ion batteries. *J. Power Sources* **2015**, *287*, 1–12. [CrossRef]
36. Wang, D.; Yang, F.; Tsui, K.L.; Zhou, Q.; Bae, S.J. Remaining Useful Life Prediction of Lithium-Ion Batteries Based on Spherical Cubature Particle Filter. *IEEE Trans. Instrum. Meas.* **2016**, *65*, 1282–1291. [CrossRef]
37. Liu, S.; Fang, L.; Zhao, X.; Wang, S.; Hu, C.; Gu, F.; Ball, A. State-of-health estimation of lithium-ion batteries using a kernel support vector machine tuned by a new nonlinear gray wolf algorithm. *J. Energy Storage* **2024**, *102*, 114052. [CrossRef]
38. Wang, S.; Zhao, L.; Su, X.; Ma, P. Prognostics of Lithium-Ion Batteries Based on Battery Performance Analysis and Flexible Support Vector Regression. *Energies* **2014**, *7*, 6492–6508. [CrossRef]
39. Dong, H.; Jin, X.; Lou, Y.; Wang, C. Lithium-ion battery state of health monitoring and remaining useful life prediction based on support vector regression-particle filter. *J. Power Sources* **2014**, *271*, 114–123. [CrossRef]
40. Klass, V.; Behm, M.; Lindbergh, G. A support vector machine-based state-of-health estimation method for lithium-ion batteries under electric vehicle operation. *J. Power Sources* **2014**, *270*, 262–272. [CrossRef]
41. Kim, J.; Lee, S.; Cho, B.H. Complementary Cooperation Algorithm Based on DEKF Combined with Pattern Recognition for SOC/Capacity Estimation and SOH Prediction. *IEEE Trans. Power Electron.* **2012**, *27*, 436–451. [CrossRef]
42. Eddahech, A.; Briat, O.; Bertrand, N.; Delétage, J.Y.; Vinassa, J.M. Behavior and state-of-health monitoring of Li-ion batteries using impedance spectroscopy and recurrent neural networks. *Int. J. Electr. Power Energy Syst.* **2012**, *42*, 487–494. [CrossRef]
43. Yang, N.; Hofmann, H.; Sun, J.; Song, Z. Remaining Useful Life Prediction of Lithium-Ion Batteries with Limited Degradation History Using Random Forest. *IEEE Trans. Transp. Electrif.* **2024**, *10*, 5049–5060. [CrossRef]
44. Wang, X.; Hu, B.; Su, X.; Xu, L.; Zhu, D. State of Health estimation for lithium-ion batteries using Random Forest and Gated Recurrent Unit. *J. Energy Storage* **2024**, *76*, 109796. [CrossRef]
45. Lu, D.; Cui, N.; Li, C. A Novel Transfer Learning Framework Combining Attention Mechanisms and Random Forest Regression for State of Health Estimation of Lithium-Ion Battery with Different Formulations. *IEEE Trans. Ind. Appl.* **2024**, *60*, 5726–5736. [CrossRef]
46. Chen, Z.; Shi, N.; Ji, Y.; Niu, M.; Wang, Y. Lithium-ion batteries remaining useful life prediction based on BLS-RVM. *Energy* **2021**, *234*, 121269. [CrossRef]
47. Lyu, Z.; Wang, G.; Gao, R. Synchronous state of health estimation and remaining useful lifetime prediction of Li-Ion battery through optimized relevance vector machine framework. *Energy* **2022**, *251*, 123852. [CrossRef]
48. Berghout, T.; Benbouzid, M.; Amirat, Y.; Yao, G. Lithium-Ion Battery State of Health Prediction with a Robust Collaborative Augmented Hidden Layer Feedforward Neural Network Approach. *IEEE Trans. Transp. Electrif.* **2023**, *9*, 4492–4502. [CrossRef]

49. Ye, Z.; Liu, W.; Wang, X.; Zhu, J.; Yin, J. Lithium battery SOH estimation through FFNN. *J. Phys. Conf. Ser.* **2022**, *2260*, 012034. [CrossRef]
50. Yuan, T.; Gao, F.; Bai, J.; Sun, H. A lithium-ion battery state of health estimation method utilizing convolutional neural networks and bidirectional long short-term memory with attention mechanisms for collaborative defense against false data injection cyber-attacks. *J. Power Sources* **2025**, *631*, 236193. [CrossRef]
51. Ouyang, T.; Su, Y.; Wang, C.; Jin, S. Combined Meta-Learning with CNN-LSTM Algorithms for State-of-Health Estimation of Lithium-Ion Battery. *IEEE Trans. Power Electron.* **2024**, *39*, 10106–10117. [CrossRef]
52. Xiao, F.; Yang, W.; Ding, Y.; Li, X.; Zhang, K.; Liu, J. A CNN-LSTM Method Based on Voltage Deviation for Predicting the State of Health of Lithium-Ion Batteries. *Battery Energy* **2025**, *4*, e20240036. [CrossRef]
53. Liu, H.; Li, Y.; Luo, L.; Zhang, C. A Lithium-Ion Battery Capacity and RUL Prediction Fusion Method Based on Decomposition Strategy and GRU. *Batteries* **2023**, *9*, 323. [CrossRef]
54. Zhou, J.; Qin, Y.; Luo, J.; Zhu, T. Remaining Useful Life Prediction by Distribution Contact Ratio Health Indicator and Consolidated Memory GRU. *IEEE Trans. Ind. Inform.* **2023**, *19*, 8472–8483. [CrossRef]
55. Shu, X.; Shen, J.; Li, G.; Zhang, Y.; Chen, Z.; Liu, Y. A Flexible State-of-Health Prediction Scheme for Lithium-Ion Battery Packs with Long Short-Term Memory Network and Transfer Learning. *IEEE Trans. Transp. Electrif.* **2021**, *7*, 2238–2248. [CrossRef]
56. Ma, Y.; Li, J.; Gao, J.; Chen, H. State of health prediction of lithium-ion batteries under early partial data based on IWOA-BiLSTM with single feature. *Energy* **2024**, *295*, 131085. [CrossRef]
57. Peng, S.; Wang, Y.; Tang, A.; Jiang, Y.; Kan, J.; Pecht, M. State of health estimation joint improved grey wolf optimization algorithm and LSTM using partial discharging health features for lithium-ion batteries. *Energy* **2025**, *315*, 134293. [CrossRef]
58. Tang, K.; Luo, B.; Chen, D.; Wang, C.; Chen, L.; Li, F.; Cao, Y.; Wang, C. The State of Health Estimation of Lithium-Ion Batteries: A Review of Health Indicators, Estimation Methods, Development Trends and Challenges. *World Electr. Veh. J.* **2025**, *16*, 429. [CrossRef]
59. Nikolian, A.; Firouz, Y.; Gopalakrishnan, R.; Timmermans, J.M.; Omar, N.; Van den Bossche, P.; Van Mierlo, J. Lithium Ion Batteries—Development of Advanced Electrical Equivalent Circuit Models for Nickel Manganese Cobalt Lithium-Ion. *Energies* **2016**, *9*, 360. [CrossRef]
60. Allafi, W.; Uddin, K.; Zhang, C.; Mazuir Raja Ahsan Sha, R.; Marco, J. On-line scheme for parameter estimation of nonlinear lithium ion battery equivalent circuit models using the simplified refined instrumental variable method for a modified Wiener continuous-time model. *Appl. Energy* **2017**, *204*, 497–508. [CrossRef]
61. Farmann, A.; Sauer, D.U. Comparative study of reduced order equivalent circuit models for on-board state-of-available-power prediction of lithium-ion batteries in electric vehicles. *Appl. Energy* **2018**, *225*, 1102–1122. [CrossRef]
62. Liu, F.; Shao, C.; Su, W.; Liu, Y. Online joint estimator of key states for battery based on a new equivalent circuit model. *J. Energy Storage* **2022**, *52*, 104780. [CrossRef]
63. Zhao, Y.; Jossen, A. Comparative Study of Parameter Identification with Frequency and Time Domain Fitting Using a Physics-Based Battery Model. *Batteries* **2022**, *8*, 222. [CrossRef]
64. LeBel, F.A.; Messier, P.; Sari, A.; Trovão, J.P.F. Lithium-ion cell equivalent circuit model identification by galvanostatic intermittent titration technique. *J. Energy Storage* **2022**, *54*, 105303. [CrossRef]
65. Barcellona, S.; Piegari, L. Lithium Ion Battery Models and Parameter Identification Techniques. *Energies* **2017**, *10*, 2007. [CrossRef]
66. Rahimi-Eichi, H.; Baronti, F.; Chow, M.Y. Online Adaptive Parameter Identification and State-of-Charge Coestimation for Lithium-Polymer Battery Cells. *IEEE Trans. Ind. Electron.* **2014**, *61*, 2053–2061. [CrossRef]
67. Meng, J.; Ricco, M.; Acharya, A.B.; Luo, G.; Swierczynski, M.; Stroe, D.I.; Teodorescu, R. Low-complexity online estimation for LiFePO4 battery state of charge in electric vehicles. *J. Power Sources* **2018**, *395*, 280–288. [CrossRef]
68. Sun, C.; Lin, H.; Cai, H.; Gao, M.; Zhu, C.; He, Z. Improved parameter identification and state-of-charge estimation for lithium-ion battery with fixed memory recursive least squares and sigma-point Kalman filter. *Electrochim. Acta* **2021**, *387*, 138501. [CrossRef]
69. He, H.; Xiong, R.; Guo, H. Online estimation of model parameters and state-of-charge of LiFePO4 batteries in electric vehicles. *Appl. Energy* **2012**, *89*, 413–420. . [CrossRef]
70. Xiong, R.; Zhang, Y.; He, H.; Zhou, X.; Pecht, M.G. A Double-Scale, Particle-Filtering, Energy State Prediction Algorithm for Lithium-Ion Batteries. *IEEE Trans. Ind. Electron.* **2018**, *65*, 1526–1538. [CrossRef]
71. Peng, J.; Meng, J.; Wu, J.; Deng, Z.; Lin, M.; Mao, S.; Stroe, D.I. A comprehensive overview and comparison of parameter benchmark methods for lithium-ion battery application. *J. Energy Storage* **2023**, *71*, 108197. [CrossRef]
72. Ranjbar, A.H.; Banaei, A.; Khoobroo, A.; Fahimi, B. Online Estimation of State of Charge in Li-Ion Batteries Using Impulse Response Concept. *IEEE Trans. Smart Grid* **2012**, *3*, 360–367. [CrossRef]
73. Yang, Z.; Patil, D.; Fahimi, B. Online Estimation of Capacity Fade and Power Fade of Lithium-Ion Batteries Based on Input–Output Response Technique. *IEEE Trans. Transp. Electrif.* **2018**, *4*, 147–156. [CrossRef]

74. Iannuzzi, D.; Ribera, M.; Satariano, P.; Fedele, E.; Pagliarini, F.; Cennamo, P.; Orsini, F.; Petrazzuoli, L.; Spinelli, M. Capacity Fade Estimation of LiFePo Cells Based on Improved Impulse Response Method: Experimental Results. In Proceedings of the 2023 IEEE International Conference on Electrical Systems for Aircraft, Railway, Ship Propulsion and Road Vehicles & International Transportation Electrification Conference (ESARS-ITEC), Venice, Italy, 29–31 March 2023; pp. 1–6. [CrossRef]
75. Barcellona, S.; Ribera, M.; Fedele, E.; Piegari, L.; Codecasa, L.; Iannuzzi, D. State of Health Estimation of LiCoO2 Cells based on Impulse Response and ARMAX Identification. In Proceedings of the 2024 IEEE International Conference on Electrical Systems for Aircraft, Railway, Ship Propulsion and Road Vehicles & International Transportation Electrification Conference (ESARS-ITEC), Naples, Italy, 26–29 November 2024; pp. 1–6. [CrossRef]
76. Miniguano, H.; Barrado, A.; Lázaro, A.; Zumel, P.; Fernández, C. General Parameter Identification Procedure and Comparative Study of Li-Ion Battery Models. *IEEE Trans. Veh. Technol.* **2020**, *69*, 235–245. [CrossRef]
77. Ma, S.; Jiang, M.; Tao, P.; Song, C.; Wu, J.; Wang, J.; Deng, T.; Shang, W. Temperature effect and thermal impact in lithium-ion batteries: A review. *Prog. Nat. Sci. Mater. Int.* **2018**, *28*, 653–666. [CrossRef]
78. Barcellona, S.; Codecasa, L.; Colnago, S.; Laurano, C.; Piegari, L.; Toscani, S. A technique for separating the impact of cycle aging and temperature on Li-ion battery capacity. *J. Energy Storage* **2024**, *91*, 112087. [CrossRef]
79. Wang, S.; Wu, T.; Xie, H.; Li, C.; Zhang, J.; Jiang, L.; Wang, Q. Effects of Current and Ambient Temperature on Thermal Response of Lithium Ion Battery. *Batteries* **2022**, *8*, 203. [CrossRef]
80. Lv, S.; Wang, X.; Lu, W.; Zhang, J.; Ni, H. The Influence of Temperature on the Capacity of Lithium Ion Batteries with Different Anodes. *Energies* **2022**, *15*, 60. [CrossRef]
81. Chang, C.-k. Factors Affecting Capacity Design of Lithium-Ion Stationary Batteries. *Batteries* **2019**, *5*, 58. [CrossRef]
82. Wang, X.; Zhang, Y.; Ni, H.; Lv, S.; Zhang, F.; Zhu, Y.; Yuan, Y.; Deng, Y. Influence of Different Ambient Temperatures on the Discharge Performance of Square Ternary Lithium-Ion Batteries. *Energies* **2022**, *15*, 5348. [CrossRef]
83. Yuan, S.; Wu, H.; Yin, C. State of Charge Estimation Using the Extended Kalman Filter for Battery Management Systems Based on the ARX Battery Model. *Energies* **2013**, *6*, 444–470. [CrossRef]
84. Barcellona, S.; Piegari, L. Effect of current on cycle aging of lithium ion batteries. *J. Energy Storage* **2020**, *29*, 101310. [CrossRef]
85. Uno, M.; Tanaka, K. Influence of High-Frequency Charge–Discharge Cycling Induced by Cell Voltage Equalizers on the Life Performance of Lithium-Ion Cells. *IEEE Trans. Veh. Technol.* **2011**, *60*, 1505–1515. [CrossRef]
86. Barcellona, S.; Brenna, M.; Foiadelli, F.; Longo, M.; Piegari, L. Analysis of Ageing Effect on Li-Polymer Batteries. *Sci. World J.* **2015**, *2015*, 979321. [CrossRef]

Disclaimer/Publisher's Note: The statements, opinions and data contained in all publications are solely those of the individual author(s) and contributor(s) and not of MDPI and/or the editor(s). MDPI and/or the editor(s) disclaim responsibility for any injury to people or property resulting from any ideas, methods, instructions or products referred to in the content.

batteries

MDPI

Article

Coupling Model and Early-Stage Internal Short Circuits Fault Diagnosis for Gel Electrolyte Lithium-Ion Batteries

Liye Wang [1,2,3,*], Jinlong Wu [1,2,3], Chunxiao Ma [1,2,3], Xianzhong Sun [2,3], Lifang Wang [1,2,3] and Chenglin Liao [1,2,3]

[1] State Key Laboratory of High Density Electromagnetic Power and Systems, Institute of Electrical Engineering, Chinese Academy of Sciences, Beijing 100190, China
[2] Institute of Electrical Engineering, Chinese Academy of Sciences, Beijing 100190, China; xzsun@mail.iee.ac.cn
[3] University of Chinese Academy of Sciences, Beijing 100190, China
* Correspondence: wangliye@mail.iee.ac.cn

Abstract

This paper presents a method for modeling and predicting ISC in gel-electrolyte lithium-ion batteries, addressing critical safety concerns in electric vehicles. While gel-electrolytes are highlighted for their superior stability and performance advantages over liquid-electrolytes, they remain susceptible to IISC due to factors such as dendrite formation or mechanical stress. This study provides a detailed analysis of the unique ISCs mechanism in gel-electrolytes, emphasizing the differences between gel-electrolyte and liquid-electrolyte batteries in terms of ion transport dynamics and thermal performance. Based on these characteristics, an electrochemical–thermal–ISC coupling model was developed, and an external short-circuit resistance test was conducted to validate the model's accuracy. By simulating various ISC states using the coupling model, a comprehensive dataset of battery ISC parameters was obtained, encompassing voltage, current, temperature, SOC, capacity loss, and internal resistance. ISC prediction models were subsequently developed using BP, CNN, and LSTM networks, with a comparative analysis of their prediction accuracy. This research advances the ISC prediction framework for gel-electrolyte batteries and demonstrates the potential of CNN-based models to achieve higher accuracy in fault prediction. Accurate ISC prediction is crucial for ensuring safe battery operation in electric vehicles.

Keywords: gel-electrolyte; lithium-ion batteries; internal short circuits; ISC prediction model; fault prediction

1. Introduction

Lithium-ion battery is a complex electrochemical system. In recent years, lithium-ion battery failures due to internal short circuits (ISCs) have been a significant concern to the entire lithium-ion cell market from consumer electronics to electric vehicles. Currently, liquid-electrolyte lithium-ion batteries have characteristics of easy leakage, flammability, and volatility, all potential safety hazards [1,2]. Therefore, safer and more efficient gel-electrolyte lithium-ion batteries have become a hot research topic for researchers [3,4]. Gel-electrolyte lithium-ion batteries provide several advantages, including high energy density, long cycle life [5,6], excellent discharge rates, and resistance to leakage [7,8] and to the formation of lithium dendrites [9,10]. Furthermore, they exhibit superior ionic conductivity and enhanced scalability [11–13]. Consequently, gel-electrolyte lithium-ion batteries may be susceptible to internal short-circuit (ISC) failures, a phenomenon also observed in liquid-electrolyte-based systems [14,15].

The mechanism of battery ISCs is highly complex, and current ISC diagnosis methods primarily rely on model-based and data-driven approaches. Model-based diagnostic methods identify ISCs by comparing the difference between a lithium-ion battery model and real-world data against a predefined threshold [16,17]. Kong X. et al. [18] conducted simulation experiments using a pseudo two-dimensional model and an impedance identification method, revealing that the effective conductivity of the separator is strongly correlated with the degree of internal short-circuiting in batteries. Sheikh M. et al. [19] performed mechanical failure analysis of thermal runaway propagation in 18650 lithium-ion batteries by developing a battery model through finite element analysis and numerical simulation techniques. Their experiments validated the accuracy of the numerical simulation model and demonstrated its utility in predicting the initial failure of batteries. Feng X. et al. [20] proposed a model-based online ISC diagnosis algorithm that utilizes the average voltage value of the battery pack. The algorithm detects ISC faults by calculating the deviation of the evaluated voltage and incorporates temperature information to enhance the robustness of the diagnosis process.

Data-driven diagnostic methods are based on a large amount of historical data on ISCs in lithium-ion batteries, extracting battery fault characteristics and using machine learning or deep learning algorithms for training. This method does not require electrochemical modeling of lithium batteries, which is relatively simple and accurate. Ojo O. et al. [21] proposed a data-driven thermal fault detection method based on the estimation of battery temperature with Long and Short Term Memory (LSTM). Samanta A. et al. [22] made a review and analysis of machine learning algorithms on lithium-ion battery safety diagnosis for the three learning methods categorized as supervised learning, unsupervised learning and reinforcement learning; the most widely used is based on the supervised learning methods, such as artificial neural network (ANN), random forest (RF), support vector machine (SVM), among which ANN algorithm is the most commonly used.

Challenges and problems:

(1) Because of the difference in ion transport and thermal performance between gel-electrolyte battery and liquid battery, there is still a gap in the research of internal short circuit safety of gel-state lithium-ion batteries.
(2) The traditional methods require the establishment of modified pseudo two-dimensional models, three-dimensional electrochemical thermal internal short circuit coupling models, or equivalent circuit models. Algorithms also require complex methods such as recursive least squares, which have complex models, large computational complexity, and high practical application thresholds.
(3) The traditional method is relatively simple, relying on threshold values and other judgment criteria. However, in actual situations, determining the parameter threshold is challenging as it requires consideration of multiple factors, resulting in low accuracy. Meanwhile, the diagnostic method based on ISC mechanisms and models involves complicated calculations, making it difficult to apply in practice.
(4) Data-driven diagnostic methods require extensive ISC data, but conducting a large number of battery ISC experiments poses certain safety risks, and these experiments exhibit poor repeatability and controllability.

Contributions of this work:

The safety problem of liquid lithium-ion batteries due to internal short circuit is the focus of current research. Traditional ISC diagnosis method has the problems of complex calculation, low accuracy and difficult data acquisition. This paper solves the problem of controllable recurrence in ISC tests by combining model simulation and experimental testing. The ISC method proposed in this paper demonstrates both simplicity and accuracy, with great application potential.

https://doi.org/10.3390/batteries12020045

(1) This study focuses on analyzing the thermal runaway process and mechanism of ISC in gel-electrolyte lithium-ion batteries. It provides a detailed analysis of the unique ISC mechanism in gel-electrolytes, highlighting the differences between gel-electrolyte batteries and liquid-electrolyte batteries in terms of ion transport and thermal performance. The research results can provide theoretical support for the safety design of battery cells and systems.

(2) A battery electrochemical–thermal–ISC coupling model for lithium-ion batteries is established, which effectively addresses the challenge of acquiring ISC data by replacing physical ISC tests with simulation methods. Through the combination of model simulation and experimental testing, this approach solves the problem of poor controllability and repeatability in internal short circuit testing.

(3) ISC prediction model grounded in deep learning was established. Deep learning model with both simplicity and accuracy and great application potential is established. Reduce complexity and improve accuracy through optimizer selection, learning rate strategy and architecture optimization.

The safety issue of liquid lithium-ion batteries arising from ISCs is a critical focus of current research. Traditional ISC diagnosis methods suffer from limitations such as complex calculations, low accuracy, and challenging data acquisition. This paper addresses these challenges by integrating model simulation with experimental testing, thereby solving the problem of controllable recurrence in ISC testing. The proposed ISC method demonstrates simplicity, high accuracy, and significant application potential.

Organization of the paper:

Section 2 presents the methodology analysis, Section 3 focuses on the mechanistic analysis of ISCs and battery ISC model designs, Section 4 details the model validation and dataset acquisition process, and Section 5 outlines the methods for predicting ISCs. The key conclusions are summarized in Sections 6 and 7. The Structure of research technology is shown in Figure 1.

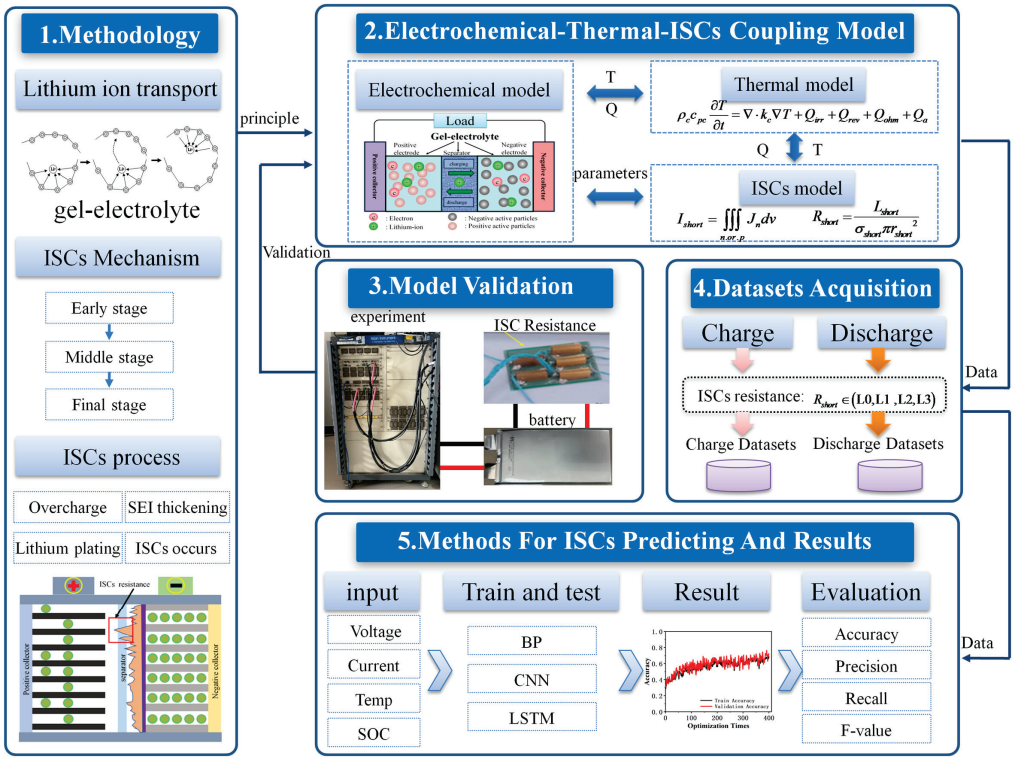

Figure 1. Structure of research technology.

2. Methodology

2.1. Principle

The structure of gel-electrolyte lithium-ion batteries consists of a negative electrode material, a positive electrode material, and a separator, as shown in Figure 2.

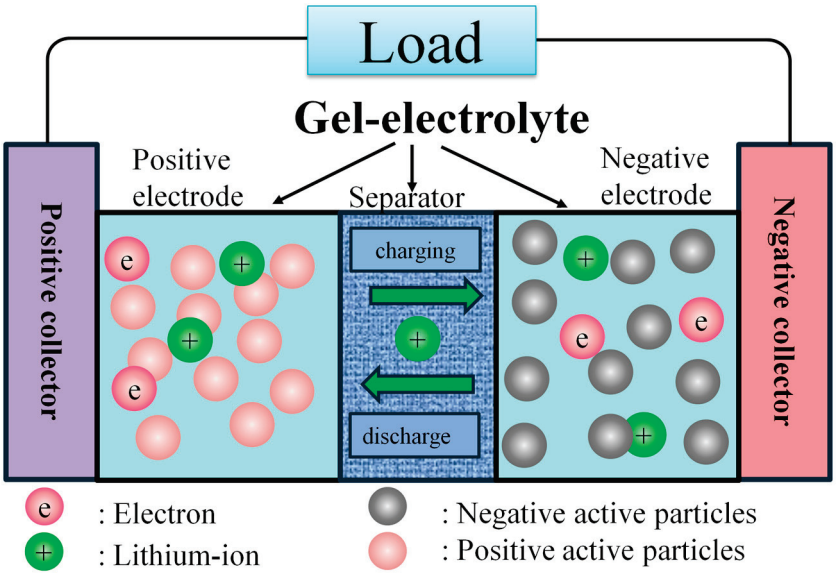

Figure 2. Structure of gel-electrolyte lithium-ion batteries.

Gel-electrolytes are composed of a polymer matrix enriched with a solvent and lithium salt. The solvent plays a crucial role in dissolving ions, which enables the transport of lithium ions through the electrolyte as they migrate along the polymer chains. This sequential movement facilitates the efficient directional transport of lithium ions, as shown in Figure 3. The gel polymer electrolyte consists of a complex microporous network formed by a polymer matrix, plasticizers, and compatible lithium salts. The solvent enables ion dissolution, allowing lithium ions to migrate through the electrolyte as the polymer chains move, ultimately facilitating the directional transport of lithium ions. The lithium salts within the electrolyte are responsible for conductivity, while the polymer provides mechanical strength to the electrolyte. Additionally, the electrolyte can act as a plasticizer within the polymer matrix, lowering the glass transition temperature and thereby enhancing the ionic conductivity of the battery. The safety of gel-electrolytes is influenced by the degree of fluid retention in the polymer. At the interface with the electrodes, the electrochemical stability of liquid-electrolytes is significantly lower than that of solid polymer electrolytes, resulting in a lower decomposition potential for gel-electrolytes.

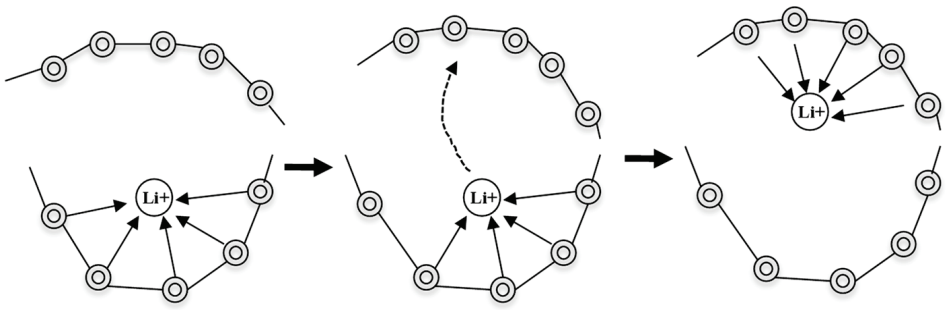

Figure 3. Lithium-ion transport in the gel-electrolyte.

2.2. Mechanism Analysis of ISCs

Under complex and severe conditions such as mechanical, electrical, and thermal abuse, gel-electrolyte lithium-ion batteries may suffer ISCs [23]. As the internal temperature of a lithium-ion battery rises, it can trigger a variety of reactions among the electrode materials, electrolyte, and gel matrix. This phenomenon serves as an early warning sign of potential ISCs. Should the temperature continue to escalate, it may further exacerbate the development of these ISCs. Such short circuits can occur at any point during the battery's operational cycle. Based on the observable characteristics of the battery's behavior, ISCs can be classified into early stage, middle stage, and final stage [24,25], as shown in Figure 4. Different stages of ISCs have significant differences in thermal and electrical characteristics, and the development speed of ISCs varies. The characteristics of the three stages are mainly as follows:

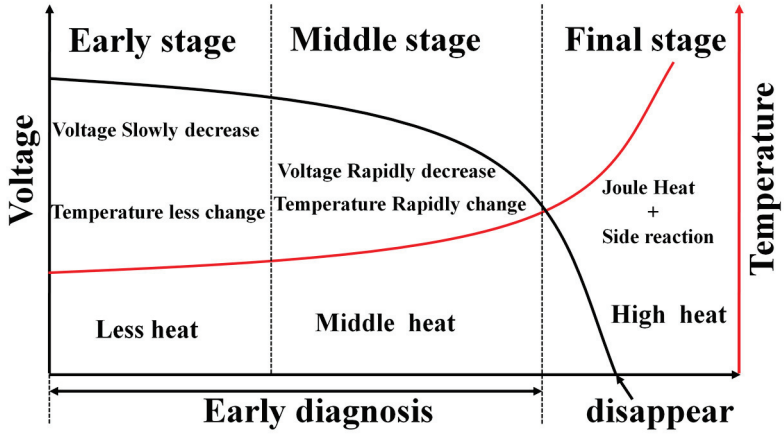

Figure 4. Battery ISC stage.

Early stage: The resistance of the internal short-circuit resistor is high, the voltage drop of the battery is slow, the Joule heating power is small, and the additional heat generated can be completely diffused, so the temperature of the battery remains basically unchanged. The voltage characteristics of the battery can be detected on a long-term scale. The development of short circuits during this stage is slow, occupying most of the entire evolution process. Inspection during this stage is difficult and often can only be achieved by observing the voltage characteristics of the battery.

Middle stage: After a period of development, the resistance of the internal short circuit decreases, and the self-discharge current gradually increases, accompanied by an increase in heating power and an increase in voltage drop rate. At this point, the heat generated by the internal short circuit cannot be dissipated by the battery in a timely manner, resulting in a significant increase in battery temperature. At this stage, the heating and voltage changes in the battery are very obvious, and the heating will accelerate the aging of the battery, causing chemical reactions or decomposition between the electrode material and the electrolyte. The diaphragm will also be affected by temperature, resulting in performance degradation or even deformation. Therefore, the occurrence rate of short circuits during this stage is very fast, often in an exponential form over time. The internal short circuit at this stage can be evaluated through electrical and thermal characteristics, and it is relatively simple.

In the final stage, as the battery structure is damaged, the internal short-circuit resistance further decreases, resulting in a further increase in heating power. Due to the increase in heat generation, the temperature of the battery further rises. When it reaches a specific limit, the separator decomposes and collapses, causing extensive contact between the positive and negative electrodes of the battery. This leads to a sudden increase in

heating power, triggering reactions and decomposition between the electrode material and the electrolyte depth, and causing thermal runaway of the battery. At this stage, the voltage of the battery will experience a significant drop, even to 0 V, and energy will be released instantly, often leading to fire and explosion, with very obvious characteristics. The internal short circuit at this stage is no longer meaningful for detection.

2.3. Analysis of the ISC Process Principle

During the use of lithium batteries, electronic pathways are formed inside, leading to internal short circuits. During the manufacturing process, if metal impurities are accidentally mixed into the electrode material, or if burrs are formed on the edges of the current collector due to cutting, internal short circuits may occur [26]. During the service process, lithium batteries usually face complex and diverse environments. Charging at low temperatures or undergoing high-rate charging can lead to lithium precipitation and growth at the negative electrode of the battery. If it pierces the separator, it will form an internal short circuit [27]. As Figure 5 shows, the mechanism process of internal short circuit caused by overcharging in lithium batteries, Figure 5a shows overcharge, Figure 5b shows SEI film thickening, Figure 5c shows lithium plating with deformation, and Figure 5d shows ISC occurrence. Overcharging can cause structural damage or even collapse of the positive electrode active material, accelerating the aging rate of the battery while increasing the internal resistance, resulting in an increase in Joule heat inside the battery and causing an increase in internal temperature. As Figure 5d shows, when lithium plating penetrate the separator, as shown in the red box of the figure, it will trigger a reaction between the electrolyte and the electrode material. When the temperature continues to rise to the tolerance value of the separator, the separator will shrink or dissolve, leading to internal short circuit [28–30].

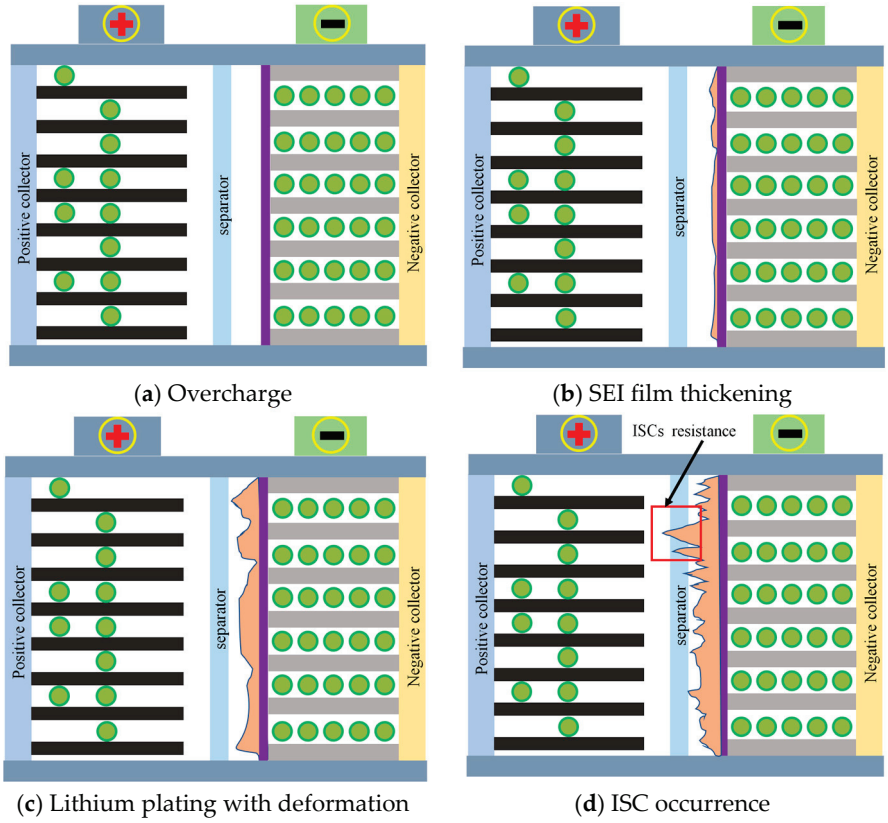

(**a**) Overcharge (**b**) SEI film thickening

(**c**) Lithium plating with deformation (**d**) ISC occurrence

Figure 5. ISC process.

The external and internal short circuits of batteries have similarities in terms of thermal runaway paths. Both external and internal short circuits are triggered by low impedance paths, resulting in a sudden increase in current. At the same time, the abnormal characteristics of the voltage curve generated by external short circuits, such as sustained low voltage, are highly consistent with the mid-term evolution stage of internal short circuits [31,32], as shown in Figure 6a,b. Therefore, external short circuit experiments can be used to simulate the risk of internal short circuits and establish correlation models and safety assessment methods.

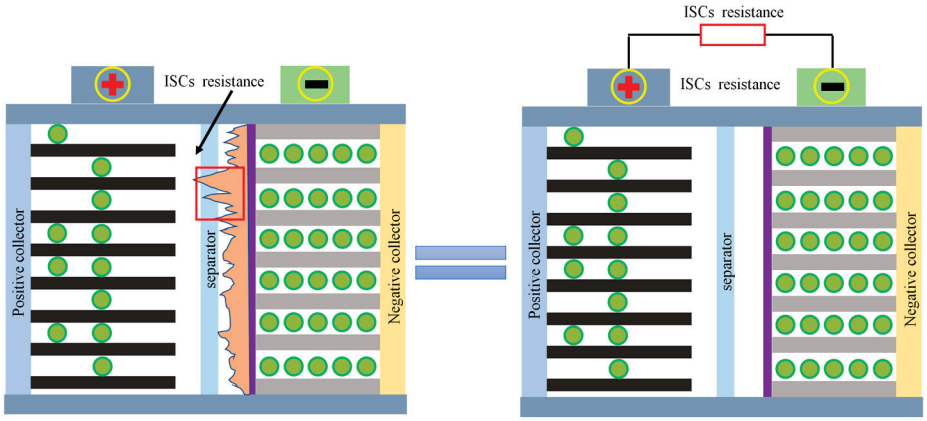

(**a**) ISCs (**b**) External short circuits

Figure 6. ISCs and external short circuits.

3. Coupling Model

3.1. Electrochemical Model

The gel-electrolyte lithium-ion batteries were composed of the positive electrode material and the negative electrode material. The positive electrode material is NCM811, the negative electrode material is graphite (Li_xC_6), and the electrolyte is composed of EC: DMC solvent with a volume ratio of 1:2, p (VdF HFP), and 2M $LiPF_6$ for simulation.

(1) Solid phase and liquid phase lithium ion diffusion process

Solid phase:

The mass balance of lithium ions in the active solid material particles of the battery is controlled by Fick's second law:

$$\frac{\partial c_{s,i}}{\partial t} = D_{s,i}\frac{1}{r^2}\frac{\partial}{\partial r}\left(r^2\frac{\partial c_{s,i}}{\partial r}\right) \tag{1}$$

where $i = p$ is the negative electrode and $i = n$ is the positive electrode. $c_{s,i}$ is the concentration of Li^+ within the active electrode particle, $D_{s,i}$ is the diffusion coefficient of lithium-ions in the solid phase, $r \in (0, R_{s,i})$ is the radial coordinate of the active particle, and $R_{s,i}$ is the radius of the assumed spherical particle.

Boundary conditions:

$$\begin{cases} -D_{s,i}\frac{\partial c_{s,i}}{\partial r}\Big|_{r=0} = 0, (particle\ center) \\ -D_{s,i}\frac{\partial c_{s,i}}{\partial r}\Big|_{r=R_{s,i}} = \frac{j_n}{a_s F}, (particle\ surface) \end{cases} \tag{2}$$

where j_n is the local electrofluid density, a_s is the specific surface area of the active electrode particles, and F is the Faraday constant.

Liquid phase:

https://doi.org/10.3390/batteries12020045

The material balance of the electrolyte in the liquid phase is as follows:

$$\varepsilon_i \frac{\partial c_i}{\partial t} = D_i^{eff} \frac{\partial^2 c_i}{\partial x^2} - \frac{i_i \cdot \nabla t_+}{F} + \frac{(1-t_+)}{F} j_n, (i = p, s, n) \tag{3}$$

where $i = s$ is the separator and the pore wall flux equals zero at the separator.

Boundary conditions:

$$-D_p^{eff} \frac{\partial c_p}{\partial x}\bigg|_{x=0} = 0, -D_n^{eff} \frac{\partial c_n}{\partial x}\bigg|_{x=L} = 0 \tag{4}$$

where ε_i is the volume fractions of the negative electrode, electrolyte, and positive electrode. $D_i^{eff} = D_i(\varepsilon_i)^{Brugg}$ is the effective diffusion coefficient of the liquid phase. x is the transverse coordinate variable. t_+ is the Li^+ transference number, and $L_n + L_s + L_p = L$ is the sum of the thicknesses of the positive electrode, negative electrode, and separator layers.

The concentration and flux of the electrolyte are continuous, as shown below.

$$\begin{cases} c_p\big|_{x=L_p^-} = c_s\big|_{x=L_p^+} \\ c_s\big|_{x=(L_p+L_s)^-} = c_n\big|_{x=(L_p+L_s)^+} \\ -D_p^{eff} \frac{\partial c_p}{\partial x}\big|_{x=L_p^-} = -D_s^{eff} \frac{\partial c_s}{\partial x}\big|_{x=L_p^+} \\ -D_s^{eff} \frac{\partial c_s}{\partial x}\big|_{x=(L_p+L_s)^-} = -D_n^{eff} \frac{\partial c_n}{\partial x}\big|_{x=(L_p+L_s)^+} \end{cases} \tag{5}$$

For gel-electrolyte lithium-ion batteries, $t_+ = 0.6$, and gel-electrolytes exhibit lower ion diffusion coefficients compared to liquid-electrolytes, which significantly impacts lithium-ion transmission rates and polarization behavior.

For gel-electrolyte lithium-ion batteries, $D_i = 5 \times 10^{-11}$ (m^2/s). The enhanced ion mobility in gel-electrolytes can restrict anion movement, thereby mitigating salt depletion under high current conditions.

For gel-electrolyte lithium-ion batteries, $\varepsilon_e = 0.1$. Gel-electrolytes fill and occupy electrode pores, leading to a reduction in effective liquid space within the electrode structure.

(2) Solid phase and liquid phase electric potential distribution

Solid phase:

The electric potential distribution in the solid phase is governed by Ohm's law:

$$\sigma_i^{eff} \frac{\partial^2 \phi_{s,i}}{\partial x^2}\bigg|_{x=0} = j_n, (i = p, n) \tag{6}$$

Boundary conditions:

$$\begin{cases} -\sigma_p^{eff} \frac{\partial \phi_{s,p}}{\partial x}\big|_{x=0} = I_{app}, (collector\ to\ negative\ electrode) \\ -\sigma_p^{eff} \frac{\partial \phi_{s,p}}{\partial x}\big|_{x=L_p} = -\sigma_n^{eff} \frac{\partial \phi_{s,n}}{\partial x}\big|_{x=L_p+L_s} = 0, (electrode\ to\ separator) \end{cases} \tag{7}$$

where I_{app} is the current density of the battery.

For gel-electrolyte lithium-ion batteries, the potential of the solid phase at the positive electrode of the battery is set to zero.

$$\phi_{s,n}\big|_{x=L_p+L_s+L_n} = 0 \tag{8}$$

liquid phase:

The expression for the charge balance in the battery based on Ohm's law is as follows:

$$\begin{cases} j_n = -\frac{\partial}{\partial x}(\kappa_i^{eff}\nabla\phi_{e,i}) + \frac{2RT\kappa_i^{eff}}{F}(1-t_+)\left(1+\frac{\partial \ln f_\pm}{\partial \ln c_{e,i}}\right)\frac{\partial}{\partial x}\left(\frac{\partial \ln c_{e,i}}{\partial x}\right), (i=p,s,n) \\ \kappa_i^{eff} = \kappa\varepsilon_i^{Brugg} \end{cases} \quad (9)$$

where κ_i^{eff} is the effective Li^+ conductivity, R is the gas constant, T is the temperature of the lithium-ion battery, $f_\pm$ is the molar activity coefficient, and κ is the Li^+ conductivity in the liquid phase.

For gel-electrolyte lithium-ion batteries, at the terminals of the battery, there is no charge flux in the liquid phase:

$$-\kappa_p^{eff}\frac{\partial\phi_{e,p}}{\partial x}\bigg|_{x=0} = -\kappa_n^{eff}\frac{\partial\phi_{e,n}}{\partial x}\bigg|_{x=L_p+L_s+L_n} = 0 \quad (10)$$

(3) Solid phase and liquid phase interface reaction

Behavior at these interfaces is determined by the Butler–Volmer equation:

$$j_n = a_s i_o\left[\exp\left(\frac{\alpha_n F}{RT}\eta\right) - \exp\left(-\frac{\alpha_p F}{RT}\eta\right)\right] \quad (11)$$

where i_o is the exchange current density, α_n is the transfer coefficient of the electrochemical reaction at the positive electrode, α_p is the transfer coefficient of the electrochemical reaction at the negative electrode, which is typically taken as 0.5, and η is the overpotential.

For gel-electrolyte lithium-ion batteries, i_o depends on the lithium concentration in the electrolyte and the solid active substance, which is as follows:

$$i_o = F(k_p)^{\alpha_n}(k_n)^{\alpha_p}(c_{s,\max}-c_s)^{\alpha_n}(c_s)^{\alpha_p}\left(\frac{c_e}{c_{e,ref}}\right)^{\alpha_n} \quad (12)$$

where $k_p = k_n = 0.04$ (m/s). The reaction rate constants for gel-electrolytes are typically one order of magnitude lower than those of liquid-electrolytes.

(4) Battery terminal voltage

Battery terminal voltage $V(t)$ can be expressed as:

$$V(t) = \phi_s|_{x=L} - \phi_s|_{x=0} \quad (13)$$

3.2. Thermal Model

The internal heat sources of gel-electrolyte lithium-ion batteries mainly comprise reversible heat, irreversible heat, and heat generated from ISCs. Battery heat energy conservation equation:

$$\rho_c c_{pc}\frac{\partial T}{\partial t} = \nabla\cdot k_c\nabla T + Q_{irr} + Q_{rev} + Q_{ohm} + Q_a \quad (14)$$

where ρ_c and c_{pc} arerespectivelythe density of the battery and the specific heat capacity. T is the battery temperature. k_c is the thermal conductivity of the battery. Q_{irr} is irreversible heat. Q_{rev} is reversible heat generation. Q_{ohm} is ohm heat. Q_a is the secondary heat exchanger.

For gel-electrolyte lithium-ion batteries, $c_{pc} = 2$ (J/(kg·K)). Gel-electrolyte lithium-ion batteries have higher specific heat capacity than liquid-electrolyte batteries.

https://doi.org/10.3390/batteries12020045

Due to the multilayer structure of gel-electrolyte lithium-ion battery, its thermal conductivity varies in different directions, where L_i is the thickness of each layer:

$$\begin{cases} k_{c,x} = \dfrac{|x|}{r}\dfrac{\sum L_i}{\sum L_i/k_{c,i}} + \dfrac{|y|}{r}\dfrac{\sum L_i k_{c,i}}{\sum L_i} \\ k_{c,y} = \dfrac{|y|}{r}\dfrac{\sum L_i}{\sum L_i/k_{c,i}} + \dfrac{|x|}{r}\dfrac{\sum L_i k_{c,i}}{\sum L_i} \\ k_{c,z} = \dfrac{\sum L_i k_{c,i}}{\sum L_i} \end{cases} \tag{15}$$

$$\begin{cases} Q_{irr} = J_n(\phi_s - \phi_e - U_{ref}(\theta)) \\ Q_{rev} = J_n * T * \frac{\partial U_{ref}(\theta)}{\partial T} \\ Q_{ohm} = \sigma^{eff}\nabla\phi_s \cdot \nabla\phi_s + (k^{eff}\nabla\phi_e \cdot \nabla\phi_e + \frac{2RTk^{eff}}{F}(1 + \frac{\partial \ln f_{\pm}}{\partial \ln c_e})\nabla \ln c_e \cdot \nabla\phi_e) \end{cases} \tag{16}$$

The heat generation equation for gel-electrolyte lithium-ion battery side reactions is established based on the Arrhenius equation. the total heat generation from side reactions, Q_a can be expressed as follows:

$$Q_a = Q_{sei} + Q_{ne} + Q_{pe} + Q_e \tag{17}$$

where Q_{sei} is the SEI decomposition heat, Q_{ne} is the negative electrode and the electrolyte, Q_{pe} is positive electrode and the electrolyte reaction, and Q_e is decomposition of the electrolyte.

The metastable components of the SEI layer begin to exothermically decompose at approximately 90 °C. The reaction rate R_{sei} of this exothermic decomposition reaction can be expressed as follows:

$$R_{sei} = A_{sei}\exp\left(-\frac{E_{a,sei}}{RT}\right)c_{sei}^{m_{sei}} \tag{18}$$

where A_{sei} is the frequency factor for SEI decomposition; $E_{a,sei}$ is the activation energy of the reaction; c_{sei} is the dimensionless concentration of the metastable lithium-containing species within the SEI layer; and m_{sei} is the reaction order.

Q_{sei} is side reaction heat of SEI decomposition, and C_{sei} is the change rate, which can be expressed as follows:

$$\begin{cases} Q_{sei} = H_{sei}W_c R_{sei} \\ \frac{dc_{sei}}{dt} = -R_{sei} \end{cases} \tag{19}$$

where H_{sei} is specific heat release, and W_c is specific carbon content.

Negative reaction:

At temperatures exceeding 120 °C, the intercalated lithium within the negative electrode interacts with the gel-electrolyte. The rate R_{ne} of negative electrode reaction is formulated as follows:

$$R_{ne} = A_{ne}\exp(-\frac{t_{sei}}{t_{sei,ref}})\exp(-\frac{E_{a,ne}}{RT})c_{ne}^{m_{ne}} \tag{20}$$

where A_{ne} is the decomposition frequency factor, $E_{a,ne}$ is the activation energy of the reaction, t_{sei} is the thickness of SEI layer, c_{ne} is dimensionless concentration of lithium in the negative electrode, and m_{ne} is the reaction order.

For gel-electrolyte lithium-ion batteries, $A_{ne} = 2 \times 10^{10}$ (S^{-1}). Gel-electrolyte lithium-ion batteries reduce this factor by 1–2 orders of magnitude, blocking interface contact and mass transfer.

Positive reaction:

https://doi.org/10.3390/batteries12020045

At more than 170 °C, the positive has an exothermic decomposition reaction due to accepting a higher temperature. And then the released oxygen directly reacts with the battery electrode to release a lot of heat. The positive reaction rate R_{pe} is as follows:

$$R_{pe} = A_{pe}\alpha^{m_{pe}}(1-\alpha)^{m_{pe}}\exp(-\frac{E_{a,pe}}{RT}) \tag{21}$$

where A_{pe} is the decomposition frequency factor, $E_{a,pe}$ is the activation energy of the reaction, α is the conversion rate of positive active substance, and m_{pe} is the reaction order.

For gel-electrolyte lithium-ion batteries, $A_{pe} = 3.5 \times 10^{13}$ (S^{-1}). Gel-electrolyte lithium-ion batteries reduce this factor by 1–3 orders of magnitude, crucial for restraining thermal runaway.

Gel-electrolyte decomposition:

The decomposition of the remaining electrolyte usually begins above 250 °C, and the reaction rate R_e is as follows:

$$R_e = A_e \exp\left(-\frac{E_{a,e}}{RT}\right)c_e^{m_e} \tag{22}$$

where A_e is the decomposition frequency factor, $E_{a,e}$ is the activation energy of the reaction, c_e is the dimensionless concentration of electrolyte, and m_e is the reaction order.

For gel-electrolyte lithium-ion batteries, $A_e = 5.14 \times 10^{25}$ (S^{-1}). Gel-electrolyte lithium-ion batteries have a greatly reduced decomposition frequency factor due to the polymer network binding reactants and slowing PEO and other polymer thermal decomposition.

For gel-electrolyte lithium-ion batteries, $E_{a,e} = 300$ (kJ/mol). Gel-electrolyte lithium-ion batteries require additional energy to break polymer covalent bonds, increasing apparent activation energy.

Convection heat transfer and radiation heat transfer on the battery surface are considered, and the following relationships are given.

$$\begin{cases} q_{conv} = h(T_s - T_{amb}) \\ q_{rad} = \varepsilon\sigma(T_s^4 - T_{amb}^4) \end{cases} \tag{23}$$

where q_{conv} and q_{rad} are the convective heat flux at boundary and the radiative heat flux and T_s and T_{amb} are battery surface temperature and the ambient temperature. h is the convection heat transfer coefficient, ε is the radiation coefficient of the lithium battery surface, and σ is the Stefan-Boltzmann constant.

3.3. ISC Model

At different ISC situations, short-circuit current path or thermal path may vary, and so it is difficult to clarify the mechanism. However, different ISCs share common characteristics: the electron current flows from the positive collector to the negative collector, and the heat generated during the short circuit accumulates in the vicinity of the short circuit region before dissipating outward. Based on these observations, the short circuit can be simulated by introducing a short circuit region, as shown in Figure 7.

The short-circuit region of the battery is conductive. The current passing through the short-circuit region can vary depending on the resistance. If the resistance of the short-circuit area is known, the short-circuit current and Joule heating generated are as follows:

$$I_{short} = \iiint_{n.or.p} J_n dv \tag{24}$$

https://doi.org/10.3390/batteries12020045

where I_{short} is the battery short-circuit current, n and p are, respectively, the positive electrode and the negative electrode, and v is the battery volume.

$$Q_{short} = I_{short}^2 R_{short} \tag{25}$$

where Q_{short} is joule heating generated by a short circuit in the battery; R_{short} is the short circuit resistance in the battery.

As a result, the electron current between the active materials and the short-circuit region can be considered negligible. Under these conditions, the short circuit resistance is as follow.

$$R_{short} = \frac{L_{short}}{\sigma_{short} \pi r_{short}^2} \tag{26}$$

where L_{short} is length of the short circuit region, σ_{short} is the conductivity of short-circuit region, and r_{short} is the radius of the region.

For gel-electrolyte lithium-ion batteries, the magnitude of the short-circuit resistance serves as an indicator of whether the battery has undergone a significant ISC. When ISC failures occur, key parameters such as voltage, current, temperature, SOC, and capacity will also exhibit corresponding changes.

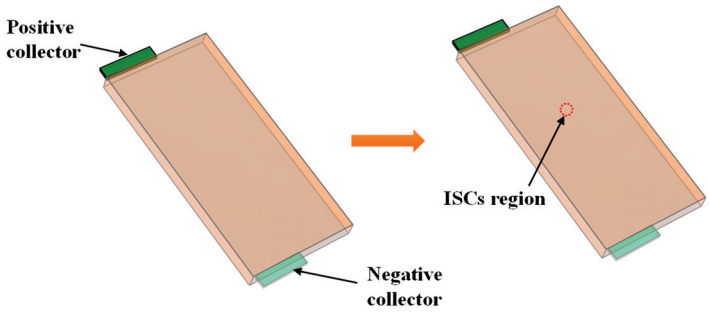

Figure 7. Battery ISC structure.

3.4. Electrochemical–Thermal–ISC Coupling Model

A coupling relationship among the electrochemical, thermal, and ISCs characteristics of lithium-ion batteries has been established, as shown in Figure 8.

When ISC failures occur, a significant amount of heat is released internally. The internal resistance of the battery during the short circuit decreases. Consequently, a coupling relationship emerges between the electrochemical and thermal models.

$$U_p^{ref} = Eeq_\text{int}1(soc) + dEeqdT_\text{int}1(soc) * (T - 298[K]) \tag{27}$$

$$U_n^{ref} = Eeq_\text{int}2(soc) + dEeqdT_\text{int}2(soc) * (T - 298[K]) \tag{28}$$

where Eeq_int1 is the positive initial equilibrium potential, SOC is the battery charged state, $dEeqdT$_int1 is the positive equilibrium potential temperature derivative, Eeq_int2 is the negative initial equilibrium potential, and $dEeqdT$_int1 is the negative equilibrium potential temperature derivative.

$$\begin{cases} D_n = 1.4523 \times 10^{-13} \times e^{\left(\frac{68025.7}{8.314 \times (\frac{1}{318[K]} - \frac{1}{T})}\right)} \\ D_p = 5 \times 10^{-13} \times e^{\left(1200 \times (\frac{1}{298[K]} - \frac{1}{T})\right)} \\ D_{ele} = DL_\text{int}3(c) \times e^{\left(\frac{16500}{8.314 \times (\frac{1}{298[K]} - \frac{1}{T})}\right)} \end{cases} \tag{29}$$

https://doi.org/10.3390/batteries12020045

where D_n is negative electrode, D_p is positive electrode, D_{ele} is electrolyte diffusion coefficient, DL_int3 is the electrolyte interpolation function, and the parameters are derived from the finite element simulation software.

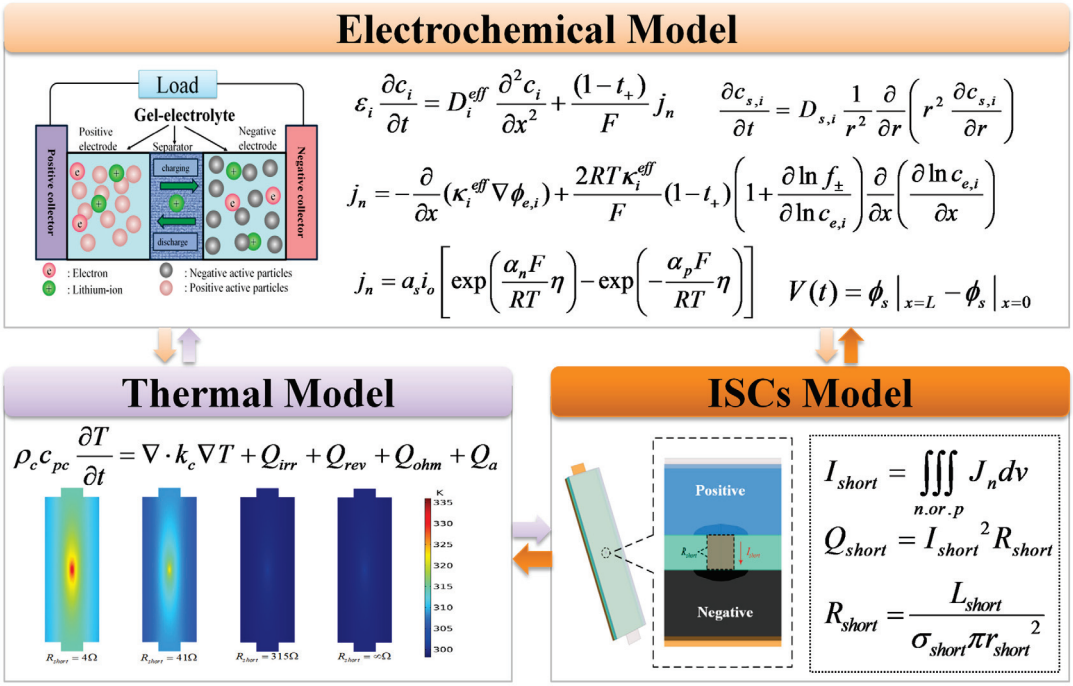

Figure 8. Electrochemical–thermal–ISC coupling.

4. Model Validation

Experimentally measuring the ISC characteristics of gel-electrolyte lithium-ion batteries validates ISC model accuracy. Battery is gel-electrolyte lithium-ion batteries, with positive materials—$Li[Ni_{0.8}Co_{0.1}Mn_{0.1}]O_2$—and negative materials—$Li_xC_6$. The schematic diagram of the ISC experiment is shown in Figure 9.

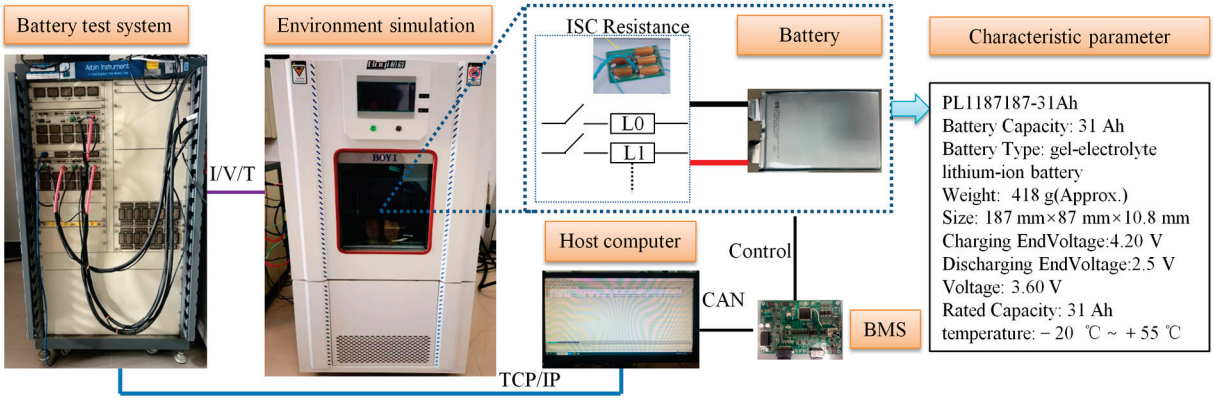

Figure 9. Experimental.

In order to verify the accuracy of the model and ensure the time and safety of the test, the test is carried out under the short-circuit resistance of 315 Ω. Battery voltage at four discharge multipliers is measured: 0.18 C, 0.33 C, 0.5 C and 1 C. Battery discharge voltage curve with different rates based on ISC model is simulated. The curves of simulation and test battery voltage as well as the comparative error curves are shown in Figure 10. The error is basically within 40 mV.

https://doi.org/10.3390/batteries12020045

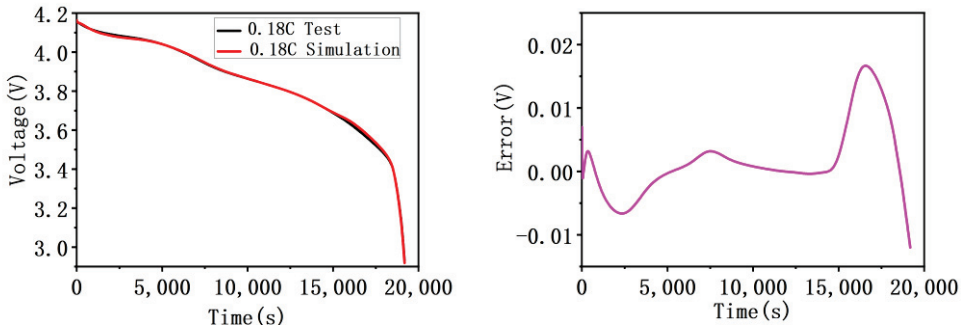

(**a**) 0.18C Test and Simulation

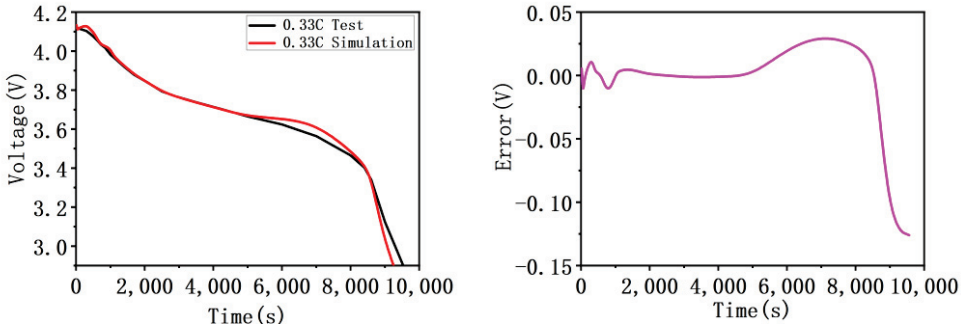

(**b**) 0.33C Test and Simulation

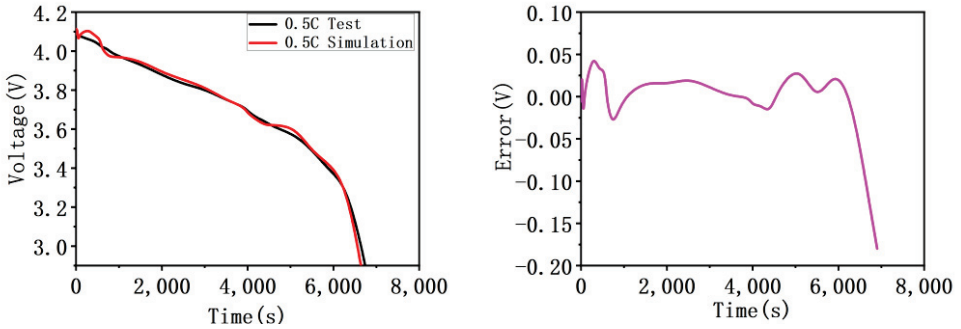

(**c**) 0.5C Test and Simulation

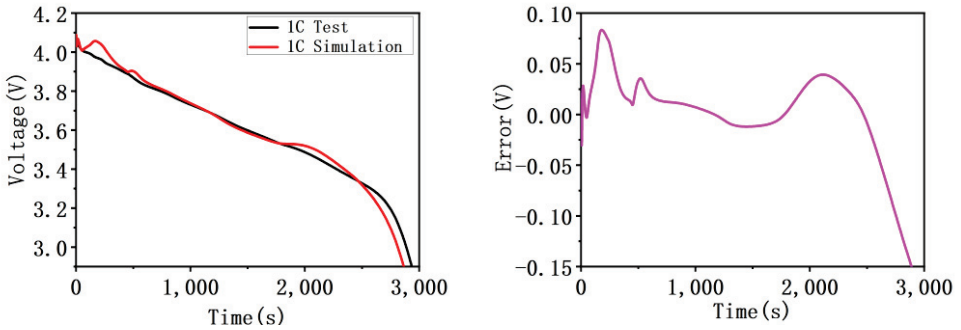

(**d**) 1C Test and Simulation

Figure 10. Simulation and test battery voltage.

Measurement of battery voltage at 1 C. Simulation of battery discharge temperature with 1 C rate based on ISC model. The curves of simulation and test battery voltage as well as the comparative error curves are shown in Figure 11. The error is basically within 0.5 °C.

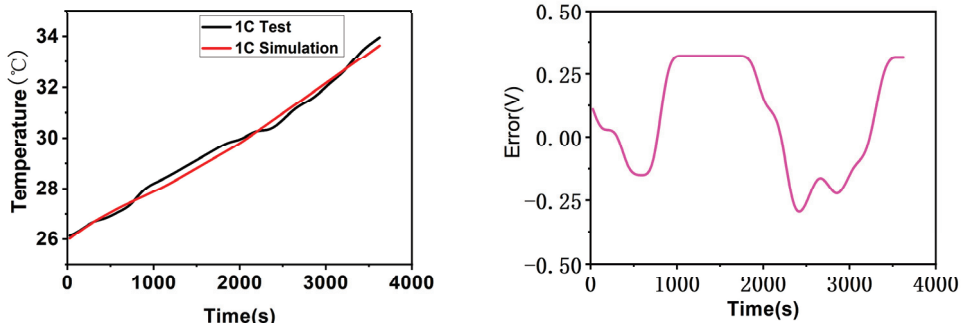

Figure 11. Simulation and test battery temperature.

Calculate the MAE of simulation voltage and test voltage, and simulation temperature and test temperature separately. The maximum voltage MAE is 25 mv, and the temperature MAE is 0.22 °C, as shown in Table 1.

Table 1. Voltage and temperature MAE.

Type	Charge/0.18 C	Charge/0.33 C	Charge/0.5 C	Charge/1 C	Temperature/1 C
MAE	0.0034 V	0.018 V	0.021 V	0.025 V	0.22 °C

5. Datasets Acquisition

The classification boundaries for ISCs in lithium-ion batteries are critical for the detection and diagnosis of battery faults [15]. Select Rshort equal to 315 Ω, 41 Ω and 4 Ω as the critical points for the severity of internal short circuits. At R_{short} = 315 Ω, the battery loses 15% of its power during self-discharge for 28 days. At R_{short} = 41 Ω, the battery loses 100% of its power due to self-discharge over a period of 28 days. At R_{short} = 4 Ω, the battery loses 100% of its power due to self-discharge over a period of 7 days. The critical points for short circuit classification are shown in Figure 12.

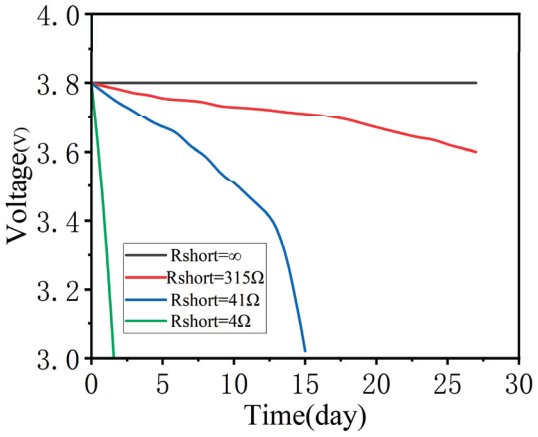

Figure 12. Battery characteristics in case of internal short circuit.

In this paper, four distinct levels are defined: L0, L1, L2, and L3, representing normal condition, Class I, Class II, and Class III severity, respectively. The higher the level, the more severe the ISCs. The level classifications are shown in Table 2.

https://doi.org/10.3390/batteries12020045

Table 2. ISC level.

ISC R_{short} Range (Ω)	Level
Up to 315	L0
41~315	L1
4~41	L2
0~4	L3

Based on ISC model, a parameterized scanning simulation acquires a total of 1215 datasets of charge/discharge, which include voltage (V), current (A), temperature (T), and SOC. ISC dataset acquisition structure diagram is shown in Figure 13.

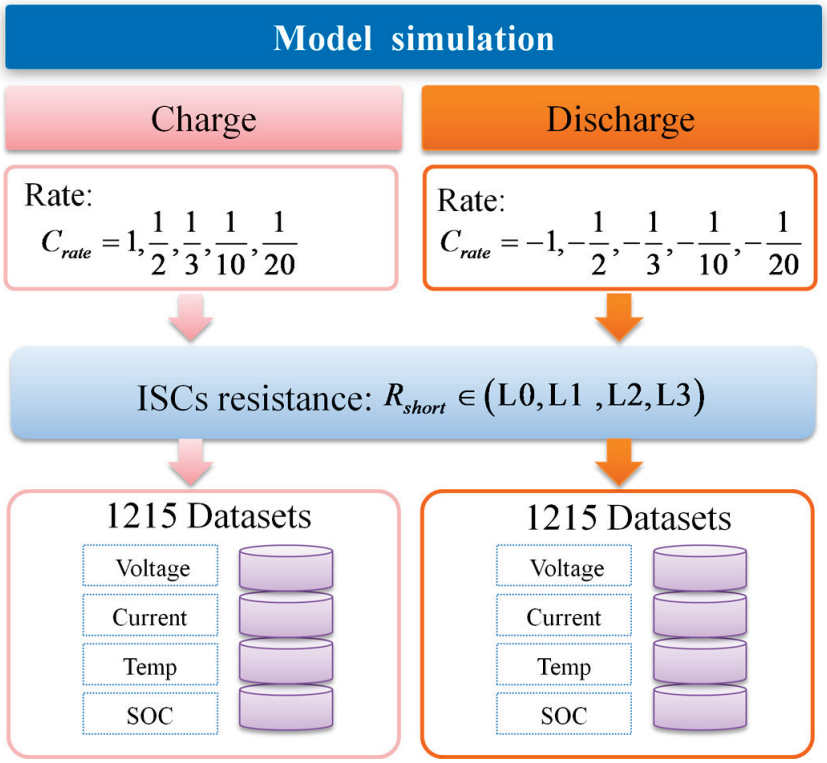

Figure 13. ISC datasets acquisition structure diagram.

6. Methods for ISC Prediction and Results

6.1. BP-CNN-LSTM ISC Prediction Model

BP ISC prediction model includes input layer, output layer, and hidden layer, and there is weight control between each node between each layer. CNN ISC prediction model includes input layer, convolutional layer, fully connected layer, and an output layer. LSTM ISC prediction model stores long-term information through a cell state and uses input gates, output gates, and forget gates to control information updates, forgetting, and output. The internal structure of prediction model is shown in Figure 14.

In this paper, the charge and discharge dataset is divided into two parts, including training dataset and validation dataset. The parameters of model are shown in Table 3.

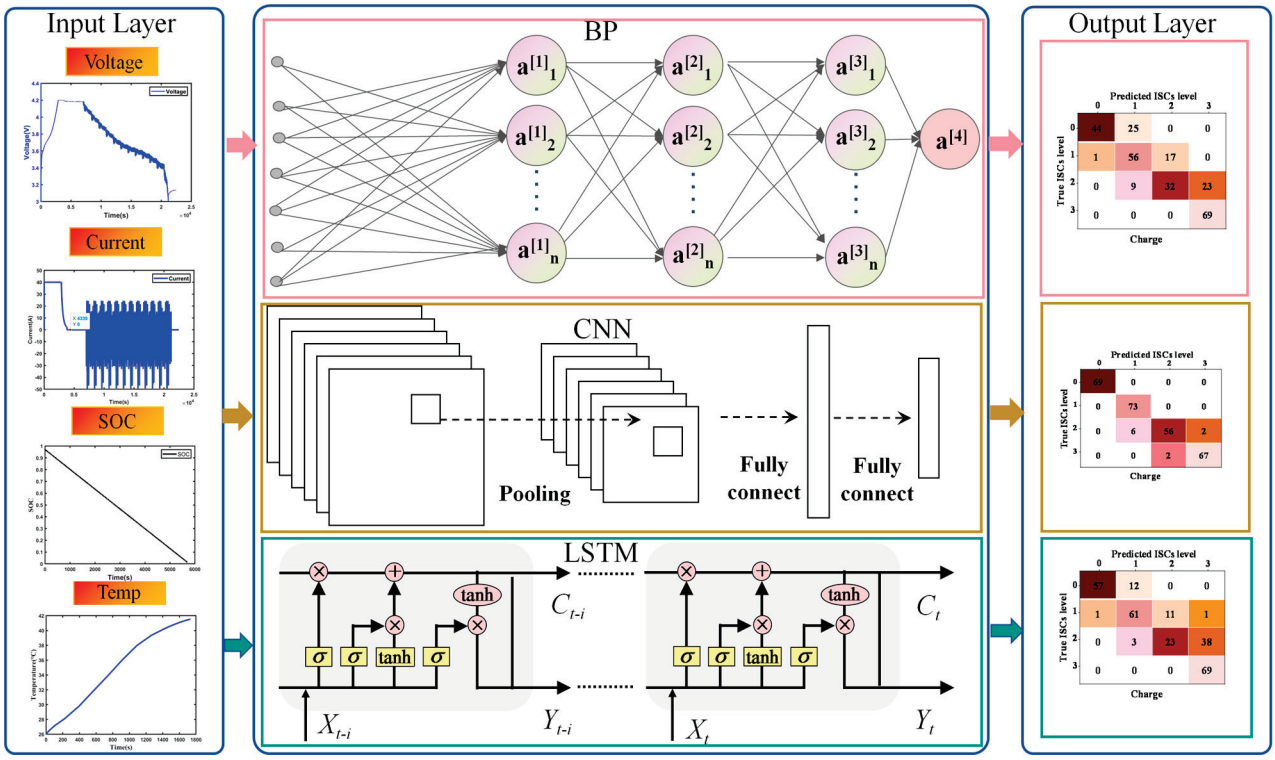

Figure 14. The internal structure of prediction model.

Table 3. Prediction model parameters.

BP	Value	CNN	Value	LSTM	Value
training dataset	939	training dataset	939	training dataset	939
validation dataset	276	validation dataset	276	validation dataset	276
layers	2	layers	4	layers	5
input neurons	1836	input neurons	1836	input neurons	2115
output neurons	4	output neurons	4	output neurons	4
Loss function	SCC	Loss function	MSE	Loss function	SCC
Optimizer	Adam	Optimizer	Adam	Optimizer	Adam
Learning rate	1×10^{-3}	Learning Rate	1×10^{-3}	Learning Rate	1×10^{-4}
Batch size	32	Batch size	32	Batch size	20
Training cycle	400	Training cycle	400	Training cycle	400

6.2. Prediction Results

The prediction algorithm is divided into charging and discharging states. Input data include voltage, current, temperature, and SOC. Output data are predicted ISC levels. The accuracy and optimization loss are shown in Figure 15. The predicted ISC level classifications are shown in Figure 16.

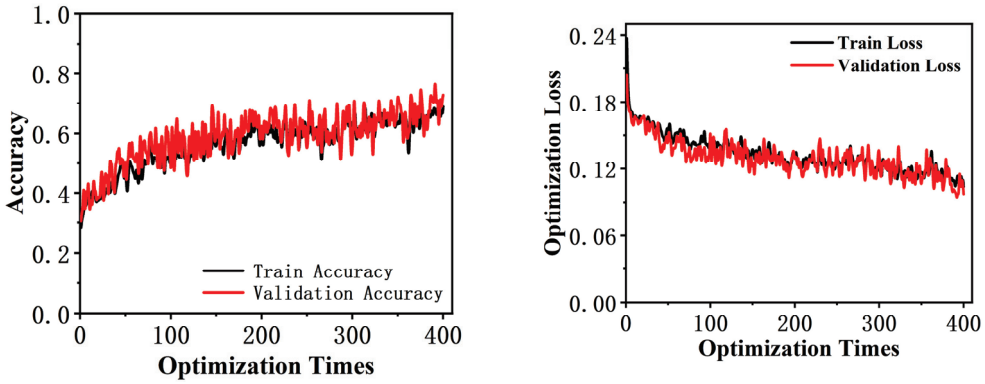

(**a**) BP prediction in the charge state

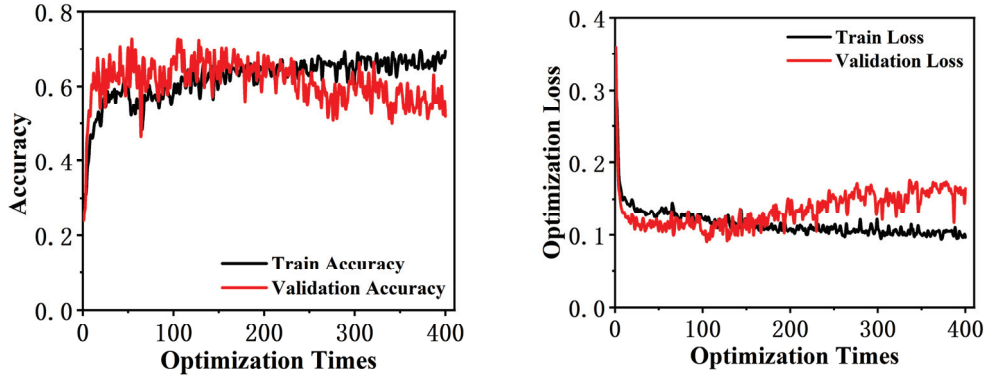

(**b**) BP prediction in the discharge state

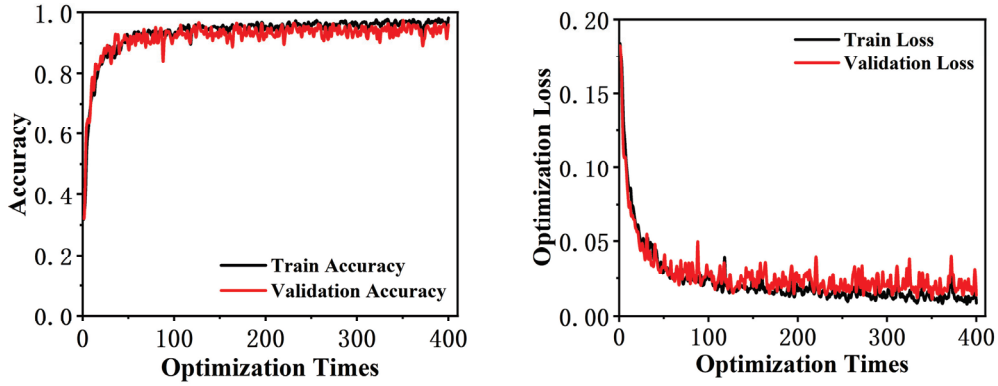

(**c**) CNN prediction in the charge state

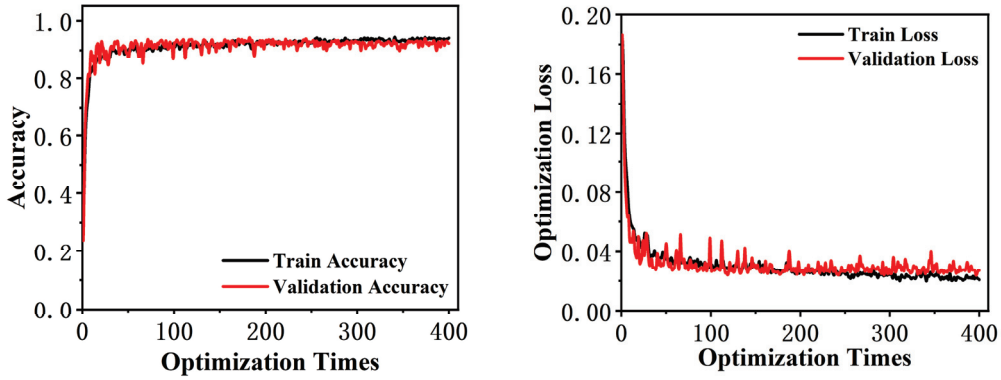

(**d**) CNN prediction in the discharged state

Figure 15. *Cont.*

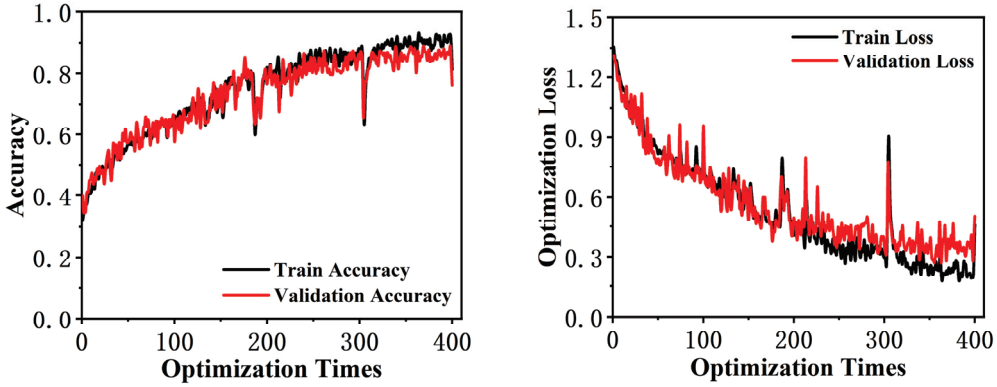

(**e**) LSTM prediction in the charge state

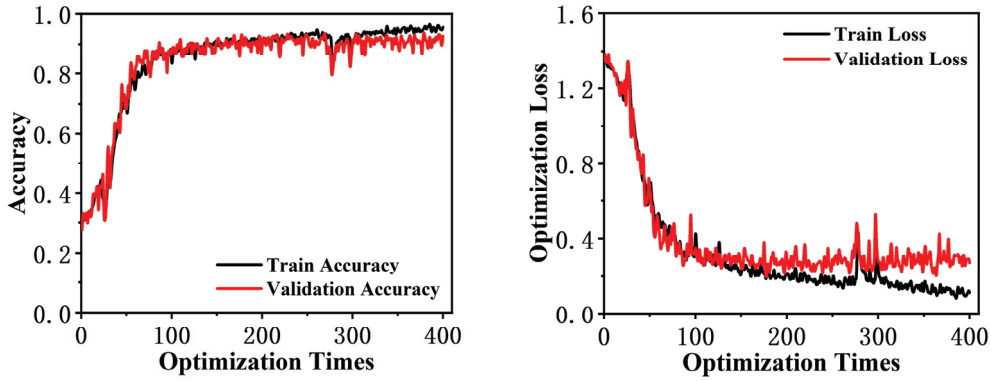

(**f**) LSTM prediction in the discharged state

Figure 15. The accuracy and optimization loss.

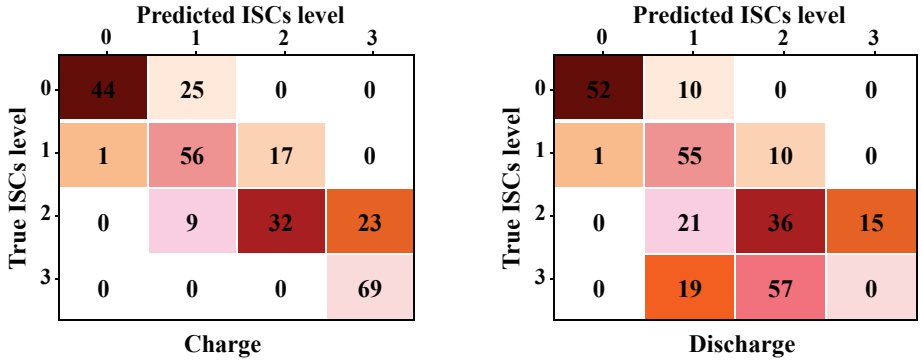

(**a**) BP prediction ISC level

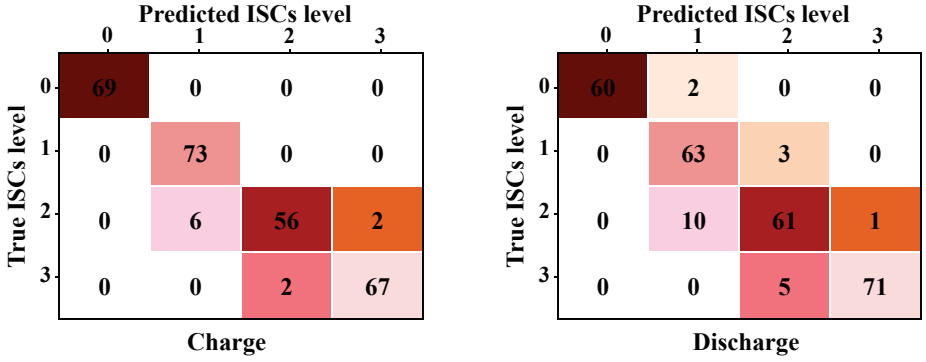

(**b**) CNN prediction ISC level

Figure 16. *Cont.*

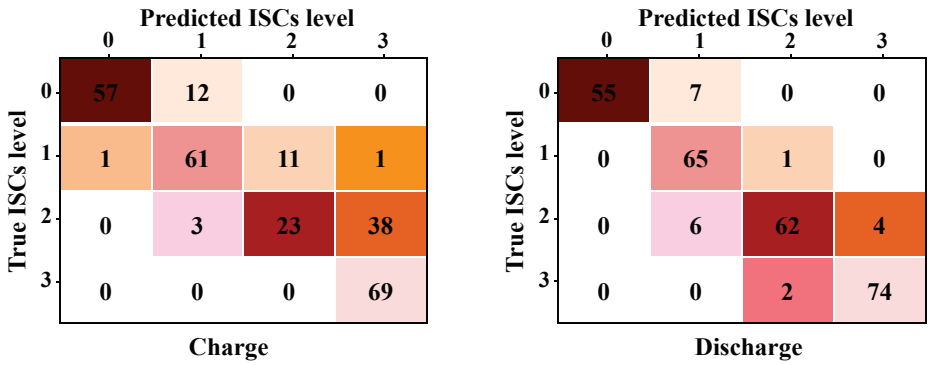

(**c**) LSTM prediction ISC level

Figure 16. Predicted ISC level.

6.3. Discussion

In order to accurately and quantitatively compare ISC prediction algorithms, four evaluation parameters, including model accuracy, precision, recall, and F-value, were used for comparison. Firstly, the test set is defined as $\Phi = \left\{(x^{(1)}, y^{(1)}), \ldots, (x^{(276)}, y^{(276)})\right\}$, with the internal short-circuit level label $y^{(n)} \in \{L3, L2, L1, L0\}$ of the battery. The test set is input into the trained model $f(x, y)$ for testing and classification, and the diagnosed level result is $\left\{\hat{y}^{(1)}, \ldots, \hat{y}^{(276)}\right\}$.

Accuracy refers to the average of the overall classification and prediction performance of the test set, calculated as follows:

$$\mathcal{A} = \frac{1}{276} \sum_{276}^{n=1} I\left(y^{(n)} = \hat{y}^{(n)}\right) \tag{30}$$

$I(\,)$ is the indicator function.

Precision and recall are used to evaluate the prediction capability of each category. For example, if the level is L1, the model classification results may have four types:

(1) True example: The true level of a test sample is L1, and the prediction result of the model is also L1. This test sample size is referred to as:

$$TP_{L1} = \sum_{276}^{n=1} I\left(y^{(n)} = \hat{y}^{(n)} = L1\right) \tag{31}$$

(2) False negative example: If the true level of a test sample is L1, but the model diagnoses a result that is not L1, then the sample size is recorded as:

$$FN_{L1} = \sum_{276}^{n=1} I\left(y^{(n)} = L1 \wedge \hat{y}^{(n)} \neq L1\right) \tag{32}$$

(3) False positive example: If the true level of a test sample is not L1, and the model diagnoses it as L1, then the sample size is recorded as:

$$FP_{L1} = \sum_{276}^{n=1} I\left(y^{(n)} \neq L1 \wedge \hat{y}^{(n)} = L1\right) \tag{33}$$

(4) True negative example: The true level of a test sample is not L1, and the prediction result of the model is also not L1. Such a test sample size is referred to as:

$$TN_{L1} = \sum_{276}^{n=1} I\left(y^{(n)} \neq L1 \wedge \hat{y}^{(n)} \neq L1\right) \tag{34}$$

https://doi.org/10.3390/batteries12020045

The precision is expressed as:

$$P_{L1} = \frac{TP_{L1}}{TP_{L1} + FP_{L1}} \tag{35}$$

The recall is expressed as:

$$\Re_{L1} = \frac{TP_{L1}}{TP_{L1} + FN_{L1}} \tag{36}$$

The accuracy and recall of the prediction model for the severity of internal short circuits in batteries are calculated on an average basis for the overall category, expressed as:

$$P_{macro} = \frac{1}{4} \sum_{L_4}^{L=L_1} P_L \tag{37}$$

$$\Re_{macro} = \frac{1}{4} \sum_{L_4}^{L=L_1} R_c \tag{38}$$

In order to harmonize the average of the overall accuracy and recall of the model, the F-value evaluation parameter is used, expressed as:

$$F = \frac{(1+\beta^2) P_{macro} \Re_{macro}}{P_{macro} + \Re_{macro}} \tag{39}$$

The results of the ISC prediction algorithm comparisons are shown in Table 4.

Table 4. Compared ISC prediction algorithms.

	BP		**CNN**		**LSTM**	
	CH	**DIS**	**CH**	**DIS**	**CH**	**DIS**
Accuracy ($\mathcal{A}$)	72.8%	72.5%	96%	92.4%	76.1%	92.8%
Precision (P_{macro})	74.7%	84.8%	98.8%	97.7%	76.3%	95.3%
Recall ($\Re_{macro}$)	94.1%	84.1%	96.9%	94.8%	96.3%	97.2%
F-value (F)	82.9%	83.5%	97.8%	96.1%	83.8%	96.2%

It can be seen that all three prediction algorithms have good performance, and the CNN has more outstanding prediction ability, which is superior to the others prediction algorithms in various evaluation indicators, with better prediction performance in charge and discharge states.

7. Conclusions

By analyzing the mechanistic characteristics of gel-electrolyte lithium-ion batteries, an electrochemical–thermal–ISC coupling model was developed. Through performance characterization of ISC, several key parameters that best represent battery ISC behavior were selected, including voltage, current, temperature, SOC, capacity loss, and internal resistance. Subsequently, the datasets were preprocessed to meet training requirements. Then, BP, CNN, and LSTM prediction models were developed and compared for accuracy. The results demonstrate that CNN achieves higher accuracy than both BP and LSTM, and this accuracy has been validated through experimental testing. ISCs in batteries exhibit

https://doi.org/10.3390/batteries12020045

potential, complexity, and danger, with a long-term development process. The main innovative contributions of this study are as follows.

(1) The transport mechanism of lithium ions in gelled electrolytes was analyzed. Lithium ions combine with the polymer matrix, and under external force, the polymer chains move. The mutual movement between chains facilitates the directional transport of lithium ions, enabling the normal operation of lithium batteries.
(2) To address the difficulty of developing and implementing a large number of internal short circuit experiments due to the poor repeatability and controllability of traditional battery internal short circuit experiments, a three-dimensional finite element electrochemical–thermal–internal short circuit coupling model for lithium-ion batteries was established. This model replaces real internal short circuit experiments through simulation testing.
(3) ISC prediction model for lithium-ion batteries has been established. The classification level of the severity of internal short circuits in batteries has been defined. ISC prediction model can provide unique insights that traditional simulations find difficult to capture, especially when dealing with complex, dynamic, or high-dimensional problems. It can detect a simulated fault and this modeling approach could be applied to empirical data.

In future work, further consideration needs to be given to battery aging and the impact of actual complex working conditions. At the same time, in reality, batteries may experience multiple faults occurring simultaneously, and these fault characteristics are interrelated. High-precision estimation of ISCs can be achieved through the fusion of intelligent algorithms and hybrid models.

Author Contributions: L.W. (Liye Wang): Writing—original draft, Writing—review and editing, Data curation, Validation, Conceptualization and Methodology. J.W.: Data curation, Writing—review and editing, Investigation, Formal analysis. C.M.: Investigation, Formal analysis. X.S.: Supervision, Conceptualization. L.W. (Lifang Wang): Supervision, Funding acquisition. C.L.: Supervision, Conceptualization. All authors have read and agreed to the published version of the manuscript.

Funding: This work was supported in part by the National Key Research and Development Program of China under Grant (2024YFB2408400), National Natural Science Foundation of China (Grant 52277228), Beijing Natural Science Foundation (L243021).

Data Availability Statement: The original contributions presented in this study are included in the article. Further inquiries can be directed to the corresponding author.

Conflicts of Interest: The authors declare no conflicts of interest.

References

1. Tang, S.; Guo, W.; Fu, Y. Advances in composite polymer electrolytes for lithium batteries and beyond. *Adv. Energy Mater.* **2021**, *11*, 2000802. [CrossRef]
2. Qiao, D.; Wei, X.; Fan, W.; Jiang, B.; Lai, X.; Zheng, Y.; Tang, X.; Dai, H. Toward safe carbon-neutral transportation: Battery internal short circuit diagnosis based on cloud data for electric vehicles. *Appl. Energy* **2022**, *317*, 119168. [CrossRef]
3. Wang, Z.; Hong, J.; Liu, P.; Zhang, L. Voltage fault diagnosis and prognosis of battery systems based on entropy and Z-score for electric vehicles. *Appl. Energy* **2017**, *196*, 289–302. [CrossRef]
4. Jia, Y.; Brancato, L.; Giglio, M.; Cadini, F. Temperature enhanced early detection of internal short circuits in lithium-ion batteries using an extended Kalman filter. *J. Power Sources* **2024**, *591*, 233874. [CrossRef]
5. Christensen, G.; Younes, H.; Hong, H.; Widener, C.; Hrabe, R.H.; Wu, J.J. Nanofluids as media for high capacity anodes of lithium-ion battery—A review. *J. Nanofluids* **2019**, *8*, 657–670. [CrossRef]

6. Xiong, R.; Kim, J.; Shen, W.; Lv, C.; Li, H.; Zhu, X.; Zhao, W.; Gao, B.; Guo, H.; Zhang, C.; et al. Key technologies for electric vehicles. *Green Energy Intell. Transp.* **2022**, *1*, 100041. [CrossRef]
7. Wang, J.; Wang, C.; Wang, W.; Li, W.; Lou, J. Carboxymethylated nanocellulose-based gel polymer electrolyte with a high lithium ion transfer number for flexible lithium-ion batteries application. *Chem. Eng. J.* **2022**, *428*, 132604. [CrossRef]
8. Hadad, S.; Hamrahjoo, M.; Dehghani, E.; Salami-Kalajahi, M.; Eliseeva, S.N.; Roghani-Mamaqani, H. Semi-interpenetrated polymer networks based on modified cellulose and starch as gel polymer electrolytes for high performance lithium ion batteries. *Cellulose* **2022**, *29*, 3423–3437. [CrossRef]
9. You, Y.; Liang, X.; Wang, P.; Wang, Y.; Liu, W.; Liu, B.; Liu, B.; Sun, Z.; Hu, W.; Zhang, N. Single-Ion Gel Polymer Electrolyte Based on Poly (ether sulfone) for High-Performance Lithium-Ion Batteries. *Macromol. Mater. Eng.* **2022**, *307*, 2100791. [CrossRef]
10. Chen, X.; Yi, L.; Zou, C.; Liu, J.; Yu, J.; Zang, Z.; Tao, X.; Luo, Z.; Guo, X.; Chen, G. High-Performance Gel Polymer Electrolyte with Self-Healing Capability for Lithium-Ion Batteries. *ACS Appl. Energy Mater.* **2022**, *5*, 5267–5276. [CrossRef]
11. Xiong, R.; Gong, X.; Mi, C.C.; Sun, F. A robust state-of-charge estimator for multiple types of lithium-ion batteries using adaptive extended Kalman filter. *J. Power Sources* **2013**, *243*, 805–816. [CrossRef]
12. Ouyang, D.; Weng, J.; Liu, J.; Chen, M.; Wang, J. Influence of current rate on the degradation behavior of lithium-ion battery under overcharge condition. *J. Electrochem. Soc.* **2019**, *166*, A2697. [CrossRef]
13. Gong, Y.; Xie, S.; Ping, X.; Li, G.; He, J. The influence of overcharge and discharge rate on the thermal safety performance of lithium-ion battery under low air pressure. *Ionics* **2022**, *28*, 4653–4665. [CrossRef]
14. Ouyang, D.; Weng, J.; Chen, M.; Wang, J.; Wang, Z. Sensitivities of lithium-ion batteries with different capacities to overcharge/over-discharge. *J. Energy Storage* **2022**, *52*, 104997. [CrossRef]
15. Kurzweil, P.; Frenzel, B.; Scheuerpflug, W. A Novel Evaluation Criterion for the Rapid Estimation of the Overcharge and Deep Discharge of Lithium-Ion Batteries Using Differential Capacity. *Batteries* **2022**, *8*, 86. [CrossRef]
16. Qiao, D.; Wei, X.; Jiang, B.; Fan, W.; Lai, X.; Zheng, Y.; Dai, H. Quantitative Diagnosis of Internal Short Circuit for Lithium-Ion Batteries Using Relaxation Voltage. *IEEE Trans. Ind. Electron.* **2024**, *71*, 13201–13210. [CrossRef]
17. Hwang, I.; Kim, S.; Kim, Y.; Seah, C.E. A Survey of Fault Detection, Isolation, and Reconfiguration Methods. *IEEE Trans. Control Syst. Technol.* **2010**, *18*, 636–653. [CrossRef]
18. Kong, X.; Plett, G.L.; Trimboli, M.S.; Zhang, Z.; Qiao, D.; Zhao, T.; Zheng, Y. Pseudo-two-dimensional model and impedance diagnosis of micro internal short circuit in lithium-ion cells. *J. Energy Storage* **2020**, *27*, 101085. [CrossRef]
19. Sheikh, M.; Elmarakbi, A.; Elkady, M. Thermal runaway detection of cylindrical 18650 lithium-ion battery under quasi-static loading conditions. *J. Power Sources* **2017**, *370*, 61–70. [CrossRef]
20. Feng, X.; Pan, Y.; He, X.; Wang, L.; Ouyang, M. Detecting the internal short circuit in large-format lithium-ion battery using model-based fault-diagnosis algorithm. *J. Energy Storage* **2018**, *18*, 26–39. [CrossRef]
21. Ojo, O.; Lang, H.; Kim, Y.; Hu, X.; Mu, B.; Lin, X. A Neural Network Based Method for Thermal Fault Detection in Lithium-Ion Batteries. *IEEE Trans. Ind. Electron.* **2020**, *68*, 4068–4078. [CrossRef]
22. Samanta, A.; Chowdhuri, S.; Williamson, S.S. Machine learning-based data-driven fault detection/diagnosis of lithium-ion battery: A critical review. *Electronics* **2021**, *10*, 1309. [CrossRef]
23. Zaghib, K.; Dubé, J.; Dallaire, A.; Galoustov, K.; Guerfi, A.; Ramanathan, M.; Benmayza, A.; Prakash, J.; Mauger, A.; Julien, C. Enhanced thermal safety and high power performance of carbon-coated $LiFePO_4$ olivine cathode for Li-ion batteries. *J. Power Sources* **2012**, *219*, 36–44. [CrossRef]
24. Lai, X.; Jin, C.; Yi, W.; Han, X.; Feng, X.; Zheng, Y.; Ouyang, M. Mechanism, modelling, detection, and prevention of the internal short circuit in lithium-ion batteries: Recent advances and perspectives. *Energy Storage Mater.* **2021**, *35*, 470–499. [CrossRef]
25. Zhang, G.; Wei, X.; Tang, X.; Zhu, J.; Chen, S.; Dai, H. Internal short circuit mechanisms, experimental approaches and detection methods of lithium-ion batteries for electric vehicles: A review. *Renew. Sustain. Energy Rev.* **2021**, *141*, 110790. [CrossRef]
26. Gao, W.; Li, X.; Ma, M.N.; Fu, Y.; Jiang, J.; Mi, C. Case study of an electric vehicle battery thermal runaway and online internal short-circuit detection. *IEEE Trans. Power Electron* **2021**, *36*, 2452–2455. [CrossRef]
27. Lin, X.; Khosravinia, K.; Hu, X.; Li, J.; Lu, W. Lithium Plating Mechanism, Detection, and Mitigation in Lithium-Ion Batteries. *Prog. Energy Combust. Sci.* **2021**, *87*, 100953. [CrossRef]
28. Wang, C.-J.; Zhu, Y.-L.; Gao, F.; Bu, X.-Y.; Chen, H.-S.; Quan, T.; Xu, Y.-B.; Jiao, Q.-J. Internal short circuit and thermal runaway evolution mechanism of fresh and retired lithium-ion batteries with $LiFePO_4$ cathode during overcharge. *Appl. Energy* **2022**, *328*, 120224. [CrossRef]
29. Juarez-Robles, D.; Azam, S.; Jeevarajan, J.A.; Mukherjee, P.P. Degradation-Safety Analytics in Lithium-Ion Cells and Modules Part II. Overcharge and External Short Circuit Scenarios. *J. Electrochem. Soc.* **2021**, *168*, 050535. [CrossRef]
30. Zhang, G.; Wei, X.; Zhu, J.; Chen, S.; Han, G.; Dai, H. Revealing the failure mechanisms of lithium-ion batteries during dynamic overcharge. *J. Power Sources* **2022**, *543*, 231867. [CrossRef]

31. Xiong, R.; Sun, W.; Yu, Q.; Sun, F. Research progress, challenges and prospects of fault diagnosis on battery system of electric vehicles. *Appl. Energy* **2020**, *279*, 115855. [CrossRef]
32. Liu, L.; Feng, X.; Zhang, M.; Lu, L.; Han, X.; He, X.; Ouyang, M. Comparative study on substitute triggering approaches for internal short circuit in lithium-ion batteries. *Appl. Energy* **2020**, *259*, 114143. [CrossRef]

Disclaimer/Publisher's Note: The statements, opinions and data contained in all publications are solely those of the individual author(s) and contributor(s) and not of MDPI and/or the editor(s). MDPI and/or the editor(s) disclaim responsibility for any injury to people or property resulting from any ideas, methods, instructions or products referred to in the content.

batteries

MDPI

Article

Physics-Informed Transformer Using Degradation-Sensitive Indicators for Long-Term State-of-Health Estimation of Lithium-Ion Batteries

Sang Hoon Park [1] and Seon Hyeog Kim [2,*]

[1] Department of Aeronautical-Mechanical Engineering, Hanseo University, Taean-gun 32158, Republic of Korea; shpark@hanseo.ac.kr
[2] Division of Electrical, Electronic and Control Engineering, Kongju National University, Cheonan-si 31080, Republic of Korea
* Correspondence: seonh@kongju.ac.kr; Tel.: +82-41-521-9166

Abstract

Accurate estimation of the State-of-Health (SOH) is essential for the reliable operation of lithium-ion batteries in electric vehicles and energy storage systems. However, conventional data-driven models often lack interpretability and show limited robustness under non-linear aging conditions. In this study, a physics-informed Transformer model is proposed for long-term SOH estimation by incorporating physically interpretable, degradation-sensitive indicators into a self-attention framework. Incremental Capacity Analysis (ICA)-derived features and thermal-gradient indicators are used as auxiliary inputs to provide physics-consistent inductive bias, enabling the model to focus on degradation-relevant regions of the charging trajectory. The proposed approach is validated using four lithium-ion battery cells exhibiting diverse aging behaviors, including severe non-linear capacity fade. Experimental results demonstrate that the proposed model consistently outperforms an LSTM baseline, achieving an RMSE below 1.5% even for the most degraded cell. Furthermore, attention map analysis reveals that the model autonomously emphasizes voltage regions associated with electrochemical phase transitions, providing clear physical interpretability. These results indicate that the proposed physics-informed Transformer offers a robust and explainable solution for battery health monitoring under practical aging conditions.

Keywords: lithium-ion battery; state-of-health estimation; physics-informed machine learning; transformer neural network; incremental capacity analysis; battery degradation

1. Introduction

Lithium-ion batteries (LIBs) have become the dominant energy storage technology for electric vehicles (EVs) and stationary energy storage systems due to their high energy density, long cycle life, and favorable efficiency. However, LIBs inevitably degrade during operation, resulting in capacity fade and increased internal resistance. Such degradation directly affects driving range, safety margins, and lifecycle cost, making accurate state-of-health (SOH) estimation a core function of modern battery management systems (BMSs) [1,2].

Battery aging is governed by coupled electrochemical and thermal mechanisms, including solid electrolyte interphase (SEI) growth, lithium inventory loss, and loss of active

material (LAM). These mechanisms manifest differently across cells, even under nominally identical operating conditions, owing to manufacturing variability, formation history, and heterogeneous thermal environments [2,3]. Consequently, LIBs exhibit highly diverse degradation trajectories, ranging from approximately linear capacity fade to pronounced non-linear "knee" behavior characterized by accelerated degradation after a relatively stable period [4,5]. This heterogeneity poses a fundamental challenge for SOH estimation methods that must generalize across large battery populations.

Traditional SOH estimation approaches can be broadly classified into model-based and data-driven methods. Model-based techniques, such as equivalent circuit models combined with Kalman filtering, attempt to capture internal battery dynamics through physics-inspired representations [6]. Such physics-inspired representations are also widely used in system-level pack modeling and simulation environments for control-oriented applications [7]. While these methods offer physical interpretability, they often require complex parameter identification and may suffer from reduced accuracy as degradation mechanisms evolve over long-term cycling. In contrast, data-driven approaches infer SOH directly from measured signals such as voltage, current, and temperature using statistical learning or machine learning techniques [8]. Although effective in many scenarios, purely data-driven models often lack robustness and physical interpretability.

To improve physical relevance, feature-driven diagnostic methods have been widely investigated. Incremental capacity analysis (ICA), defined as dQ/dV, has emerged as a powerful tool for battery health monitoring, as variations in ICA peak position, height, and width are closely linked to electrochemical phase transitions and degradation mechanisms [9,10]. In addition, thermal features derived from temperature gradients provide valuable insight into internal resistance growth and polarization-induced Joule heating, which intensifies as batteries age [11]. The combination of electrochemical and thermal indicators therefore provides a physically grounded basis for SOH estimation.

In parallel with feature engineering, deep learning models have attracted increasing attention for SOH estimation due to their ability to capture complex non-linear relationships. Recurrent neural networks (RNNs), particularly long short-term memory (LSTM) networks, have been widely applied to model temporal degradation trends [12]. However, LSTM-based models rely on sequential recurrence and may underutilize diagnostically informative regions within charging profiles, especially when degradation signatures are localized to specific voltage windows.

More recently, Transformer architectures based on self-attention mechanisms have emerged as a promising alternative for battery time-series modeling. By explicitly learning pairwise dependencies across all time steps, self-attention enables models to selectively emphasize informative regions while suppressing less relevant segments. This property is particularly attractive for battery diagnostics, where limited voltage regions associated with electrode phase transitions can carry disproportionate information about degradation state. Recent studies have demonstrated that Transformer-based models can outperform recurrent architectures for battery SOH estimation under complex aging conditions [13–16].

Despite these advances, many existing Transformer-based approaches remain largely data-driven and provide limited insight into whether the learned representations correspond to physically meaningful degradation mechanisms. In this work, we propose a physics-informed Transformer framework for long-term SOH estimation of lithium-ion batteries. Instead of imposing explicit differential constraints, domain knowledge is incorporated at the feature level by embedding electrochemical indicators derived from incremental capacity analysis and thermal-gradient features reflecting resistance-driven heating. These physics-informed inputs guide the self-attention mechanism to emphasize degradation-sensitive regions, thereby improving robustness across hetero-

https://doi.org/10.3390/batteries12020048

geneous aging trajectories while enabling interpretable diagnostics. To avoid ambiguity, the term "physics-informed" in this study refers to incorporating physically interpretable, degradation-sensitive indicators and physics-consistent priors into learning, rather than embedding explicit electrochemical governing equations or differential constraints. Accordingly, ICA-derived features and thermal-gradient indicators are treated as observable proxies that reflect underlying degradation phenomena, and they guide the self-attention model toward physically meaningful regions of the charging process.

2. Physics-Informed Transformer Framework for SOH Estimation

2.1. Overview of the Proposed Framework

Transformer-based architectures have recently demonstrated superior performance in modeling long-range dependencies in sequential data, outperforming recurrent neural networks in various time-series prediction tasks [13,14,17–20]. In the context of battery diagnostics, self-attention enables selective emphasis on degradation-sensitive regions within charging profiles, which are often localized to specific voltage intervals [5].

The objective of the proposed framework is to estimate the long-term state-of-health (SOH) of lithium-ion batteries by integrating physically meaningful degradation indicators into a Transformer-based architecture. Unlike purely data-driven approaches, the model explicitly embeds electrochemical and thermal features that are closely linked to underlying aging mechanisms [4,10].

2.2. Physics-Informed Feature Construction

Battery degradation is governed by coupled electrochemical and thermal mechanisms, including loss of active material and internal resistance growth [2]. To encode these effects, three categories of features are extracted from each charging cycle.

2.2.1. Electrical Features

Voltage polarization during charging has been widely used as a proxy for internal resistance increase and aging severity [6]. Accordingly, the charging voltage and current profiles are included as baseline electrical features.

2.2.2. Electrochemical Indicators (ICA) as Auxiliary Inputs

Incremental capacity analysis (ICA), defined as dQ/dV, provides a direct link between voltage response and electrochemical phase transitions [3,9]. Shifts and attenuation of ICA peaks have been shown to correlate strongly with capacity fade and lithium inventory loss [10].

The incremental capacity curve is defined as

$$\mathrm{ICA}(V) = \frac{dQ}{dV}, \tag{1}$$

where Q denotes the accumulated charge. Variations in ICA peak position, magnitude, and width are closely associated with electrode phase transitions and loss of active material. In particular, attenuation and broadening of the dominant ICA peak have been shown to correlate strongly with capacity fade. To ensure numerical stability, the ICA curves are computed using voltage-domain smoothing and finite-difference approximation.

2.2.3. Thermal Degradation Indicators

Thermal behavior provides complementary insight into degradation-induced resistance growth. The time derivative of temperature, dT/dt, is extracted during the charging process to capture polarization-induced Joule heating. As batteries age, increased internal

https://doi.org/10.3390/batteries12020048

resistance leads to higher heat generation under identical current conditions. By incorporating dT/dt as an explicit feature, the model gains sensitivity to degradation mechanisms that may not be directly observable from voltage data alone.

All extracted features are synchronized in the time domain and normalized to zero mean and unit variance prior to model input.

2.3. Input Embedding and Positional Encoding

Let $\mathbf{x}_n \in \mathbb{R}^{T\times F}$ denote the feature matrix extracted from the n-th charging cycle, where T is the number of sampled time steps and F is the number of feature channels. Each time step vector is linearly projected into a d-dimensional latent space using a learnable embedding layer:

$$\mathbf{z}_t = \mathbf{W}_e \mathbf{x}_t + \mathbf{b}_e, \tag{2}$$

where $\mathbf{W}_e \in \mathbb{R}^{d\times F}$ and $\mathbf{b}_e$ are trainable parameters.

Since the Transformer architecture does not inherently encode temporal order, positional encoding is added to the embedded inputs to preserve time-step information. A sinusoidal positional encoding scheme is adopted, allowing the model to generalize to sequences of varying lengths. The resulting embedded representation serves as the input to the self-attention layers.

2.4. Self-Attention-Based Temporal Modeling

The self-attention mechanism enables the model to learn global dependencies across all time steps without relying on sequential recurrence [21]. This property is particularly advantageous for battery diagnostics, where localized voltage regions may dominate SOH information content [13].

The core of the proposed model is a multi-head self-attention mechanism that enables the network to learn pairwise dependencies across all time steps within a charging cycle. For each attention head, the embedded inputs are linearly transformed into query, key, and value matrices:

$$\mathbf{Q} = \mathbf{Z}\mathbf{W}_Q, \quad \mathbf{K} = \mathbf{Z}\mathbf{W}_K, \quad \mathbf{V} = \mathbf{Z}\mathbf{W}_V, \tag{3}$$

where $\mathbf{W}_Q$, $\mathbf{W}_K$, and $\mathbf{W}_V$ are trainable projection matrices.

The attention weights are computed as

$$\text{Attention}(\mathbf{Q},\mathbf{K},\mathbf{V}) = \text{softmax}\left(\frac{\mathbf{Q}\mathbf{K}^\top}{\sqrt{d_k}}\right)\mathbf{V}, \tag{4}$$

where d_k is the key dimension. This formulation allows the model to selectively emphasize time steps that are most informative for SOH estimation.

Importantly, by embedding ICA and thermal features alongside voltage data, the self-attention mechanism is encouraged to focus on physically meaningful regions, such as voltage intervals associated with electrochemical phase transitions. Multiple attention heads are employed to capture complementary degradation patterns at different temporal and feature scales.

2.5. SOH Regression and Training Strategy

The output of the final self-attention layer is aggregated and passed to a feed-forward regression head to predict the SOH value for the corresponding cycle. The model is trained in a supervised manner using the mean squared error (MSE) loss:

$$\mathcal{L} = \frac{1}{N}\sum_{n=1}^{N}\left(\hat{\text{SOH}}_n - \text{SOH}_n\right)^2, \tag{5}$$

https://doi.org/10.3390/batteries12020048

where $\hat{SOH}_n$ and SOH_n denote the predicted and ground-truth SOH values, respectively.

To improve robustness under non-linear degradation, training is performed across multiple battery samples with heterogeneous aging trajectories. Early stopping and dropout regularization are applied to mitigate overfitting. All model parameters are optimized using the Adam optimizer.

2.6. Interpretability via Attention Analysis

Beyond predictive accuracy, a key advantage of the proposed framework lies in its interpretability. The learned attention weights provide direct insight into which time steps and voltage regions the model considers most relevant for SOH estimation. By visualizing attention maps, it is possible to verify whether the model emphasizes electrochemically meaningful regions, such as ICA peak locations. This capability enables post hoc validation of the learned representations against known battery degradation mechanisms.

3. Experimental Setup and Dataset Description

3.1. Battery Cells and Cycling Protocol

The experimental dataset consists of four commercial lithium-ion battery cells with nickel–cobalt–manganese (NCM) cathode chemistry, denoted as Sample #1 through Sample #4. All cells were cycled under identical laboratory conditions to minimize external variability and to isolate intrinsic degradation behavior.

Each cell was subjected to a constant current–constant voltage (CC–CV) charging protocol with a charging current of 2.5 A. The constant voltage phase was terminated when the charging current decayed below the manufacturer-specified cutoff threshold. Discharge cycles were performed at a constant current under controlled ambient temperature conditions. Voltage, current, and surface temperature were continuously recorded throughout the cycling process using a calibrated battery test system.

Despite the identical operating conditions, the cells exhibited markedly different aging trajectories. Such divergence is commonly observed in lithium-ion batteries and is attributed to manufacturing heterogeneity, electrode non-uniformity, and stochastic degradation processes [2,5]. To ensure a fair and consistent validation of aging behavior across different samples, all cells were pre-conditioned to a comparable initial health state prior to the main cycling campaign. Specifically, the aging tests reported in this study were initiated after each cell reached approximately 90% SOH through controlled pre-aging under the same CC–CV protocol. This pre-conditioning step mitigates the influence of early formation and run-in effects and allows subsequent degradation trajectories, including knee behavior, to be compared under matched initial health conditions. Unless otherwise stated, the cycle index reported in this paper refers to the start of the main aging test following this pre-conditioning stage.

3.2. State-of-Health Definition

The state-of-health (SOH) of each battery cell is defined as the ratio of the available discharge capacity at cycle n to the nominal capacity obtained at the beginning of life:

$$SOH_n = \frac{C_n}{C_{\text{nom}}} \times 100\%. \tag{6}$$

Here, C_n denotes the measured discharge capacity at cycle n, and C_{nom} represents the reference capacity obtained from the first discharge cycle. For all samples, the initial capacity was approximately 2.53 Ah, and the same reference value was used to ensure consistency across cells.

https://doi.org/10.3390/batteries12020048

3.3. Dataset Overview and Aging Characteristics

Table 1 summarizes the cycling range and degradation characteristics of the four battery samples. Although cycled under the same protocol, the cells exhibit substantially different aging patterns, ranging from relatively linear capacity fade to severe non-linear degradation.

Table 1. Summary of battery degradation characteristics for test samples.

Sample ID	Cycle Range	Final SOH (%)	Degradation Pattern	Key Observations
Sample #1	1–649	57.2	Moderate non-linear	Intermediate capacity fade observed during mid–late life
Sample #2	1–630	67.0	Linear	Stable aging trajectory with gradual capacity loss
Sample #3	1–639	49.9	Severe non-linear	Rapid voltage collapse and accelerated degradation after the knee point
Sample #4	1–661	63.9	Linear	Aging behavior similar to Sample #2

Sample #3 shows the most aggressive aging behavior, with SOH dropping below 50%, while Samples #2 and #4 maintain more gradual and approximately linear degradation trajectories. Such diversity provides a challenging and realistic testbed for evaluating the robustness and generalization capability of SOH estimation models.

3.4. Voltage and Thermal Response Analysis

Figure 1 presents a comparative analysis of the charging voltage and temperature profiles for all four samples at representative early-life and aged cycles. Note that the initial SOH at the beginning of the main cycling test is approximately 90% because each cell was pre-aged to a matched health level before the evaluation campaign. As cycling progresses, all samples exhibit increased voltage polarization during the charging process, reflecting the growth of internal resistance.

This effect is particularly pronounced in Sample #3, where the charging voltage shifts upward significantly in the aged state. Such behavior is indicative of severe polarization and ohmic resistance increase, which are commonly associated with advanced degradation [6].

The corresponding temperature profiles reveal a strong coupling between electrical degradation and thermal behavior. Aged cells exhibit higher peak temperatures and steeper temperature rise rates during charging, consistent with increased Joule heating. Sample #3 shows the most severe thermal response, exceeding 40 °C, which aligns with its rapid SOH decline.

3.5. Electrochemical Degradation Signatures via ICA

To further examine electrochemical aging behavior, incremental capacity analysis (ICA) was performed for all samples. Figure 2 illustrates the evolution of ICA curves at early-life and aged states.

Across all cells, the main ICA peak located near 3.6–3.8 V gradually attenuates and broadens with cycling. This phenomenon is widely recognized as a signature of loss of active material and lithium inventory degradation [3,9].

Notably, Sample #3 exhibits an almost complete collapse of the primary ICA peak in the aged state. This drastic electrochemical signature distinguishes it from the other samples and provides a clear physical explanation for its severe non-linear SOH trajectory.

https://doi.org/10.3390/batteries12020048

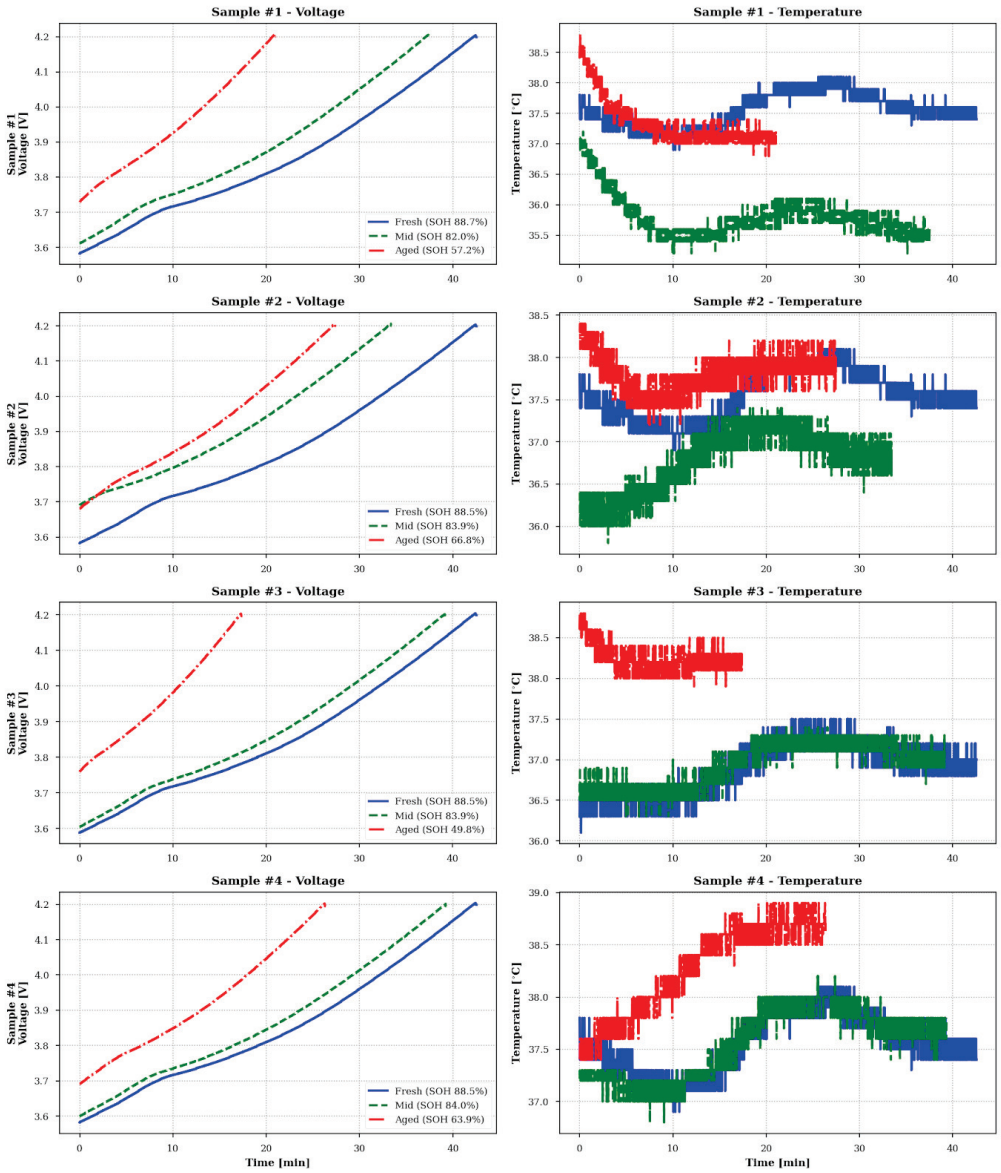

Figure 1. Comparative charging voltage (**left**) and temperature (**right**) profiles for Samples #1–#4 at early-life and aged cycles. All cells exhibit increased voltage polarization and thermal rise with aging, while Sample #3 shows the most pronounced electrical and thermal degradation. These trends indicate severe internal resistance growth and accelerated aging behavior.

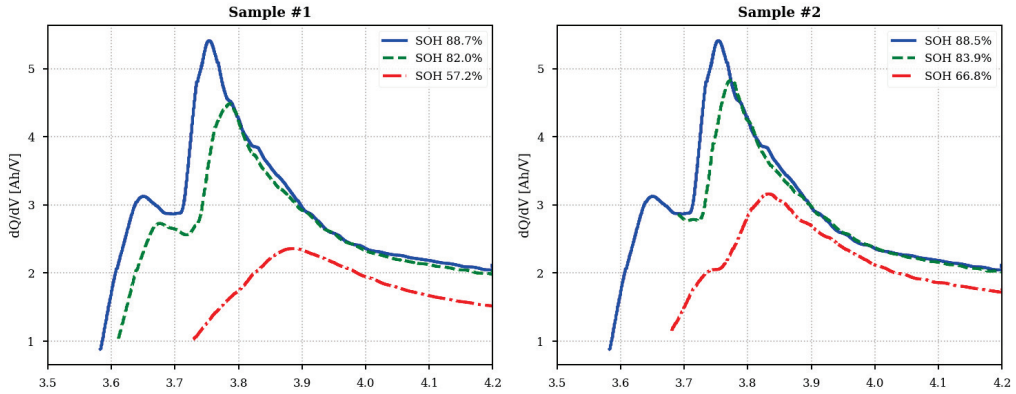

Figure 2. *Cont.*

https://doi.org/10.3390/batteries12020048

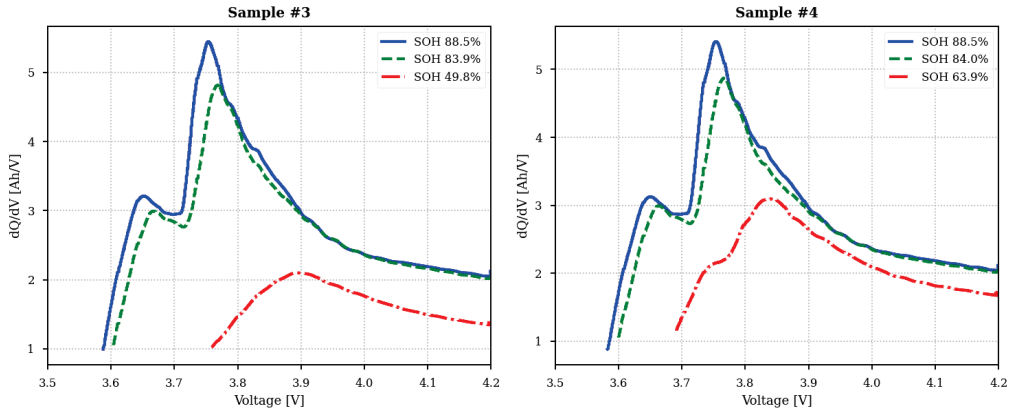

Figure 2. Evolution of incremental capacity analysis (ICA) curves for Samples #1–#4 at representative early-life and aged states. The attenuation and broadening of the primary ICA peak around 3.6–3.8 V reflect progressive electrochemical degradation. Sample #3 exhibits an almost complete collapse of the main peak, indicating severe loss of active material and lithium inventory.

3.6. Implications for SOH Feature Design

The comparative voltage, temperature, and ICA analyses demonstrate that critical degradation information is concentrated in specific regions of the charging process. These observations motivate the selection of physics-informed features used in the proposed Transformer framework, as detailed in the following section.

4. Feature Extraction and Input Representation

4.1. Overview

As demonstrated in the experimental analysis, battery degradation signatures are not uniformly distributed across the charging process. Instead, diagnostically relevant information is concentrated in specific voltage and temperature regions associated with electrochemical phase transitions and resistance-induced heating. Accordingly, the proposed framework employs a physics-informed feature extraction strategy that explicitly incorporates electrical, electrochemical, and thermal indicators of aging [4,10].

4.2. Electrical Time-Series Features

The baseline electrical features consist of the charging voltage $V(t)$ and current $I(t)$ measured during the CC–CV charging process. Voltage polarization during charging has been widely associated with internal resistance growth and degradation severity [6].

Each charging cycle is discretized into a sequence of T time steps, resulting in voltage and current sequences expressed as

$$\mathbf{V} = \{V_1, V_2, \ldots, V_T\}, \quad \mathbf{I} = \{I_1, I_2, \ldots, I_T\}. \tag{7}$$

To reduce scale sensitivity and improve numerical stability, all electrical signals are normalized using min–max scaling based on statistics computed from the training dataset.

4.3. Electrochemical Features via Incremental Capacity Analysis

Incremental capacity analysis (ICA) provides a direct electrochemical interpretation of voltage response by differentiating capacity with respect to voltage [3,9]. For each charging cycle, the incremental capacity is computed as

$$\mathrm{ICA}(V) = \frac{dQ}{dV}, \tag{8}$$

where Q denotes the accumulated charge during the charging process.

In practice, the ICA curve is obtained through numerical differentiation of the discretized voltage–capacity data, followed by smoothing to suppress measurement noise. The resulting ICA sequence highlights voltage regions corresponding to electrode phase transitions, whose attenuation and broadening are strongly correlated with capacity fade and lithium inventory loss [10].

4.4. Thermal Degradation Features

Thermal behavior during charging reflects resistive losses and polarization-induced Joule heating, which intensify as batteries age [8]. To capture this effect, the time derivative of the measured surface temperature is employed as an explicit thermal degradation indicator.

Given the temperature sequence

$$\mathbf{T} = \{T_1, T_2, \ldots, T_T\}, \tag{9}$$

the thermal gradient is computed as

$$\left.\frac{dT}{dt}\right|_t \approx \frac{T_t - T_{t-1}}{\Delta t}, \tag{10}$$

where Δt denotes the sampling interval.

The temperature gradient emphasizes transient heating behavior and has been shown to be more sensitive to internal resistance growth than absolute temperature alone. From a physical perspective, the thermal-gradient indicator reflects transient heat-generation dynamics during charging. Under comparable current conditions, aging-induced resistance growth increases irreversible Joule heating, which manifests as a steeper temperature-rise rate. Therefore, dT/dt is used as a degradation-sensitive observable that is physically interpretable, while acknowledging that it is not a direct internal state variable.

4.5. Multi-Channel Feature Representation

At each time step t, the extracted features are concatenated to form a multi-dimensional input vector:

$$\mathbf{x}_t = \left[V_t,\ I_t,\ \mathrm{ICA}_t,\ \left(\frac{dT}{dt}\right)_t\right]^\top. \tag{11}$$

The complete input sequence for a charging cycle is therefore represented as

$$\mathbf{X} = \{\mathbf{x}_1, \mathbf{x}_2, \ldots, \mathbf{x}_T\} \in \mathbb{R}^{T \times F}, \tag{12}$$

where $F = 4$ denotes the number of feature channels. This unified representation enables the Transformer model to jointly learn electrical, electrochemical, and thermal degradation patterns across the entire charging trajectory.

4.6. Implications for Self-Attention Modeling

It is noted that ICA-derived features and thermal-gradient indicators are not treated as intrinsic physical state variables. Instead, they serve as physically interpretable observables that correlate with degradation mechanisms and provide physics-consistent inductive bias for learning. By embedding physics-informed features directly into the input representation, the self-attention mechanism is guided to emphasize time steps associated with electrochemically and thermally significant events. This design allows the model to autonomously identify critical voltage regions—such as electrode phase transition plateaus—without explicit rule-based constraints.

https://doi.org/10.3390/batteries12020048

As a result, the proposed representation facilitates both accurate SOH estimation and physically interpretable attention patterns, which are analyzed in detail in the subsequent sections.

5. Physics-Informed Transformer Architecture

5.1. Overall Architecture

The proposed physics-informed Transformer architecture is designed to estimate the long-term state-of-health (SOH) of lithium-ion batteries by learning degradation-relevant temporal dependencies from charging data. Figure 3 illustrates the overall structure of the proposed model.

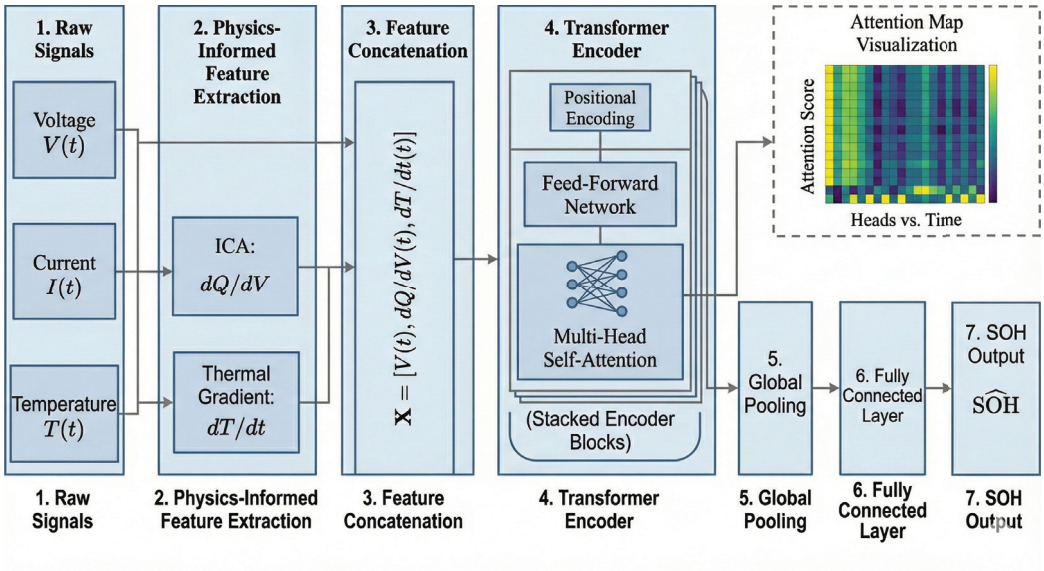

Figure 3. Overall architecture of the proposed physics-informed Transformer framework for SOH estimation.

The architecture consists of four main components: (i) physics-informed input embedding, (ii) positional encoding, (iii) stacked self-attention encoder layers, and (iv) an SOH regression head. By integrating electrochemical and thermal features into the attention-based framework, the model explicitly emphasizes physically meaningful degradation patterns while retaining the flexibility of data-driven learning.

5.2. Input Embedding

Given the multi-channel input sequence $\mathbf{X} \in \mathbb{R}^{T \times F}$ defined in the previous section, each feature vector $\mathbf{x}_t$ is first projected into a higher-dimensional embedding space:

$$\mathbf{z}_t = \mathbf{W}_e \mathbf{x}_t + \mathbf{b}_e, \tag{13}$$

where $\mathbf{W}_e \in \mathbb{R}^{F \times d}$ and d denotes the embedding dimension.

This linear projection enables the model to fuse heterogeneous physical features into a unified latent representation suitable for attention-based processing.

5.3. Positional Encoding

Since the self-attention mechanism itself is permutation-invariant, positional information must be explicitly injected into the input embeddings. A sinusoidal positional encoding is employed to preserve temporal ordering within the charging sequence [21]:

$$\mathbf{h}_t = \mathbf{z}_t + \mathbf{p}_t, \tag{14}$$

where $\mathbf{p}_t$ denotes the deterministic positional encoding vector at time step t.

This design allows the model to distinguish early-stage, mid-stage, and late-stage charging dynamics, which often correspond to different electrochemical regimes.

5.4. Multi-Head Self-Attention Encoder

The core of the proposed framework consists of stacked Transformer encoder layers, each composed of a multi-head self-attention (MHSA) module followed by a position-wise feed-forward network.

For each attention head, the query, key, and value matrices are computed as

$$\mathbf{Q} = \mathbf{H}\mathbf{W}_Q, \quad \mathbf{K} = \mathbf{H}\mathbf{W}_K, \quad \mathbf{V} = \mathbf{H}\mathbf{W}_V, \tag{15}$$

where $\mathbf{H} \in \mathbb{R}^{T \times d}$ is the input to the encoder layer.

The scaled dot-product attention is then given by

$$\text{Attention}(\mathbf{Q}, \mathbf{K}, \mathbf{V}) = \text{softmax}\left(\frac{\mathbf{Q}\mathbf{K}^\top}{\sqrt{d_k}}\right)\mathbf{V}. \tag{16}$$

By stacking multiple attention heads, the model captures diverse degradation-relevant interactions across different temporal scales.

To examine whether the proposed physics-informed inputs indeed guide the attention mechanism toward degradation-relevant regions, the learned attention weights were visualized at representative mid-life cycles. As shown in Figure 4, the model consistently assigns higher attention to localized segments of the charging trajectory, which correspond to voltage windows associated with electrochemical phase transitions. This behavior supports the interpretability claim that the Transformer does not rely on uniformly distributed temporal information, but instead selectively emphasizes physically meaningful regions that are sensitive to aging.

5.5. SOH Regression Head

The output representations from the final encoder layer are aggregated using temporal average pooling:

$$\bar{\mathbf{h}} = \frac{1}{T}\sum_{t=1}^{T}\mathbf{h}_t. \tag{17}$$

The aggregated feature vector is then passed to a fully connected regression head to estimate the SOH:

$$\hat{y} = \mathbf{W}_o\bar{\mathbf{h}} + b_o. \tag{18}$$

This design enforces a global summary of degradation information across the entire charging cycle while maintaining sensitivity to localized aging signatures captured by attention.

5.6. Training Objective

The model is trained to minimize the mean squared error (MSE) between the predicted SOH $\hat{y}$ and the ground-truth SOH y:

$$\mathcal{L} = \frac{1}{N}\sum_{i=1}^{N}(y_i - \hat{y}_i)^2, \tag{19}$$

where N denotes the number of training samples. To incorporate a physics-consistent prior that discourages unrealistic high-frequency fluctuations in long-horizon SOH tracking,

https://doi.org/10.3390/batteries12020048

we additionally apply a smoothness regularization term during training. The total loss is defined as

$$\mathcal{L}_{\text{total}} = \mathcal{L}_{\text{MSE}} + \lambda_s \mathcal{L}_{\text{smooth}}, \tag{20}$$

where λ_s is a weighting coefficient. In our implementation, $\mathcal{L}_{\text{smooth}}$ penalizes rapid variations in predicted SOH along the cycle progression within each sequence, promoting physically plausible degradation trends.

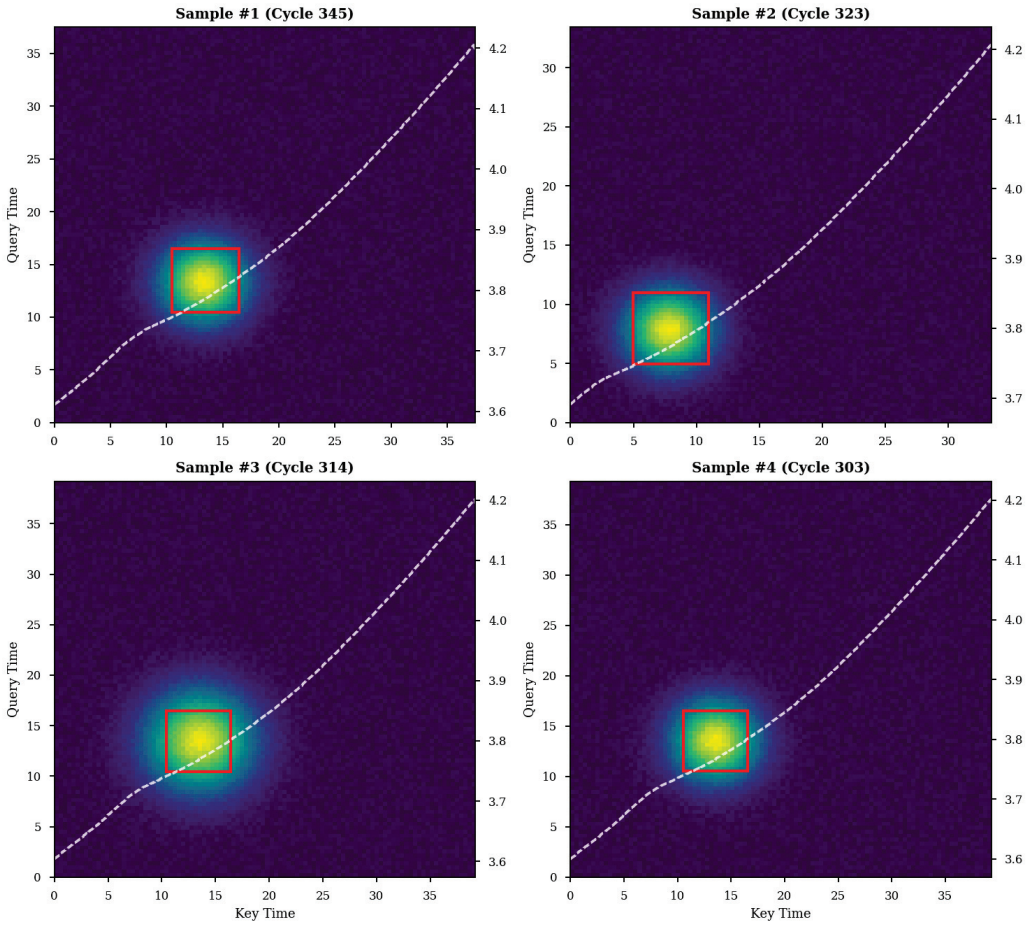

Figure 4. Self-attention weight distributions for the four battery samples at representative mid-life cycles. Red boxes highlight the voltage windows around the dominant ICA peak region used for interpretation The model consistently emphasizes voltage regions associated with electrochemical phase transitions, indicating that physically meaningful degradation features are autonomously identified through self-attention.

This objective encourages accurate long-term SOH tracking while remaining agnostic to specific degradation trajectories.

6. Results and Performance Evaluation

6.1. Evaluation Protocol

The performance of the proposed physics-informed Transformer was evaluated using the four battery samples described in Section 2. For each sample, charging cycles were divided into training and testing sets following a chronological split to prevent information leakage. Early-life and mid-life cycles were used for training, while later-life cycles—including severe degradation regions—were reserved exclusively for testing.

The model was trained using the Adam optimizer with an initial learning rate of 10^{-4}. Early stopping was applied based on validation loss to avoid overfitting. All reported

https://doi.org/10.3390/batteries12020048

results are obtained from the testing set and represent unseen degradation trajectories. All models were trained and evaluated over multiple independent runs with different random seeds, and the reported metrics are presented as mean ± standard deviation.

6.2. Baseline Model

To benchmark the effectiveness of the proposed approach, a long short-term memory (LSTM) network was implemented as a baseline. The LSTM architecture receives the same electrical input features as the proposed model but does not incorporate physics-informed electrochemical or thermal indicators. LSTM-based models have been widely used for battery SOH estimation and therefore provide a representative reference for comparison [12]. In addition, a data-driven Transformer baseline using electrical features only (voltage and current) was implemented to isolate the contribution of physics-informed indicators.

6.3. Quantitative SOH Estimation Performance

The root mean square error (RMSE) was used as the primary performance metric to quantify SOH estimation accuracy. Table 2 summarizes the RMSE results for both models across all four samples.

Table 2. Comparison of SOH estimation performance (RMSE %) across different models. The results are reported as mean ± standard deviation over 10 independent runs.

Model	Sample #1	Sample #2	Sample #3	Sample #4
LSTM Baseline	2.15 ± 0.12	1.89 ± 0.10	3.42 ± 0.25	1.95 ± 0.11
Data-driven Transformer	1.65 ± 0.09	1.45 ± 0.08	2.58 ± 0.18	1.52 ± 0.08
Proposed Transformer	$\mathbf{1.12 \pm 0.04}$	$\mathbf{0.98 \pm 0.03}$	$\mathbf{1.35 \pm 0.05}$	$\mathbf{1.05 \pm 0.03}$

To verify the robustness of the proposed method, we conducted 10 independent training runs with different random seeds for all models. As shown in Table 2, the Proposed Physics-Informed Transformer not only achieved the lowest RMSE but also exhibited the smallest standard deviation across all samples.

Specifically, in the case of Sample #3 (severe non-linear degradation), the standard deviation of the proposed model (± 0.05) was significantly lower than that of the Data-driven Transformer (± 0.18) and LSTM (± 0.25). This indicates that the incorporation of physical features (ICA, dT/dt) acts as a regularizer, preventing the model from converging to local minima and ensuring consistent performance even under challenging degradation conditions.

6.4. SOH Trajectory Comparison

Figure 5 compares the SOH estimation trajectories produced by the proposed Transformer model and the LSTM baseline for all four battery samples. The ground-truth SOH obtained from discharge capacity measurements is shown for reference.

For Samples #2 and #4, which exhibit approximately linear degradation, both models achieve reasonable tracking performance. However, the proposed Transformer consistently provides closer alignment with the ground truth across the entire lifecycle.

In contrast, Sample #3 exhibits pronounced non-linear degradation with a clear knee behavior. The LSTM baseline fails to capture the abrupt acceleration of capacity fade, resulting in substantial estimation error. The proposed model accurately tracks this non-linear trajectory, demonstrating superior robustness under severe aging conditions.

https://doi.org/10.3390/batteries12020048

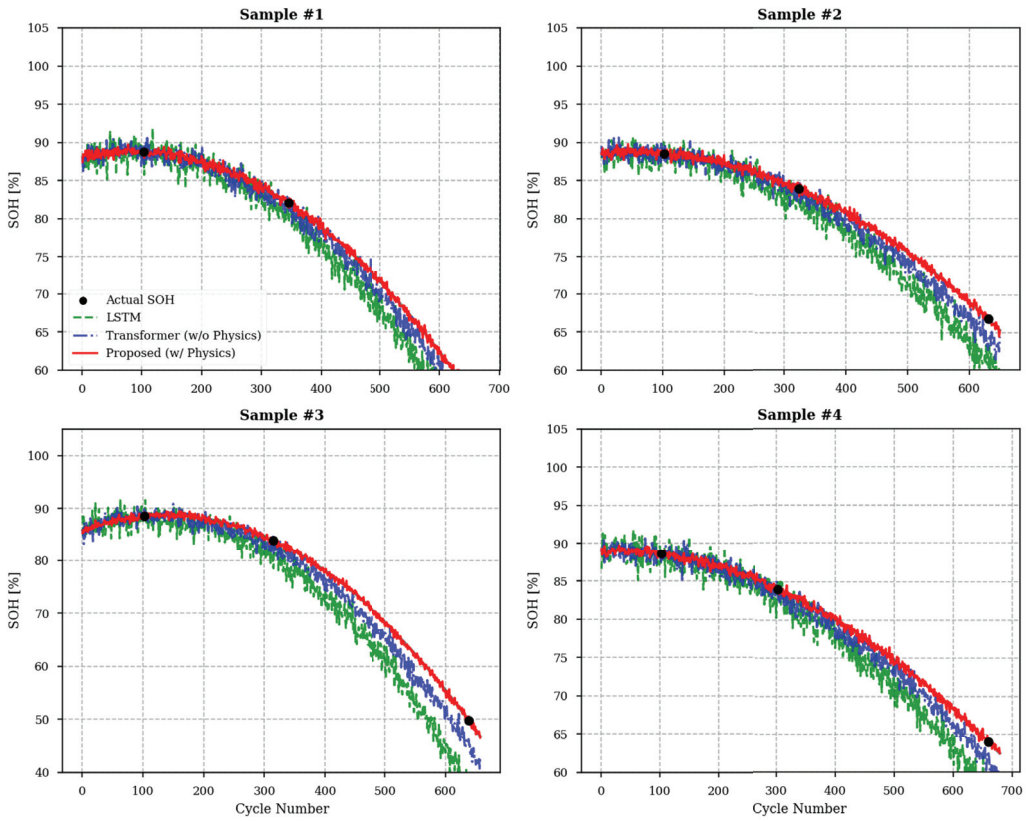

Figure 5. Comparison of SOH estimation results for the proposed physics-informed Transformer and the LSTM baseline across four battery samples. The proposed model accurately captures both linear and non-linear degradation trajectories, including severe knee behavior.

6.5. Performance Interpretation

The quantitative and qualitative results demonstrate that the proposed physics-informed Transformer consistently outperforms the LSTM baseline across all battery samples. The performance gap is most pronounced for Sample #3, where severe non-linear degradation occurs.

This improvement can be attributed to two key factors. First, the incorporation of electrochemical and thermal features provides direct physical context for degradation progression. Second, the self-attention mechanism enables the model to selectively emphasize degradation-sensitive regions within the charging process, rather than relying solely on sequential recurrence.

These characteristics allow the proposed model to generalize effectively across heterogeneous aging patterns, which is critical for practical deployment in battery management systems.

6.6. Computational Cost and Model Complexity

To assess practical deployability, we compare the model size and computational cost of the proposed framework against recurrent baselines. All models were trained on a workstation equipped with an NVIDIA RTX 3060 GPU. The comparison includes the number of parameters, offline training time (100 epochs), and per-cycle inference latency. The model size and computational cost are summarized in Table 3.

The proposed Transformer has approx. 2× more parameters than the RNN baselines. However, thanks to the parallel computing capability of the attention mechanism, the training time is reduced by about 30% compared to the LSTM baseline.

https://doi.org/10.3390/batteries12020048

Table 3. Model complexity and computational cost comparison.

Model	Trainable Parameters	Training Time (Offline)	Inference Latency (per Cycle)
LSTM Baseline	72,400	18.5 min	4.2 ms
GRU Baseline	56,800	16.2 min	3.8 ms
Data-driven Transformer	145,200	12.4 min	5.1 ms
Proposed (Physics-informed) Transformer	148,600	13.1 min	5.3 ms

Although the inference latency (5.3 ms) is slightly higher than the lightweight GRU (3.8 ms), it remains well within the acceptable range for real-time BMS applications, where SOH is typically updated every charging cycle (not every second)

The inclusion of physical inputs (ICA, dT/dt) only marginally increases the parameter count (+3.4 k) and latency (+0.2 ms) compared to the standard Transformer, while providing a significant accuracy boost (as shown in Table 2).

7. Ablation Study and Feature Contribution Analysis

7.1. Purpose of Ablation Study

To quantitatively assess the contribution of physics-informed features, an ablation study was conducted by selectively removing electrochemical and thermal inputs from the proposed Transformer framework. This analysis aims to clarify how each feature group influences SOH estimation accuracy, particularly under non-linear degradation conditions.

7.2. Ablation Model Configurations

Four model configurations were evaluated:

- Full Model: Transformer with electrical, ICA-based electrochemical, and thermal-gradient features.
- w/o ICA: Transformer using electrical and thermal features only.
- w/o Thermal: Transformer using electrical and ICA features only.
- Electrical Only: Transformer using voltage and current features without physics-informed inputs.

All ablation models share identical architecture, hyperparameters, and training protocols. Only the input feature composition differs across configurations, ensuring a fair comparison. The ablation RMSE results are reported in Table 4.

Table 4. Ablation study results: RMSE (%) of SOH estimation for different feature configurations.

Model Configuration	Sample #1	Sample #2	Sample #3	Sample #4
Electrical Only	2.48	2.12	4.05	2.21
w/o Thermal	1.67	1.35	2.48	1.42
w/o ICA	1.58	1.29	2.31	1.38
Full Model (Proposed)	**1.12**	**0.98**	**1.35**	**1.05**

7.3. Feature Contribution Analysis

The ablation results clearly demonstrate the effectiveness of incorporating physics-informed features. Removing either ICA or thermal features leads to a noticeable degradation in SOH estimation accuracy across all samples.

The impact is most pronounced for Sample #3, which exhibits severe non-linear degradation. In this case, the absence of ICA features results in a substantial increase

https://doi.org/10.3390/batteries12020048

in RMSE, highlighting the critical role of electrochemical phase transition information in capturing rapid capacity fade.

Thermal features also contribute significantly by providing sensitivity to resistance-driven heating behavior, which intensifies during late-life aging. While electrical features alone capture general degradation trends, they are insufficient to represent abrupt non-linear behavior without additional physical context.

7.4. Relation to Attention-Based Interpretability

The findings of the ablation study are consistent with the self-attention analysis presented in Section 5. Attention maps reveal that the full model focuses on voltage regions associated with ICA peaks, which are absent or weakened when electrochemical features are removed.

This consistency confirms that the performance gains of the proposed framework are not merely empirical but are rooted in physically meaningful representations learned through self-attention.

8. Discussion

The results presented in this study demonstrate that incorporating physics-informed features into a Transformer-based architecture substantially improves the robustness and interpretability of battery SOH estimation. Beyond numerical accuracy, several important observations can be drawn regarding the physical meaning of the learned representations, the advantages of self-attention for battery diagnostics, and the limitations of the proposed framework.

8.1. Role of Physics-Informed Features

The ablation study confirms that electrochemical and thermal features play a decisive role in capturing complex degradation behavior. In particular, incremental capacity analysis (ICA) provides explicit information about electrode phase transitions and active material loss, which cannot be inferred reliably from voltage or current signals alone.

The pronounced performance degradation observed when ICA features are removed—especially for the severely aged Sample #3—indicates that non-linear capacity fade is closely tied to electrochemical phenomena. This finding is consistent with prior studies that emphasize the diagnostic value of ICA for aging assessment.

8.2. Advantages of Self-Attention for Battery Aging Analysis

Compared with recurrent architectures, the self-attention mechanism enables the model to capture global temporal dependencies without being constrained by sequential recurrence. This capability is particularly beneficial for battery health estimation, where diagnostically relevant information is often localized within narrow voltage windows rather than distributed uniformly over time.

The attention maps reveal that the model consistently focuses on voltage regions associated with electrochemical phase transitions. This behavior explains the superior performance of the proposed model in tracking knee behavior, where degradation accelerates rapidly after a relatively stable period. Such behavior is difficult for LSTM-based models to capture due to their reliance on incremental state propagation.

8.3. Interpretability and Practical Implications

A key advantage of the proposed framework is its inherent interpretability. By analyzing self-attention weights, it is possible to identify which regions of the charging process contribute most strongly to SOH estimation. This property provides valuable insight for battery diagnostics and can support condition-based maintenance strategies.

From a practical perspective, the proposed model is well suited for integration into advanced battery management systems. The required input signals—voltage, current, and temperature—are commonly available in modern BMS hardware, and the additional computation required for ICA and thermal gradients can be implemented offline or at low frequency.

8.4. Deployment Considerations for Resource-Constrained BMS Hardware

In practical BMS deployment, model training can be performed offline using historical data, while on-device execution is typically limited to inference. The proposed framework is compatible with standard BMS sensing capabilities because it relies on voltage, current, and temperature measurements that are routinely available. ICA and thermal-gradient indicators can be computed at a reduced frequency (e.g., periodic diagnostic charging segments) or offloaded to an edge gateway, depending on the computational budget. Moreover, the inference latency summarized in Section 6.6 indicates that real-time execution per charging cycle is feasible for embedded or edge-assisted BMS architectures.

8.5. Limitations and Future Work

Despite its promising performance, this study has several limitations. First, the experimental validation is conducted on a limited number of cells under a single cycling protocol. Future work should extend the analysis to larger battery populations, different chemistries, and varying operating conditions to further assess generalization capability.

Second, the proposed framework focuses on charging data only. Incorporating discharge dynamics and rest-period information may further enhance SOH estimation accuracy. Finally, while attention maps provide qualitative interpretability, more rigorous quantitative links between attention weights and specific degradation mechanisms remain an open research direction.

9. Conclusions

This study proposed a physics-informed Transformer framework for long-term state-of-health estimation of lithium-ion batteries. By integrating electrochemical indicators derived from incremental capacity analysis and thermal-gradient features into a self-attention architecture, the proposed model achieves robust and interpretable SOH estimation across diverse aging behaviors.

Experimental results on four battery samples demonstrate that the proposed approach consistently outperforms an LSTM baseline, particularly under severe non-linear degradation conditions characterized by knee behavior. The ablation study further confirms that physics-informed features are critical for capturing rapid capacity fade, while attention analysis reveals that the model autonomously focuses on physically meaningful voltage regions associated with electrochemical phase transitions.

Overall, the proposed framework provides a practical and explainable solution for battery health monitoring and highlights the potential of combining domain knowledge with attention-based deep learning for advanced battery diagnostics.

Author Contributions: Conceptualization, S.H.P. and S.H.K.; methodology, S.H.K.; software, S.H.P. and S.H.K.; validation, S.H.K. and S.H.P.; formal analysis, S.H.K.; investigation, S.H.P.; resources, S.H.K.; data curation, S.H.P.; writing—original draft preparation, S.H.P. and S.H.K.; writing—review and editing, S.H.K.; visualization, S.H.K.; supervision, S.H.K.; project administration, S.H.K.; funding acquisition, S.H.K. All authors have read and agreed to the published version of the manuscript.

Funding: This research was supported by the Energy Technology Development Program of the Ministry of Trade, Industry and Energy (MOTIE) and the Korea Institute for Advancement of

Technology (KIAT) under Project No. RS-2025-04752996, and by the research grant of Kongju National University in 2025/2026.

Data Availability Statement: The data presented in this study are available from the corresponding author upon reasonable request.

Conflicts of Interest: The authors declare no conflicts of interest.

References

1. Huang, H.; Meng, J.; Wang, Y.; Feng, F.; Cai, L.; Peng, J.; Liu, T. A comprehensively optimized lithium-ion battery state-of-health estimator based on Local Coulomb Counting Curve. *Appl. Energy* **2022**, *322*, 119469. [CrossRef]
2. Seok, J.; Lee, W.; Lee, H.; Park, S.; Chung, C.; Hwang, S.; Yoon, W.S. Aging mechanisms of lithium-ion batteries. *J. Electrochem. Sci. Technol.* **2024**, *15*, 51–66. [CrossRef]
3. Liu, J.; Duan, Q.; Qi, K.; Liu, Y.; Sun, J.; Wang, Z.; Wang, Q. Capacity fading mechanisms and state of health prediction of commercial lithium-ion battery in total lifespan. *J. Energy Storage* **2022**, *46*, 103910. [CrossRef]
4. Roy, P.K.; Shahjalal, M.; Shams, T.; Fly, A.; Stoyanov, S.; Ahsan, M.; Haider, J. A critical review on battery aging and state estimation technologies of lithium-ion batteries: Prospects and issues. *Electronics* **2023**, *12*, 4105. [CrossRef]
5. Wang, J.; Zhang, S.; Li, C.; Wu, L.; Wang, Y. A data-driven method with mode decomposition mechanism for remaining useful life prediction of lithium-ion batteries. *IEEE Trans. Power Electron.* **2022**, *37*, 13684–13695. [CrossRef]
6. Yang, F.; Shi, D.; Lam, K.-h. Modified extended Kalman filtering algorithm for precise voltage and state-of-charge estimations of rechargeable batteries. *J. Energy Storage* **2022**, *56*, 105831. [CrossRef]
7. Theodore, A.M.; Şahin, M.E. Modeling and simulation of a series and parallel battery pack model in MATLAB/Simulink. *Turk. J. Electr. Power Energy Syst.* **2024**, *4*, 2–12. [CrossRef]
8. Buchanan, S.; Crawford, C. Probabilistic lithium-ion battery state-of-health prediction using convolutional neural networks and Gaussian process regression. *J. Energy Storage* **2024**, *76*, 109799. [CrossRef]
9. Bokstaller, J.; Schneider, J.; Lux, S.; vom Brocke, J. Battery health index: Combination of physical and ML-based SoH for continuous health tracking. *IEEE Internet Things J.* **2024**, *11*, 33624–33641. [CrossRef]
10. Dubarry, M.; Anseán, D. Best practices for incremental capacity analysis. *Front. Energy Res.* **2022**, *10*, 1023555. [CrossRef]
11. Thelen, A.; Lui, Y.H.; Shen, S.; Laflamme, S.; Hu, S.; Ye, H.; Hu, C. Integrating physics-based modeling and machine learning for degradation diagnostics of lithium-ion batteries. *Energy Storage Mater.* **2022**, *50*, 668–695. [CrossRef]
12. Ahmed, F.; Abulsaud, K.; Massoud, A.M. On Equivalent Circuit Model-Based State-of-Charge Estimation for Lithium-ion Batteries in Electric Vehicles. *IEEE Access* **2025**, *13*, 69950–69966. [CrossRef]
13. Chen, L.; Xie, S.; Lopes, A.M.; Bao, X. A vision transformer-based deep neural network for state of health estimation of lithium-ion batteries. *Int. J. Electr. Power Energy Syst.* **2023**, *152*, 109233. [CrossRef]
14. Luo, K.; Zheng, H.; Shi, Z. A simple feature extraction method for estimating the whole life cycle state of health of lithium-ion batteries using transformer-based neural network. *J. Power Sources* **2023**, *576*, 233139. [CrossRef]
15. Wang, T.; Zhu, Y.; Zhao, W.; Gong, Y.; Zhang, Z.; Gao, W.; Shang, Y. Capacity degradation analysis and knee point prediction for lithium-ion batteries. *Green Energy Intell. Transp.* **2024**, *3*, 100171. [CrossRef]
16. E, L.; Wang, J.; Yang, R.; Wang, C.; Li, H.; Xiong, R. A physics-informed neural network-based method for predicting degradation trajectories and remaining useful life of supercapacitors. *Green Energy Intell. Transp.* **2025**, *4*, 100291. [CrossRef]
17. Wang, H.; Chen, K.; Chen, Z.; Li, S.; Wang, J.; Wang, P.; Yang, L. State-of-health prediction of lithium-ion batteries: A novel PLO-transformer-LSTM framework with DRT feature engineering. *Comput. Chem. Eng.* **2025**, *205*, 109473. [CrossRef]
18. Li, Y.; Kang, L.; Wang, X.; Xie, D.; Wang, S. State of Health Prediction of Lithium-Ion Batteries Based on Dual-Time-Scale Self-Supervised Learning. *Batteries* **2025**, *11*, 302. [CrossRef]
19. Zhao, Y.; Behdad, S. State of health estimation of electric vehicle batteries using transformer-based neural network. *J. Energy Resour. Technol.* **2024**, *146*, 101703. [CrossRef]
20. Beg, M.; Alcock, K.M.; Sam, V.; Rakshit, S.; Paul, S.; Yu, H.; Goh, K. Transformer autoencoder framework for estimating core temperature of lithium-ion battery from pulse discharge dynamics. *Appl. Therm. Eng.* **2025**, *288*, 129552. [CrossRef]
21. Vaswani, A.; Shazeer, N.; Parmar, N.; Uszkoreit, J.; Jones, L.; Gomez, A.N.; Kaiser, Ł.; Polosukhin, I. Attention is all you need. In *Advances in Neural Information Processing Systems 30*; NIPS Foundation: La Jolla, CA, USA, 2017; Volume 30.

Disclaimer/Publisher's Note: The statements, opinions and data contained in all publications are solely those of the individual author(s) and contributor(s) and not of MDPI and/or the editor(s). MDPI and/or the editor(s) disclaim responsibility for any injury to people or property resulting from any ideas, methods, instructions or products referred to in the content.

batteries

MDPI

Review

A Review of Modelling, State of Charge Estimation and Management Methods of EV Lithium-Ion Batteries

Moayad Albakri and Ahmed Darwish *

School of Engineering, Lancaster University, Lancaster LA1 4YW, UK; m.albakri@lancaster.ac.uk
* Correspondence: a.badawy@lancaster.ac.uk

Abstract

Electric Vehicles (EVs) can contribute significantly to reducing greenhouse gas emissions and addressing climate change problems. Modern EVs are primarily powered by electro-chemical batteries such as lead-acid (Pb-acid), nickel-metal hydride (NiMH), sodium-ion (Na-ion), solid-state and lithium-ion (Li-ion) batteries. When compared to other battery types, Li-ion batteries are the most suitable for EV applications due to their practical features such as their high energy density, high charging and discharging efficiency and extended lifetime. However, the main risk of Li-ion batteries is that they are exposed to thermal runaway phenomena, which raises severe concerns about the safety of EV propulsion systems. Thermal runaways should be considered carefully as they cannot be stopped once they start and can lead to battery explosion. One of the main reasons leading to this phenomenon is abusing the state of charge (SoC) of the battery. Therefore, the battery management system (BMS) plays a crucial role in mitigating the stimulation of the thermal runaway process by accurately estimating and properly managing the battery cells. To help researchers and designers with understanding this matter, this paper proposes a review of the most effective SoC estimation methods for EV Li-ion batteries and links these methods with practical energy management systems in the EV market.

Keywords: electric vehicles; state of charge; battery management systems

1. Introduction

The world is facing a serious climate change issue due to increased pollution caused by greenhouse gas emissions. The global surface temperature has increased by 1.24 °C when compared to levels in the previous century, which has led the global sea level to rise by approximately 25 cm since then [1–3]. The effect of this increase on both temperature and sea level forms a major threat to the future of the planet. Thus, governments and policymakers are focusing on finding solutions that can tackle this threat by reducing dependence on fossil fuels while ensuring that economic growth remains unaffected [4–6].

Transportation is one of the sectors that can contribute to the mitigation of this issue because it is responsible for more than 25% of greenhouse gas emissions. Globally, there are around 1.4 billion light-duty vehicles on the roads, with a prediction to reach 1.75 billion by 2050, and they form a major part of greenhouse gas emissions [7–10]. In this context, electric vehicles (EVs) can play an important role in reducing the pollution associated with the transportation sector by depending on electro-chemical batteries as the energy source instead of petrol or diesel [11–14]. The positive effect of promoting EVs in the transportation sector can be materialised if the batteries are charged by clean energy sources such as solar photovoltaic (PV), wind, tidal, and other similar renewable energy sources. Recently, there

has been strong progress in improving these clean sources, with about 32% of the total electricity being produced by renewable energy sources [7]. The increased deployment of EVs, associated with increased dependence on renewable energy sources, can play a massive role in addressing climate change issues and help bring the global temperature back to a normal, pre-Industrial Revolution level.

As shown in Figure 1, the propulsion system of a typical battery EV (BEV) consists of the traction battery pack, which stores the electrochemical energy, the traction inverter, which directs the electrical energy produced by the battery to the traction motor, the motor controller, which regulates the motor speed and torque, the on-board charger, and other auxiliary components [15]. The battery pack is the most critical component of this propulsion system since it holds a high amount of energy, especially when the travel range of the vehicle is large [16]. Lead-acid (Pb-acid) batteries are safe and mature technologies. However, they have a relatively low energy density of around 60 watt-hour (Wh) per litre and 40 Wh per kg when compared with petrol, which has a useful energy density at the wheels of around 2000 Wh per litre and 2700 Wh per kg [17]. Accordingly, the use of Pb-acid batteries is limited to the low-voltage control system, which is responsible for powering the controllers, the lighting system, and other auxiliary systems that require low currents [18]. The nickel-metal hydride batteries (NiMH) have low energy density, higher self-discharge, and higher cost than the Pb-acid batteries, which makes them unsuitable for EV applications [19]. Sodium-ion (Na-ion) batteries form new technologies that can have lower costs and better safety when compared to other types, such as Lithium-ion (Li-ion) batteries. Their supply chain security is high, and they have fewer geopolitical constraints. However, it is still immature technology and needs significant research effort to be compatible with the modern EV, especially with the desired large travel range of more than 600 km. Solid-state batteries are a promising technology but, similarly to Na-ion batteries, are still immature and expensive. Li-ion batteries have several advantages that make them the most suitable for EV applications. They have the highest energy density and efficiency of 600 Wh per litre and 250 Wh per kg [20–23]. Also, their operational range can last for 3000 charging/discharging cycles, which extends their lifetime to around 15 years. The charging/discharging efficiency can reach 95% with a relatively low self-discharge rate when compared to other battery types [24,25]. The Li-ion batteries benefited from a long research effort to improve their electrical performance, establish their supply chain, and reduce their manufacturing costs. For these reasons, they emerged as powerhouses in both EV and renewable energy storage applications [24,25]. Further information regarding the rationale behind battery cell material design can be found in [26].

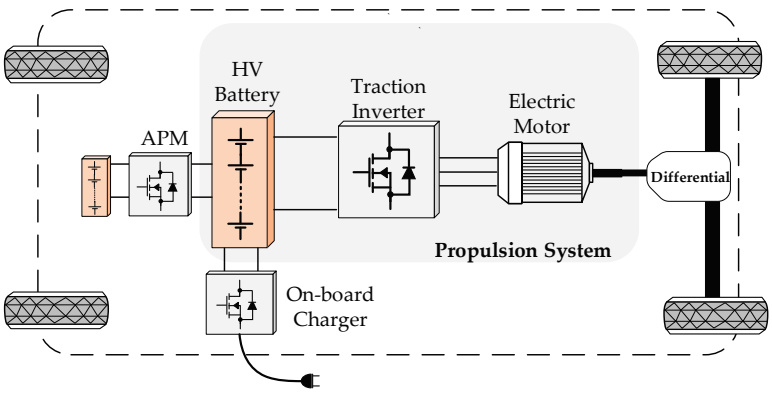

Figure 1. Propulsion system of a typical EV.

Despite the advantages of Li-ion batteries, they suffer from numerous critical operational and safety issues that must be carefully considered to improve the deployment of

EVs and the trust of customers in them [5,27–30]. Li-ion batteries are viewed as a real safety threat since they are thermally unstable, which means that they can catch fire if abused or mishandled during the storage or transportation stages [31]. This can stimulate the thermal runaway process, which can occur days or even weeks after the incident. Allianz group in the United Kingdom warned car traders that there has been an increased rate in the frequency and intensity of EV battery fires in the previous five years [32]. The toxic materials that can be produced from such fires may cause severe consequences to buildings, equipment, and lives [33]. Several incidents occurred between 2020 and 2025, among which a faulty EV battery was dismantled and stored in the maintenance workshop to be inspected, where the thermal runaway process occurred during this waiting period [34,35]. Therefore, understanding the thermal runaway process of Li-ion batteries and dealing properly with this phenomenon is critical for the future of EV deployment, should the Li-ion batteries not be replaced by another safer technology. The proper design of a rechargeable Li-ion battery pack with a liquid-cooled system can improve the thermal management under high discharge rate while ensuring that the cell temperatures stay within the acceptable operating limits [26]. The research in [36] introduced a liquid-cooled hexagonal battery module configuration, which managed to reduce the temperature rise and thermal gradients even at double and triple the maximum discharge currents. The strong heat dissipation capabilities were confirmed by the lowered thermal resistance, showing that the developed modular architecture is a promising solution for both EV and energy storage applications requiring reliable and scalable thermal control.

While driving an EV, its battery pack is discharged, and therefore the battery cells' state-of-charge (SoC) will drop to a low level as the motor is absorbing electrical energy. On-board and off-board chargers are then needed to bring the SoC back to its usual full charge of 100%, provided that the charger has not been disconnected before [37–39]. Several studies have revealed that the probability of the thermal runaway phenomenon increases when the SoC is high and increases further when the cells are either overcharged or have mechanical deformation. When several cells are embedded in a battery pack, either in parallel or in series, the probability of the thermal runaway becomes dependent on several parameters, among which is the balancing technique of the Li-ion cells [40–42]. Thus, the battery management system (BMS), which is responsible for balancing the cells and ensuring that they are operating in the acceptable range, becomes crucial in the safety process [43]. The BMS monitors the battery cells constantly and ensures that they operate at reasonable voltages, currents, and temperature values [44].

The thermal runaway is a chemical process that occurs in Li-ion batteries, producing a huge amount of energy. The process progresses very quickly once started, and it becomes impossible to stop it with any type of cooling, leading to an uncontrollable rise in cell temperature, which is in the range of 150 to 180 °C [45,46]. Usually, the process starts in one cell and spreads quickly to the adjacent ones, even if they are not faulty [47]. The main reasons for this process are mechanical deformation, such as crushing or puncturing the cells, electrical failures resulting from higher voltages or currents, or over-discharging, which leads to reducing the voltages of the cells below the minimum values [48,49]. Also, internal faults in the cells that can be formed during manufacturing or excessive usage can lead to thermal runaway [50,51]. As this phenomenon is dangerous and can affect the progress of EV applications negatively, battery cells and packs must be designed to assume there will be a thermal runaway at least in one cell. Accordingly, the design should reduce the probability of igniting the thermal runaway process, guarantee that the reason can be found if it occurs, reduce the exposure to humans, and reducing the consequences and effects [52,53].

BMSs play a critical role in cell monitoring and balancing functions necessary to ensure even distribution of charge and temperature between the different cells in the battery modules [54–56]. The BMS of a typical EV monitors all voltages, currents, temperatures, and SoCs, controls the charging and discharging processes, and protects them from faults and short circuits [57–61]. Thus, it is necessary for the BMS to be able to measure, detect, and predict the SoC accurately and practically to enable the control algorithms to operate as intended. The accurate detection becomes more complicated when the discharging currents, and accordingly temperatures, vary significantly during the driving mode.

To help EV researchers and designers understand the BMS, this paper reviews the most effective methods and algorithms for SoC estimation in Li-ion batteries. Compared with other reviews in the literature on the same topic, the paper will present the SoC estimation methods to the real-world traction control systems in EVs, with the aim of offering insights that are useful for both academic researchers and practicing engineers in industry.

Section 2 in this paper presents the main parameters of Li-ion batteries that are necessary to understand the operation within the context of EV applications. Section 3 presents the main charge estimation methods for Li-ion batteries, especially those employed in present EV systems. Section 4 reviews the main battery management systems employed in modern EVs as well as the motorsport industry. Section 5 presents the main conclusions of this review.

2. Li-Ion Battery Parameters

The performance of the Li-ion cells depends on many factors that determine the response of the whole battery pack to the required operating conditions of the EV [62]. Thus, understanding these parameters is necessary to help EV battery designers to improve the efficiency of the developed systems, reduce the generated heat, health deterioration with time, and other safety requirements according to the EV specifications. The following subsections present the main parameters:

2.1. Capacity (C)

The battery capacity, which is measured in Ampere-hour (Ah), represents the total electric charge that can be delivered to the EV during a specific period of time at a specified current. The typical capacity of a Li-ion battery varies between 20 Ah and 200 Ah, depending on its construction. For low-capacity cells, the batteries are usually connected in series-parallel combinations to increase the operational capacity and voltage. For example, the Tesla Model 3 EV employs cylindrical 21700 battery cells, which have an average cell capacity of 4.9 Ah and a nominal voltage of 3.6 V [42–44]. The cylindrical cells are usually designed with dimensions of 21 mm in diameter and 70 mm in height, while the weight of the cell is 70 g approximately. To reach the required voltage and capacity, the battery pack of the EV is designed by connecting 96 cells in series and 46 in parallel (91s46p) with a total number of cells of 4416. Therefore, the total nominal voltage and capacity of the battery pack are 355 V and 255 Ah. Table 1 shows the voltage, capacity, and energy of other common EV structures in the industry.

https://doi.org/10.3390/batteries12030092

Table 1. Common EV battery cells and packs.

EV	Cell Type	Cell Capacity (Ah) and Voltage (V)	Pack Construction	Pack Capacity (Ah)	Pack Voltage (V)	Pack Useful Energy (kWh)
Tesla Model 3	Cylindrical 21700 	~4.9 and ~3.6	91s46p	255	355	~80
Chevy Bolt	Pouch NMC622 	~55 and ~3.65	96s3p	165	350	~57
Nissan Leaf	Prismatic NMC 	~55 and ~4	96s4p	260	360	~40
BYD Han	Blade 	~65 and ~3.2	110s3p	195	352	~68.5

The capacity of Li-ion cells is affected negatively by current stresses during both acceleration, regenerative braking, and DC fast charging. During light driving, the typical current absorbed from the battery pack is between 50 A and 100 A, while it increases to 300–800 A during acceleration and DC fast charging [63]. Consequently, the associated power losses increase the temperature of the battery cells, which creates lithium plating risks. The temperatures of the cells must be kept within a specified range to ensure that the lifetime of the cells is not deteriorated [64].

The capacity, and hence the useful energy of the cell, decreases significantly at low temperatures. Operating at high temperatures leads to fast degradation of the cell's capacity and increases the risk of fire ignition. Operating the battery pack under uneven temperatures leads to uneven ageing of the battery cells [65–68]. In this context, the cooling system of the EV battery pack is critical to control the temperatures of the cells and ensure a safe operation. The capacity of Li-ion battery cells reduces with the number of discharged cycles. Figure 2 shows the experimental results of discharging three packs of Li-ion batteries at different discharge currents. The packs are composed of eight Samsung 18650 cells connected in parallel to form a 3.6 V–20 Ah module. The study in [8] presents different long-term tests for different cells.

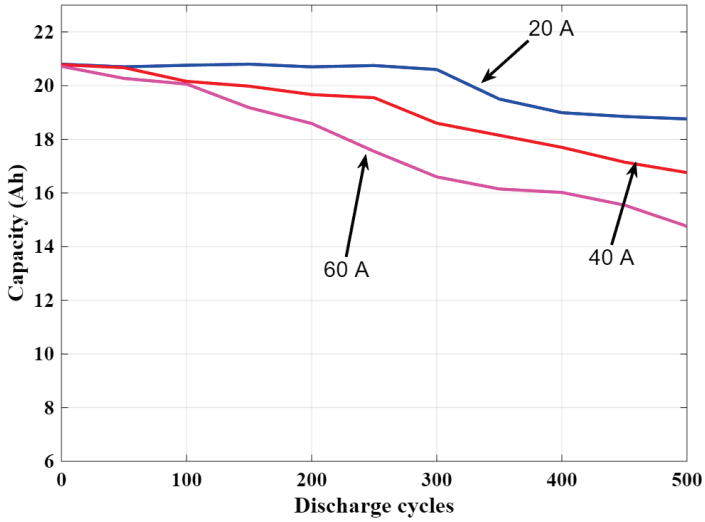

Figure 2. Experimental testing for Li-ion 18650 battery cells under different discharge currents.

Because of the nature of the operation, EV battery packs are subject to high vibrations, especially during acceleration and braking. Excessive vibrations have a negative effect on the capacity of battery cells, where the highest degradation effect occurs at 50 Hz [9–11].

2.2. Internal Resistance (R_i)

The chemical reaction taking place inside the battery cell is a non-linear complicated process. From an electrical design perspective, estimating the internal resistance of Li-ion batteries is necessary in the electrical design process to calculate the voltage loss, heat generation, power capability, and the efficiency of the battery [17–19]. The internal resistance appears in the equivalent electrical circuit of the cell, which can be represented in different structures, see Figure 3. The equivalent circuit comprises an open circuit voltage (E), which is dependent on the SoC of the cell. The internal resistance (R_i) simulates the charge dissipation in the electrical double layer [23,68]. The dynamic resistance and capacitance (R_D and C_D) simulate the diffusion process during current variations.

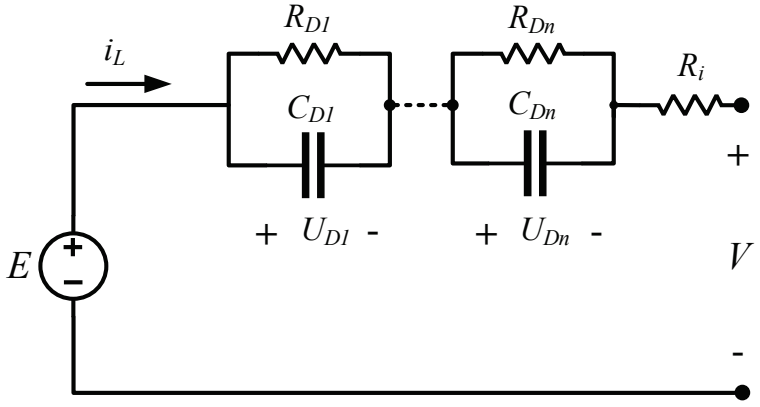

Figure 3. Equivalent circuit of Li-ion battery cell.

An accurate estimation of R_i enables the correct calculation for voltage drops during acceleration and voltage rise during either regenerative braking or charging, which is required to determine the set points for the BMS operation [2]. Also, R_i is used to determine the heat dissipation and, accordingly, the required cooling system. The value can be used to predict hot spots in the battery pack and thermal runaway.

https://doi.org/10.3390/batteries12030092

The solid electrolyte interphase (SEI) is a thin graphite layer created on the anode surface, which plays an important role in protecting the cell, preventing continuous decomposition in the electrolyte, and improving the performance of the cell. However, this layer becomes thicker with operation, leading the internal resistance to increase due to the poor electronic paths [63]. The thickening process of the SEI is accelerated by aggressive driving and harsh braking as the current absorbed from the whole battery pack becomes higher. The thickness of the SEI layer is increased by storing the cells for long durations with either high or low SoC [39,40]. Other mechanical factors, including poor electrolyte wetting, delamination of electrodes, and cell swelling, can increase the thickness of the SEI and hence increase the internal resistance of the cells. Increasing the value of R_i beyond the design limits leads to reducing the output voltage, and hence the current, of the battery pack, meaning that lower torques will be produced [53]. Also, the heat dissipation will increase beyond the capability of the cooling system, which increases the risks of fires, especially when local hotspots are created [54]. High R_i values require a higher voltage from the charger to inject the same current into the battery cells. This means that either the charging process will be slower or it will not be possible, in case the charger cannot increase its output DC voltage [29].

2.3. Energy Efficiency

The amount of the useful energy extracted from the battery cell as a percentage of the charged energy is defined as the energy efficiency (EF). The EF is an indicator of the cell's capability to convert chemical energy to electricity and vice versa [5,20–29]. The EF of a typical Li-ion battery reduces when the SoC is either higher than 80% or lower than 20%. Fast charging and discharging deteriorate the EF of the cell as the increased currents lead to the lithium plating phenomenon, which consumes the charge irreversibly.

To present the EF parameter practically, Figure 4 shows the experimental testing of a Panasonic NCR18650 Li-ion battery (C_{nom} = 3450 mAh and V_{nom} = 3.6 V) during charging at a constant current of 1.75 A, then a constant voltage of 4.2 V. Figure 5 shows the calculated energy stored in the battery cell, where the final value was estimated as 14.66 Wh. It can be seen from Figures 4–6 that the EF for this specific battery cell is ~90% at 670 mA. It has been reduced by increasing the current until it reached ~76% at 6.7 A.

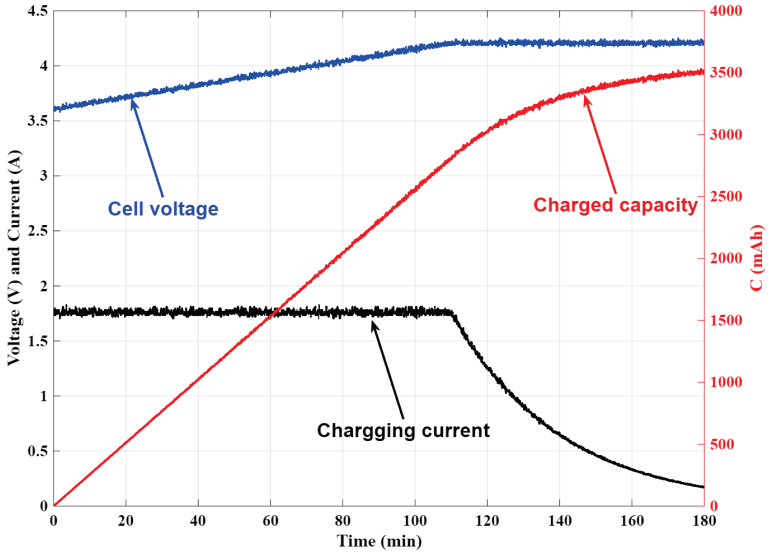

Figure 4. Testing of a Panasonic 18650 Li-ion battery during charging.

https://doi.org/10.3390/batteries12030092

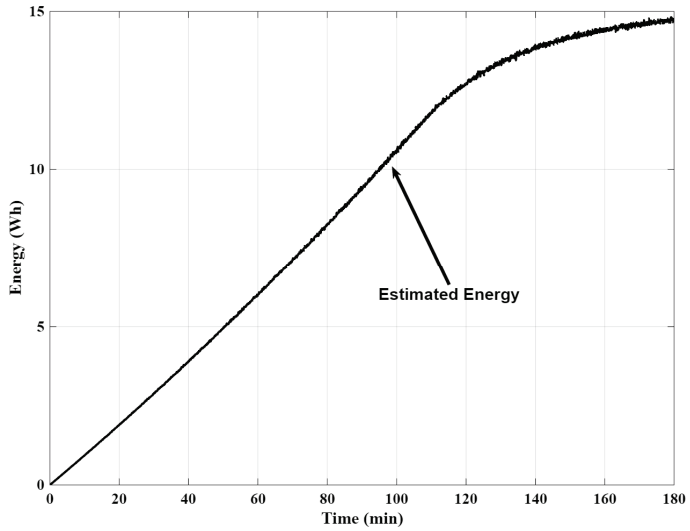

Figure 5. Estimation of the stored energy in the Panasonic 18650 Li-ion battery.

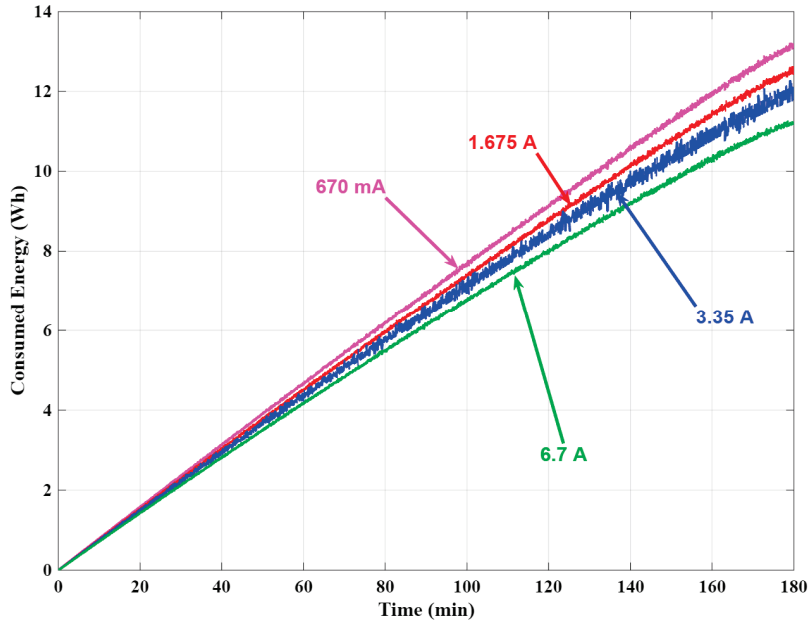

Figure 6. Useful energy of the Panasonic 18650 Li-ion battery cell at constant discharge currents.

2.4. State of Health (SoH)

It should be noted that the previous tests were conducted on one Li-ion battery cell and therefore the values may vary with other cells depending on their state of health (SoH). The SoH is represented as 100% for a new battery and declines with the operation and time. The most critical factor that affects the SoH is the high temperature because it accelerates the side reactions, grows the SEI layer, and can cause electrolyte breakdown. It is estimated that the SoH degradation is doubled for every 10 °C rise in temperature [5]. Also, extremely low temperatures may cause lithium plating risks during charging. Excessive fast charging and discharging have a negative impact on the SoH of the battery and can cause permanent capacity loss due to lithium plating. The internal resistance of the battery cell may increase with higher discharge currents. It is usually advised by battery manufacturers that the cells should not be discharged beyond a certain limit known as the maximum depth of discharge (DoD). The DoD can be calculated from 100%-SoC [2]. It is advised that the cycle life of an EV battery pack can be increased by around 3 times if the DoD is kept above 30%. As the DoD and SoC are directly related to the cell voltage, keeping the latter in the correct

limit is crucial for improving the SoH and extending the lifetime of the battery. In this context, the BMS plays a crucial role in improving the SoH of the EV battery by monitoring, estimating, and controlling the whole system [69].

The SoH of a Li-ion battery has a direct impact on the SoC estimation methods because they rely on the relationship between voltage, current and stored energy, where these relationships are affected by ageing. The degradation of the SoH reduces the nominal capacity of the battery, which means that it holds less energy than assumed. The increase in the internal resistance raises the voltage drops under loading conditions, which in turn affects the SoC estimation.

Several strategies were proposed to improve the SoH of Li-ion batteries and reduce the deterioration due to fast charging and discharge [26,36]. This includes multi-stage constant current (CC) and constant voltage (CV) optimisation, pulse charging, temperature, and adaptive charging profiles according to the estimated SoC. When lithium plating risk is detected at low temperature or high SoC, these strategies can dynamically limit the current to maintain fast charging capability while reducing electrochemical stresses [70–72].

Moreover, effective thermal management can play a crucial role in reducing the growth of the SEI layer, as it can reduce the cell temperatures. Charging control algorithms can incorporate real-time thermal feedback in order to derate the current when the critical thermal conditions are detected [70–72].

2.5. Self-Discharge

Due to the internal chemical reactions that continue to take place inside the cell, Li-ion batteries can lose the stored energy over time, even if they are connected to an electrical load. This self-discharge is accelerated by storing the cells in a high-temperature room, and it can be doubled when the storage temperature exceeds 40 °C. Increasing the SoC above 80% or reducing it below 10% before storage increases the self-discharge phenomenon. Storing a Li-ion battery at a room temperature of 20–25 °C can lead the battery to lose 1–3% of its stored charge per month. This percentage drops to 0.5–1% if the temperature reduces to 10–15 °C [73]. The Li-ion cells have a lower self-discharge when compared with other types, such as nickel-cadmium or lead-acid batteries; however, it is still a critical issue with the progress of EV applications, especially in some African and Asian countries.

3. SoC Estimation

It can be seen from the previous sections that measuring the Li-ion cells' temperature and estimating their SoC are crucial for improving the performance of EV batteries and ensuring the safety of the users. The probability of thermal runaways increases dramatically with high temperatures and over-charging due to lithium plating and electrolyte decomposition. Besides the safety reasons, EV users need to have an accurate prediction for the remaining energy and travel distance, which is directly dependent on the SoC. The accurate estimation of the SoC enables the necessary functions such as determining the charge and discharge limits, torque and speed control, regenerative braking limits, detecting unbalanced cells, and controlling the temperature of the cells. Providing customers with the correct EV warranty conditions depends on the accurate measurement of the SoC, and therefore, it is necessary to improve user trust as users expect the SoC calculations in the EV to be accurate and stable [18–25]. The internal temperature of the Li-ion battery cannot be measured directly due to technical challenges and a lack of sensors. However, the surface temperature can be measured using different sensors, and therefore, the internal temperature can be estimated. Thermocouples can be used to measure the cell surface temperature as well as the temperature of the cooling plates. They can provide a wide temperature range and have a fast response.

https://doi.org/10.3390/batteries12030092

However, they are less accurate when compared with other types, especially when the environment inside the battery box is noisy due to high-frequency switching. Thermistors use semiconductor resistance, which varies strongly with temperature, to sense the surface temperature of the cells as well as the temperature in between the adjacent cells. They can be manufactured with a small size, low cost, and provide high sensitivity to temperature variation. On the downside, they have a nonlinear response to the temperature, which means that the values must be calibrated inside the BMS, and also, unlike thermocouples, they have a limited temperature range. Widely used BMSs such as Orion BMS 2 employ thermistors directly connected to the cells, with the possibility to add an expansion pack, which allows monitoring of different spots in the battery pack. Other automotive-related battery products use temperature sensors that behave like Zener diodes, such as the ones in Li8P25RT battery modules. The module has four-built-in temperature sensors placed in contact with battery cells. The output voltage of the Zener diodes is inversely proportional to the temperature, which can be measured in the range between −40 °C and 120 °C. A summary of the temperature sensing method is presented in Table 2.

Table 2. Summary of temperature sensing of Li-ion EV batteries.

Type	Method	Location	Advantages	Disadvantages
Thermocouple	Voltage generated by temperature difference	▪ Surface	▪ Wide range ▪ Fast response ▪ Low cost	▪ Low accuracy
Resistance Temperature Detector (RTD)	Resistance changes with temperature	▪ Surface ▪ Between cells	▪ Good accuracy ▪ Linear	▪ Expensive ▪ Slow response
Thermistors	Semiconductor resistance varies strongly with temperature	▪ Surface ▪ Between cells ▪ Cooling plates	▪ Small ▪ Sensitive ▪ Low cost	▪ Nonlinear ▪ Low temp. range
Zener diode	Generate voltage inversely proportional to the temperature	▪ Surface ▪ Between cells ▪ Cooling plates	▪ Small ▪ Sensitive	▪ Nonlinear ▪ Expensive

Unlike the temperature, the SoC is not directly measurable and therefore can be only estimated from the voltage, current, and temperature. The next subsections present the most effective methods for SoC estimation that are used in practical BMS devices for EV battery systems.

3.1. Coulomb Counting

Coulomb counting is the most intuitive method to measure the SoC of battery cells as it measures the current $i(t)$ fed into or generated from the battery cell and uses this value to estimate the charge over time t. This charge $Q(t)$ can be calculated from:

$$Q(t) = \int_{t_0}^{t_1} i(t)\, dt \quad (1)$$

https://doi.org/10.3390/batteries12030092

where t_0 is the initial time and t_1 is the time after charging or discharging. Accordingly, the SoC can be estimated from:

$$SoC(t) = SoC(t_0) \; - \; \frac{1}{C_{nom}} \int_{t_0}^{t_1} i(\tau) \, d\tau \tag{2}$$

SoC(t_0) denotes the state of charge at the initial conditions while C_{nom} is the nominal battery capacity in Ah. The integration is conducted continuously in real time as shown in Figure 7.

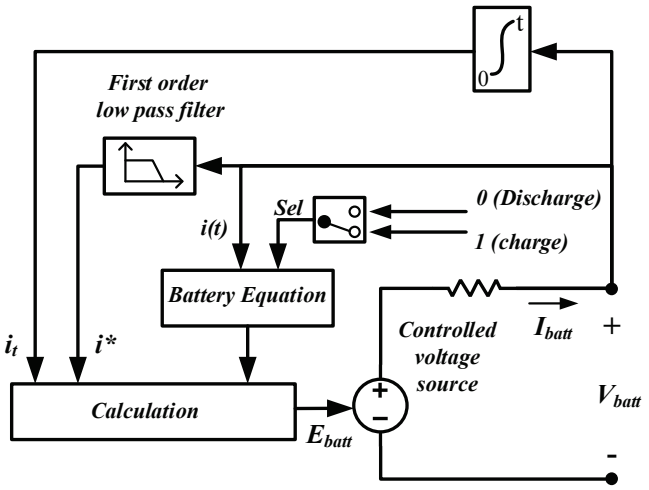

Figure 7. Simplified schematic for coulomb counting method.

The BMS implements the digital integrator using the following discrete equation:

$$SoC_k = SoC_{k-1} - \frac{I_k \cdot \Delta t}{C_{nom}} \tag{3}$$

where I_k is the measured current at a digital sample k and Δt is the sampling interval. It can be seen from Equations (1)–(3) that the coulomb counting method is computationally simple to be conducted by the BMS microcontroller. Also, it works efficiently if the sampling time is short enough to linearize the calculations. The calculations can be conducted online while the EV is driving, braking or when the battery is charging. The main drawback of this method is that the calculations depend mainly on the nominal capacity of the battery cell, which drifts over time as mentioned in Section 2.1. Also, a large error in the current sensor measurement can lead to large drifts in the SoC calculations if not compensated and corrected by the algorithm. The current is usually measured by a Hall effect sensor, which generates a 0–5 V signal compatible with the analogue-to-digital (ADC) converter of the BMS microcontroller, see Figure 8. Other BMSs may use a shunt resistor in series with the battery, where the generated voltage is used to estimate the current. Although this method is cheap, it can cause inaccuracy in the current measurement when the value of the series resistance drifts with the temperature. The initial estimation for the SoC is crucial and must be corrected over time.

Due to the change in the total ampere-hour baseline, the degradation of the SoH of the battery cell can cause underestimation as well as overestimation of the cell's SoC. Therefore, the cell's capacity will need to be recalibrated dynamically using the measured SoH and combined with the periodic recalibration.

https://doi.org/10.3390/batteries12030092

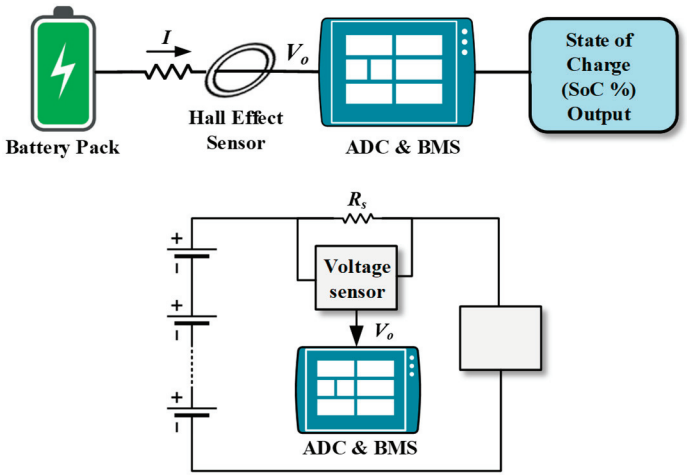

Figure 8. Current measurements in the coulomb counting method.

3.2. Coulomb Counting with Open-Circuit Voltage Loop-Up Table

This method is introduced to improve the performance of the previous method by adding further accuracy for calculating the initial SoC at the beginning of the operation. It can be seen from Figure 4 that there is a direct relation between the voltage and the SoC, although this relation is not linear. This method depends on the coulomb counting method during normal operation, whether driving or charging. Then, the open-circuit voltage (OCV) look-up table is used to calibrate the SoC value and fix the errors that occur over time. The BMS stores a calibrated curve showing the relation between the SoC and the OCV as:

$$SoC = f(OCV, T) \tag{4}$$

where T is the temperature of the cell. Before the operation starts, the BMS measures the voltage of the battery cells and uses the look-up table to estimate the initial SoC at the beginning. Figure 9 shows an example of the function in Equation (4) for a 18650 Li-ion battery cell. During the operation, the BMS uses Equation (4) to estimate the running SoC with time. The BMS then compares the battery's voltage with the stored value when the battery is at rest or when the current is very low. The BMS will then apply correction algorithms to ensure that the stored values are corrected with time. Usually, the Kalman Filter (KF) is used to correct the voltage drifts optimally and update the stored look-up tables.

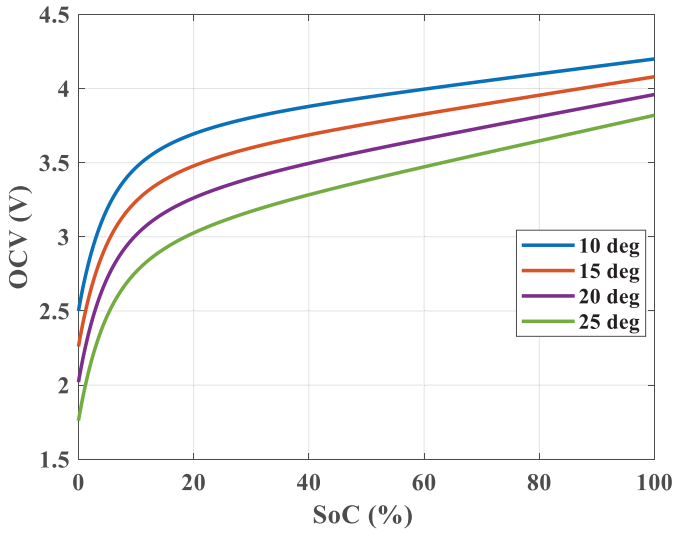

Figure 9. An example of Li-ion battery cell OCV.

https://doi.org/10.3390/batteries12030092

The OCV curves vary with ageing, especially at high and low SoC values, which means that the SoC estimation will drift. Therefore, adaptive OCV tables and SoH correction factors are implemented with the algorithm.

3.3. Model-Based Estimation Methods

Evaluation of the mathematical model of the battery cell can be used to explain the behaviour of the cell at different voltages, currents, charge, and temperature. There are three main categories for model-based SoC estimation methods [38]. The Electrochemical (EM) method, Equivalent Circuit Model (ECM) method, and Electrochemical Impedance Model (EIM) method. The EM method attempts to describe the oxidation, diffusion, and kinetics that occur inside the battery cell [39]. An example is the Doyle-Fuller-Newman model, which uses differential equations to describe the lithium concentration and its effects on the electrochemical voltage and currents [40–42]. Although it is an accurate method, it is complicated mathematically and requires high computational efforts that may not be possible by the microcontroller of the BMS [43]. The ECM method depends on the electrical circuit of the battery cell and attempts to describe the behaviour using equivalent resistors, capacitors, and voltage sources. In this way, the ECM does not describe the internal physical reactions of the cell and therefore depends on the parameter identification. On the other hand, they required lower computational effort because they did not need accurate physical quantities [18]. The EIM method represents the behaviour of the battery cell using the analysis of the electrochemical impedance as a function of frequency. It employs the ohmic resistance, charge transfer resistance, double-layer capacitance and diffusion phenomenon [19]. The EIM method is very sensitive to changes in SoC and can provide better fault detection and diagnosis. However, because of its complexity and dependence on frequency analysis, it is less common for practical EV BMSs [58].

The three model-based methods can be integrated with mathematical algorithms such as the Kalman Filter (KM), which can aid in an accurate estimation of the SoC [16]. The KM predicts the next state using the prediction mathematical algorithm and then corrects the model using the real measurements in the next sample [19]. The accuracy and speed of the algorithm convergence depend mainly on the parameter selections of the filter. Also, the performance is affected significantly by Gaussian noise and the errors in estimating the initial SoC.

The parameters used in the model-based method, such as internal resistance, polarisation, and diffusion elements, vary with time and ageing, which can lead to model divergence. Therefore, adaptive parameter estimation, such as dual KF for both SoC and SoH, can be employed to allow online identification of resistances and capacitances.

3.4. Data-Driven SoC Estimation Methods

The internal structure of the battery cell can be modelled without the need for describing the parameters explicitly. This means that the battery cell can be modelled as a black box which predicts the system behaviour using the measured quantities without relying on the physical knowledge of the system's internal chemical behaviour. This data-driven method is effective in processing the non-linear behaviour of the Li-ion battery cell and estimating the SoC. It can provide a high level of prediction where the complex relationship between the inputs and outputs is extracted without the need for an explicit physical model.

Artificial Neural Networks (ANNs) have been used where the currents, voltages and temperatures are fed as inputs while the SoC is extracted as an output [74,75]. Fuzzy logic controllers and support vector machines can be used to represent the complicated nonlinear behaviour of the Li-ion battery cells, which can provide good predictions and convergence if they are given sufficient initial and operational conditions. A good example is given

in [76] where the proposed SoC estimation method employs a Gaussian Process Regression (GPR) algorithm with KF to improve the prediction of the system's parameters. The GPR algorithm learns the battery behaviour from data while the KF recursively estimates the SoC during the operation. As shown in Figure 10, the measured current and voltage are divided into training data to build the GPR models and test data to validate the models online. The GPR-based state model learns the SoC changing behaviour as a function of current and time [77]. Using a Gaussian process hypothesis and Hyperparameter optimisation, it then captures the dynamics of the battery without an explicit physical model. The GPR-based model then learns the relationship between the SoC, flowing currents, and terminal voltages to predict the battery cell's voltage from the estimated SoC and measured current [78]. The KF runs in real time to predict the SoC in the next sample and estimates the associated uncertainty. In the next sample, it corrects the SoC from the measured voltage and current and then re-evaluates the uncertainty.

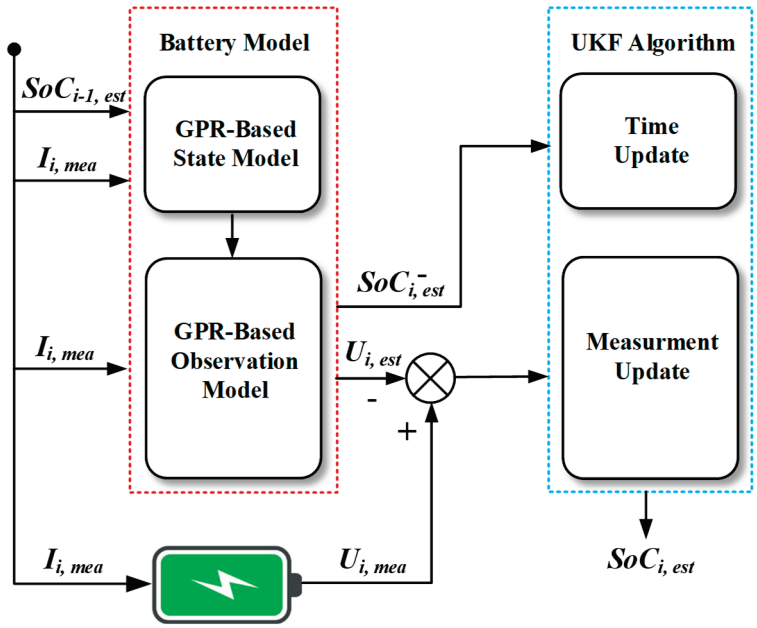

Figure 10. Schematic diagram for the Data Driven method in [76].

The method in Figure 10 has been reproduced experimentally using a 18650 Li-ion battery, where the results of these experiments are shown in Figure 11. The voltage of the cell is measured as shown in Figure 11a with the current profile as in Figure 11b. The estimated and reference SoCs are shown together in Figure 11c.

The method allows for a good prediction of the remaining SoC in the EV battery cells according to the tuning of the GPR algorithms. The experimental results confirmed the good accuracy and the low estimation error with good robustness. However, it is noted that the online algorithm requires a high computational burden, which necessitates an expensive microcontroller in the BMS. Therefore, the method can be used as an assistive high-level algorithm, depending on the conventional coulomb counting methods as primary SoC estimators [73–78].

The data-driven and Artificial Intelligence methods are usually trained on fresh battery cells, and therefore, the prediction may degrade when the SoH declines. Thus, periodic retraining and/or online learning may be required to include the effect of SoH degradation on the model and its resultant data.

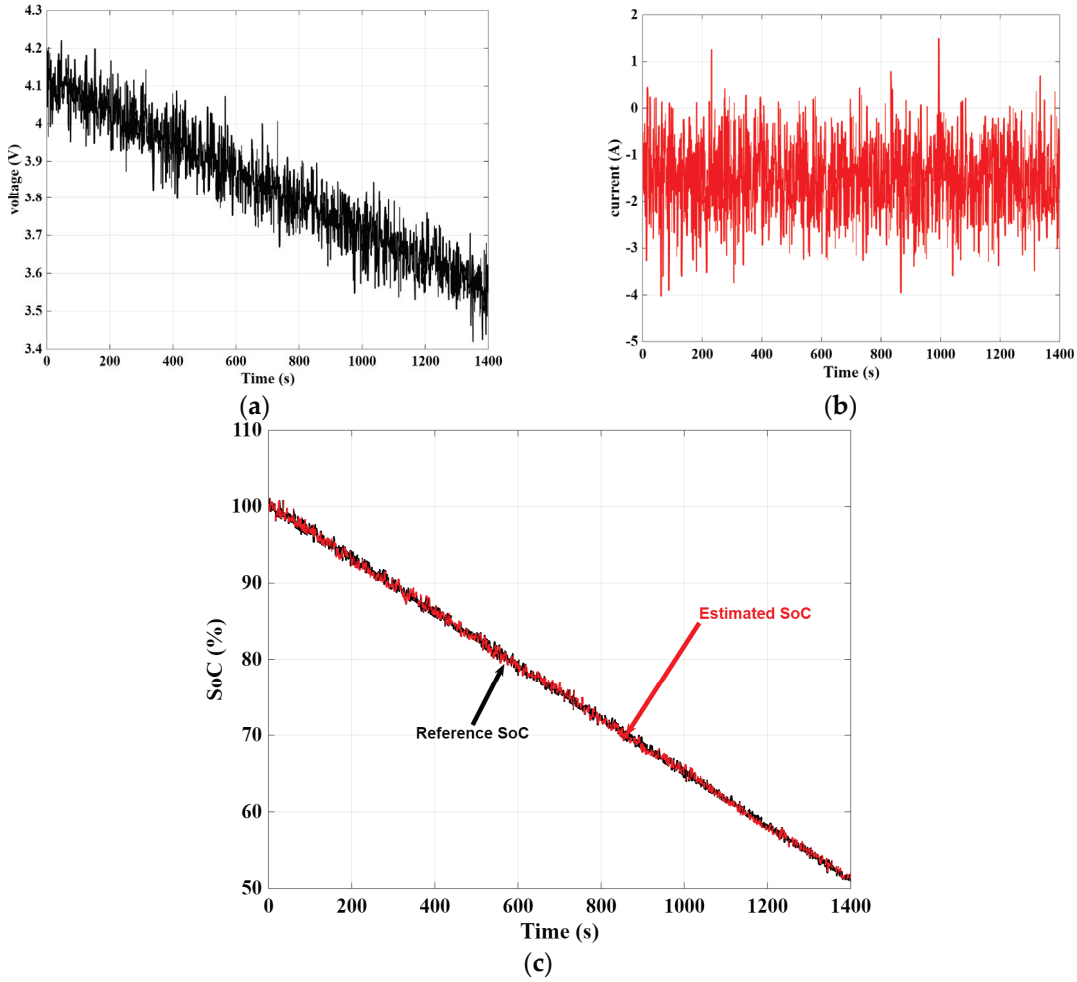

Figure 11. Reproduced SoC estimation of 18650 battery cell based on the data-driven method in [76]: (**a**) cell voltage, (**b**) current, and (**c**) references and estimated SoC.

3.5. Comparative Evaluation of SoC Estimation Methods

Based on the presented methods, this subsection will provide a comparative evaluation of SoC estimation methods in terms of accuracy, computational cost, robustness, and suitability for EV applications.

3.5.1. Accuracy

Pure coulomb counting methods are accurate in short-time intervals but suffer from cumulative charge calculation drifts during long durations. The error in estimating the SoC of a typical EV battery can exceed 5% overtime, which may not be corrected, as it may increase to 10% with current sensor inaccuracy, capacity uncertainty, and discretisation errors by the microcontroller during integrating the charger. Thus, adding a periodic correction using an OCV-SoC lookup table can improve the long-term accuracy. It should be noted that this will mainly depend on the availability of rest durations where the algorithm can rectify the errors. In EV applications, the accuracy of a coulomb counting method with an OCV lookup table can provide moderate accuracy.

The Model-based SoC methods, including KF-based techniques, can provide high dynamic accuracy by combining the discrete current integration with voltage feedback correction techniques. The error of these methods in EV applications is usually in the range of 2–3% under standard EV driving cycles. It should be noted that the performance of these methods will depend mainly on the correct parameter identification and the effectiveness of the model fidelity.

https://doi.org/10.3390/batteries12030092

The data-driven methods provide lower errors compared to the model-based SoC estimation methods. The accuracy in these methods depends mainly on the correct representation of the trained datasets, the level of including the temperature and ageing effects, and the modification of the data with any degradation under unseen conditions.

3.5.2. Computation Cost

The computational demand of the coulomb counting methods is minimal, as a single numerical integration step is conducted in each sampling period. Accordingly, the required memory is relatively small when compared to other methods, which makes this method more suitable for low-cost microcontrollers. Incorporating an OCV lookup table to improve the accuracy will add more computational efforts, especially when interpolation is required. However, this method remains feasible for EV applications, especially for low-end automotive hardware systems.

The Model-based model SoC estimation methods require moderate computational cost, especially when matrix multiplication is needed. However, there are several microcontrollers available in the EV market that can handle the implementation of these methods effectively while keeping the cost balanced with the performance gains.

The data-driven methods require higher computational efforts, especially when the feedforward neural networks and deep models are necessary. The required memory is significantly larger than that of the other SoC estimation methods, especially when real-time operation is required.

3.5.3. Robustness

Compared to other SoC estimation methods, the coulomb counting method exhibits lower robustness due to its sensitivity to errors and offsets in current measurement, in ability to correct the integrated errors, and its incapability to detect ageing. Adding an OCV lookup table to the coulomb counting technique can improve the robustness if the rest periods are sufficient to update the OCV curves with ageing. It should be noted that the performance will deteriorate if temperature and ageing are not detected and modelled.

The Model-based methods increase the robustness of the SoC estimation as they can include the temperature states of the battery cells. The method can also mitigate the errors in the current and voltage measurements using internal filtering. The SoH estimation can be included to extend the robustness of the whole estimation method.

The data-driven methods improve the robustness significantly within the training domain. However, as it is a data-dependent method, it becomes weaker outside the training distribution with new chemistries, and ageing will require data retraining.

3.5.4. Suitability for EV Applications

Based on the presented discussion, it can be understood that coulomb counting methods are not suitable for EV applications as standalone SoC estimators for the EV battery pack because of their drift and limited robustness. Incorporating the OCV lookup table makes the SoC estimator more suitable for low-cost EVs, medium hybrid vehicles, and EV systems with long rest periods. Model-based SoC estimators are highly suitable for commercial EV battery systems as they offer high dynamic accuracy, real-time feasibility, and strong noise rejection. It can be seen as the optimum trade-off between performance, cost and complexity. The data-driven SoC estimators are promising for next-generation BMSs, especially if they can be combined with adaptive learning, where the models can update themselves after deployment to include battery ageing, temperature dependence, cell-to-cell variability, and other relevant issues. However, this comes at the cost of increased sensitivity to domain change, higher computational efforts, and increased challenges to

https://doi.org/10.3390/batteries12030092

comply with the strict EV safety conditions. The main findings of this comparison are summarised in Table 3.

Table 3. Summary of comparison of SoC estimators.

Method	Coulomb Counting	Coulomb Counting with OCV	Model-Based	Data Driven
Accuracy	Low	Medium	High	High with training
Drift	Poor due to accumulating errors	Moderate	Good	Retraining-dependent
Temperature robustness	Poor	Moderate	Good	Data-dependent
Ageing robustness	Poor	Limited	Good	Limited without training
Computational cost	Very low	Low	Medium	High
Memory	Minimal	Low	Moderate	High
Sensors	Current	Current Voltage	Current Voltage Temperature	Current Voltage Temperature
Implementation complexity	Simple	Simple	Moderate	High
Real-time feasibility in automotive applications	Excellent	Excellent	Excellent	Feasible
Suitability for EV applications	Limited	Moderate	Highly suitable	Promising but not dominant

3.5.5. Examples for EV SoC Estimators

Recently, model-based SoC estimators have been used widely in modern EV battery systems [79–83]. However, EV manufacturers usually combine more than one method of SoC estimation. For example, the Toyota Prius employs robust KF observers with a conservative lookup table for calibration. Their old Plug-in Hybrid EV (PHEV) combined the coulomb counting method with an OCV lookup table for calibration. Tesla (Model S, 3, X, and Y) uses advanced KF variants for SoH and SoC estimators, where these techniques are usually patented. They also use a capacity buffer and multiple correction strategies to ensure accuracy and protect the system against over- or under-estimation. BMW (iX, i4, iX3) has an energy management system based on a robust model estimation with the SoC tracked across the temperature ranges. Other companies, such as Renault and Nissan, still use coulomb counting methods with periodic OCV corrections. Table 4 summarises the main SoC estimation methods employed in common modern EVs.

Table 4. Main SoC estimation methods in common modern EVs.

Make	Likely SoC Estimation Approach	Notes
Tesla	Model-based (KF) + Coulomb Counting + OCV	Advanced observer filters
GM Ultium	Model-based + Adaptive Filtering	Modular battery system with wireless BMS
Hyundai/Kia (E-GMP)	Model-based (KF)	Predictive BMS

Table 4. *Cont.*

Make	Likely SoC Estimation Approach	Notes
Mercedes-Benz EQ	Model-based (KF)	Modular BMS
Ford Mach-E/F-150 Lightning	Model-based	Conventional Automotive System
Lucid Air	Model-based	High accuracy
Porsche Taycan	Adaptive Model-based	Emphasis on thermal monitoring
Jaguar i-PACE	Model-based	Automotive filter logic
Honda e/Acura EVs	Model-based	-
Chinese EVs (NIO/XPeng/Li Auto)	Not reported	Likely Model-based

4. Energy Management Systems

A BMS in an EV is a critical electronic and electrical system responsible for monitoring the cells' voltages, currents, and temperatures in addition to other components such as SoC and SoH [84–86]. The BMS protects the cells from being charged above or below the safe limits [57]. It monitors the thermal quantities and operates the cooling system as required [54]. It also plays an important role in balancing the charge evenly across the cells. The number of cells increases with the energy capacity of the EV. Increasing this capacity is essential to increase the travel distance of the EV and therefore reduce customers' anxiety about EVs [58]. The BMS functions become more challenging with the increased number of Li-ion battery cells in the system because the physical connections become numerous and the computational effort increases accordingly [59].

Because several cells are connected in series, their voltage differences must be maintained within a small range, practically 10 mV, with a temperature difference of around 3 °C. If the voltage differences are high while the current flowing through from the cells is the same during discharging, the absorbed energy from the cells will be different, which will be reflected in their temperatures [60]. Also, the low-SoC cells may be over-discharged, which can cause copper dissolution and possible internal fault [61]. During the charging process, the cells with high SoC may overcharge, which leads to lithium plating risks and potentially thermal runaway [45–48]. A large mismatch between the cells' voltages, and hence SoCs, can lead to different ageing rates, which means that the total pack's voltage can be within the safe range while some cells are at risk of destruction [51–53]. The BMS helps the EV system to unify the states of the cells as much as possible, so their lifetime is increased. The lifetime of a typical EV battery pack is in the range of 10–15 years.

Balancing the SoC of Li-ion batteries is the only practical solution in the EV application because replacing the cells individually is not usually possible, which means that the battery pack is as strong as its weakest battery cell [87]. Thus, the BMS should measure cell voltages, identify divergence, and balance cells either actively or passively. The balancing process prevents this divergence from becoming catastrophic [39,43].

A typical EV battery system is composed of series modules, sometimes referred to as segments, which boost the voltage to the required voltage. These modules are composed of a series/parallel combination of Li-ion battery cells to boost both voltage and capacity. For example, the 355 V Tesla Model X battery is composed of 16 modules in series, each module is composed of 6 in series and 74 in parallel cylindrical 18650 Li-ion battery cells. In total, the EV battery pack is seen as a 96s74p system, see Figure 12. The next subsections will present an overview of the main configurations and requirements of practical BMSs in the EV market.

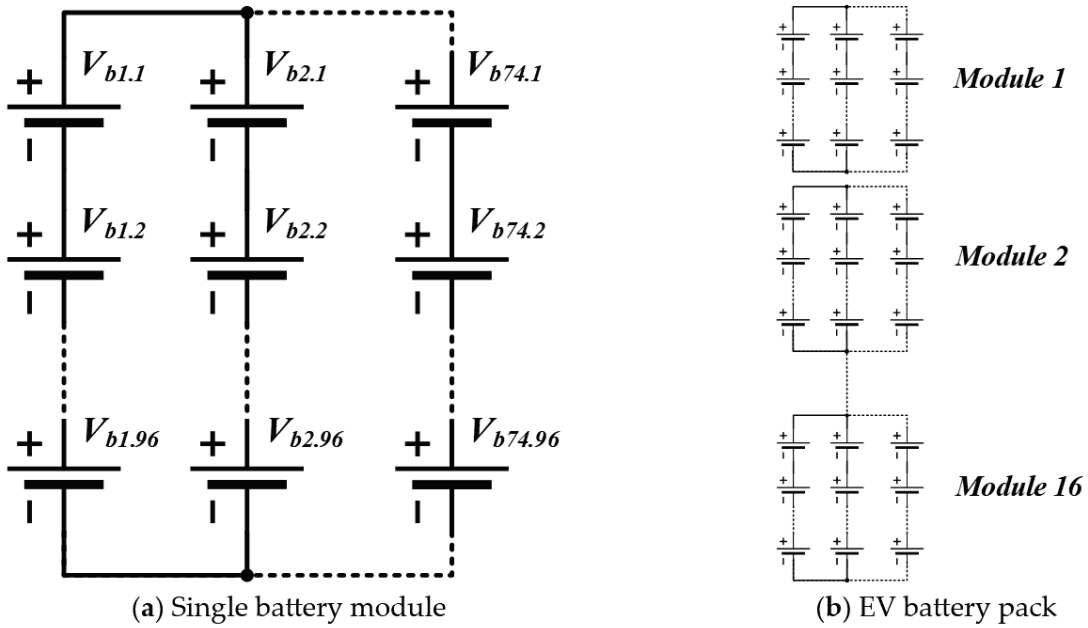

Figure 12. Tesla Model X battery configuration.

4.1. Centralised BMS

A centralised BMS monitors all cells or modules using one controller, where the voltage, current, and temperature-sensing wires are connected directly between the components and this single unit [88–91]. The cell balancing, charge estimation, device protection, and fault diagnostics are handled in one electronic control unit (ECU), see Figure 13, where a single printed circuit board (PCB) is responsible for monitoring the battery cells and taking the appropriate actions.

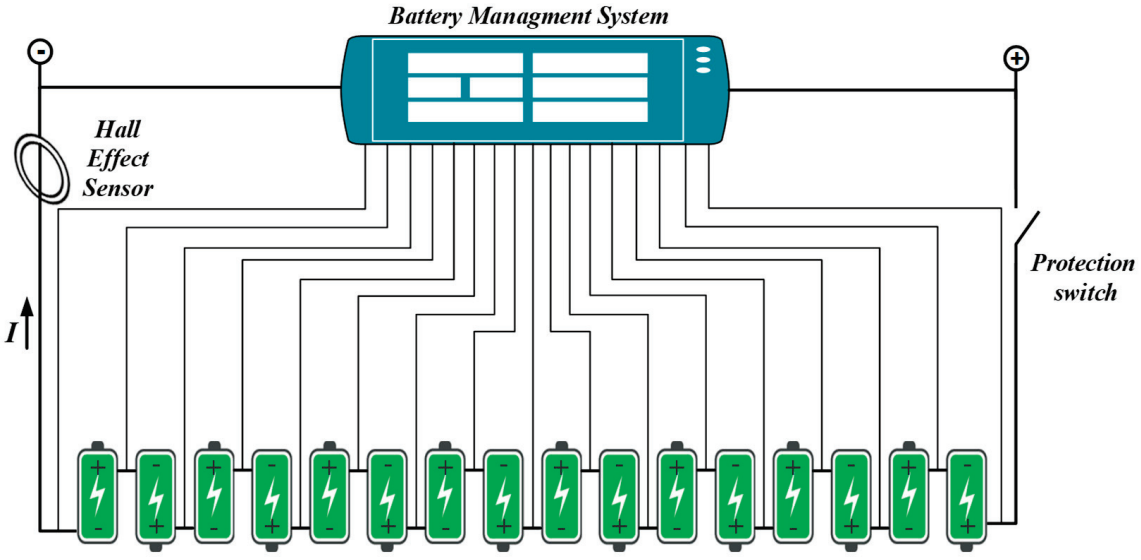

Figure 13. Centralised BMS system.

The centralised BMSs have been preferred in EV systems during the past decades because of their simple and economical construction compared to other decentralised and modular systems. Because there are no master–slave communication channels, fewer ECUs can be used, which makes it easier to design, manufacture, commission, and debug. The reduced component count leads to reduced overall cost, which makes it attractive for low-voltage and low-cell-count systems [92,93]. The direct measurement of all cells

using hardware connections and wires reduces the latency of measurement signals, which improves the fast protection of the battery components [94,95]. Because the measurements are sent directly to the central ECU, the SoC estimation and balancing algorithm run in the same unit, which improves the efficiency and simplifies the validation and safety analyses.

On the downside, wiring becomes excessive when the cell counts increase. An example is shown in Figure 14, where when the number of series cells increases to 72, the number of voltage measurement wires increases to 73, which adds complexity to the design process. The long analogue signal wires increase the noise susceptibility in the system and add to the weight of the system. Also, the troubleshooting process becomes more complicated with a single-point failure with one ECU, which means that the whole system will be out of service if this central unit is damaged. Also, these configurations have constraints on the placement of the thermal measurement sensors, as they should be close to the ECU for signal integrity issues. This goes against the main target of distributed thermal measurement sensors, which is to measure the hotspot areas in the battery pack, especially those that are at the corners of the container and between the plates.

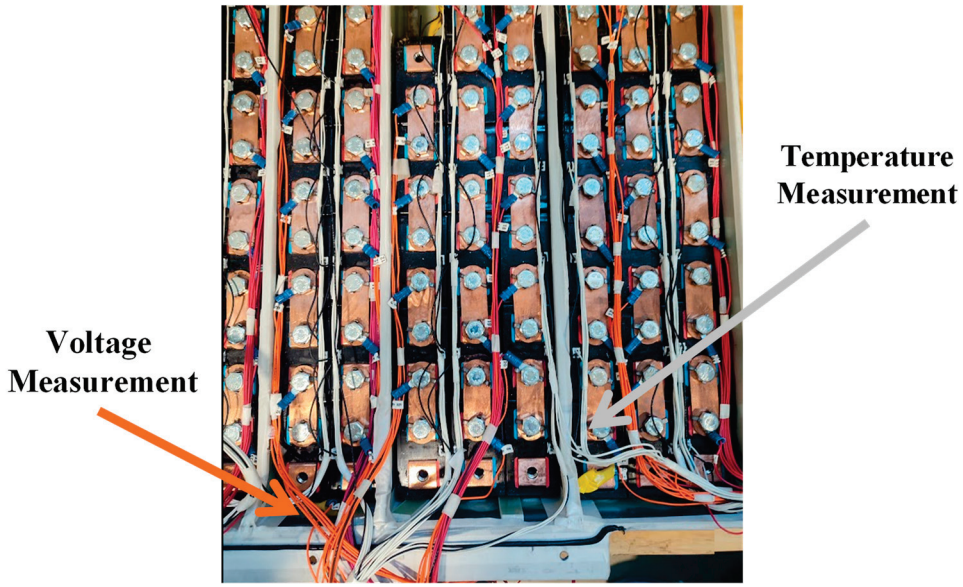

Figure 14. An example of connections in a centralised BMS.

For these reasons, a centralised BMS is more suitable for small-sized EVs that are designed to operate at low speeds and hence require lower voltages. Centralised BMS configurations are widely used in motorsport EVs, especially in university undergraduate student competitions, as well as in research vehicles. An example is the ORION BMS2 centralised system, which is used extensively in Formula Student (FS) competitions. As shown in Figure 15, the central unit measures cell voltages, temperatures and currents using the directly connected cables and estimates the SoC of the cells and pack using the coulomb counting method with the aid of look-up tables, as explained earlier in Section 3.

https://doi.org/10.3390/batteries12030092

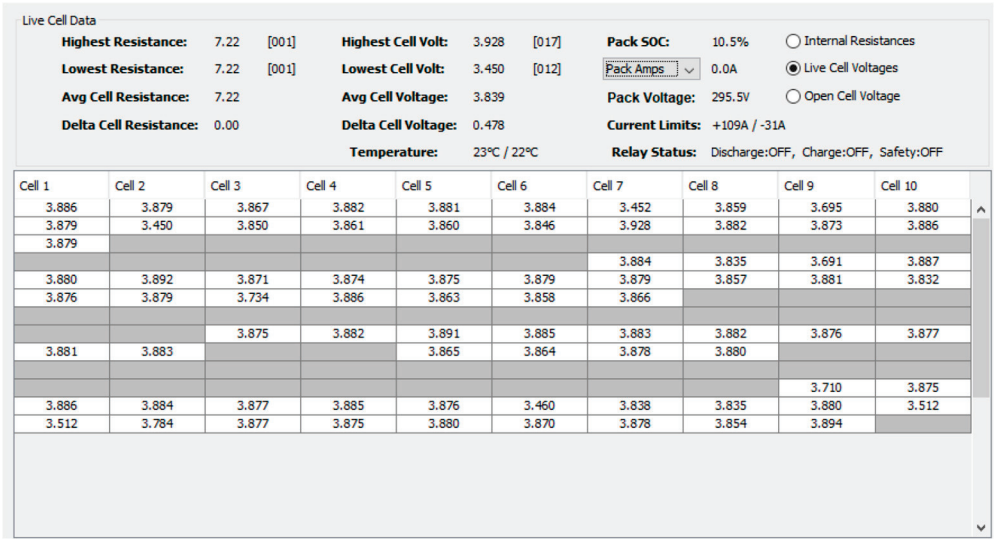

(**a**)

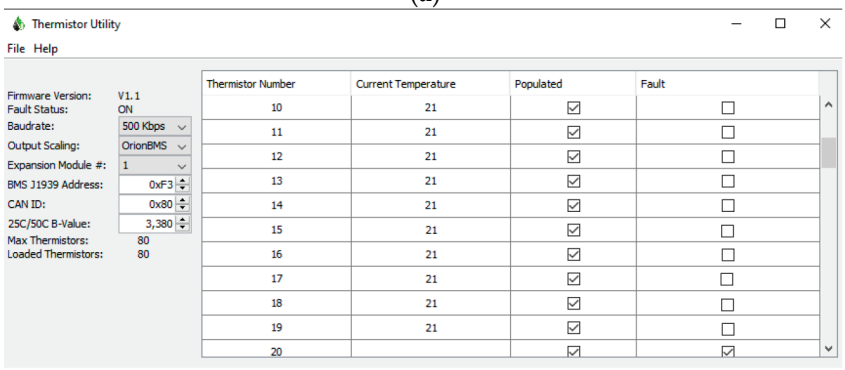

(**b**)

Figure 15. Live results from a centralised BMS: (**a**) voltages, currents, and SoC. (**b**) Temperatures.

4.2. Modular BMS

Modular BMS architectures are widely used in modern EV propulsion systems, especially when the battery capacity and voltage are increased. The modular BMS is referred to in some textbooks, papers, and industrial notes as Distributed BMS [96–99]. In such systems, local monitoring ECUs are installed on each battery module, from where they communicate with a global ECU that coordinates the local ones via a suitable communication link. The most common communication link is the Controller Area Network (CAN) bus.

The modular BMS structure allows for a high degree of scalability when additional battery modules are required. As shown in Figure 16, each group of battery cells is controlled by a local BMS module, which monitors the voltages, currents, and temperature of the group. The local BMS module sends the measurements to the master controller via the communication link. Unlike the centralised structure, the modular BMS allows operating at 800 V, which is a trend in the EV market recently. Voltage and temperature sensors can be placed very close to the battery cells, allowing better observability and controllability over the battery pack. There is no need for long high-voltage wires connected between the cells and the global BMS because this is replaced by the digital communication link. This reduces the harness weight and the number of hardware failure points [99–101]. The modular structure improves the fault diagnostic process and helps in identifying the faulty cell in a shorter time compared to the centralised BMS. One of the most important features of this type is that each module can be tested before the pack is assembled in the EV. For these reasons, several major EV manufacturers depend on the modular BMS architecture for their designs, see Table 5.

https://doi.org/10.3390/batteries12030092

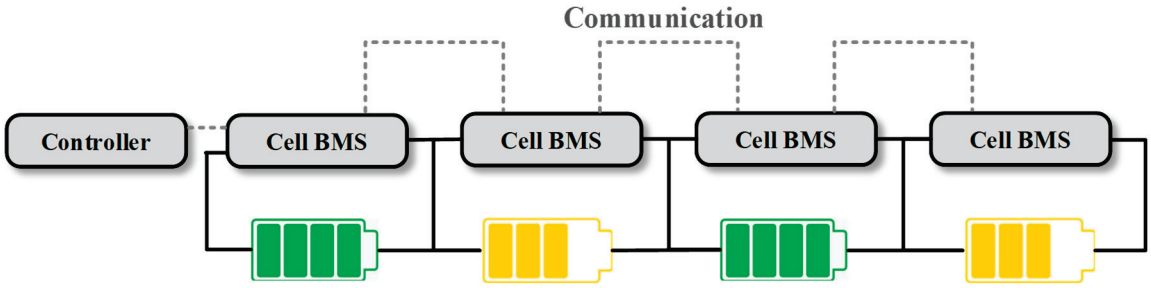

Figure 16. Modular BMS.

Table 5. Examples for EVs with modular BMS.

Model	Energy	Voltage	Target Range	Notes
Tesla Model 3	82 kWh (76 kWh usable)	375 V	470 km	Cylindrical NCA cells
Nissan Leaf	40 kWh (39 kWh usable)	350 V	270 km	Prismatic
Chevrolet Bolt	65 kWh	350–400 V	410 km	Pouch
BYD Han Base	76.9 kWh	400 V	605 km	LFP Blade
BYD Hand Flagship	76.9 kWh	400	610 km	LFP Blade

On the downside, the cost of modular BMS is higher than that of the centralised system, especially for low-voltage packs. This is due to the increased count of PCBs, ECUs, and isolation systems. The robustness of the communication link is critical for the operation of the EV.

The failure of the communication link due to interference issues, which increase with the increasing switching frequency of the propulsion inverter. Increasing this switching frequency is essential in modern EV systems to reduce the size and weight of the propulsion inverters and motors. The high mechanical vibration and shocks that are natural in this application can lead to severe issues in the communication link, which must be carefully addressed. One of the common examples of modular BMS employed in the automotive and motorsport industry is the EMUS BMS shown in Figure 17. The system is suitable for Li-ion cylindrical and pouch cells with a CAN communication link, which can operate at baud rates from 50 to 1000 kbits per second. The cells are monitored and managed by cell group modules, which can accommodate up to 16 cells in series. The cell group modules can be powered by the cells themselves, and the communication between cell group modules is established via a daisy chain. The system can work efficiently for up to 800 V and high-capacity EVs.

Usually, the BMS is required to send a safety signal to the central controller of the EV to ensure that all components are operating within an acceptable range in terms of voltages, temperatures, SoC, and currents. This safety signal trips the propulsion system by disconnecting the EV battery from the propulsion inverter as a safety measure. One of the major drawbacks of connecting the cell group modules in series is the exposure to losing the whole link if a segment of the chain is broken due to mechanical or vibration shocks. This leads to sending a false tripping signal to the central controller and disconnecting the propulsion system unnecessarily. Figure 18 shows the experiments for this unnecessary tripping case when the daisy chain communication of a 400 V battery system is disconnected from a BAMOCARD3 three-phase voltage source inverter driving an EMRAX 208 Permanent Magnet Synchronous Motor. Figure 18a shows the total current absorbed by the battery pack, and Figure 18b shows the total voltage of the battery pack as measured by the three-phase inverter, along with the real voltage of the battery pack. Figure 18c shows the torque and speed of the motor.

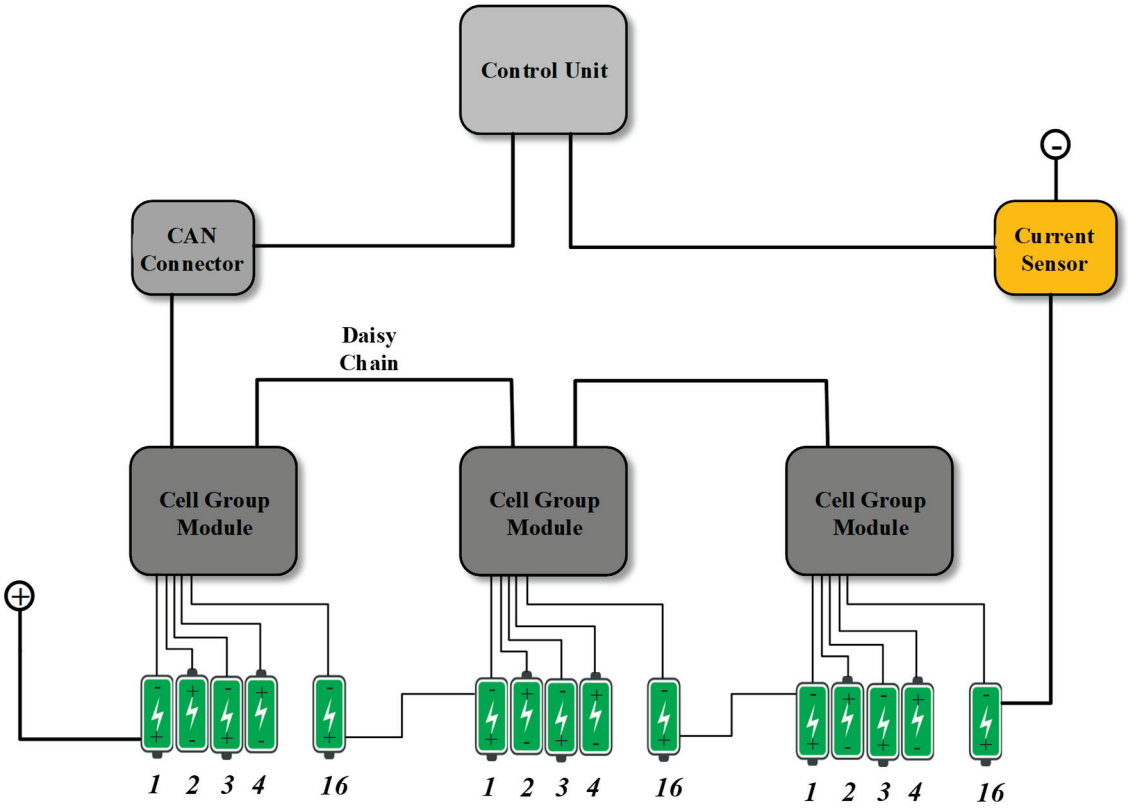

Figure 17. EMUS modular (distributed) BMS.

Some research efforts have attempted to address this practical problem and reduce the impact of communication failures on the performance of the EV propulsion system. In [102], a redundant Modula BMS included a multi-channel, bi-directional daisy-chained communication loop, which improves the redundancy of the communication link.

As shown in Figure 19, the central microcontroller manages the components at a system level, where it communicates with the local units through the redundant daisy chain. Each local unit monitors, controls corresponding battery cells, and communicates commands via the differentially connected daisy-chain loop, which uses several communication channels in different frequency ranges in parallel. Although the proposed system is likely to fix the false tripping issue discussed in Figure 18, it should be noted that the authors could not test this practically in this review paper.

4.3. Decentralised BMS

In this system, each cell or a small group of cells has its own control system and there is no central BMS unit to master the communication, commands, and responses [44]. This architecture is introduced to reduce the problems of the centralised control structures, see Figure 20. The BMS local units monitor and control the cells individually and function locally [57]. The communication link eases the exchange of information and the coordination between the local units. The system reduces the points of failure, increases the controllability and observability of the cells, and improves the scalability of the system [58]. On the other hand, the system is expensive when compared to other types due to the increased electronics per cell. Due to the lack of a central controller, the local units make decisions individually, which requires a very complicated software algorithm for each unit to communicate and synchronise with other units safely [61]. Usually, droop control algorithms are used to ensure even power sharing between the series-connected batteries in the group [103–105].

https://doi.org/10.3390/batteries12030092

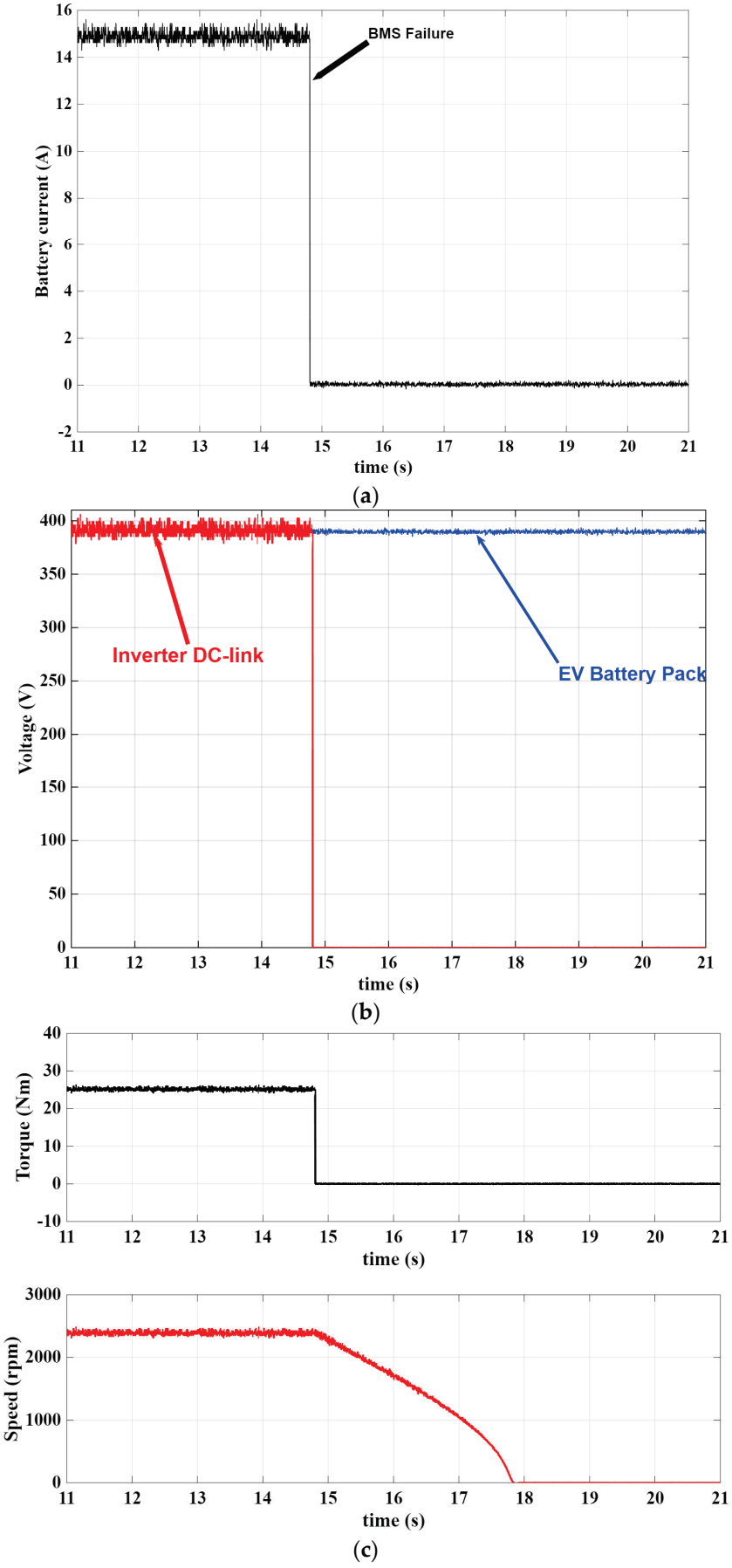

Figure 18. Experimental results for a modular BMS-based EV system: (**a**) EV battery current, (**b**) battery and DC-link voltage, and (**c**) EV torque and speed.

https://doi.org/10.3390/batteries12030092

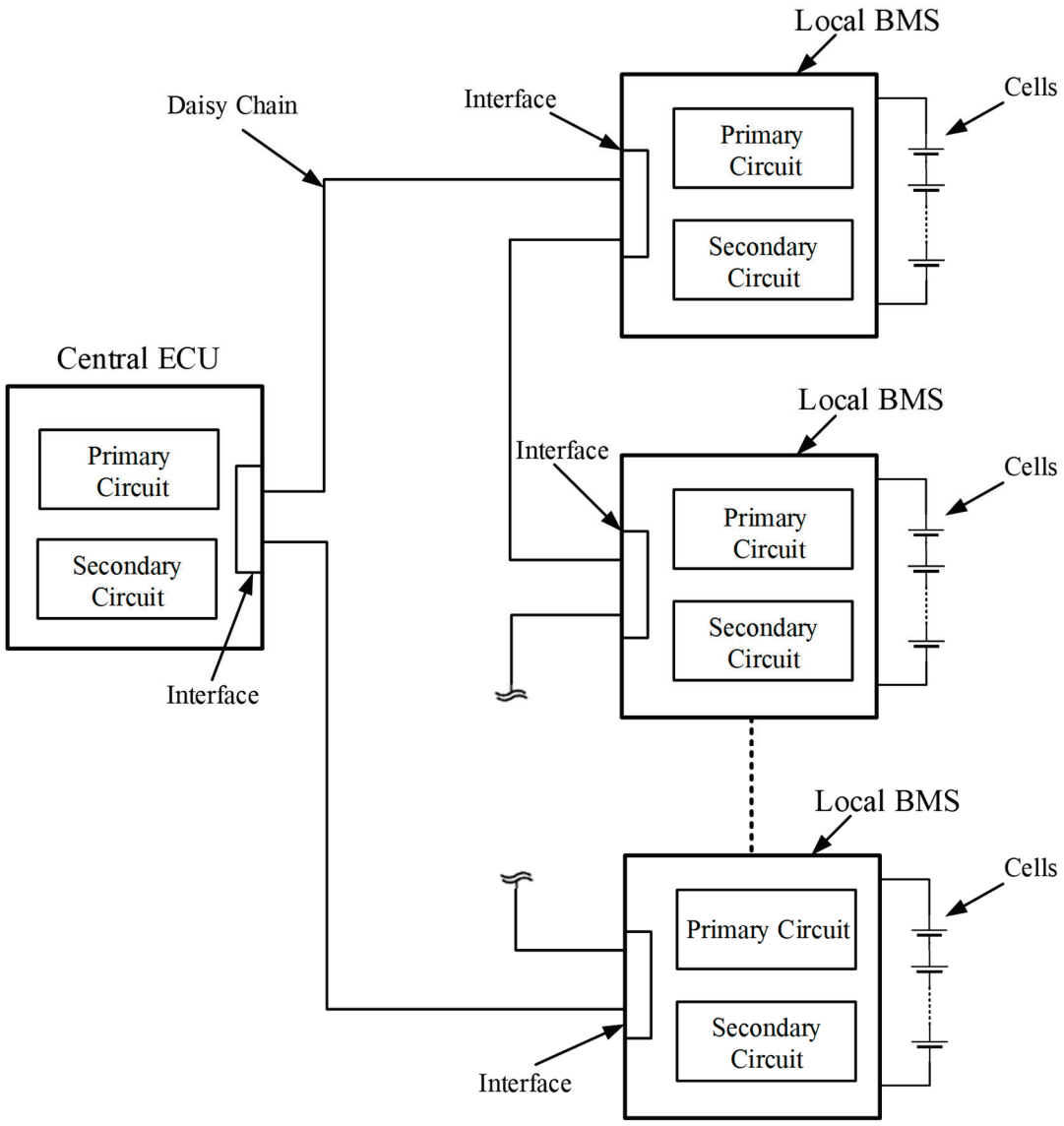

Figure 19. Multi-channel modular BMS in [102].

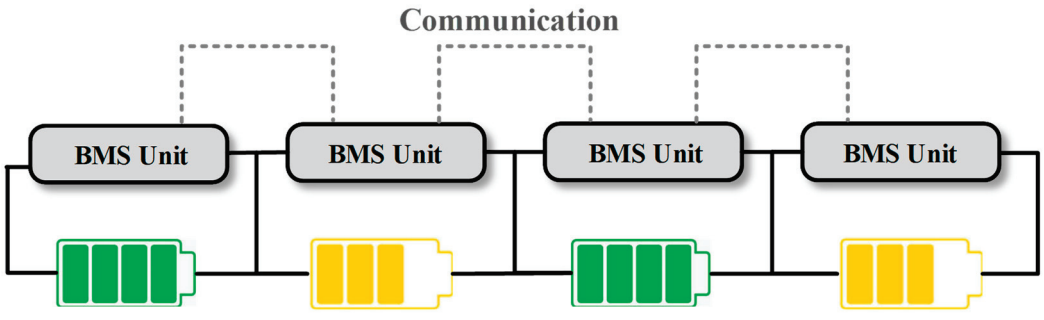

Figure 20. Fully decentralised BMS.

So far, the employment of fully decentralised BMS architecture is limited to aerospace and military battery systems with minimal involvement in EV propulsion systems. Although the ISO 26262 standard, which regulates EV systems in many countries, does not explicitly ban the use of fully decentralised BMS architectures, its safety requirements tend to discourage EVs from adopting fully decentralised BMS designs. For example, the ISO 26262 standard states that the BMS should be responsible for over-voltage and

overload protections as well as the contactor control between the battery pack and the motor inverter. It should also be responsible for thermal shutdown and torque derating at increased temperatures. In the fully decentralised BMS, this responsibility is shared between different peers and there is no clear authority in the system. Another example is that the ISO 26262 standard dictates that determinism is mandatory for safety, which means that using the same feeding inputs should lead to the same outputs. However, in a fully decentralised BMS architecture, the messages may be communicated between the local units in different orders, which means that different decisions may be made for the same inputs.

For these reasons, the fully decentralised BMS may not be used in the EV propulsion systems in the foreseeable future. However, the concept of decentralised control can influence other designs due to the proposed features. These features include the close intelligence to the battery cells, which provides more local monitoring and diagnostics.

4.4. Comparative Evaluation of EV BMS Architectures

One of the most important aspects of designing a BMS for an EV system is the scalability and expandability of the design. The voltages of a typical EV battery pack range from 48 V in medium hybrid vehicles to 800 V in high-performance EVs, with 400 V being the typical average value for a long time. The BMS architecture must be capable of handling the increase in cell count and pack voltage which will lead to an increase in the module count. The centralised BMS architecture has limited scalability, with the wiring complexity increasing significantly with the increasing cell count, which makes it impractical for large packs. The modular BMS architecture provides higher scalability, where each module monitors a segment of cells, and therefore, these segments can be extended to increase the size of the battery pack. The decentralised BMS architecture is very scalable, which is ideal for futuristic high-cell-count systems.

The EV electrical subsystems must adhere to functional safety requirements such as ISO 26262, which requires reducing the single point of failure risk, increasing the ability to isolate faulty modules, and ensuring predictability and determinism. The centralised BMS architecture has an increased single point of failure risk because a single master controller is responsible for monitoring and control. Modular BMS architectures improve fault isolation and reduce the risk of losing the full system if one module fails. However, this must be accompanied by modularising the power electronic system as well. Decentralised BMSs have better fault containment potential where local processing reduces cascaded failures. However, they struggle to adhere to the EV safety standards, especially when predictability and determinism are not proven.

Wiring complexity and physical integration are important aspects that are considered when selecting the BMS architecture for an EV. The wiring loom directly impacts the cost, reliability, assembly complexity and susceptibility to electro-magnetic interference (EMI). Centralised BMSs have long sensing wires to all cells, which increases the risk of noise and EMI interference and leads to heavy cable harness. Modular BMSs require shorter local-sensing wires and exhibit better EMI rejection. Also, they have reduced harness length. Decentralised BMSs require minimal sensing harness because communication networks replace the long analogue wiring. However, this communication network must be robust and immune to EMI.

Cost and implementation complexity should be considered before choosing a suitable BMS for an EV. This includes the cost of the hardware components, the number of required PCBs, the number of required microcontrollers, the communication network cost, and the development complexity. From the previous sections, it can be noted that the centralised BMS architectures have the lowest hardware cost, especially when they are

https://doi.org/10.3390/batteries12030092

employed in low-voltage small EVs. The modular BMSs are considered a balanced trade-off between performance and cost. Decentralised BMSs have a higher component count and therefore a higher cost. Moreover, the complexity of the required software, as well as the advanced communication and synchronisation, adds to the total cost of the system. Table 6 summarises and compares the main features of EV BMS architectures.

Table 6. Summary of comparison of BMS architectures for EV systems.

Parameter	Centralised	Modular	Decentralised
Scalability	Low	High	Very high
Fault tolerance	Low	Medium-High	High
Wiring complexity	High	Medium	Low
Cost	Low	Medium	High
Implementation complexity	Low	Medium	High
Memory	Minimal	Low	Moderate
Sensors	Current	Current Voltage	Current Voltage Temperature
Implementation complexity	Simple	Simple	Moderate

5. Conclusions

The performance of EV battery packs deteriorates with time and with the style of charging and discharging the battery cells. For BMS devices that manage the operation of the battery pack, it is necessary to estimate the battery cells' SoC in both a fast and accurate manner. The paper presented several methods for estimating the SoC of Li-ion batteries accurately, especially those that are used in modern EV propulsion systems. The estimation methods vary between being fast and practical and being thorough and complicated. The traditional estimation methods, such as OCV algorithms, are not suitable for modern EVs as they are unreliable due to their dependence on open circuit voltage, not to mention other important factors such as battery cycling patterns, cell characteristics, and other power components. The combination of fast algorithms with more advanced algorithms seems to be a viable solution for achieving both accuracy and speed. Algorithms based on artificial intelligence that deal with the battery system as a black box are promising in this application if they are combined with other reliable, robust, and well-established methodologies, such as coulomb counting with a voltage lookup table. Thus, this combination is seen in several modern EVs, with the latter being in the primary layer, whereas the former is used in the secondary layer as a complementary approach.

BMSs are important in this context to carry out the estimation process and then act upon it to balance the battery cells and determine the conditions of the battery system before delivering power to the propulsion system. Centralised BMSs may not be suitable for future EVs because of several practical reasons, including the need for numerous connections between the battery cells and the central control unit. Most current EV battery systems employ a modular BMS, also referred to as a distributed approach, to monitor and control the battery pack. Modular BMS devices combine the modularity required for practicality and size reduction with the predictability and clearly defined authority of a central controller, which is necessary for compliance with ISO 26262 standards.

https://doi.org/10.3390/batteries12030092

Author Contributions: Conceptualization, M.A. and A.D.; methodology, M.A. and A.D.; software, M.A. and A.D.; validation, M.A. and A.D.; formal analysis, A.D.; investigation, A.D.; resources, A.D.; data curation, M.A. and A.D.; writing—original draft preparation, M.A. and A.D.; writing—review and editing, A.D.; visualisation, M.A. and A.D.; supervision, A.D.; project administration, A.D.; funding acquisition, A.D. All authors have read and agreed to the published version of the manuscript.

Funding: This research received no external funding.

Data Availability Statement: No new data were created or analysed in this study. Data sharing is not applicable to this article.

Conflicts of Interest: The authors declare no conflicts of interest.

References

1. Li, J.; Zhang, X.; Guo, L.; Zhong, J.; Wang, D.; Wu, C.; Jiang, L. If Some Critical Regions Achieve Carbon Neutrality, How Will the Global Atmospheric CO_2 Concentration Change? *Remote Sens.* **2024**, *16*, 1486. [CrossRef]
2. Alawi, A.; Saeed, A.; Sharqawy, M.H.; Al Janaideh, M. A comprehensive review of thermal management challenges and safety considerations in lithium-ion batteries for electric vehicles. *Batteries* **2025**, *11*, 275. [CrossRef]
3. Nasr Esfahani, F.; Darwish, A.; Massoud, A. PV/Battery Grid Integration Using a Modular Multilevel Isolated SEPIC-Based Converter. *Energies* **2022**, *15*, 5462. [CrossRef]
4. Cavus, M.; Bell, M. Enabling Smart Grid Resilience with Deep Learning-Based Battery Health Prediction in EV Fleets. *Batteries* **2025**, *11*, 283. [CrossRef]
5. Ghandi, A.; Paltsev, S. Global CO_2 impacts of light-duty electric vehicles. *Transp. Res. Part D Transp. Environ.* **2020**, *87*, 102524. [CrossRef]
6. Benitto, A.; Rajendran, G.; Sathyabalu, H.V.; Balamurugan, S. Real-Time Implementation of Battery Management System in Electric Vehicles. In *2021 Innovations in Power and Advanced Computing Technologies (i-PACT)*; IEEE: New York, NY, USA, 2021; pp. 1–6.
7. Twidale, S. Renewables Provided Record 32% of Global Electricity in 2024, Ember Says. Reuters. 8 April 2025. Available online: https://www.reuters.com/sustainability/climate-energy/renewables-provided-record-32-global-electricity-2024-ember-says-2025-04-07/ (accessed on 1 March 2026).
8. Novak, M.; Chysky, J.; Novak, L. Data from long time testing of 18650 lithium polymer batteries. *Data Brief* **2020**, *29*, 105137. [CrossRef]
9. Shi, D.; Cui, Y.; Shen, X.; Gao, Z.; Ma, X.; Li, X.; Fang, Y.; Wang, S.; Fang, S. A review of the combined effects of environmental and operational factors on lithium-ion battery performance: Temperature, vibration, and charging/discharging cycles. *RSC Adv.* **2025**, *15*, 13272–13283. [CrossRef]
10. Hooper, M.; Williams, D.; Roberts-Bee, K.; McGordon, A.; Whiffin, P.; Marco, J. Defining a vibration test profile for assessing the durability of electric motorcycle battery assemblies. *J. Power Sources* **2023**, *557*, 232541. [CrossRef]
11. Hadj Abdallah, S.; Almousa, M.T.; Ben Salem, F.; Tounsi, S. Systemic Optimization of Electric Vehicles Power System. *World Electr. Veh. J.* **2025**, *16*, 207. [CrossRef]
12. Darwish, A.; Elgenedy, M.A.; Williams, B.W. A Review of Modular Electrical Sub-Systems of Electric Vehicles. *Energies* **2024**, *17*, 3474. [CrossRef]
13. Darwish, A. A Modular Step-Up DC/DC Converter for Electric Vehicles. *Energies* **2024**, *17*, 6305. [CrossRef]
14. Abolghasemi, M.; Soltani, I.; Shivaie, M.; Vahedi, H. Recent advances of step-up multi-stage DC-DC converters: A review on classifications, structures and grid applications. *Energy Rep.* **2025**, *13*, 3050–3081. [CrossRef]
15. Nasr Esfahani, F.; Suri, N.; Ma, X. Machine Learning Forecasting and GAN-Based Scenario Control for EV Charging and PV Integration. In Proceedings of the IECON 2025—51st Annual Conference of the IEEE Industrial Electronics Society, Madrid, Spain, 14–17 October 2025.
16. Fesli, U.; Özdemir, M.B. Electric Vehicles: A Comprehensive Review of Technologies, Integration, Adoption, and Optimization. *IEEE Access* **2024**, *12*, 140908–140931. [CrossRef]
17. Chen, C.; Xiong, R.; Shen, W. A lithium-ion battery-in-the-loop approach to test and validate multiscale dual H infinity filters for state-of-charge and capacity estimation. *IEEE Trans. Power Electron.* **2017**, *33*, 332–342. [CrossRef]
18. Dini, P.; Colicelli, A.; Saponara, S. Review on modeling and soc/soh estimation of batteries for automotive applications. *Batteries* **2024**, *10*, 34. [CrossRef]
19. Xiong, R.; Cao, J.; Yu, Q.; He, H.; Sun, F. Critical review on the battery state of charge estimation methods for electric vehicles. *IEEE Access* **2017**, *6*, 1832–1843. [CrossRef]

20. Hassan, F.; El-Bably, M.; Mubarak, R.I. State of Charge (SoC) Accurate Estimation Using Different Models of LSTM. *World Electr. Veh. J.* **2025**, *16*, 572. [CrossRef]
21. Karmakar, S.; Bohre, A.K.; Bera, T.K. Recent Advancements in Cell Balancing Techniques of BMS for EVs: A Critical Review. *IEEE Trans. Ind. Appl.* **2025**, *61*, 3468–3484. [CrossRef]
22. Link, S.; Neef, C.; Wicke, T. Trends in automotive battery cell design: A statistical analysis of empirical data. *Batteries* **2023**, *9*, 261. [CrossRef]
23. Liu, K.; Zou, C.; Li, K.; Wik, T. Charging pattern optimization for lithium-ion batteries with an electrothermal-aging model. *IEEE Trans. Ind. Inform.* **2018**, *14*, 5463–5474. [CrossRef]
24. Meng, J.; Luo, G.; Ricco, M.; Swierczynski, M.; Stroe, D.-I.; Teodorescu, R. Overview of lithium-ion battery modeling methods for state-of-charge estimation in electrical vehicles. *Appl. Sci.* **2018**, *8*, 659. [CrossRef]
25. Pinto, C.; Barreras, J.V.; Schaltz, E.; Araujo, R.E. Evaluation of advanced control for Li-ion battery balancing systems using convex optimization. *IEEE Trans. Sustain. Energy* **2016**, *7*, 1703–1717. [CrossRef]
26. Divakaran, A.M.; Minakshi, M.; Arabzadeh Bahri, P.; Paul, S.; Kumari, P.; Divakaran, A.M.; Manjunatha, K.N. Rational design on materials for developing next generation lithium-ion secondary battery. *Prog. Solid State Chem.* **2021**, *62*, 100298. [CrossRef]
27. Vaideeswaran, V.; Bhuvanesh, S.; Devasena, M. Battery management systems for electric vehicles using lithium ion batteries. In *2019 Innovations in Power and Advanced Computing Technologies (i-PACT)*; IEEE: New York, NY, USA, 2019; Volume 1, pp. 1–9.
28. Shirguppikar, S.; Gavali, P.; Ganachari, V.; Jadhav, P.; Zubairuddin, M.; Khot, S.; Mulla, J.; Todkar, A.S.; Prabhakar, S. Characterization of Li-ion battery and state of charge Estimation methods for diverse battery chemistries: A review. *Discov. Appl. Sci.* **2025**, *7*, 1443. [CrossRef]
29. Shu, X.; Chen, Z.; Shen, J.; Guo, F.; Zhang, Y.; Liu, Y. State of charge estimation for lithium-ion battery based on hybrid compensation modeling and adaptive H-infinity filter. *IEEE Trans. Transp. Electrif.* **2022**, *9*, 945–957. [CrossRef]
30. Pisani Orta, M.A.; García Elvira, D.; Valderrama Blaví, H. Review of State-of-Charge Estimation Methods for Electric Vehicle Applications. *World Electr. Veh. J.* **2025**, *16*, 87. [CrossRef]
31. Sun, P.; Bisschop, R.; Niu, H.; Huang, X. A review of battery fires in electric vehicles. *Fire Technol.* **2020**, *56*, 1361–1410. [CrossRef]
32. Allianz UK. Allianz UK Warns Motor Traders of High Risks and Costs of EV Battery Fires, Allianz UK News & Insight. 28 January 2025. Available online: https://www.allianz.co.uk/news-and-insight/news/allianz-uk-warns-motor-traders-of-high-risks-and-costs-of-ev-battery-fires.html (accessed on 10 February 2026).
33. Wang, Q. Study on Fire and Fire Spread Characteristics of Lithium-Ion Batteries. In Proceedings of the 2018 China National Symposium on Combustion, Harbin, China, 13–16 September 2018.
34. Office for Product Safety and Standards. *PLEV Battery Safety Research: Executive Summary and Conclusions*; GOV.UK: London, UK, 2025. Available online: https://www.gov.uk/government/publications/personal-light-electric-vehicle-plev-battery-safety-research/plev-battery-safety-research-executive-summary-and-conclusions (accessed on 10 February 2026).
35. Hu, X.; Wang, Y.; Feng, X.; Wang, L.; Ouyang, M.; Zhang, Q. Thermal stability of ionic liquids for lithium-ion batteries: A review. *Renew. Sustain. Energy Rev.* **2025**, *207*, 114949. [CrossRef]
36. Divakaran, A.M.; Hamilton, D.; Manjunatha, K.N.; Minakshi, M. Design, Development and Thermal Analysis of Reusable Li-Ion Battery Module for Future Mobile and Stationary Applications. *Energies* **2020**, *13*, 1477. [CrossRef]
37. Xu, D.; Wang, L.; Yang, J. Research on li-ion battery management system. In *2010 International Conference on Electrical and Control Engineering*; IEEE: New York, NY, USA, 2010; pp. 4106–4109.
38. Saw, L.; Tay, A.; Zhang, L.W. Thermal management of lithium-ion battery pack with liquid cooling. In *2015 31st Thermal Measurement, Modeling & Management Symposium (SEMI-THERM)*; IEEE: New York, NY, USA, 2015; pp. 298–302.
39. Reddy, P.; Soni, B.P.; Singh, S. SOC Estimation-Based Battery Management System for Electric Bicycles: Design and Implementation. *Eng. Proc.* **2025**, *118*, 76. [CrossRef]
40. Zhou, W.; Zheng, Y.; Pan, Z.; Lu, Q. Review on the battery model and SOC estimation method. *Processes* **2021**, *9*, 1685. [CrossRef]
41. Parasumanna, A.B.K.; Karle, U.S.; Saraf, M.R. Material characterization and analysis on the effect of vibration and nail penetration on lithium-ion battery. *World Electr. Veh. J.* **2019**, *10*, 69. [CrossRef]
42. Jia, Z.; Jin, K.; Mei, W.; Peng, Q.; Sun, J.; Wang, Q. Advances and perspectives in fire safety of lithium-ion battery energy storage systems. *eTransportation* **2025**, *24*, 100390. [CrossRef]
43. Bruen, T.; Hooper, J.M.; Marco, J.; Gama, M.; Chouchelamane, G.H. Analysis of a battery management system (BMS) control strategy for vibration-aged nickel manganese cobalt oxide (NMC) lithium-ion 18650 battery cells. *Energies* **2016**, *9*, 255. [CrossRef]
44. Reindl, A.; Meier, H.; Niemetz, M. Scalable, decentralized battery management system based on self-organizing nodes. In *Proceedings of the Architecture of Computing Systems—ARCS 2020, Innsbruck, Austria, 12 June 2020*; Springer: Cham, Switzerland, 2020; pp. 171–184. [PubMed Central]
45. Javor, D.; Krstić, D.; Raičević, N.; Petrović, N.; Suljović, S.; Procopio, R. Analysis of the Causes and Environmental Consequences of Electric Vehicle Fires. In Proceedings of the 3rd International EUROSA Conference, Vrnjačka Banja, Serbia, 14–17 May 2025.

46. Di Liberto, E.; Borchiellini, R.; Fruhwirt, D.; Papurello, D. A Review of Safety Measures in Battery Electric Buses. *Fire* **2025**, *8*, 159. [CrossRef]
47. Lindhout, P.; Reniers, G. A Thorough Investigation into the Current State of the Art in Safety Management on Battery Fire and Explosion Risks. *Sustainability* **2025**, *17*, 10578. [CrossRef]
48. Wang, Y.F.; Wang, Y.; Li, X.; Qiao, J.; Wang, Y.; Zhang, H.; Liu, J. Review of Lithium Battery Thermal Runaway Fault Diagnosis Methods and Fire Detection Applications in Electric Vehicles. *SSRN* **2025**, *48*. [CrossRef]
49. Bindal, R.; Nigam, A. Study of Battery Management System (BMS) on Fire Mitigation Techniques of Electric Vehicles. In *Innovations in Non-Conventional Energy Sources*, 1st ed.; CRC Press: Boca Raton, FL, USA, 2025; pp. 15–32. [CrossRef]
50. Wang, T.; Liu, H.; Wang, W.; Jiang, W.; Xu, Y.; Zhu, S.; Sheng, Q. Advances in Thermal Management of Lithium-Ion Batteries: Causes of Thermal Runaway and Mitigation Strategies. *Processes* **2025**, *13*, 2499. [CrossRef]
51. Deng, J.; Hu, Z.; Chen, J.; Zhao, J.; Bai, Z. Safety Methods for Mitigating Thermal Runaway of Lithium-Ion Batteries—A Review. *Fire* **2025**, *8*, 223. [CrossRef]
52. Sorensen, A.; Utgikar, V.; Belt, J. A Study of Thermal Runaway Mechanisms in Lithium-Ion Batteries and Predictive Numerical Modeling Techniques. *Batteries* **2024**, *10*, 116. [CrossRef]
53. Yao, Y.; Peng, X.; Gao, L.; Xing, H.; Xu, X.; Gu, J.; Liu, L.; Yue, S.; Qiu, Y.; Wang, Y.; et al. Experimental and Simulation-Based Study on Thermal Runaway Characteristics of 18650 Lithium-Ion Batteries and Thermal Propagation Patterns in Battery Packs. *Batteries* **2025**, *11*, 202. [CrossRef]
54. Yao, Y.; Liu, L.; Gu, J.; Xing, H.; Liu, H.; Cheng, Y.; Wang, Y.; Yue, S.; Qiu, Y.; Zhang, Z. Characteristic Differences of Thermal Runaway Triggered by Overheating and Overcharging in Lithium-Ion Batteries and Multi-Dimensional Safety Protection Strategies. *Batteries* **2025**, *11*, 242. [CrossRef]
55. Elsner, F.; Gerhards, P.; Berrier, G.; Vincent, R.; Dubourg, S.; Pischinger, S. Detailed Characterization of Thermal Runaway Particle Emissions from a Prismatic NMC622 Lithium-Ion Battery. *Batteries* **2025**, *11*, 225. [CrossRef]
56. Sallard, S.; Nolte, O.; von Roemer, L.; Soltani, B.; Fandakov, A.; Mueller, K.; Kalogirou, M.; Sens, M. Exploring Thermal Runaway: Role of Battery Chemistry and Testing Methodology. *World Electr. Veh. J.* **2025**, *16*, 153. [CrossRef]
57. Zhang, Q.; Shang, Y.; Li, Y.; Zhu, R. A Concise Review of Power Batteries and Battery Management Systems for Electric and Hybrid Vehicles. *Energies* **2025**, *18*, 3750. [CrossRef]
58. Kertész, N.; Szabó, L. Advances and Future Trends in Battery Management Systems. *Eng. Proc.* **2024**, *79*, 66. [CrossRef]
59. Balasingam, B.; Ahmed, M.; Pattipati, K. Battery Management Systems—Challenges and Some Solutions. *Energies* **2020**, *13*, 2825. [CrossRef]
60. Khawaja, Y.; Shankar, N.; Qiqieh, I.; Alzubi, J.; Alzubi, O.; Nallakaruppan, M.K.; Padmanaban, S. Battery Management Solutions for Li-ion Batteries Based on Artificial Intelligence. *Ain Shams Eng. J.* **2023**, *14*, 102213. [CrossRef]
61. Kurkin, A.; Chivenkov, A.; Aleshin, D.; Trofimov, I.; Shalukho, A.; Vilkov, D. Battery Management System for Electric Vehicles: Comprehensive Review of Circuitry Configuration and Algorithms. *World Electr. Veh. J.* **2025**, *16*, 451. [CrossRef]
62. Demirci, O.; Taskin, S.; Schaltz, E.; Demirci, B.A. Review of Battery State Estimation Methods for Electric Vehicles—Part I: SOC Estimation. *J. Energy Storage* **2024**, *87*, 111435. [CrossRef]
63. Nasr Esfahani, F.; Darwish, A.; Massoud, A.M. Loop-Shaping Control Design for a New Modular Integrated On-Board EV Charger with RHP Zero Compensation. *IET Power Electron.* **2025**, *18*, e70061. [CrossRef]
64. Cavus, M.; Bell, M. A Health-Aware Hybrid Reinforcement–Predictive Control Framework for Sustainable Energy Management in Photovoltaic–Electric Vehicle Microgrids. *Batteries* **2026**, *12*, 5. [CrossRef]
65. Abbas, S.M.; Gstrein, G.; Golubkov, A.W.; Korak, O.; Erker, S.; Ellersdorfer, C. Influence of Lithium Plating on the Thermal Properties of Automotive High Energy Pouch Batteries. *Batteries* **2025**, *11*, 338. [CrossRef]
66. Gao, Z.-W.; Lan, T.; Yin, H.; Liu, Y. Development and Commercial Application of Lithium-Ion Batteries in Electric Vehicles: A Review. *Processes* **2025**, *13*, 756. [CrossRef]
67. Parvizi, P.; Jalilian, M.; Amidi, A.M.; Zangeneh, M.R.; Riba, J.-R. From Present Innovations to Future Potential: The Promising Journey of Lithium-Ion Batteries. *Micromachines* **2025**, *16*, 194. [CrossRef]
68. Pesaran, A.A. Lithium-Ion Battery Technologies for Electric Vehicles: Progress and Challenges. *IEEE Electrif. Mag.* **2023**, *11*, 35–43. [CrossRef]
69. Tang, K.; Luo, B.; Chen, D.; Wang, C.; Chen, L.; Li, F.; Cao, Y.; Wang, C. The State of Health Estimation of Lithium-Ion Batteries: A Review of Health Indicators, Estimation Methods, Development Trends and Challenges. *World Electr. Veh. J.* **2025**, *16*, 429. [CrossRef]
70. Lin, X.; Khosravinia, K.; Hu, X.; Li, J.; Lu, W. Lithium plating mechanism, detection, and mitigation in lithium-ion batteries. *Prog. Energy Combust. Sci.* **2021**, *87*, 100953. [CrossRef]
71. Wassiliadis, N.; Schneider, J.; Frank, A.; Wildfeuer, L.; Lin, X.; Jossen, A.; Lienkamp, M. Review of fast charging strategies for lithium-ion battery systems and their applicability for battery electric vehicles. *J. Energy Storage* **2021**, *44*, 103306. [CrossRef]

72. Dong, G.; Feng, Y.; Lou, Y.; Zhang, M.; Wei, J. Data-driven fast charging optimization for lithium-ion battery using Bayesian optimization with fast convergence. *IEEE Trans. Transp. Electrif.* **2024**, *10*, 4173–4183. [CrossRef]
73. Phogat, P.; Deya, S.; Wana, M. Powering the sustainable future: A review of emerging battery technologies and their environmental impact. *RSC Sustain.* **2025**, *3*, 3266–3306. [CrossRef]
74. Santhanagopalan, S.; White, R.E. State of charge estimation using an unscented filter for high power lithium ion cells. *Int. J. Energy Res.* **2010**, *34*, 152–163. [CrossRef]
75. Zhang, F.; Liu, G.; Fang, L. Battery state estimation using unscented Kalman filter. In Proceedings of the 2009 IEEE International Conference on Robotics and Automation, Kobe, Japan, 12–17 May 2009; pp. 1863–1868. [CrossRef]
76. Chen, X.; Chen, X.; Chen, X. A Novel Framework for Lithium-Ion Battery State of Charge Estimation Based on Kalman Filter Gaussian Process Regression. *Energy Rep.* **2021**, *7*, 5498–5510. [CrossRef]
77. Peng, S.; Chen, C.; Shi, H.; Yao, Z. State of charge estimation of battery energy storage systems based on adaptive unscented Kalman filter with a noise statistics estimator. *IEEE Access* **2017**, *5*, 13202–13212. [CrossRef]
78. Xu, Y.; Hu, M.; Zhou, A.; Li, Y.; Li, S.; Fu, C.; Gong, C. State of charge estimation for lithium-ion batteries based on adaptive dual Kalman filter. *Appl. Math. Model.* **2020**, *77*, 1255–1272. [CrossRef]
79. Choi, J.H. Battery Management System, Battery Management Method, Battery Pack and Electric Vehicle. U.S. Patent 2021/0199724 A1, 1 July 2021.
80. Noirjean, J. Method for Estimating the State of Charge of a Battery in a System Having a Low Power Consumption, and System for Implementing the Estimation Method. U.S. Patent 2024/0319279 A1, 26 September 2024.
81. Uchida, Y.; Machida, K.; Moriya, Y.; Tanaka, N.; Kubo, K.; Uchiyama, M. Battery System and SOC Estimation Method for Secondary Battery. U.S. Patent 11,353,514 B2, 7 June 2022.
82. Tesla Motors, Inc. Response System for Detection of Overcharge Event in a Series Connected Battery Element. U.S. Patent Application US10355498B2, 27 March 2014.
83. Bayerische Motoren Werke AG. System and Method for Estimating State of Charge of a Battery in a Motor Vehicle. Canadian Patent Application CA3162747A1, 27 September 2017.
84. Kim, C.H.; Kim, M.Y.; Moon, G.W. A modularized charge equalizer using a battery monitoring IC for series-connected Li-Ion battery strings in electric vehicles. *IEEE Trans. Power Electron.* **2013**, *28*, 3779–3787. [CrossRef]
85. Li, L.; Zhao, X.; Zhu, J.; Xing, J.; Xing, S. Research on dynamic equalization for lithium battery management system. In *IEEE 29th Chinese Control And Decision Conference (CCDC)*; IEEE: New York, NY, USA, 2017; pp. 6884–6888.
86. Lorentz, V.; Wenger, M.; Giegerich, M.; Zeltner, S.; März, M.; Frey, L. Smart battery cell monitoring with contactless data transmission. In *Advanced Microsystems for Automotive Applications 2012*; Meyer, G., Ed.; Springer: Heidelberg, Germany, 2012; pp. 15–26.
87. Nasr Esfahani, F.; Darwish, A.; Alotaibi, S.; Campean, F. Hierarchical Control Design of a Modular Integrated OBC for Dual-Motor Electric Vehicle Applications. *IEEE Access* **2025**, *13*, 196306–196327. [CrossRef]
88. Reindl, A.; Meier, H.; Park, M.N.S. Decentralized Battery Management System with Customized Hardware Components. In Proceedings of the 2021 IEEE 19th Student Conference on Research and Development (SCOReD), Kota Kinabalu, Malaysia, 23–25 November 2021; pp. 350–355.
89. Shiue, M.-T.; Ou, Y.-C.; Wu, C.-F.; Wang, Y.-F.; Liu, B.-J. Design and Implementation of a Decentralized Node-Level Battery Management System Chip Based on Deep Neural Network Algorithms. *Electronics* **2026**, *15*, 296. [CrossRef]
90. Čermák, K.; Bartl, M. Decentralized Battery Management System. In Proceedings of the 2014 15th International Scientific Conference on Electric Power Engineering (EPE), Brno-Bystrc, Czech Republic, 12–14 May 2014; pp. 599–603.
91. Caspar, M.; Schürmann, T.; Anneken, M.; Hohmann, S. Active Balancing Control for Distributed Battery Systems Based on Cooperative Game Theory. *J. Energy Storage* **2023**, *68*, 107585. [CrossRef]
92. García, E.; Quiles, E.; Correcher, A. Distributed Intelligent Battery Management System Using a Real-World Cloud Computing System. *Sensors* **2023**, *23*, 3417. [CrossRef]
93. Cao, Z.; Gao, W.; Fu, Y.; Mi, C. Wireless Battery Management Systems: Innovations, Challenges, and Future Perspectives. *Energies* **2024**, *17*, 3277. [CrossRef]
94. Ghazali, A.K.; Aziz, N.A.A.; Hassan, M.K. Advanced Algorithms in Battery Management Systems for Electric Vehicles: A Comprehensive Review. *Symmetry* **2025**, *17*, 321. [CrossRef]
95. Gabbar, H.A.; Othman, A.M.; Abdussami, M.R. Review of Battery Management Systems (BMS) Development and Industrial Standards. *Technologies* **2021**, *9*, 28. [CrossRef]
96. Gozdur, R.; Przerywacz, T.; Bogdański, D. Low Power Modular Battery Management System with a Wireless Communication Interface. *Energies* **2021**, *14*, 6320. [CrossRef]
97. Cevallos-Sierra, J.; Santos Silva, C. Modelling Decentralised Energy Storage Systems Using Urban Building Energy Models. *Urban Sci.* **2025**, *9*, 468. [CrossRef]

98. Chatzigeorgiou, N.G.; Theocharides, S.; Makrides, G.; Georghiou, G.E. A Review on Battery Energy Storage Systems: Applications, Developments and Research Trends of Hybrid Installations in the End-User Sector. *J. Energy Storage* **2024**, *86*, 111192. [CrossRef]
99. Lipu, M.S.H.; Al Mamun, A.; Ansari, S.; Miah, M.S.; Hasan, K.; Meraj, S.T.; Abdolrasol, M.G.M.; Rahman, T.; Maruf, M.H.; Sarker, M.R.; et al. Battery Management, Key Technologies, Methods, Issues, and Future Trends of Electric Vehicles: A Pathway toward Achieving Sustainable Development Goals. *Batteries* **2022**, *8*, 119. [CrossRef]
100. Triviño, A.; López, A.; Yuste, A.J.; Cuevas, J.C. Decentralized EV Charging and Discharging Scheduling Algorithm Based on Type-II Fuzzy-Logic Controllers. *J. Energy Storage* **2024**, *93*, 112054. [CrossRef]
101. Bhushan, N.; Mekhilef, S.; Tey, K.S.; Shaaban, M.; Seyedmahmoudian, M.; Stojcevski, A. Overview of Model- and Non-Model-Based Online Battery Management Systems for Electric Vehicle Applications: A Comprehensive Review of Experimental and Simulation Studies. *Sustainability* **2022**, *14*, 15912. [CrossRef]
102. Martin, N.; Mitros, A.; Mellone, C.A.; Dimen, I. Multi-Channel and Bi-Directional Battery Management System. U.S. Patent 10741888B2, 11 August 2018.
103. Papageorgiou, P.; Oureilidis, K.; Tsakiri, A.; Christoforidis, G. A Modified Decentralized Droop Control Method to Eliminate Battery Short-Term Operation in a Hybrid Supercapacitor/Battery Energy Storage System. *Energies* **2023**, *16*, 2858. [CrossRef]
104. Staņa, Ģ.; Kroičs, K. Adaptive Droop Control for Power Distribution of Hybrid Energy Storage Systems in PV-Fed DC Microgrids. *Energies* **2025**, *18*, 5137. [CrossRef]
105. Berschneider, E.; Wagner, B.; Meindl, M.; Eckardt, B. Centralized SoC Balancing for Batteries with Droop-Controlled DC/DC Converters for Electric Aircraft. *Batteries* **2025**, *11*, 411. [CrossRef]

Disclaimer/Publisher's Note: The statements, opinions and data contained in all publications are solely those of the individual author(s) and contributor(s) and not of MDPI and/or the editor(s). MDPI and/or the editor(s) disclaim responsibility for any injury to people or property resulting from any ideas, methods, instructions or products referred to in the content.

batteries

MDPI

Article

Geometry-Regulated Thermal Performance of Sedimentation-Stable MicroPCM Composite Capsules for Battery Thermal Management Systems Fabricated via 3D Printing

Xuguang Zhang [1], Michael C. Halbig [2], Mrityunjay Singh [3], Amjad Almansour [2] and Yi Zheng [1,4,*]

[1] Department of Mechanical and Industrial Engineering, Northeastern University, Boston, MA 02115, USA
[2] NASA Glenn Research Center, Cleveland, OH 44135, USA
[3] Ohio Aerospace Institute, Cleveland, OH 44142, USA
[4] Department of Chemical Engineering, Northeastern University, Boston, MA 02115, USA
* Correspondence: y.zheng@northeastern.edu

Abstract

Thermal management is critical for maintaining the safety and performance of lithium-ion batteries. Phase change materials (PCMs) have been widely studied as passive cooling media due to their high latent heat capacity, but major technical challenges remain due to their relatively low thermal conductivity and nanoparticle sedimentation in composite systems. In this work, a composite phase change material (PCM) consisting of paraffin wax, a microencapsulated phase change material (MicroPCM 28D), and nano carbon black is developed to enhance thermal stability and suppress particle sedimentation through increased viscosity of the PCM matrix. Five capsule geometries fabricated by fused filament fabrication (FFF) 3D printing are experimentally investigated under airflow velocities ranging from 0 to 10 m s^{-1}. Wind tunnel experiments with infrared thermography are used to evaluate the thermal response of the PCM capsules. The results show that airflow velocity and capsule geometry strongly influence heat dissipation behavior. Compared with conventional wax composites, the MicroPCM 28D composite capsules reduce peak temperature by approximately 2–4 °C under airflow velocities of 0–10 m/s. These findings provide insights into geometry-regulated convection and stable composite PCM design for lithium-ion battery thermal management systems.

Keywords: lithium-ion battery thermal management; phase change materials (PCM); wind tunnel experimentation; airflow convection cooling; geometry-dependent heat dissipation

1. Introduction

Lithium-ion batteries have become the dominant energy storage technology in electric vehicles, portable electronics, and grid-scale energy storage systems due to their high energy density and long cycle life. However, thermal issues remain a critical bottleneck for safety and durability [1]. Elevated temperature accelerates degradation, and non-uniform temperature distribution aggravates performance imbalance, while abusive thermal conditions may trigger thermal runaway accompanied by fire and explosion hazards [2–4]. Therefore, battery thermal management systems (BTMSs) are essential for maintaining cells within a safe temperature window and improving thermal uniformity at both cell and pack levels [5]. This work focuses on capsule geometry optimization and novel MicroPCM

28D formulations to investigate their combined effects on battery thermal management performance under forced convection conditions.

Among various BTMS strategies, air cooling is attractive due to its simplicity and low cost, but its heat removal capability can be insufficient under high heat flux conditions. As a complementary approach, phase change materials (PCMs) have been extensively explored because latent heat absorption during melting can effectively buffer temperature rise during transient heating [6,7]. PCM selection, thermal storage mechanisms, and practical implementation constraints have been widely reviewed, including fundamental PCM energy storage principles and broader PCM applications [6], PCM-based thermal management in electronics and batteries [7], and PCM families and selection guidelines for thermal storage [8]. More recently, PCM-based BTMS research has advanced rapidly, and recent reviews summarize both progress and remaining challenges, such as limited thermal conductivity and regeneration issues under repeated cycling [9].

A central limitation of most organic PCMs is their low intrinsic thermal conductivity, which restricts heat spreading and can delay heat extraction from the heat source. Microencapsulation and encapsulation technologies are frequently adopted to improve handling, mitigate leakage, and enable modular integration. A comprehensive review of solid–liquid PCMs and encapsulation technologies provides the key design considerations for encapsulated PCM systems [10]. In parallel, recent microcapsule studies highlight the opportunity to integrate thermally conductive reinforcements into PCM microcapsules to improve effective heat transfer while retaining latent heat storage functionality [11]. These encapsulation concepts motivate capsule-based PCM configurations in battery thermal management, where geometry and packaging can be deliberately engineered.

To further enhance heat transfer, nano-enhanced PCMs and composite PCMs have been widely studied. Reviews on thermal conductivity enhancement of PCMs summarize the roles of conductive fillers, percolation pathways, and processing strategies, while also emphasizing challenges such as dispersion stability and long-term reliability [12]. Recent comprehensive reviews of nano-enhanced PCMs further consolidate the advances in nanoparticle-based enhancement for thermal energy storage applications and discuss limitations associated with agglomeration, sedimentation, and viscosity-driven processing constraints [13]. A recent review focusing on nano-enhanced PCMs in thermal management systems reinforces that conductivity enhancement is often accompanied by practical issues in manufacturability and stability, which remain critical barriers for real-world deployment [14]. Representative experimental work has demonstrated that graphene and carbon nanotubes can significantly improve the thermal performance of composite PCMs and indicate their potential for lithium-ion power battery applications [15]. In addition, advanced fabrication strategies such as alternating positive and negative pressures during perfusion have been reported to enhance the thermal conductivity of graphene-based phase change composites, illustrating continued progress in composite PCM processing [16].

Besides material-level enhancement, structural and hybrid system-level designs are widely adopted to amplify PCM effectiveness. Fin-enhanced PCM designs increase heat transfer area and provide conductive pathways, and a recent system using internal–external fin-enhanced PCM demonstrates improved thermal management for cylindrical lithium-ion batteries [17]. Similarly, integrating PCM with metal foam and fins has been investigated via parametric studies using CFD and data-driven models, emphasizing the coupled effects of PCM properties, enhanced structures, and operating conditions [18]. Hybrid configurations that combine PCM with active cooling approaches further increase heat removal capability. An optimized channel design in a hybrid PCM–liquid cooling system demonstrates enhanced thermal management performance, especially under higher heat loads where passive buffering alone may be insufficient [19]. Another hybrid PCM–heat-pipe–

https://doi.org/10.3390/batteries12040144

thermoelectric system illustrates the potential of multi-physics coupling to achieve stronger temperature suppression under demanding operating conditions [20]. Recent experimental studies also validate that PCM-based passive thermal management can effectively reduce peak temperature in practical configurations, while highlighting the importance of system architecture and operating environment for sustained performance [21]. Moreover, numerical and experimental investigations of hybrid BTMSs for high-rate applications further underscore that airflow and system-level heat transfer pathways strongly influence achievable temperature reduction [22].

Despite these advances, two gaps remain highly relevant for PCM capsule-based BTMS design. First, most prior studies emphasize either composite PCM development or structural enhancements such as fins and metal foams, while the role of capsule geometry, especially its interaction with airflow regimes from weak convection to strong forced convection, is less systematically quantified. Second, although conductive nano-additives are widely used, long-term dispersion stability and sedimentation resistance remain practical challenges that can directly affect repeatability and durability of thermal performance. Addressing these gaps requires an experimentally grounded comparison coupling material formulation, capsule geometry, and controlled airflow conditions within a unified evaluation framework.

In recent studies, various hybrid heat dissipation approaches for battery packs have been investigated, including the development and optimization of hybrid heat dissipation systems [23], comprehensive analyses of thermal heat dissipation for lithium-ion battery packs [24], hybrid thermal systems incorporating composite PCMs [25], and innovative 3D-printed hybrid cooling systems for pouch cells [26,27]. Building upon these studies, the present work experimentally investigates composite PCM capsules with multiple geometries under controlled airflow conditions. By systematically comparing peak temperature, steady-state characteristics, and cooling dynamics across airflow regimes, this study aims to provide design-relevant insights for geometry-regulated convection enhancement and stable nano-enhanced PCM capsule integration in lithium-ion battery thermal management.

2. Materials and Methods

A microencapsulated phase change material, MicroPCM 28D (Microtek Laboratories, Inc., Dayton, OH, USA), composed of a n-octadecane core encapsulated within a melamine-formaldehyde shell, was employed as the primary latent heat storage component. The microencapsulated phase change material MicroPCM 28D was commercially purchased, while paraffin wax was commercially obtained from an online supplier. The nano carbon black additive was provided by NASA Glenn Research Center. Paraffin wax was used as the reference phase change material. Nanocarbon black was incorporated as a thermally conductive additive. Conventional paraffin and nano carbon black systems often suffer from severe particle sedimentation due to the low viscosity of molten paraffin, resulting in non-uniform thermal distribution after solidification. In contrast, the incorporation of MicroPCM 28D significantly increases the effective viscosity of the liquid composite without substantially reducing the overall latent heat storage capacity. Even in the molten state, the 28D-based composite exhibits a noticeably thicker consistency compared with molten paraffin wax.

The MicroPCM 28D composite was prepared by mixing 40 wt% paraffin wax and 60 wt% MicroPCM 28D. The mixture was heated to 100 °C on a hot plate until complete melting was achieved, followed by continuous manual stirring using a glass rod to promote uniform dispersion and homogeneous liquefaction. Stirring was maintained for approximately 5–10 min until no visible phase separation or particle agglomeration was observed. Homogeneity was initially assessed based on visual inspection of uniform color and texture

and further supported by consistent DSC phase-change behavior across repeated thermal cycles. The blending and cooling process is shown in Figure 1b. After full melting, 2 wt% nano carbon black, relative to the total PCM mass of paraffin and 28D, was added and thoroughly mixed. Due to the high viscosity of the molten composite, direct casting into the capsule cavity was not feasible. After solidification, the composite was broken into small pieces and milled into micrometer-scale powder. The powder was then packed into the PCM storage region of the capsule. A post-filling thermal cycle was applied to remelt the composite inside the cavity, allowing the material to coalesce and eliminate internal voids. The smooth surface morphology of the solidified composite after cooling can be observed in Figure 1b.

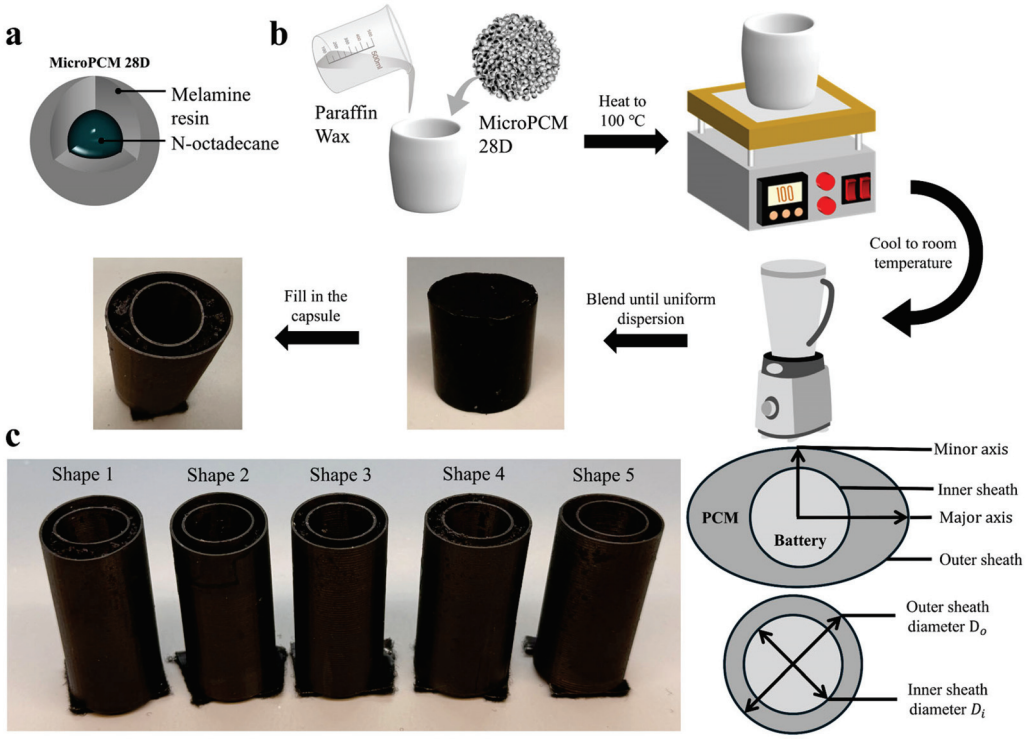

Figure 1. Fabrication process and geometric design of the MicroPCM 28D composite battery capsules. (**a**) Structural schematic of MicroPCM 28D showing the melamine resin shell and n-octadecane core. (**b**) Thermal blending procedure of paraffin wax and MicroPCM 28D at 100 °C, followed by uniform dispersion and filling into the capsule cavity. (**c**) Five 3D-printed capsule geometries (Shape 1–Shape 5) designed to investigate geometry-dependent thermal performance under airflow conditions. The capsules consist of an inner sheath accommodating the battery and an outer sheath containing the PCM. The cross-sectional schematic illustrates the definitions of the major and minor axes of the oval geometries, as well as the inner sheath diameter D_i and outer sheath diameter D_o.

For comparison to a baseline material with no PCM, a reference material consisting of pure paraffin wax with 2 wt% nano carbon black was prepared via direct melt blending. Paraffin was heated to 100 °C, followed by the addition and stirring of nano carbon black until uniform dispersion was achieved. The molten composite was directly injected into the capsule cavity using a drop-casting method before solidification. All phase change materials were injected into the region between the inner and outer sheaths of the capsule, which was specifically designed as the PCM storage layer.

The five capsule geometries fabricated via 3D printing are shown in Figure 1c. The capsules were manufactured using fused filament fabrication on a Markforged Mark 2 printer (Markforged Holding Corporation, Waltham, WA, USA). The printing filament was Onyx®, a nylon-based composite reinforced with micro carbon fibers. Due to the relatively

small thickness of the sheath compared with the PCM region, its contribution to thermal energy storage is limited. The integrated one-piece design reduced the risk of leakage during phase transition. Three oval geometries, labeled Shapes 1 to 3, and two circular geometries, labeled Shapes 4 and 5, were designed. All capsules maintained identical height and internal PCM volume, while geometric variations were introduced in the major and minor axes to modulate airflow interaction. The specific dimensions were listed in Table 1. For each geometry, two capsules were prepared, one filled with the 28D composite and the other filled with the paraffin and carbon black composite.

Table 1. Geometric dimensions of the five capsule designs.

Shape	Geometry Type	Major Axis/Diameter (mm)	Minor Axis/Diameter (mm)	Aspect Ratio (Major/Minor)	Inner Sheath Diameter D_i (mm)	Capsule Height h (mm)
1	Oval	36.18	28.44	1.27	18.00	60.00
2	Oval	33.81	28.65	1.18	18.00	60.00
3	Oval	31.77	29.03	1.09	18.00	60.00
4	Round	31.69	31.69	1.00	18.00	60.00
5	Round	29.09	39.09	1.000	18.00	60.00

Thermal performance testing was conducted in a wind tunnel system, as illustrated in Figure 2a. The airflow velocity was adjustable from 0 to 10 m/s with an accuracy of ±0.1 m/s. In practical battery cooling systems, lower airflow velocities in this range correspond to weak convection conditions such as natural convection or low-speed fan cooling, while higher airflow velocities represent strong forced-air cooling typically used in actively cooled battery modules. A honeycomb flow straightener was installed upstream of the test section to reduce turbulence intensity. The overall experimental configuration is shown in Figure 2b. Four capsules were positioned inside the test chamber with a center-to-center spacing of 5.08 cm, as shown in Figure 2c. During wind tunnel testing, all four capsules were simultaneously heated.

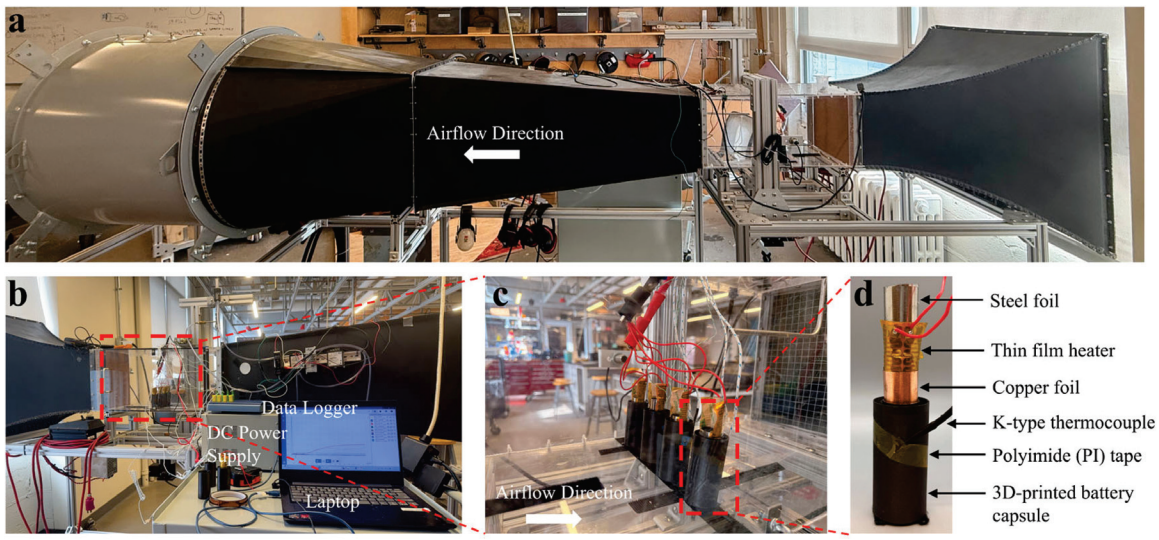

Figure 2. Experimental setup for forced convection thermal testing. (**a**) Wind tunnel system indicating airflow direction. (**b**) Overall experimental arrangement including DC power supply, data logger, and IR camera. (**c**) Capsules positioned in the test section under controlled airflow. (**d**) Exploded view of the heating assembly, including steel foil, thin-film heater, copper foil, K-type thermocouple, polyimide (PI) tape, and 3D-printed battery capsule.

The heating assembly for a single capsule is presented in Figure 2d. Heating was provided by a thin-film heater powered by a regulated DC supply at 9 V and 0.46 A, corre-

sponding to a constant power input of 4.14 W per capsule. This heating level is comparable to the typical heat generation range of cylindrical lithium-ion cells under moderate-to-high discharge conditions and therefore represents realistic battery thermal management scenarios. The use of a thin-film heater also provides a spatially uniform heat source, enabling controlled comparison of geometry-dependent thermal performance independent of specific battery electrochemistry. A copper foil layer was placed between the thin-film heater and the inner sheath of the capsule to improve temperature uniformity. A steel foil layer was applied externally to ensure proper mechanical contact. K-type thermocouples were used to monitor temperature evolution. The inner-sheath thermocouple was positioned between the copper foil and the inner sheath to simulate battery core temperature. The outer-sheath thermocouple was attached to the external capsule surface using polyimide tape. All thermocouples were located at the mid-height of the capsule and positioned on the downstream side, where peak temperature is expected to occur. Temperature data were recorded using a data logger connected to a laptop for continuous acquisition.

3. Thermal Response Characteristics

To understand the thermal regulation behavior of the proposed phase change composite, infrared thermography experiments were conducted under forced convection conditions. The experimental setup is illustrated in Figure 3a, where two battery capsules were simultaneously tested under identical heating and airflow conditions. Shape 3 was selected as a representative case because its aspect ratio is close to unity while still maintaining an oval geometry, providing an intermediate configuration between elongated and circular shapes. One capsule was filled with the MicroPCM 28D composite material, while the other contained a baseline conventional wax-based composite with 2 wt% nano carbon black. The heating process was powered by a DC power supply, and the temperature evolution of the capsule surfaces was recorded by an infrared camera. Representative thermal images captured during the heating and cooling process are presented in Figure 3b–g.

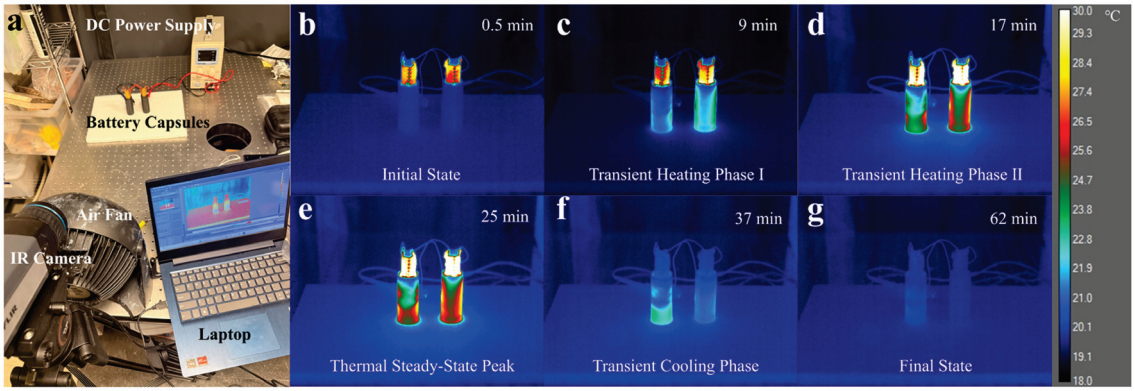

Figure 3. Thermal evolution of battery capsules with Shape 3 geometry under a controlled airflow of 2 m·s^{-1}. The left capsule contains the MicroPCM 28D composite, and the right capsule contains the baseline wax composite. (**a**) Experimental setup including DC power supply, battery capsules, air fan, infrared camera, and data acquisition system. (**b**) Initial state at 0.5 min near ambient temperature (~20 °C). (**c**) Transient heating Phase I at 9 min dominated by sensible heating. (**d**) Transient heating Phase II at 17 min as phase change begins. (**e**) Thermal steady-state peak at 25 min. (**f**) Transient cooling at 37 min after the power is turned off. (**g**) Final state at 62 min when the capsules return close to ambient temperature. The color scale represents surface temperature in °C.

Figure 3b shows the initial state of the capsules before heating, where both samples remain near the ambient temperature of 20 °C. As heating begins, the temperature gradually increases and enters the first transient heating stage, as shown in Figure 3c at 9 min. During

this stage, the temperature rise is mainly governed by sensible heat storage in the composite materials. As heating continues, the capsules enter a second transient heating stage, shown in Figure 3d at 17 min, where phase change gradually begins, and latent heat storage starts to influence the temperature evolution. The peak temperature state is observed in Figure 3e at 25 min, corresponding to the thermal steady-state condition of the system, where the temperature variation becomes minimal. After the heating power is turned off, the capsules undergo a transient cooling stage as shown in Figure 3f at 37 min, followed by the final state where the capsules return close to the ambient temperature at around 62 min, as illustrated in Figure 3g. The full thermal cycle presented in Figure 3 therefore provides a direct visualization of the transient heating, steady-state, and cooling processes that occur in the phase change thermal management system.

The thermophysical properties of the two composite materials used in the experiment are summarized in Table 2. The MicroPCM 28D composite and the baseline wax composite exhibit similar densities (872 and 800 $kg \cdot m^{-3}$, respectively). However, the thermal conductivity of the MicroPCM 28D composite increases from 0.2497 $W \cdot m^{-1} \cdot K^{-1}$ for the wax composite to 0.3775 $W \cdot m^{-1} \cdot K^{-1}$, corresponding to an enhancement of approximately 51%. Similarly, the thermal diffusivity increases from 0.1607 $mm^2 \cdot s^{-1}$ to 0.3742 $mm^2 \cdot s^{-1}$, representing an increase of about 133%. These enhanced thermal transport properties contribute to faster heat propagation inside the composite material and more efficient heat redistribution within the capsule. The latent heat of the MicroPCM 28D composite (140,000 $J \cdot kg^{-1}$) remains comparable to that of the wax composite (173,400 $J \cdot kg^{-1}$), indicating that the incorporation of MicroPCM 28D maintains significant phase change energy storage capability while improving thermal transport performance.

Table 2. Thermophysical properties of the 28D composite and wax composite.

Property	28D Composite	Wax Composite	Unit
Density, ρ	872	800	$kg \cdot m^{-3}$
Thermal conductivity, k	0.3775	0.2497	$W \cdot m^{-1} \cdot K^{-1}$
Thermal diffusivity	0.3742	0.1607	$mm^2 \cdot s^{-1}$
Latent heat, ΔH	140,000	173,400	$J \cdot kg^{-1}$
Specific heat capacity, c_p	1157	1943	$J \cdot kg^{-1} \cdot K^{-1}$

Another important difference between the two systems lies in their rheological behavior during melting. Previous studies have shown that mixtures containing approximately 60 wt% microencapsulated PCM particles can exhibit slurry-like or paste-like characteristics due to particle–particle interactions that form a spatial network structure [22]. This network structure significantly increases the effective viscosity of the mixture and suppresses liquid flow during melting. In the present work, this property plays a critical role in stabilizing the dispersion of nano carbon black particles inside the composite material. This stability is important for long-term battery operation, as sedimentation could lead to non-uniform thermal conductivity and localized overheating. In contrast to conventional paraffin systems, where nano additives tend to sediment over time, the high-viscosity nature of the 28D composite effectively prevents particle sedimentation and ensures a uniform distribution of thermal conductivity enhancers throughout the material.

Based on the experimental observations in Figure 3 and the thermophysical properties summarized in Table 2, the thermal behavior of the capsule system can be described using a unified thermal response framework. During the initial heating stage, heat is primarily stored through sensible heat accumulation in the composite material. As the temperature approaches the phase change range of the PCM, latent heat storage becomes the dominant mechanism that buffers the temperature rise. Once the latent heat storage capacity is exhausted, the system reaches the thermal steady-state peak temperature. After the heating

https://doi.org/10.3390/batteries12040144

power is removed, the stored thermal energy is gradually released during the cooling stage through both convective heat transfer and phase change solidification. This thermal response system provides the basis for the quantitative comparison of capsule geometries and airflow conditions presented in the following section.

To further verify the phase change behavior and thermal stability of the PCM systems used in this study, differential scanning calorimetry (DSC) and thermogravimetric analysis (TGA) measurements were conducted, as shown in Figure 4. Three materials were characterized, including paraffin wax, a 28D-wax mixture (60 wt% MicroPCM 28D and 40 wt% paraffin), and the 28D composite containing an additional 2 wt% nano carbon black. For DSC measurements, repeated heating–cooling cycles were performed between 10 °C and 60 °C to evaluate phase change temperature, latent heat, and thermal cycling stability. The DSC curve of paraffin wax (Figure 4a) exhibits a single phase change peak centered around 45 °C with a melting enthalpy of approximately 185 J g^{-1}. The nearly overlapping curves for cycles 2, 10, and 20 indicate stable phase change behavior during repeated thermal cycling.

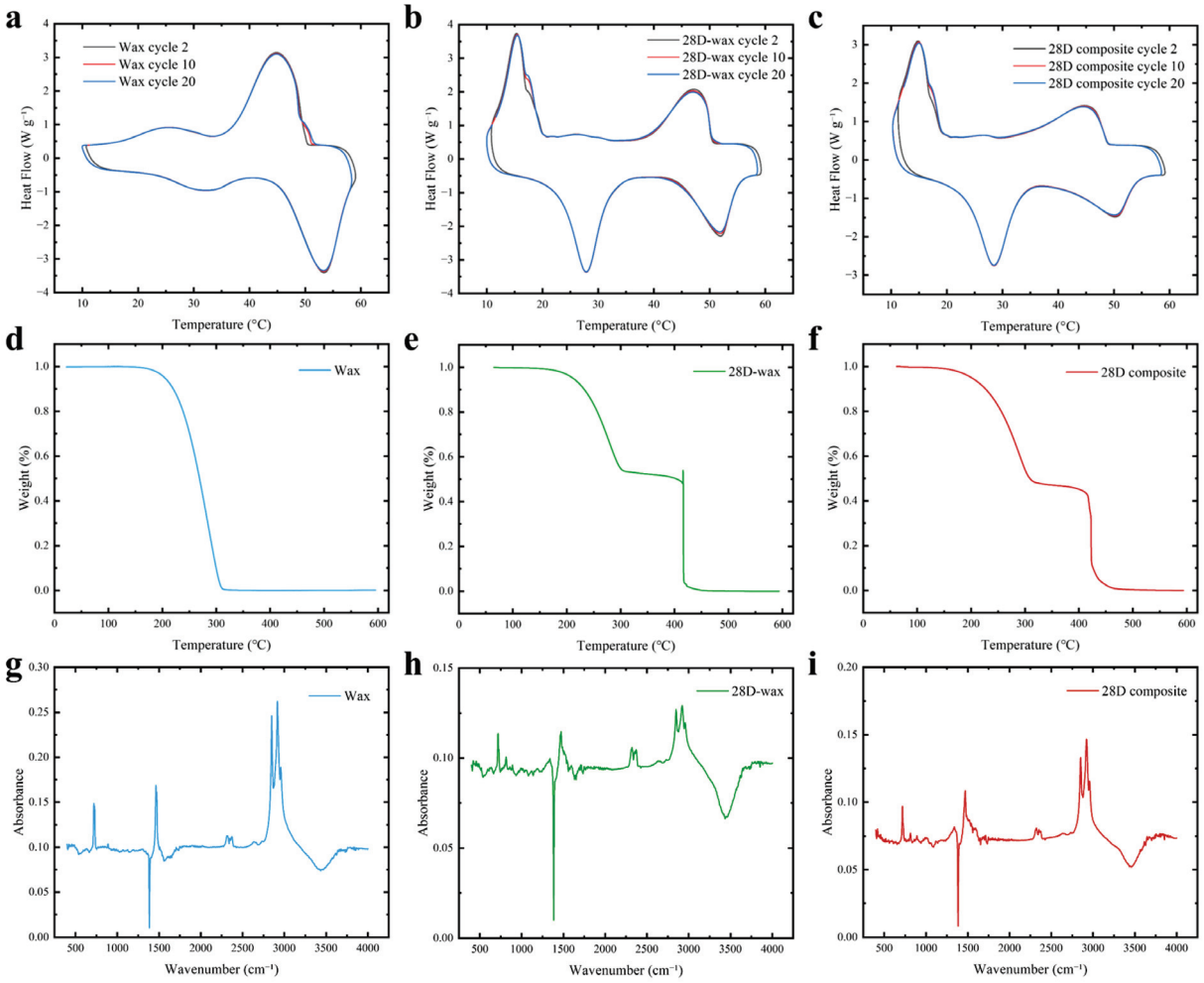

Figure 4. Thermal characterization of PCM used in this study. (**a**) DSC curves of paraffin wax. (**b**) DSC curves of 28D-wax mixture (60 wt% MicroPCM 28D with 40 wt% paraffin). (**c**) DSC curves of 28D composite with 2 wt% nano carbon black. (**d**) TGA curve of paraffin wax. (**e**) TGA curve of 28D-wax mixture. (**f**) TGA curve of 28D composite. (**g**) FTIR spectrum of paraffin wax. (**h**) FTIR spectrum of 28D-wax mixture. (**i**) FTIR spectrum of 28D composite.

The DSC curves of the 28D-wax mixture and 28D composite are shown in Figure 4b,c, respectively. Two distinct phase transition peaks are observed for both materials. The

https://doi.org/10.3390/batteries12040144

low-temperature peak near 28 °C corresponds to the MicroPCM 28D component, consistent with the manufacturer-reported melting temperature, while the higher-temperature peak corresponds to the paraffin wax phase transition. The total melting enthalpy of the 28D-wax mixture is approximately 195–200 J g^{-1}, indicating that the addition of MicroPCM 28D maintains comparable latent heat storage capacity. After introducing 2 wt% nano carbon black, the melting enthalpy slightly decreases to approximately 175–180 J g^{-1}, while the phase change temperature remains nearly unchanged. The consistent peak positions and overlapping curves across repeated cycles demonstrate that the composite materials maintain stable phase change behavior and good thermal cycling stability.

The TGA curves of the three materials are presented in Figure 4d–f. Paraffin wax exhibits single-step thermal decomposition, whereas the 28D-based materials undergo multi-stage degradation due to the presence of microencapsulated PCM and additives. The 28D composite retains a small residual mass after decomposition, which is attributed to the nano carbon black content. These results indicate that the composite PCM systems maintain good thermal stability within the operating temperature range of battery thermal management applications.

For the 28D-wax mixture and the 28D composite (Figure 4h,i), the major absorption peaks associated with paraffin remain unchanged, indicating that the fundamental chemical structure of the PCM matrix is preserved after mixing. No new characteristic peaks are observed after incorporating MicroPCM 28D and nano carbon black, suggesting that the composite formation is dominated by physical blending rather than chemical reactions. Minor variations in peak intensity are attributed to the presence of microencapsulated PCM particles and nano carbon additives. These results confirm the chemical compatibility of the composite components and support the thermal stability observed in DSC and TGA measurements.

4. Quantitative Performance Comparison

Figure 5 presents the transient temperature evolution of the battery capsules under different airflow conditions and capsule geometries. Figure 5a shows the infrared temperature evolution measured on the front surface of the capsule for Shape 3, which provides a representative comparison between the two PCM systems. The temperature rise of the 28D composite capsule is lower than that of the wax capsule, indicating a stronger thermal buffering effect during the heating stage.

Figure 5b further compares the inside and outside temperatures of the capsule for Shape 2 under an airflow speed of 5 m·s^{-1}. The results show that the inside temperature of the capsule is consistently higher than the outside temperature due to the internal heat source. Compared with the wax composite, the 28D composite exhibits a lower inside temperature and a more gradual temperature rise, indicating improved internal heat distribution and enhanced phase change buffering.

Figure 5c–g present the complete transient temperature responses of the five capsule geometries under all airflow conditions. Each subfigure corresponds to a specific capsule shape, where Figure 4c shows Shape 1, Figure 4d shows Shape 2, Figure 4e shows Shape 3, Figure 4f shows Shape 4, and Figure 4g shows Shape 5. For each geometry, five distinct temperature peaks can be observed in the inside temperature curves. From left to right, the peaks correspond to airflow speeds of 10, 5, 3, 1, and 0 m·s^{-1}, respectively. Each airflow condition was tested independently, and the capsule was allowed to cool down to ambient temperature before the next heating cycle was initiated.

https://doi.org/10.3390/batteries12040144

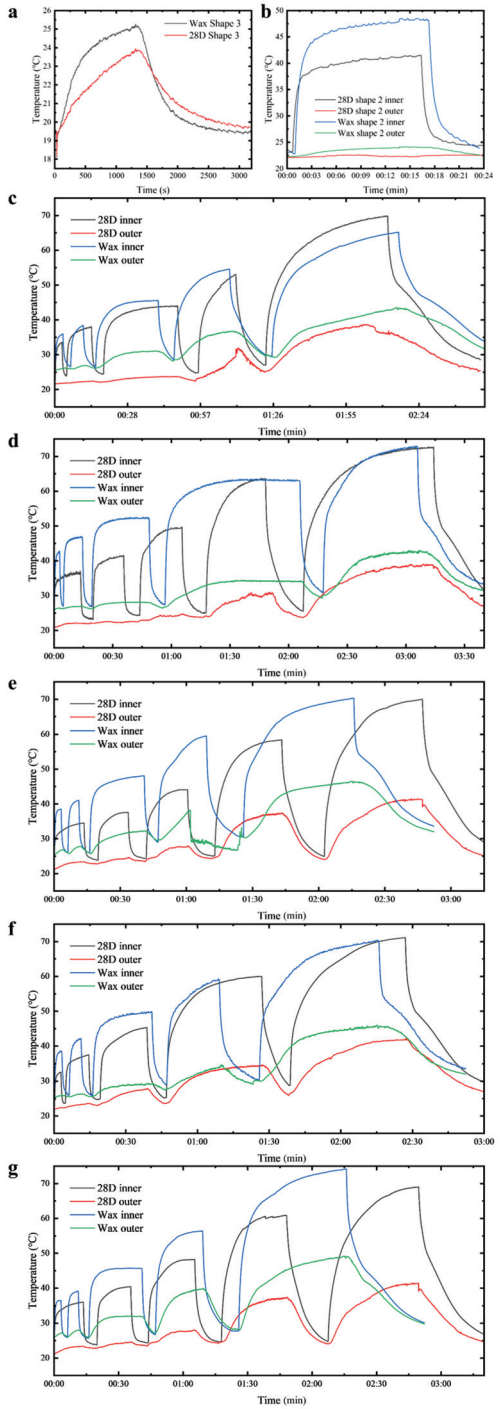

Figure 5. Temperature evolution of battery capsules filled with 28D composite and wax composite under different geometric designs and airflow conditions. In all cases, the internal thermocouple measures the simulated battery temperature inside the capsule while the external thermocouple measures the outer capsule surface temperature. (**a**) Infrared camera temperature measurement of the front surface for Shape 3 capsules, comparing the wax composite and the 28D composite during a heating and cooling cycle. (**b**) Comparison of internal and external temperature evolution between the 28D composite capsule and the wax composite capsule for Shape 2 under an airflow speed of 5 $m \cdot s^{-1}$. (**c**) Temperature evolution of Shape 1 capsules under different airflow speeds of 10, 5, 3, 1, and 0 $m \cdot s^{-1}$ from left to right. (**d**) Temperature evolution of Shape 2 capsules under airflow speeds of 10, 5, 3, 1, and 0 $m \cdot s^{-1}$. (**e**) Temperature evolution of Shape 3 capsules under airflow speeds of 10, 5, 3, 1, and 0 $m \cdot s^{-1}$. (**f**) Temperature evolution of Shape 4 capsules under airflow speeds of 10, 5, 3, 1, and 0 $m \cdot s^{-1}$. (**g**) Temperature evolution of Shape 5 capsules under airflow speeds of 10, 5, 3, 1, and 0 $m \cdot s^{-1}$.

https://doi.org/10.3390/batteries12040144

Since the experiments for the 28D composite and the wax composite were conducted under slightly different ambient temperatures, a baseline correction was applied to the wax data before comparison. The experiments for the 28D composite were conducted during the daytime with an ambient temperature of approximately 25 °C, while the wax experiments were performed at night with an ambient temperature of approximately 21 °C. To compensate for this difference, the wax temperature data were corrected using

$$T_{wax}^{corr}(t) = T_{wax}(t) + (T_{amb,28D} - T_{amb,wax}) \quad (1)$$

where $T_{amb,28D}$ and $T_{amb,wax}$ represent the ambient temperatures during the two experimental sessions. This correction aligns the temperature baselines of the two datasets without altering the temperature evolution trends.

To facilitate comparison between corresponding airflow conditions, minor temporal alignment was also performed. For each airflow segment i, the peak temperature time was identified using the inside thermocouple temperature:

$$t_i^{peak} = \text{argmax} T_{in}(t) \quad (2)$$

A small portion of the steady-state plateau region near the peak of the 28D curve was adjusted to align the peak positions under identical airflow conditions. This adjustment slightly modifies the duration of the steady-state plateau but does not affect the peak temperature values or the overall heating and cooling trends. Therefore, the comparison of peak temperature and transient thermal behavior remains valid.

The airflow around the capsules corresponds to external crossflow over non-axisymmetric geometries. In this context, the characteristic length is defined as the representative length scale in the direction normal to the incoming airflow. For circular capsules, this length corresponds to the diameter, while for oval capsules, it is approximated by the minor axis, which represents the projected frontal dimension exposed to the airflow. This definition is adopted to provide a consistent geometric basis for comparing different capsule shapes. Accordingly, the present study focuses on experimentally observed trends in convection intensity rather than predictive heat transfer modeling.

Under these convection-dominated conditions, the advantage of the 28D composite becomes more evident. The MicroPCM 28D particles provide distributed latent heat storage throughout the composite, while the uniformly dispersed nano carbon black enhances internal thermal transport. As a result, heat generated inside the capsule can be more effectively redistributed toward the capsule surface, where it can be removed by the external airflow. This effect explains why the temperature reduction of the 28D composite becomes more pronounced at higher airflow speeds.

The capsule geometry also influences the thermal performance under forced convection. The oval capsules (Shapes 1–3) were designed with the major axis aligned with the incoming airflow. Under this configuration, the oval cross sections are more streamlined than circular ones and can delay flow separation and reduce the size of the downstream wake region. Because the thermocouples were positioned on the downstream side of the capsule, the local temperature response is strongly influenced by the wake development behind the capsule. A smaller wake region generally enhances the convective heat transfer on the backside surface. This trend is also related to the capsule aspect ratio, where elongated geometries with higher aspect ratios tend to produce smaller wake regions and improve heat removal, resulting in lower peak temperatures.

The oval shapes can be characterized by the aspect ratio defined as the ratio between the major and minor axes. The aspect ratios are approximately 1.272, 1.180, and 1.094 for Shapes 1, 2, and 3, respectively, gradually approaching the circular case. Because the minor

https://doi.org/10.3390/batteries12040144

axes of the oval capsules are close to the diameters of the circular capsules, the frontal blockage differences are relatively small. Therefore, geometry dependent thermal behavior is mainly associated with differences in flow separation and wake behavior rather than large variations in flow conditions.

To quantitatively compare the thermal performance of the two PCM systems, three evaluation metrics were defined based on the temperature curves. The peak temperature difference is defined as

$$\Delta T_{peak} = T_{wax}^{peak} - T_{28D}^{peak} \tag{3}$$

where T_{wax}^{peak} is the maximum temperature measured for the wax composite capsule, and T_{28D}^{peak} is the maximum temperature measured for the 28D composite capsule. A positive value of ΔT_{peak} indicates that the 28D composite achieves a lower peak temperature than the wax composite.

The delay in reaching the peak temperature is defined as

$$\Delta t_{peak} = t_{28D}^{peak} - t_{wax}^{peak} \tag{4}$$

where t_{28D}^{peak} and t_{wax}^{peak} represent the times required for the 28D composite and wax composite capsules to reach their respective peak temperatures. A positive value of Δt_{peak} indicates that the 28D composite maintains the phase change buffering process for a longer duration before reaching the steady state peak temperature.

The difference in cooling duration is defined as

$$\Delta t_{cooling} = t_{28D}^{cool} - t_{wax}^{cool} \tag{5}$$

where t_{28D}^{cool} and t_{wax}^{cool} represent the times required for the 28D composite and wax composite capsules to cool down to near the ambient temperature after the heating power is turned off. Therefore, the positive value of $\Delta t_{cooling}$ indicates that the 28D composite releases heat more slowly during the cooling stage.

The quantitative comparison across all capsule geometries and airflow conditions is summarized in Figure 6. Overall, the 28D composite shows lower peak temperatures, delayed peak occurrence, and longer cooling durations compared with conventional wax, particularly under strong forced convection. Figure 6a shows the peak temperature differences between the two PCM systems. Positive values dominate at higher airflow speeds, indicating that the 28D composite generally achieves lower peak temperatures under strong forced convection. Figure 6b presents the delay in reaching the peak temperature, which is mostly positive across different geometries and airflow conditions. This result suggests that the MicroPCM-based composite can extend the effective thermal buffering period. Figure 6c compares the cooling durations, where positive values indicate slower heat release for the 28D composite. The longer cooling duration reflects the enhanced latent heat storage capability of the MicroPCM 28D particles as well as the higher viscosity of the composite matrix.

In addition to improving short term thermal buffering, the MicroPCM 28D suspension also enhances the long-term stability of the composite system. The high viscosity of the 28D composite prevents nano carbon black particles from sedimentation during repeated heating and cooling cycles. In contrast, nano additives in conventional paraffin systems are more susceptible to long-term sedimentation, which can gradually degrade the uniformity of thermal conductivity within the capsule. As a result, the 28D composite is expected to maintain more stable thermal performance over extended operating periods.

https://doi.org/10.3390/batteries12040144

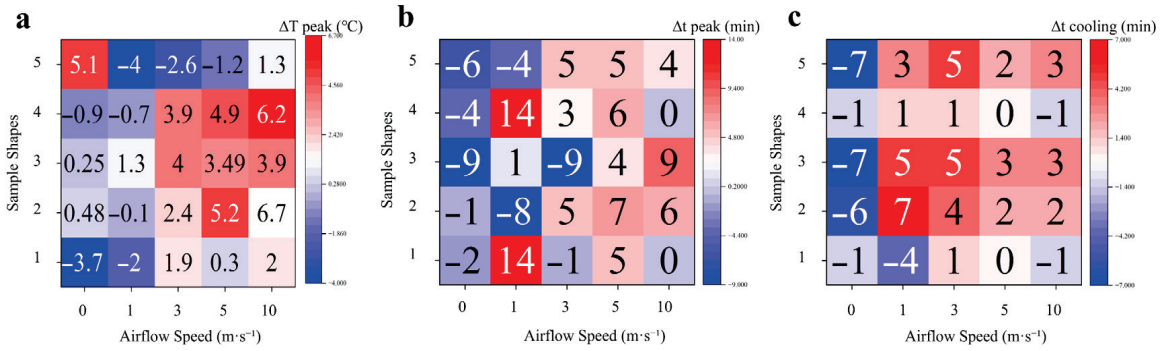

Figure 6. Quantitative comparison of thermal regulation performance for battery capsules filled with the 28D composite material under different capsule geometries and airflow speeds. The horizontal axis represents airflow speed (0, 1, 3, 5, and 10 m·s^{-1}), and the vertical axis represents the five capsule shapes investigated in this study. The color scale indicates the performance difference between the 28D composite capsule and the wax composite capsule. (**a**) Difference in peak temperature (ΔT_peak). Positive values indicate that the 28D composite achieves a lower peak temperature than the wax composite, while negative values indicate that the wax composite reaches a lower peak temperature. (**b**) Difference in the time required to reach the steady-state peak temperature (Δt_peak). Positive values indicate that the 28D composite maintains the phase-change buffering effect for a longer time, delaying the steady-state temperature compared with the wax composite. (**c**) Difference in cooling duration (Δt_cooling). Positive values indicate that the 28D composite releases stored heat more slowly, resulting in a longer cooling process compared with the wax composite.

5. Conclusions

This study investigated the thermal regulation performance of MicroPCM-based composite capsules for battery thermal management under different airflow conditions and capsule geometries. A sedimentation-stable composite consisting of 60 wt% MicroPCM 28D, 40 wt% paraffin wax, and an additional 2 wt% nano carbon black was developed and compared with a conventional wax-based composite system. Five capsule geometries were fabricated using fused filament fabrication 3D printing with Onyx material, including three oval shapes and two circular shapes, to examine the influence of geometry on convective heat dissipation.

Infrared thermography and wind tunnel experiments were conducted to characterize the transient thermal behavior of the capsules. The results show that the thermal response of the capsule system can be divided into three stages: sensible heating, phase change buffering, and cooling after power removal. The MicroPCM-based composite exhibited improved internal heat redistribution and stronger phase change buffering compared with the wax composite. Under low airflow conditions (0–1 m·s^{-1}), the heat transfer process was dominated by conduction, and the temperature difference between the two composite systems was relatively small. As the airflow increased to 3–10 m·s^{-1}, forced convection became the dominant heat transfer mechanism, and the advantage of the 28D composite became increasingly evident.

Quantitative performance analysis based on peak temperature difference, peak delay time, and cooling duration demonstrates that the MicroPCM 28D composite generally achieves lower peak temperatures and longer thermal buffering durations under moderate and strong convection conditions. The results also show that capsule geometry influences the thermal performance through its interaction with external airflow. Oval capsules with the major axis aligned with the incoming flow modify the flow separation and wake development near the downstream surface, which improves convective heat dissipation compared with circular geometries.

https://doi.org/10.3390/batteries12040144

In addition to improved thermal regulation performance, the MicroPCM-based composite also provides enhanced long-term material stability. The high viscosity of the MicroPCM 28D suspension suppresses the sedimentation of nano carbon black particles during repeated melting and solidification cycles, ensuring a more uniform thermal conductivity distribution within the composite. This property addresses one of the major limitations of conventional paraffin-based nanocomposites.

Overall, the results demonstrate that the combination of MicroPCM-based composite materials and geometry-regulated capsule design provides an effective strategy for improving passive thermal management of battery systems. The findings provide useful design guidelines for future phase change thermal management structures in battery modules and other energy storage applications.

Author Contributions: X.Z.: Writing—original draft, Resources, Writing—review and editing. M.C.H.: Writing—review and editing, Resources. A.A.: Writing—review and editing, Resources. M.S.: Writing—review and editing, Resources. Y.Z.: Writing—review and editing, Supervision, Resources, Project administration. All authors have read and agreed to the published version of the manuscript.

Funding: This project is partially supported by the National Aeronautics and Space Administration Glenn Research Center (NASA GRC) Faculty Fellowship.

Data Availability Statement: The original contributions presented in this study are included in the article. Further inquiries can be directed to the corresponding author.

Conflicts of Interest: The authors declare that they have no known competing financial interests or personal relationships that could have appeared to influence the work reported in this paper.

References

1. Zhang, C.-Z.; Xie, L.-J.; Tang, Y.; Li, Y.; Jiang, J.-C.; Huang, A.-C. Thermal Safety Evaluation of Silane Polymer Compounds as Electrolyte Additives for Silicon-Based Anode Lithium-Ion Batteries. *Processes* **2022**, *10*, 1581. [CrossRef]
2. Bandhauer, T.M.; Garimella, S.; Fuller, T.F. A Critical Review of Thermal Issues in Lithium-Ion Batteries. *J. Electrochem. Soc.* **2011**, *158*, R1. [CrossRef]
3. Feng, X.; Ouyang, M.; Liu, X.; Lu, L.; Xia, Y.; He, X. Thermal Runaway Mechanism of Lithium Ion Battery for Electric Vehicles: A Review. *Energy Storage Mater.* **2018**, *10*, 246–267. [CrossRef]
4. Wang, Q.; Ping, P.; Zhao, X.; Chu, G.; Sun, J.; Chen, C. Thermal Runaway Caused Fire and Explosion of Lithium Ion Battery. *J. Power Sources* **2012**, *208*, 210–224. [CrossRef]
5. Rao, Z.; Wang, S. A Review of Power Battery Thermal Energy Management. *Renew. Sustain. Energy Rev.* **2011**, *15*, 4554–4571. [CrossRef]
6. Sharma, A.; Tyagi, V.V.; Chen, C.R.; Buddhi, D. Review on Thermal Energy Storage with Phase Change Materials and Applications. *Renew. Sustain. Energy Rev.* **2009**, *13*, 318–345. [CrossRef]
7. Ling, Z.; Zhang, Z.; Shi, G.; Fang, X.; Wang, L.; Gao, X.; Fang, Y.; Xu, T.; Wang, S.; Liu, X. Review on Thermal Management Systems Using Phase Change Materials for Electronic Components, Li-Ion Batteries and Photovoltaic Modules. *Renew. Sustain. Energy Rev.* **2014**, *31*, 427–438. [CrossRef]
8. Cabeza, L.F.; Castell, A.; Barreneche, C.; de Gracia, A.; Fernández, A.I. Materials Used as PCM in Thermal Energy Storage in Buildings: A Review. *Renew. Sustain. Energy Rev.* **2011**, *15*, 1675–1695. [CrossRef]
9. Nasiri, M.; Hadim, H. Thermal Management of Li-Ion Batteries Using Phase Change Materials: Recent Advances and Future Challenges. *J. Energy Storage* **2025**, *111*, 115440. [CrossRef]
10. Su, W.; Darkwa, J.; Kokogiannakis, G. Review of Solid–Liquid Phase Change Materials and Their Encapsulation Technologies. *Renew. Sustain. Energy Rev.* **2015**, *48*, 373–391. [CrossRef]
11. Cui, Y.; Li, L.; Liu, J.; Liu, P. Phase Change Microcapsules Modified by Thermal Conductivity Reinforced Materials for Enhanced Thermal Energy Storage. *Aust. J. Chem.* **2025**, *78*, CH25092. [CrossRef]
12. Qureshi, Z.; Ali, H.M.; Khushnood, S. Recent Advances on Thermal Conductivity Enhancement of Phase Change Materials for Energy Storage System: A Review. *Int. J. Heat Mass Transf.* **2018**, *127*, 838–856. [CrossRef]

13. Adera, B.; Ancha, V.R.; Tadiwose, T.; Getahun, E. Nano Enhanced Phase Change Materials for Thermal Energy Storage System Applications: A Comprehensive Review of Recent Advancements and Future Challenges. *Int. J. Thermofluids* **2025**, *30*, 101418. [CrossRef]
14. Gupta, S.K.; Kumari, S.; Singh, A.P. A Review on Recent Development and Applications of Nano-Enhanced Phase Change Material in Thermal Management System. *Energy Storage Sav.* **2026**, *5*, 100234. [CrossRef]
15. Zou, D.; Ma, X.; Liu, X.; Zheng, P.; Hu, Y. Thermal Performance Enhancement of Composite Phase Change Materials Using Graphene and Carbon Nanotubes as Additives for the Potential Application in Lithium-Ion Power Battery. *Int. J. Heat Mass Transf.* **2018**, *120*, 33–41. [CrossRef]
16. Li, R.; Sun, X.; Zhang, R.; Wang, S.; Liu, Q.; Bai, P.; Yuan, Y.; Li, Y. Enhancement of Thermal Conductivity of Graphene-Based Phase Change Composites by Alternating Positive and Negative Pressures during Perfusion. *Chem. Eng. J.* **2025**, *504*, 158964. [CrossRef]
17. Zare, P.; Perera, N.; Lahr, J.; Hasan, R. A Novel Thermal Management System for Cylindrical Lithium-Ion Batteries Using Internal–External Fin-Enhanced Phase Change Material. *Appl. Therm. Eng.* **2024**, *238*, 121985. [CrossRef]
18. Najafi Khaboshan, H.; Jaliliantabar, F.; Abdullah, A.A.; Panchal, S.; Azarinia, A. Parametric Investigation of Battery Thermal Management System with Phase Change Material, Metal Foam, and Fins; Utilizing CFD and ANN Models. *Appl. Therm. Eng.* **2024**, *247*, 123080. [CrossRef]
19. Hyun, S.W.; Kim, J.H.; Shin, D.H. Hybrid PCM–Liquid Cooling System with Optimized Channel Design for Enhanced Thermal Management of Lithium-Ion Batteries. *Energies* **2025**, *18*, 4996. [CrossRef]
20. Wu, Z.; Chen, H.; Jiang, L.; Zhang, P.; Ji, Z.; Luo, D. Thermal Management of Lithium-Ion Batteries Using a PCM–HP–TEC Hybrid BTMS: A Numerical Study. *Int. Commun. Heat Mass Transf.* **2025**, *169*, 109702. [CrossRef]
21. Hussien, H.M.; Ali, A.B.; Alkhatib, O.J.; Mahariq, I. Enhanced Passive Thermal Management of Lithium-Ion Batteries Using Phase Change Materials. *Sci. Rep.* **2025**, *15*, 4321. [CrossRef]
22. Xiang, X.; Routsi, A.M.; Nagarajan, R.; Wang, Q.; Yang, R.; Esfahani, I.C.; Hoffman, D.; Sun, H. Numerical and Experimental Investigation of a Hybrid Battery Thermal Management System for High-Rate Applications. *J. Energy Storage* **2026**, *141*, 119081. [CrossRef]
23. Zhang, X.; Liu, Y.; Halbig, M.; Singh, M.; Almansour, A.; Zheng, Y. Development and Optimization of Hybrid Heat Dissipation System for Lithium-Ion Battery Packs. *Appl. Therm. Eng.* **2024**, *254*, 123912. [CrossRef]
24. Zhang, X.; Zhang, H.; Almansour, A.; Singh, M.; Kiser, J.D.; Zhu, H.; Halbig, M.C.; Zheng, Y. A Comprehensive Analysis of Thermal Heat Dissipation for Lithium-Ion Battery Packs. *Energies* **2025**, *18*, 2234. [CrossRef]
25. Zhu, H.; Xiang, X.; Zhang, X.; Liu, H.; Zhang, H.; Sun, H.; Zheng, Y. Analysis of Hybrid Thermal Systems Incorporating Composite Phase Change Materials. *ASME Open J. Eng.* **2025**, *4*, 041017. [CrossRef]
26. Zhang, X.; Halbig, M.C.; Almansour, A.; Singh, M.; Ranaiefar, M.; Zheng, Y. Innovative 3D-Printed Hybrid Cooling Systems for Thermal Management of Lithium-Ion Pouch Cells. *J. Energy Storage* **2026**, *142*, 119469. [CrossRef]
27. Theodore, A.M. Structural, electrical, and electrochemical studies of the olivine LiMPO4 (M = Fe, Co, Cr, Mn, V) as cathode materials for lithium-ion rechargeable batteries based on the intercalation principle. *Mater. Open Res.* **2023**, *2*, 11. [CrossRef]

Disclaimer/Publisher's Note: The statements, opinions and data contained in all publications are solely those of the individual author(s) and contributor(s) and not of MDPI and/or the editor(s). MDPI and/or the editor(s) disclaim responsibility for any injury to people or property resulting from any ideas, methods, instructions or products referred to in the content.

batteries

MDPI

Article

Data-Driven Modeling of Auxiliary Consumption in Utility-Scale BESS

Aleksandar Dimovski [1,*], Matteo Spiller [1], Mershad Pakjoo [2], Giulio Cantoni [3], Giacomo Gorni [4], Luigi Piegari [2] and Marco Merlo [1,*]

[1] Department of Energy (DENG), Politecnico di Milano, 20156 Milano, Italy; matteo.spiller@polimi.it
[2] Department of Electronics, Information Technology and Bioenergy (DEIB), Politecnico di Milano, 20133 Milano, Italy; luigi.piegari@polimi.it (L.P.)
[3] Renewable, New Energies, and Material Science Research Center, Eni S.p.A., 28100 Novara, Italy; giulio.cantoni@eni.com
[4] Eni S.p.A., 00144 Rome, Italy
* Correspondence: aleksandar.dimovski@polimi.it (A.D.); marco.merlo@polimi.it (M.M.)

Abstract

Accurately modeling the auxiliary power consumption of Battery Energy Storage Systems (BESSs) is increasingly important as grid-scale storage assets are becoming involved in electricity markets. In this paper, we develop a data-driven framework to characterize and forecast auxiliary consumption using operational data from a utility-scale BESS deployed in Italy. To capture the short-term thermal inertia of the system and the delayed response of the cooling systems, a set of predictors based on moving averages of power and ambient temperature is constructed. Two novel modeling approaches are proposed: a three-dimensional look-up table (LUT) representation that provides an interpretable characterization of system behavior, as well as a Random Forest (RF) regression model capable of capturing complex non-linear relationships between parameters. These are evaluated in comparison with a two-dimensional LUT from the literature. The analysis showed a superior performance of the RF model that comes at the cost of reduced interpretability and computational efficiency, while both proposed models outperform the literature-based LUT. Moreover, the impact of the number and type of predictors on model performance is systematically assessed, to shed light on what constitutes the requirements for a reasonably accurate estimation of the auxiliary systems. Finally, the concept of forecasting uncertainty for the temperature and day-ahead forecasting applicability for the auxiliary systems is investigated by introducing a persistence-based logic and an evaluation of the impact on the results. Overall, the study highlights the importance of explicitly modeling auxiliary consumption in grid-scale BESSs, proposes well-performing models for its estimation, and provides practical guidelines for their implementation in energy management and forecasting applications.

Keywords: Battery Energy Storage Systems (BESSs); BESS auxiliary consumption; data-driven modeling; moving-average predictors; machine learning; Random Forest regression

1. Introduction

Global efforts to decarbonize the energy system focus on a drastic reduction in greenhouse emissions to meet the Paris Agreement targets and limit global warming. The ambitious decarbonization targets include achieving net-zero emissions by 2050 and significantly scaling up clean energy deployment by 2030 to electrify emerging rural areas

and to support the electrification of loads, such as the cases of electric vehicles and heat pumps. These strategies are outlined by the International Energy Agency's (IEA) Net Zero Roadmap and COP28 energy goals, which aim to triple the renewable energy capacity and double energy efficiency during this decade. However, due to their inherent intermittency and partial predictability, they pose two key challenges to the traditional power system paradigm: first, the temporal mismatch between consumption and generation complicates real-time energy balancing; and, second, the variability in generation can cause voltage and frequency regulation issues, stressing the grid stability [1]. Thus, integrating high shares of variable renewables into the electric grid requires significant upgrades in transmission infrastructure, flexibility mechanisms, and energy storage solutions in order to maintain reliability and stability. For example, authors in the USA [2] investigated various scenarios coupling demand, generation, and weather trends, simulated on synthetic grid topologies, and concluded that, regardless of the scenario, the net demand curves get deeper in the middle of the day, leading to extremely volatile electricity prices and outages leading to the loss of load events.

This need, paramount to the safe and reliable operation of the future power system [3], has given a meteoric rise in the procurement of Battery Energy Storage Systems (BESSs), most notably, the larger installations connected directly to the electrical transmission or distribution network, known as grid-scale BESSs. Their attractiveness comes from the wide range of services that they can provide to support the energy transition and the integration of RES, often more quickly and efficiently than their traditional counterparts. In their special Batteries and Secure Energy Transitions report [4] published in 2024, the IEA states that the global BESS installments rose from approximately 1 GW in 2013, to 85 GW in 2023, 42 GW of which were added in that year alone, showing a strong recent trend. However, specific deployment patterns differ across regions. For example, Europe has seen a strong inclination towards behind-the-meter installations driven by high retail prices, whereas grid-scale installations have remained economically infeasible.

The need for more strategically planned grid-scale installations has been widely recognized by national regulators and public bodies in Europe, leading to the integration of BESS capacity market frameworks and similar long-term procurement mechanisms. For example, Italy has introduced a dedicated support mechanism for utility-scale electricity storage established under Legislative Decree No. 210/2021. Thus, the first official auction took place at the end of 2025, awarding incentives to 10 GWh of grid-scale BESSs to enter service by 2028. Similarly, Poland's capacity market has allocated 2.5 GW for delivery by 2029, with similar mechanisms being activated across the continent to support long-term system adequacy. These measures support large-scale deployment, ensure system adequacy, and maintain economic feasibility by reducing the financial uncertainty caused by both the rapid changes in the power systems, as well as the evolving cost trends of the technology itself. Indeed, looking at the future outlook, the IEA Net Zero Emissions (NZE) scenario forecasts BESS installations to rise to an astounding 1200 GW, 1000 GW of which would be grid-scale [4].

The anticipated expansion of grid-scale storage introduces unique complexities that extend beyond the scope of the vast amount of conventional battery research focusing on the cell technology. These complexities arise from the sheer size and multitude of the components, dynamic operation conditions, and interaction with electricity markets, requiring specific tools to optimize their operational and economic performance over the assets' lifetime. Until recently, the limited deployment of utility-scale BESSs, coupled with the high costs associated with detailed system-level studies, has constrained the research in this area. A wide overview of the modeling approaches for grid-connected storage technologies was recently published in [5], where the authors indeed note "generic

https://doi.org/10.3390/batteries12080288

modeling" as one of their conclusions and defended that, even though it comes with certain benefits, its drawback is the lack of case- and technology-specific details which can lead to reduced accuracy.

The authors in [6] noted this gap and focused on bridging the existing modeling methods for Li-Ion cells to stationary grid-scale BESSs by building a Thevenin equivalent circuit populated by Open-Circuit Voltage (OCV) and internal resistance measurements. However, the focus is still solely on the battery pack and does not completely bridge the gap; instead, it aims to represent the BESS as one large cell and avoid the need for single-cell testing. Similar effort was done by the work presented in [7] that utilized an equivalent circuit model to model the State-of-Charge (SoC) of a BESS for off-grid applications. In general, grid-scale BESSs are modeled with a fixed efficiency that aims to represent all the losses that occur during the charging and discharging processes [8]. However, this over-generalization fails to grasp specific non-linear dependencies that are difficult to characterize, such as those arising in cooling systems, as well as well-defined non-linear loss mechanisms like ohmic losses in wires and transformers.

An analytical approach was proposed in [9], where the authors developed separate models for efficiency and auxiliary consumption. The auxiliary demand is estimated through a thermal model based on Joule losses, combined with an HVAC coefficient of performance to represent the cooling power required to remove heat. While this is a well-structured analytical representation, it treats the BESS as a closed system driven mainly by internally generated heat, without explicitly accounting for external influences such as ambient temperature or site-specific conditions. This represents a significant simplification with respect to real utility-scale operation. The authors in [10] laid the groundwork for a more detailed, data-driven modeling of a large-scale BESS specifically for power grid applications, where the model included not only the battery pack, but also the Power Conversion System (PCS) and auxiliaries. The paper proposes a test procedure to develop a look-up table (LUT)-based model for characterizing BESS performance. This includes efficiency and power-delivery capability as a function of SoC and power, as well as the auxiliary power consumption as a function of ambient temperature and power. The end goal was a more accurate estimation of the potential to provide services, to assure compliance with the capacity offered on the market. The model developed was subsequently applied to evaluate the overall BESS efficiency during ancillary service provision [11], simulating several operating profiles and seasonal conditions. The authors compared the simulations, including auxiliary consumption, against a base case in which they were neglected. The analysis showed that the impact was more significant for low-power operation and longer idle periods, especially in the summer period when, due to external heat, the thermal-management demand persists independently of the BESS operation. In this scenario, the study reported significant errors of up to 10% in the estimated operational efficiency [11]. The results showed that this effect depends on the BESS's utilization, highlighting the importance of accounting for auxiliary consumption with dedicated modeling—especially when the asset is underutilized. The work in [12] goes one step beyond and proposes SoC restoration techniques utilizing the participation to the Ancillary Services Market (ASM), where the authors found that the SoC restoration requirements are 25–45% of the energy dedicated to service provision themselves, severely impacting the technical and economical dispatch of the asset.

The overview of grid-scale-focused BESS models showed that auxiliary power consumption is often overlooked, typically incorporated together with the battery pack in a simplified manner, rather than treated as a separate component. In other cases such as the model proposed in [10], the authors correctly point out its importance, but with a simplification that does not account for the preceding thermal or operational history,

such as moving averages (MAs) and cumulative effects. Aside from the energy exchanged with the grid, a BESS continuously absorbs energy to support equipment such as thermal management systems, control hardware, and safety apparatus. In particular, cooling units required to maintain battery cells within safe operating temperatures could account for a meaningful share of the overall energy throughput, especially under variable ambient conditions and dynamic operating modes. Failing to properly account for this additional consumption can lead to inaccurate SoC estimates, which, in turn, could cause infeasible dispatch schedules, reduced reserve availability for the power system, and financial losses for the asset owner.

The main contribution of the paper is to provide a methodology for accurately estimating and forecasting the auxiliary consumption of grid-scale BESSs, going beyond a simple function of instantaneous parameters, which is the current best practice. The proposed approach is validated through a real-life case study, demonstrating its applicability to an asset actively providing grid services. By explicitly forecasting auxiliary consumption, the proposed framework enables more reliable SoC estimation, and an improved assessment of both technical and economic performance.

The remaining part of the paper is organized as follows: Section 2 presents the concept of an auxiliary consumption and outlines possible techniques to forecast it. Section 3 describes a case study and the modeling framework to model and forecast the auxiliary consumption in a utility-scale BESS, whereas Section 4 presents the simulation results and analyzes key observations in parameter selection. Finally, Section 5 provides a comprehensive discussion, concludes the paper, and provides future research directions.

2. Auxiliary Consumption in Battery Energy Storage Systems

In a broad sense, auxiliary load in a BESS refers to the electric power consumed by supporting subsystems that are necessary for the operation, safety, control, and protection of a BESS, but do not contribute to storing or delivering energy to the grid. This includes the thermal management systems, and the monitoring systems alongside the sensors, as well as any additional equipment including but not limited to transformers, switchboards, and instrumentation power. In modern BESSs, by far the largest contributor is the thermal management system. However, in real-life deployments, auxiliary consumption is typically available only as an aggregate measurement, whereas a quantitative breakdown among each component is unavailable. Moreover, component-level consumption and internal control logics are often proprietary and not disclosed to the asset manager. Therefore, a general system-level modeling perspective is a reasonable tradeoff that accurately addresses these data availability constraints.

Temperature is widely recognized as a dominant factor influencing lithium-ion batteries' performance, degradation, and safety. Operating at low temperatures leads to an increased internal resistance and reduced power capability, whereas elevated temperatures accelerate ageing mechanisms, affecting the system reliability and lifetime [13,14]. These effects are particularly critical because during normal operation at ambient conditions, lithium-ion batteries generally generate heat due to charge transfer processes and electrochemical reactions. Heat generation strongly depends on operating conditions such as the current rate (C-rate), SoC, and internal resistance, and may become significant during high-power operation [15]. Nevertheless, it should be noted that the tests were performed on a relatively small battery with a very high C-rate. Consequently, the battery temperature results from the combined effect of internally generated heat and external environmental conditions, making thermal control a fundamental requirement rather than an optional design feature. For these reasons, an effective Battery Thermal Management System (BTMS) is essential in order to maintain batteries within their optimal temperature range and ensure

https://doi.org/10.3390/batteries12080288

a consistent performance over a wide range of operating conditions and overtime [14,16]. The thermal management of lithium-ion batteries has been widely investigated in the literature, leading to a variety of works discussing the trade-offs between different strategies. In that sense, several review articles provide comprehensive classifications of BTMS distinguishing between air-based, liquid-based, and advanced or hybrid solutions [16,17]. Although the details of these systems are outside of scope of this paper, the literature agrees that no single strategy outperforms the rest across all operating conditions. More importantly, recent overviews emphasize that thermal management should be analyzed at the system level considering the operation dynamics and external conditions [18].

In practical modeling terms, these systems do not behave as constant or proportional loads that can be easily represented by offsets. On the contrary, their power consumption is strongly dependent on both the temperature dynamics and control behavior, leading to a non-linear, state-dependent behavior that can affect overall performance over its lifetime. Although direct experimental evidence for large-scale BESSs is scarce, extensive studies in the Electric Vehicle (EV) and Heating, Ventilation, and Air Conditioning (HVAC) domains demonstrate that auxiliary energy consumption exhibits a strong non-linear dependence on ambient temperature [19,20]. On top of this, the literature has demonstrated that machine-learning algorithms can be an effective pathway towards modeling auxiliary consumption, with [19] proposing the XGBoost model to predict auxiliary consumption in an EV and enhance the energy management system. Auxiliary demand increases sharply outside moderate temperature ranges, with distinct regimes associated with heating and cooling operation. These behaviors depend not only on the thermal load intensity, but also on control logic and compressor cycling, leading to discontinuous and history-dependent power consumption. Thermal inertia further amplifies non-linear behavior. The large thermal mass of battery assemblies causes delayed temperature responses, leading to prolonged cooling or heating cycles even after operating conditions change. As a result, the auxiliary power demand depends not only on the instantaneous temperature, but may also be impacted by the recent thermal history of the system [21]. This effect is particularly relevant for containerized BESSs, where thermal equilibrium is rarely instantaneous.

3. Materials and Methods

This chapter presents the modeling framework proposed to reconstruct and forecast the auxiliary consumption of a utility-scale BESS. The analysis is focused on real-life operational data, and focuses on understanding how ambient temperature and battery utilization influence the thermal inertia of the system and, thus, its thermal management demand. It should be noted that the thermal inertia of a utility-scale BESS could not be accurately represented by a single characteristic time constant, as the response of the HVAC system depends not only on passive thermal dynamics, but also on control settings, power perturbations, and ambient temperature transients, as well as previous state of the container. Therefore, we treat the thermal inertia as an aggregate, adopting a data-driven approach that aims to arrive at a "characteristic-time-constant-like" evaluation, without imposing a rigid physical thermal model.

After introducing the technical characteristics of the case study and describing the preprocessing steps, an exploratory analysis is conducted to identify the main drivers of auxiliary consumption and to investigate the role of thermal inertia. In addition, the analysis of the auxiliary consumption shows that it represents a non-negligible share of the total delivered energy, emphasizing the need for accurate forecasting. Building on these insights, two parallel modeling approaches are proposed, and compared against a literature-based model.

https://doi.org/10.3390/batteries12080288

First, a two-dimensional LUT-based model was proposed in [10], serving as a reference found in the state-of-the-art model. Second, a non-parametric three-dimensional LUT is constructed using a stochastic discretization procedure. Last, a Random Forest (RF) model is implemented to overcome the dimensionality limitations of the LUT and to better capture non-linear interactions between the target parameters. Within this approach, a structured predictor-expansion framework is proposed to systematically evaluate the contribution of moving-average predictors and to compare the performance of the approaches proposed.

3.1. Case Study Description

The BESS considered in this study is located in Sardinia, Italy, and entered operation in July 2023. The plant was contracted within the pilot project promoted by Terna for the provision of the Fast Reserve service, aimed at improving the dynamic frequency response of the power system during the first instants following frequency disturbances. Outside these availability windows, as well as for the remaining uncontracted capacity, the BESS can participate in the energy market, enabling additional revenue streams and operational flexibility.

The BESS is a Lithium Iron Phosphate (LFP) electrochemical storage system with a rated power of 14.7 MW and an energy capacity of 8.8 MWh. The plant is characterized by a modular and hierarchical architecture: it is divided into four nominally identical feeders, connected in parallel at the high-voltage node. Each feeder is interfaced through a double secondary transformer, featuring two low-voltage secondary windings on the battery side. Each secondary winding supplies two power conversion systems (inverters), which are, in turn, connected to an aggregated control unit of the storage system, referred to as the Battery Administration Unit (BAU). Each BAU supervises and controls three Battery Cluster Units (BCUs) connected in parallel. Overall, the plant includes 16 BAUs and 48 BCUs. At the lowest level of the hierarchy, each BCU comprises 15 battery modules connected in series, with each module consisting of 24 individual cells.

Given the geographical location of the site, the thermal management of the BESS relies exclusively on an air-based cooling system, implemented through industrial HVAC units installed within the battery containers. No active heating system or heat pump is present. The thermal dynamics of the system are therefore predominantly associated with heat removal from the battery containers, driven by internal heat generation during charge and discharge operations and by external ambient conditions. The auxiliary system's aim is thus to maintain the internal temperature of the battery enclosures within a target range of approximately 23–28 °C. This temperature window represents a compromise between enabling high C-rate operation—required for fast frequency response services—and limiting battery degradation, thereby preserving long-term system performance and reliability. The cooling system is structured by separating the BCUs into different containers. Each container contains sixteen BCUs and is equipped with four HVAC units as shown in Figure 1. A separate fifth feeder is provided to supply all the auxiliaries in the system, comprising the HVAC units from the three containers.

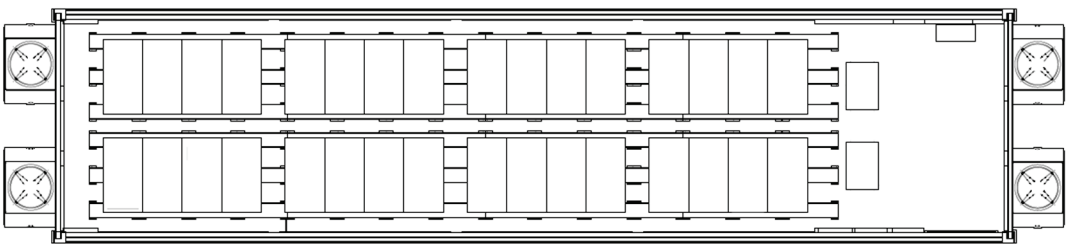

Figure 1. BESS container layout.

3.2. Data Description and Preprocessing

The data collection from the physical plant spanned between the months of September 2023 and November 2024, allowing for 13 months of samples. The main variables of interest were the power exchanged by the BESS (P_{BESS}), the ambient temperature measured by the nearby weather station (T_{amb}), and the consumption of the auxiliaries that are fed by a separate feeder (P_{aux}). Furthermore, an additional set of temperature measurements for each cluster unit ($T_{clus,i}$) was analyzed exclusively for exploratory purposes, aiming to understand the containers' thermal behavior and the system's thermal management. Instead, they were not utilized for the modeling itself and fall outside of the main parameters for the approaches that are proposed. The measurements were obtained through individual measurement devices and sampled with a 5-min resolution. Figure 2 depicts a sample time series used in the analysis, showing the main input variables for the period of October 2023, where the BESS power is expressed according to the generator sign convention. Even over this short window, the auxiliary consumption never really drops to zero, and, through the idle stretches, it appears to follow the ambient temperature more closely than the BESS operation.

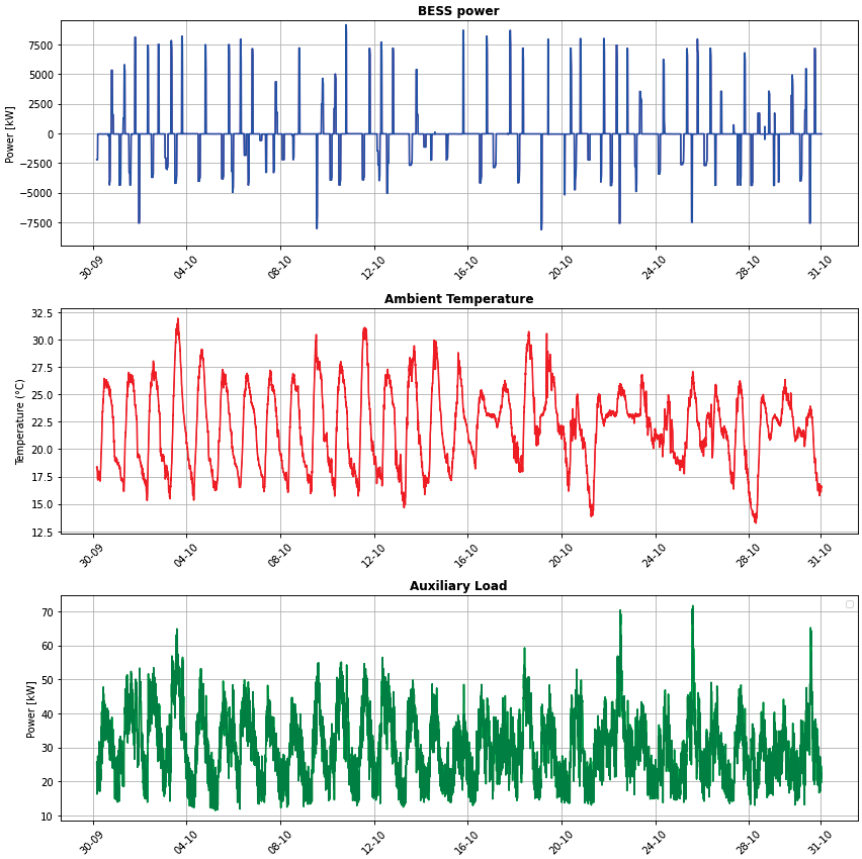

Figure 2. Example time series of measured variables.

The first step was to resample the dataset to a 15-min interval, following the time discretization of the Italian Electricity Market, excluding timestamps in which at least one of the parameters contained corrupted data. Corrupted data was identified as either missing or unphysical values far outside of nominal values, attributed to measurement or communication errors. In practice, this issue occurred only in the power measurements and was limited to less than 0.5% of the samples, most of which were simply missing. Further filtering was not applied to avoid misrepresentation of normal behavior as irregular. In practice, anything below a 15-min time interval would not provide a meaningful benefit.

https://doi.org/10.3390/batteries12080288

Moreover, all models rely on the absolute value of the BESS output, as heat generation is mainly related to the magnitude of the power, rather than its direction. As previously introduced, the main idea is to gain understanding of how the power output of the BESS and the ambient temperature affect the consumption of the auxiliary systems; then, this knowledge can serve to build a forecasting service.

3.3. Exploratory Data Analysis

In order to gain understanding about the dataset and make initial hypotheses correlated to the findings in the literature, an exploratory campaign was initiated. The initial question was to better understand the utilization of the BESS and to form assumptions on the impact of its scheduling and operation on the consumption of the auxiliaries. First, an analysis of the daily auxiliary consumption was conducted by comparing the daily auxiliary energy with the total daily energy exchanged by the BESS. The results showed that the auxiliary share ranges from approximately 1.5% to nearly 100% on days when the BESS remains mostly idle, with a median value of 4.5%. These findings demonstrate that auxiliary consumption can represent a non-negligible portion of the system's daily energy balance and can certainly affect SoC estimation. In absolute terms, the auxiliaries were consuming between 8.5 and 72 kW, with a mean value of 29 kW over the observed period.

The spreadsheet data indicates that the maximum achievable C-rate is 1.67, which is relatively high for a grid-scale BESS. This suggests that the utilization would occur either in longer durations with a more limited C-rate, or shorter periods at higher C-rates. Thus, to better understand the utilization patterns, an initial analysis was conducted by classifying operation in six groups based on the C-rate levels. Interestingly, it was discovered that the BESS was in idle for 80.39% of the time, and was, in any case, operated with a C-rate lower than 0.5 for 97.17% of the time, and almost never surpassing 1 (Figure 3). These operating conditions, together with the relatively high average temperatures reported in Figure 2, correspond to the scenario identified in [11] as most sensitive to auxiliary consumption, where dedicated modeling is needed to avoid errors in the overall efficiency estimation. This by itself suggests that the heating due to BESS utilization is likely not the sole driving factor of the auxiliaries. We then excluded any timestamps with a C-rate above 1. These made up just 0.04% of the observation period, which is roughly four hours across the full thirteen months. We opted to drop them for two specific reasons. First, because few samples at such extreme utilization rates would end up in their own thinly populated LUT bins, adding little that the model could learn from, while congesting the available resolution for the far more common operating conditions. Second, because their share is so small, removing them barely shifts the distribution of the training or testing sets, both of which still reflect how the asset actually operates.

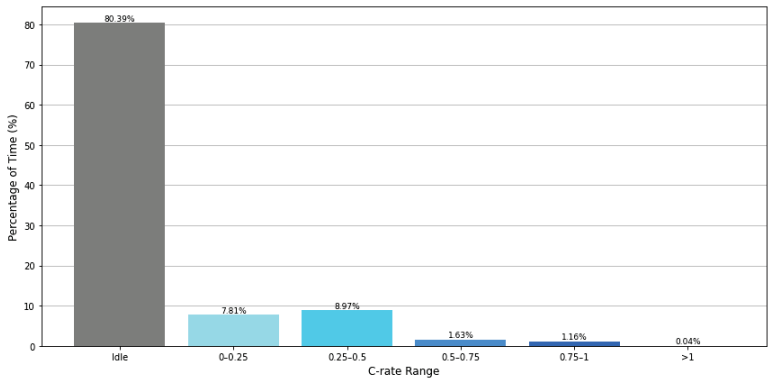

Figure 3. BESS utilization patterns.

https://doi.org/10.3390/batteries12080288

Next, the ambient temperature was investigated, always keeping in mind the setting of the cooling systems that was previously introduced. Indeed, looking at Figure 4 that presents the Cumulative Distribution Function (CDF) of the temperature for the period under investigation, it can be seen that the ambient temperature can be a more significant factor. For each value on the horizontal axis, the curve gives the fraction of time the ambient temperature stayed at or below it, which lets us read off directly how often the cooling thresholds were exceeded. The ambient temperature surpassed 23 °C for 31.9% of the time and 28 °C for 10.3% of the time, suggesting that the cooling system would need to be active even without the presence of additional operational heating.

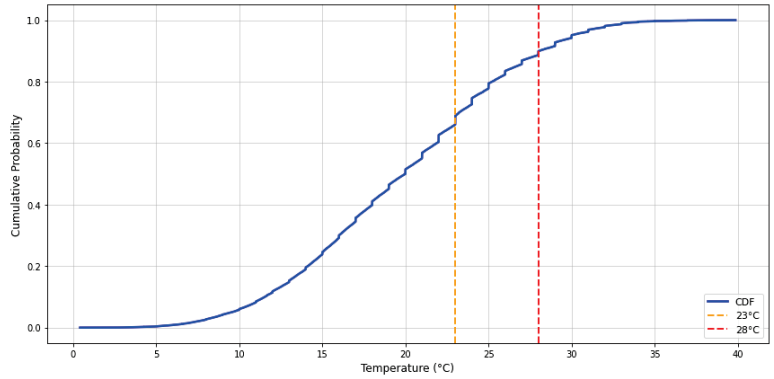

Figure 4. Ambient temperature distribution.

Based on the hypothesis that thermal inertia is a significant factor influencing the instantaneous consumption of the auxiliaries, a statistical analysis was conducted to investigate the Pearson (linear) correlation between the auxiliary load and the moving averages of the predicting variables. The analysis displayed on Figure 5, where the horizontal axis is the length of the moving average and the vertical axis the resulting Pearson correlation coefficient, shows that the ambient temperature exhibits a significantly stronger correlation to the auxiliary consumption compared to the power output. Moreover, the correlation decreases as the temperature moving-average window increases, whereas, for power, the opposite trend is true.

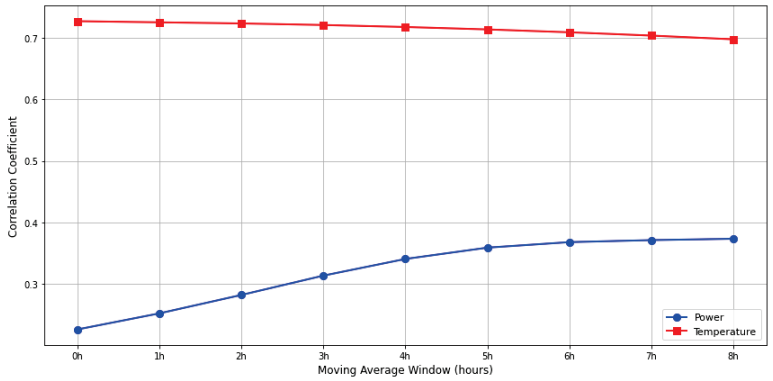

Figure 5. Temperature and power correlation with auxiliary consumption.

Even though the absolute value of the correlation may be guided by the low utilization rate of the BESS, the behavior of the moving averages hints at very important notion regarding the thermal inertia. In fact, the impact of the ambient temperature seems to have a much lower time constant, directly affecting the temperature inside the container and, thus, the need for cooling. On the other hand, the power output of the BESS seems to have a much more lasting effect, where the correlation visually increases up to a moving-average

window of 6 h. Practically speaking, this implies that the impact of the heating caused by the operation of the BESS persists for a longer duration. It should be clarified that this provides only a direction for further analysis, as it is clear that the actual correlation is not linear.

The behavior described above can also be illustrated using a specific example presented on Figure 6, where the BESS power output, ambient temperature, and auxiliary consumption are visualized for a relatively warm day in October. To better capture the underlying trend in auxiliary consumption, a 1 h MA is applied to reduce the effect of the on/off cycling of the auxiliary systems. In addition, temperature measurements inside the containers are recorded as a supplementary plot, providing insights into the thermal dynamics of the containers.

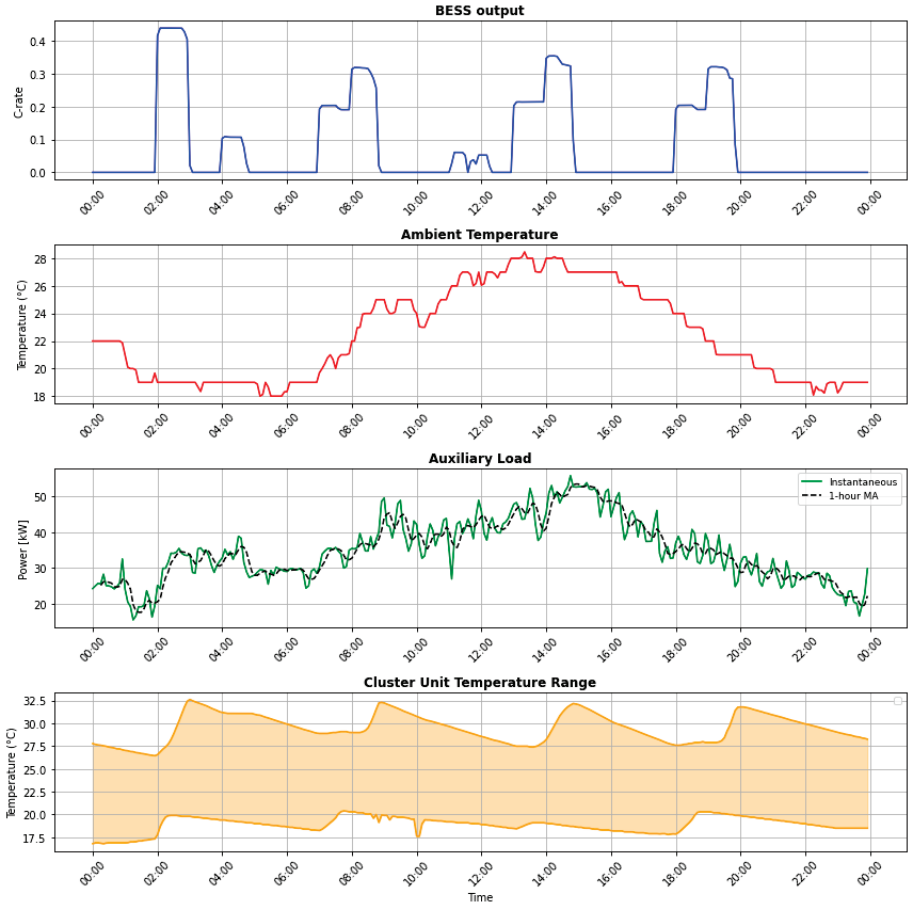

Figure 6. Example daily trend for the behavior of temperature, power, and auxiliary consumption.

First, a clear relationship can be observed between ambient temperature and auxiliary consumption, particularly when the ambient temperature exceeds the activation thresholds of the cooling system. Moreover, Figure 6 also highlights the asymmetric thermal behavior of the container. Heating occurs relatively quickly due to the coupled impact of BESS utilization and higher ambient temperatures, whereas the subsequent cooling phase takes considerably longer. This difference in the thermal behavior clearly demonstrates that the system could not be adequately described by a single characteristic time constant as the containers exhibit operating-dependent time-constant-like behavior. This notion is examined numerically below. This is something that makes the forecast of the auxiliary consumption required to maintain normal temperature rather challenging, as it complicates the correlations and dependencies between the variables. Clearly, this emphasizes the limitations of relying only on instantaneous variables to characterize the auxiliary consumption.

To complement the qualitative discussion above with a quantitative estimate, the cooling consumption was modeled as a first-order dynamic response toward an equilibrium value determined by the operating conditions. The equilibrium auxiliary consumption $P_{aux,eq}$ is taken as a function of the absolute BESS power ($P_{BESS,abs}$) and the ambient temperature, and its temporal evolution is described by Equations (1) and (2), where β is the fraction of the gap between the current and equilibrium consumption recovered within one sampling interval. In practice, the two relations were combined into a single one-step-ahead expression, in which the auxiliary consumption at the following interval is a linear function of its current value, the absolute BESS power, and the ambient temperature. This expression was fitted by linear regression on consecutive measurements: the coefficient associated with the current consumption yields the relaxation parameter β, while the remaining coefficients recover the equilibrium relationship of Equation (1). Converting β to an equivalent thermal time constant (τ) through Equation (3) yields a characteristic response time of approximately 29 min. The linear identification is used here solely to extract the characteristic relaxation timescale, and not as a predictive model of auxiliary consumption; consistent with the non-linear behavior discussed above, its role is to quantify the response time rather than to replace the data-driven models developed in the following sections.

$$P_{aux,eq} = f(P_{BESS,abs}, T_{amb}) \quad (1)$$

$$P_{aux}(k+1) = P_{aux}(k) + \beta\left(P_{aux,eq}(k) - P_{aux}(k)\right) \quad (2)$$

$$\tau = {}^{\Delta t}/_{\ln(1-\beta)} \quad (3)$$

This value should be interpreted with care. As the asset is idle for the large majority of the observation period, the estimate is dominated by transitions occurring under quiescent conditions, and, therefore, reflects the relatively fast relaxation of the cooling system toward its immediate equilibrium rather than a single time constant valid across all operating regimes. During and after active power provision, the effective response is considerably slower, as the operational heat propagates through the thermal mass and sustains the cooling demand well beyond the immediate interval—consistent with the multi-hour influence of BESS power observed in the moving-average correlation analysis (Figure 5). The two observations are complementary: the short response time characterizes how quickly the cooling system tracks its equilibrium, while the long moving-average dependence characterizes how long operational heat perturbs that equilibrium. Taken together, they confirm that the system cannot be adequately represented by a single characteristic time constant, and they provide a data-driven justification for the use of multiple moving-average windows—a short one to capture the fast thermal response and longer ones to capture the persistent effect of prior operation.

Instead, the use of moving-average predictors could provide a more appropriate representation of the thermal processes. As can be seen from the example, the auxiliary systems remain active long after the BESS utilization that generated the heat. This effect is particularly clear following the service interval between 02:00 and 03:00 (Figure 6), where a period of relatively high C-rate operation leads to a gradual increase in auxiliary consumption. It then remains elevated for a longer period, even though the ambient temperature remains relatively low, whereas the temperatures inside the container gradually decrease.

The sections below summarize the different approaches investigated. In all the cases, the available dataset is first split between training and testing, using the random 80–20 split, in order to enable an unbiased evaluation of the models' generalization performance and allow for an equal-ground comparison among them. The main performance evaluation metric to assess model accuracy is the Root Mean Square Error (RMSE), a well-established evaluation metric in the field as it penalizes larger prediction errors and provides a direction-

https://doi.org/10.3390/batteries12080288

independent measure of model performance. Finally, to complement the comparison along the models, the Mean Absolute Error (MAE) is also computed, as it penalizes all errors linearly, thereby improving outcome interpretability and providing a measure of typical operational accuracy.

3.4. 2-Dimensional Look-Up Table (LUT) Taken from the Literature

This section briefly summarizes the approach proposed by the authors in [10], utilized as a literature reference for evaluation of the results. It is based on the creation of a 2-dimensional LUT utilizing BESS power and ambient temperature as predictors. For each dimension, the range between the minimum and maximum observed values is evenly divided using eight breakpoints to create the bins. Then, the values of the lookup table at each grid point are computed as the average of the data within the corresponding bin. Similarly, data samples within each bin are averaged to compute the corresponding auxiliary consumption. In the LUT obtained, each bin is represented by the average value on each of the two dimensions. The LUT evaluation is then performed using linear interpolation between the nearest grid points for each data sample in the testing dataset.

3.5. 3-Dimensional Look-Up Table (LUT)

Given the correlation discovered in the exploratory analysis that showed high importance of the power moving average, the first approach proposed by this paper to building a model is to propose a more detailed LUT that can be used to estimate the auxiliary consumption. In this case, the idea is to go one step further from the 2-D LUT approach proposed by the literature [10] and briefly explained in Section 3.1, and propose a 3-D LUT that, on top of the instantaneous power and ambient temperature, incorporates a selected moving average of the power with a duration h hours MA(P_{BESS}, h). This selection is motivated by the findings of the exploratory analysis performed using the Pearson correlation shown in Figure 5, which indicates not only a correlation between the power moving average and auxiliary consumption, but also that the correlation increases with the duration (h) of the moving average. On top of it, the approach does not fix the number of breakpoints, but, instead, allows the algorithm to search for a well-performing configuration. Algorithm 1 presents a step-by-step pseudocode description of the proposed procedure.

The developed framework is a probabilistic Monte Carlo grid-based non-parametric estimator. As one of its main features, it does not require the fixing of its discretization structure a priori. Instead, a stochastic sampling procedure was employed to explore different partition granularities. For each iteration until convergence is reached, the moving-average window length (h) for the power of the battery MA(P_{BESS}, h), and the number of breakpoints per predictor ($n_{BP,Pbess,}$, $n_{BP,Tamb}$, $n_{BP,MA}$) were randomly sampled from predefined uniform distributions. The allowed values are ranging from three up to a predefined maximum (N_{BP}). In this way, the approach targets a good break-point configuration with a probabilistic criterion. Given the sampled breakpoint count, partition boundaries were constructed across the observed variable range, respecting the minimum and maximum values for each predictor, resulting in a candidate three-dimensional grid. Each cell of the grid represents a specific combination of intervals for each of the three predictor variables. Then, the auxiliary consumption associated with each cell was computed as the average of all samples falling within the corresponding parameter ranges.

Once the LUT is created, its performance is evaluated using the testing dataset. For each observation, the corresponding region in the three-dimensional predictor space was identified, and the auxiliary consumption was estimated with a linear interpolation between adjacent grid cells. The LUT configuration achieving the lowest RMSE is then selected as the final model for the 3-Dimensional LUT approach.

https://doi.org/10.3390/batteries12080288

Algorithm 1. Monte Carlo approach for the creation of a 3-D lookup table

Input: P_{BESS}—power time series; T_{amb}—temperature time series; P_{AUX}—auxiliary consumption time series; N_{MA}—max BESS power MA window [h]; N_{BP}—max possible breakpoints per dimension
IT_{MAX}—max iterations; ε—convergence criterion [iterations without improvement]
Output: Best configuration: lookup table (LUT*), RMSE*

1: Construct feature set: $F \leftarrow \{P_{BESS}, T_{amb}\}$
2: Append MA of P_{BESS}: {MA(P_{BESS}, k): $k = 1 \ldots N_{MA}$} to F
3: Append P_{AUX} to obtain the dataset and split in training/testing: D_{TRAIN}, $D_{TEST} \leftarrow \{F, P_{AUX}\}$
4: Initialize parameters: RMSE* $\leftarrow \infty$; $counter_{NoImprove} \leftarrow 0$; $counter_{iterations} \leftarrow 0$; $LUT^* \leftarrow \emptyset$
5: **while** counter < ε **and** it < IT_{MAX} **do:**
6: Sample number of breakpoints: $n_{BP,Pbess,}$, $n_{BP,Tamb}$, $n_{BP,MA} \sim U\{3, \ldots, N_{BP}\}$
7: Sample MA window: $h \sim U\{1, \ldots, N_{MA}\}$
8: Define the set of three dimensions D {P_{BESS}, $MA(P_{BESS},h)$, T_{amb}}
9: Sample breakpoints for each d $\in D$: $BP_{S,d} \leftarrow (n_d - 2)$ interior values $\sim U(min_d, max_d)$
10: Set the breakpoints vector for each d $\in$ D: $BP_d \leftarrow \{min_d\} \cup \{BP_{S,d}\} \cup \{max_d\}$
11: Split training dataset (D_{TRAIN}) in each bin (i, j, k) defined by the breakpoints $BP_d \rightarrow D_{I,J,K}$
12: Calculate LUT value for each bin: LUT[i, j, k] $\leftarrow$ mean($P_{AUX} \in D_{I,J,K}$)
13: Query LUT and calculate auxiliary load using linear interpolation of the closest BPs: $\rightarrow \hat{P}_{AUX}$
14: Evaluate RMSE on testing dataset: $\rightarrow$ RMSE = RMSE(P_{AUX}, $\hat{P}_{AUX}$)
15: **if** $RMSE_{IT}$ < RMSE* **then:**
16: RMSE* $\leftarrow RMSE_{IT}$; $LUT^* \leftarrow$ LUT; $counter_{NoImprove} \leftarrow 0$
17: **else**
18: $counter_{NoImprove} \leftarrow counter_{NoImprove} + 1$
19: **end if**
20: it $\leftarrow$ it + 1
21: **end while**
22: **return** LUT*, RMSE*

3.6. Random Forest Regression

In addition to the grid-based 3-D LUT approach, a machine-learning method based on RF was also evaluated. RF is an ensemble learning method that builds a large number of decision trees using bootstrap resampling of the training data and random subsets of predictor variables at each split. Practically speaking, each tree is built using different subsets of the training data and predictor variables. The final prediction is obtained by averaging the outputs of the individual trees. This practice of combining bootstrap aggregation with random feature selection reduces variance and mitigates overfitting, effectively improving generalization. This is done while preserving the ability of decision trees to model complex non-linear relationships between the predictors and target variable. Unlike the LUT approach which relies on explicit discretization of the predictor space into predefined grid cells, RF performs recursive partitioning of the search space. Owing to this underlying feature, it can capture the non-linear interactions between the instantaneous temperature and power, alongside their different moving averages, without requiring manual selection of breakpoints or dimensionality constraints.

Indeed, one of the limitations of the LUT concept is the dimensionality, since, by adding predictors such as multiple moving-average horizons, the number of grid-cells would grow exponentially, leading to very sparsely populated regions and unreliable estimates. Thus, only a limited number of dimensions can be included while maintaining sufficient samples per cell. Indeed, the approach proposed considered only three

https://doi.org/10.3390/batteries12080288

dimensions, one of which was a uniformly selected time horizon of the power moving average. On the opposite, RF is not subject to this restriction in the same way. Because splits are created adaptively and the algorithm can select which predictors are the best to use, the method can incorporate multiple moving-average features simultaneously without requiring explicit binning. On top of it, it removes the need to select a single "best" moving-average window to be used for forecasting purposes, allowing the model to internally determine the relative importance of different windows.

Even though the RF algorithm involves several hyperparameters such as the number of trees, maximum tree depth, and minimum samples per leaf, the tuning of these parameters was considered outside of scope of this paper. The main rationale is that, in limited datasets, the impact on these parameters is very modest and, thus, default values from the literature can be adopted [22]. As introduced before, the key indicator used during training and evaluation was the RMSE.

In order to systematically evaluate these advantages over the LUT-based approaches, as well as find the best trade-off in terms of model expansion, a hierarchical feature-addition framework was adopted. It adopts a brute-force strategy to assess the impact of adding calculated predictors in the form of moving averages on the performance metrics. The incremental addition of predictors enables the evaluation of whether increasing feature complexity improves performance, or, beyond a certain point, begins to degrade it. The procedure is summarized in a high-level pseudocode in Algorithm 2.

Similarly to the LUT-based approaches, the analysis was structured along two dimensions, ambient temperature and BESS power. In the outer layer, the predictors related to the temperature are progressively expanded, starting from instantaneous temperature and incorporating moving-average features with increasing window lengths, each time adding one hour. Practically speaking, Algorithm 2 needs to be executed once without the instantaneous temperature, and then iterate the different moving averages, controlled with the Boolean T_{BOOL}. For each temperature configuration, an inner cycle is performed in which power moving-average predictors are incrementally added, adding one hour to the moving-average calculation per iteration. Essentially, it can be visualized as a nested "for" cycle, where the temperature is the upper level.

This nested evaluation strategy enables an organized evaluation of the combined effects of power and temperature on the thermal inertia of the system, effectively evaluating the time constants associated. In this way, the framework not only facilitates a direct performance with the LUT-based approaches, but also provides a structured assessment of how accuracy is impacted when additional temporal information is included.

Finally, to simulate realistic operational conditions, the trained estimator was also tested under a persistence-based temperature forecasting scenario. In the testing dataset, ambient temperature inputs were replaced with the corresponding values from the previous day, therefore simulating forecasting uncertainty. This approach is particularly relevant for potential day-ahead scheduling applications where, even though the power dispatch profile is generally known in advance, temperature can only be forecasted. The persistence model forecast is a well-documented and acceptable approach especially for the case of temperatures, given that day-to-day variations are nonetheless quite limited on average. Therefore, this analysis should be interpreted as a robustness test for the proposed approach in the absence of temperature forecasting information, where temperature forecast errors may vary. It is worth noting, however, that persistence forecasting is generally regarded as a conservative baseline, since a dedicated forecast service would typically outperform it. Therefore, the increase in prediction error obtained here is not expected to be a systematic underestimate of the impact of temperature forecasting. Accordingly, this analysis should be read as a robustness test of the proposed approach under imperfect temperature

https://doi.org/10.3390/batteries12080288

information, providing only an indicative rather than exact quantification of the impact of forecast uncertainty.

Algorithm 2. Random Forest Moving-Average window search

Input: P_{BESS}—power time series; T_{amb}—ambient temperature time series; P_{AUX}—auxiliary consumption time series; N_p—max BESS power MA window [h]; N_t—max temperature MA window [h]; T_{BOOL}—consider instantaneous temperature
Output: Best RMSE value (RMSE*) and corresponding configuration (n_p*, n_t*)

for $n_p = 0$ **to** N_p **do:**
  Construct feature set: $F_p \leftarrow \{P_{BESS}\}$
  if $n_p > 0$ **then:**
    Append power MA to F: $F_p \leftarrow F_p \cup \{MA(P_{BESS}, k)$: $k = 1 \ldots n_p\}$ to F_p
  end if
  for $n_t = 0$ **to** N_t **do:**
    if T_{BOOL} **then:**
      Update feature set: $F \leftarrow F_p \cup \{T_{amb}\}$
    else:
      Update feature set: $F \leftarrow F_p$
    end if
    if $n_t > 0$ **then:**
      Append $\{MA(T_{amb}, k)$: $k = 1 \ldots n_t\}$ to F
    end if
    Train/test split: F_{TRAIN}, $F_{TEST} \leftarrow F$
    Train Random Forest on feature matrix X built from $F_{TRAIN} \rightarrow RF(F_{TRAIN})$
    Evaluate auxiliary consumption for the testing dataset: $\hat{P}_{AUX} \leftarrow RF(F_{TEST})$
    Evaluate RMSE on testing dataset: $\rightarrow RMSE = RMSE(P_{AUX}, \hat{P}_{AUX})$
    if RMSE < RMSE* **then:**
      RMSE* $\leftarrow \varepsilon$; best_config* $\leftarrow$ (n_p*, n_t*)
    end if
  end for
end for

return RMSE*, config*

4. Results

The following section introduces the outcomes of the three approaches investigated—the 2-D LUT-based approach adapted from the literature, alongside the 3-D LUT-based and RF-based frameworks proposed by this paper. Each approach is analyzed separately to emphasize its performance and main characteristics, and address its limitations. To provide a reference for the computational effort indicators reported below, the simulations were performed on a Windows machine equipped with a 12th Generation Intel Core i7-1260P processor, integrated UHD Graphics Card, and 16 GB of RAM.

4.1. 2-Dimensional LUT Outcome

The LUT obtained with the approach proposed by the literature [10] is provided as a heatmap on Figure 7. The model achieved an RMSE of 6.81 kW, which is 9.4% of the maximum recorded auxiliary consumption, and 23.4% of the mean.

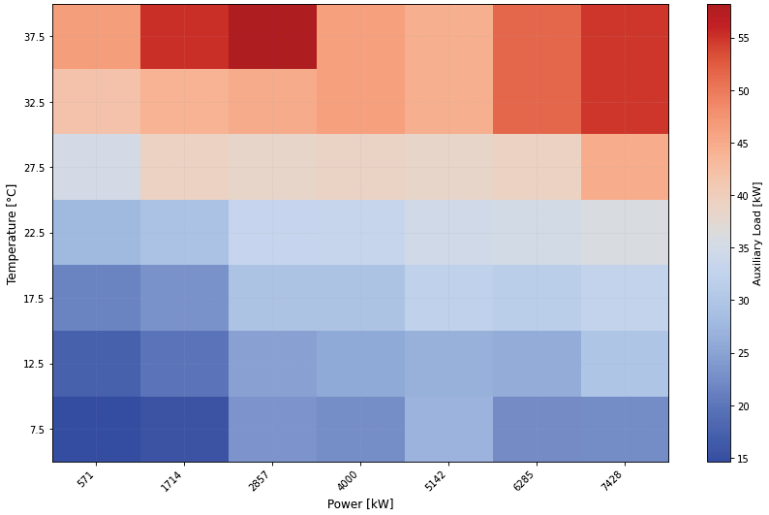

Figure 7. 2-D LUT outcome.

Even though the approach is clearly able to decently capture a correlation between temperature and auxiliary consumption, evidenced from the increasing values along the y-axis, it fails to accurately represent the correlation with the BESS utilization. For example, the model obtained suggests that a low utilization of the BESS at high temperature results in a lower cooling demand than higher power operation, something that does not reflect the real thermal dynamics of the system. Nevertheless, the approach can certainly provide a reasonable first estimate, especially during prolonged idle times when clearly the main driving factor would be the ambient temperature. Given the characteristics of the dataset, particularly the high proportion of idle operation, the resulting RMSE can be seen as acceptable. However, a more in-depth analysis enabled by Figure 7 shows that the model is far from capturing the true thermal dynamics and the dependency of the auxiliary consumption on BESS utilization. The computational complexity in this case is negligible, as the LUT is obtained with a one-shot processing of the data.

To examine whether the baseline error concentrates in specific operating regimes, the RMSE of the 2-D LUT was computed per bin of the temperature–power grid. It was found that, in absolute terms, the error grows with both temperature and power, ranging from approximately 3.2 kW in the idle and low-power bins, to 10.8 kW at the highest power and near-highest temperature. This trend, however, is affected by the higher auxiliary consumption in those conditions: once the per-bin RMSE is normalized by the average auxiliary consumption of each bin, the values are more dispersed (between 0.16 and 0.28) and show no clear dependence on the operating conditions.

4.2. 3-Dimensional LUT Outcome

The LUT algorithm was executed with a threshold of maximum 10,000 iterations (IT_{MAX}), with the stopping criterion (ε) of 500 consecutive iterations without an improvement in the RMSE metric. These relatively large limits were chosen to ensure a robust search of the solution space. The maximum number of breakpoints (N_{BP}) for each predictor was set to 10, while, as previously described, the actual breakpoint values were constrained by the observed minimum and maximum values for each predictor, respectively. The maximum moving-average window (N_{MA}) used for the power calculation was set to extend up to 8 h.

The LUT that provided the best representation of auxiliary consumption corresponded with a 5 h moving average, emphasizing the dominant influence of the longer time constant of power on auxiliary consumption. In the best-performing configuration, the algorithm

selected five breakpoints for the instantaneous power, nine breakpoints for the instantaneous temperature, and nine breakpoints for the 5 h moving average to best capture the correlation structure. This outcome further supports the initial hypothesis that the moving-average power is more relevant than the instantaneous value, as it better captures the complex thermal effects within the container. More specifically, the combination of the instantaneous power with a longer moving average reflects the two-timescale nature of the cooling response identified in Section 3.2: the instantaneous power captures the fast component of the thermal response, characterized by the short equilibrium relaxation time, while the 5 h moving average accounts for the slower, persistent effect of the prior operation on the container temperature. The predictor structure selected by the algorithm is, therefore, consistent with the underlying thermal dynamics, rather than being a purely data-driven artifact. In terms of the computational complexity, the solution took a total of 1190 iterations and 325 s to converge.

The higher dimensionality of the LUT complicates the visualization and interpretation of the outcome, so, to best address this issue, one dimension is represented through multiple subplots, while the remaining two are displayed using heatmaps. In line with the structure of the solution, four subplots were provided for the instantaneous power, with the moving-average power and the ambient temperature provided on the two axes. Figure 8 demonstrates the resulting breakpoints, the associated bins, and the average auxiliary consumption associated with each breakpoint.

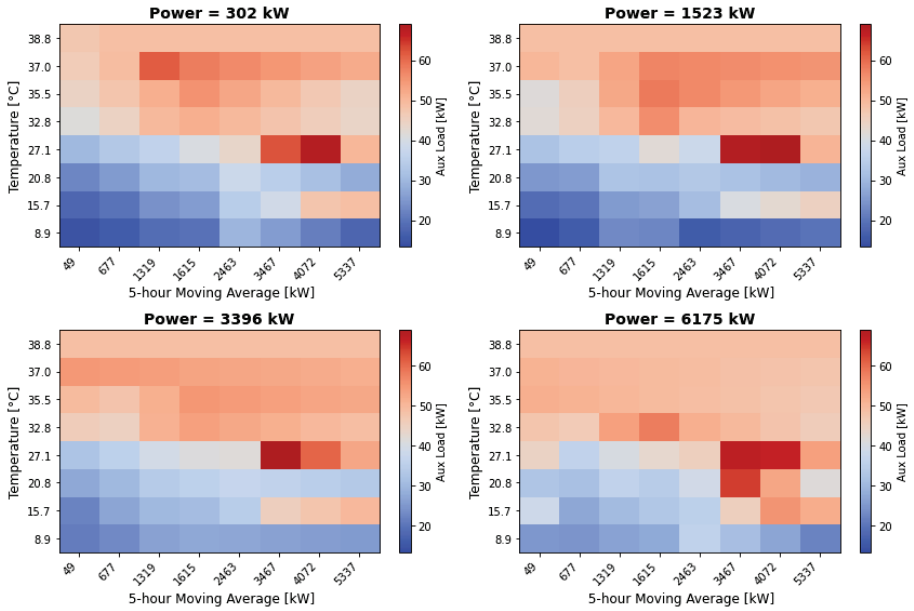

Figure 8. Best-performing 3-D LUT structure and auxiliary consumption heatmaps.

Applying the LUT to the testing dataset, the predicted auxiliary consumption achieved an RMSE of 5.32 kW, indicating a reasonably accurate estimation of the system behavior. In relative terms, this represents 7.4% with respect to the maximum auxiliary consumption, and 18.3% with respect to the mean. Nevertheless, considering the much larger size of the BESS itself, this outcome can be seen as very prominent for practical applications. Looking at Figure 8, it can be seen that the LUT approach was able to capture the operational characteristics of the BESS plant, which is typically operated at a lower C-rate (Figure 3). Indeed, we can see that the breakpoints both on the instantaneous and moving-average power are on the lower side of the 14.7 MW rated power of the plant. On the other hand, the breakpoints for the temperature spread wider across the different operational conditions.

https://doi.org/10.3390/batteries12080288

In terms of auxiliary load estimation, it is clear that it has a positive, but not exactly linear, correlation with the predictor variables, which was expected. For example, we can see that, at lower ambient temperatures, the power output of the BESS has a minor impact on auxiliary consumption, as it takes more time to arrive at a temperature inside the container that requires the activation of the HVAC systems. At the same time, Figure 8 provides insights into the imperfections and areas where the approach falls short. For example, the breakpoint defined by T_{amb} = 27.1 °C and MA(P_{BESS}, 5) = 3467 kW is a particularly strange case, where, based on the solution, the auxiliary consumption for an instantaneous power of P_{BESS} = 3396 kW seems to be higher than the one for the P_{BESS} = 6175 kW. Nevertheless, this can and should be interpreted as not an issue of the approach itself, but simply an issue of dimensionality and insufficient data to train the model with. It also clarifies that going beyond the three-dimensionality of the problem and the limitations in terms of the breakpoints' threshold would not only be impractical, but would most likely reduce performance.

4.3. Random Forest Regression Outcome

The RF framework introduced in detail in Algorithm 2 was applied to the same dataset, as it enables an equal-grounds comparison. The analysis focuses not only on its predictive accuracy, but also the influence of the addition of calculated predictors, as well as its ability to better represent the complex relationships between the parameters that the LUT approach may have failed to capture.

In terms of setup parameters, similar to the case for the LUT approach, the maximum number of moving averages to be added for the power (N_p) was set to eight hours. However, this number was reduced for the temperature (N_t), as, from the exploratory analysis, it was clear that the impact of the ambient temperature is significantly more instantaneous compared to the impact of the power. Thus, this step was taken to avoid redundant iterations and avoid potentially over-fitting the model without a physical meaning. The training of the models took between 6 s for the case with only 2 predictors, up to 55 s for the case with 13 predictors, whereas the entire hierarchical feature-addition framework took a total of 1540 s. The training and testing of the RF model was performed by using the scikit-learn library (version 1.6.1) in python.

The outcome of the recursive addition of moving-average predictors is presented on Figure 9, alongside a comparison with the values obtained from the LUT-based approaches. Moreover, it should be clarified that the x-axis represents the "up-to" power moving average added. For example, the value of 3 signifies that the 1 h, 2 h, and 3 h moving averages have been added as predictors. For clarity, from this moment on, a moving average of 0 represents simply the instantaneous value.

For clarity, it should be noted that the black line ("Without temp") represents the results obtained by executing Algorithm 2 with T_{BOOL} = False, whereas the rest are obtained with T_{BOOL} = True. In order to provide a more effective comparison with the LUT-based approaches, their performances are added on Figure 9. The main outcome of the analysis is the best configuration for the RF model, and, looking at Figure 9. it is clear that the best outcome is achieved by including the maximum number of predictors, up to 8 h of the power moving average, and up to 3 h of the temperature moving average, achieving an RMSE of 3.13 kW. Obviously, this is a significant improvement of 41.1% over the 3-D LUT approach; however, in absolute terms, the practical impact could be limited. Notably, configurations including the ambient temperature and at least three predictors, as is the case of the 3-D LUT approach, performed better, which is a testament to RF's superiority in creating a powerful regressor by accurately modeling complex non-linearities.

https://doi.org/10.3390/batteries12080288

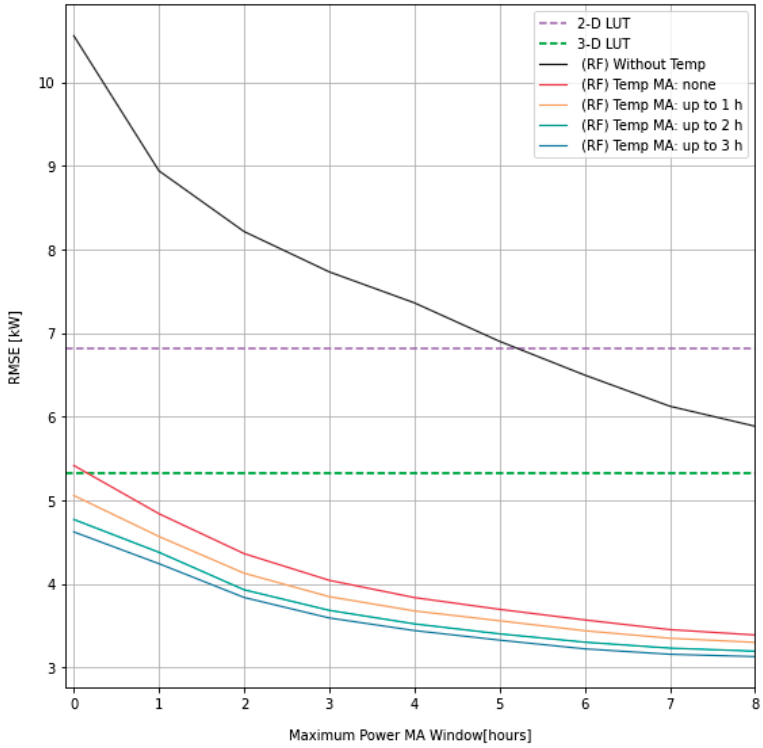

Figure 9. Impact of power and temperature moving-average features on prediction RMSE.

A second key interpretation of the results is the effect of the ambient temperature. The separation between the black line (without instantaneous temperature) and red line (with instantaneous temperature) highlights that the main improvement in accuracy is achieved by using the instantaneous ambient temperature as a predictor. Even though adding power moving-averages leads to improvements, the importance is not comparable. For example, using solely the instantaneous power is obviously not sufficient and arrives at an RMSE of 10.55 kW. However, starting from this point and adding a 1 h moving average of the power only improves the RMSE to 8.94 kW, whereas adding solely the instantaneous temperature arrives at 5.42 kW, which is a drastically more significant improvement (Figure 9). Nevertheless, from Figure 9, it is also clear that the further inclusion of temperature moving-averages leads to only minor improvements, with diminishing returns when continuing to add more predictors. Understanding the theoretical background of the RF method, it is clear that this may lead to overfitting. Thus, by examining the shapes of the curves on Figure 9 and searching for the "knee", it becomes clear that even adding a few power moving averages, together with either just the instantaneous temperature or also the first-hour moving average, could provide adequate performances.

Another metric that can be used to perform the same analysis is the feature importance, or feature utilization of the RF method. Indeed, because the RF prediction consists of many decision trees, features that are frequently used to make informative splits are considered more important, as they tend to reduce the variance in the case of regression. More precisely, the importance of a feature is measured by how much it reduces the prediction variance across all the splits where it is used, normalized so that the values sum to one; a larger value simply means the model leaned on that predictor more. Thus, Figure 10 provides an example of the case with $n_p = 3$ (or up to 3 h power moving averages) and $n_t = 1$ (up to 1 h temperature moving average), while also considering the instantaneous temperature as well. The outcome clearly shows the importance of the instantaneous temperature above all, followed by long-lasting moving-average power values to best correlate with the thermal processes and cooling requirements of the containers.

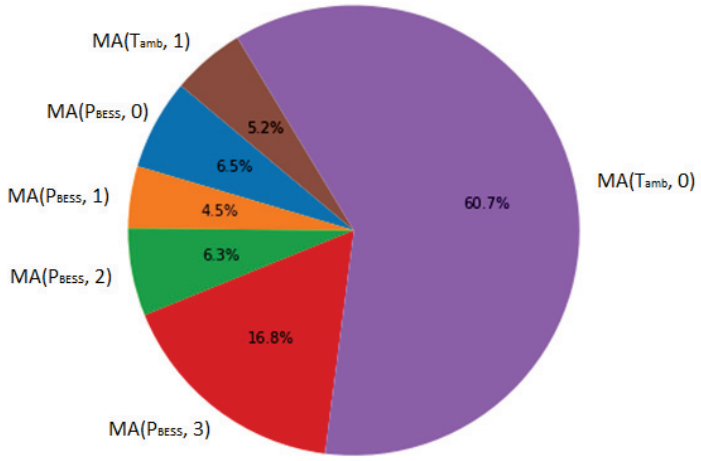

Figure 10. Feature importance for the case $n_p = 3$ and $n_t = 1$.

That said, it should be noted that this behavior is definitely impacted by the utilization patterns of the BESS, and is thus a quite specific behavior, as Figure 3 reported more than 80% of idle time. During those times, it is clear that the main driver of auxiliary consumption must be the temperature, as the battery is not utilized and does not heat the container.

Finally, as introduced in the methodology section, the same analysis was repeated by using a modified dataset using a persistence temperature forecast, allowing us to simulate the performance of the approach for day-ahead auxiliary consumption predictions when reliable ambient temperature forecast data are not available. It should be clarified that this modification is only applied to the testing dataset, assuming that the forecast affects the evaluation, whereas the training of the model is performed with known data. The outcome was an average of a 1.13 kW increase in the RMSE in absolute terms, or 30% in relative terms. In the best-case scenario with the maximum number of predictors, the error increased from 3.13 kW to 4.39 kW, effectively introducing the maximum increase of 40% in relative RMSE. With that being said, it should be noted that these values remain within an acceptable range for the practical implementation of these forecasts, supporting the applicability of the approach while acknowledging that a dedicated temperature forecast would refine this estimate.

4.4. Model Comparison and Time-Series Application

This section compares the two approaches proposed against the one proposed in the literature. In terms of the RF, the best performance with the maximum number of predictors will be considered. First, Table 1 summarizes the RMSE and MAE error metrics for the three models investigated.

Table 1. Model performance comparison.

	RMSE [kW]	MAE [kW]
2-D LUT [10]	6.81	4.92
3-D LUT	5.32	4.11
Random Forest	3.13	2.38

It is evident that the two approaches proposed outperform the 2-D LUT method proposed by the literature by a significant margin. Considering the RMSE as a reference metric, the 3-D LUT approach yields a 21.9% improvement over the literature method, while the RF achieves a significant 54% performance gain. A consistent trend is observed when comparing the MAE, with improvements of 16.4% and 51.6% for the 3-D LUT and

RF methods, respectively. Although the computational time is more significant for the two proposed approaches than for the literature LUT, in all cases, it remains well within the time available to the operator in a day-ahead setting, where the models are rebuilt once per day. It, therefore, does not represent a limiting factor in the selection of the model for this application. However, these performance indices alone may not adequately reflect the real implications of the observed performance. This is why the two LUT methods and the trained RF model were applied on a separate three-day interval that was not utilized during the training and testing of the models. The interval selected had frequent operation intervals, allowing for the investigation of the correlation of both main predictors with respect to the auxiliary consumption. The main outcome of the analysis, joined by the time series of the power exchanged by the BESS and ambient temperature over the observed interval are displayed on Figure 11. The upper panels show the BESS power and the ambient temperature over the interval, and the lower panel puts the measured auxiliary consumption side by side with the three model predictions on the same time axis, so each model's error can be read against the conditions that caused it. This allows for a clear comparison of the different performance of the investigated models, and the superiority of the RF over the LUT-based approaches. The main improvements can be seen once the cooling requirements increase due to BESS utilization, particularly during periods where the ambient temperature is also high. Over those intervals, the 2-D LUT tends to underpredict the real demand: it cannot account for the leftover heat from earlier operation. The 3-D LUT recovers some of that through the power moving average, and the Random Forest tracks the measured curve most closely—including as consumption slowly tails off once operation stops. This was also observable from Figure 7 where it was clear that the literature model lacks the capability of accurately merging the impacts of ambient temperature and BESS utilization. Nevertheless, it is clear that the 3-D LUT provides a much more accurate representation of the auxiliary consumption over the literature model, arriving at the conclusion that a power moving average is a necessary addition to the modeling of auxiliary consumption in utility-scale BESSs.

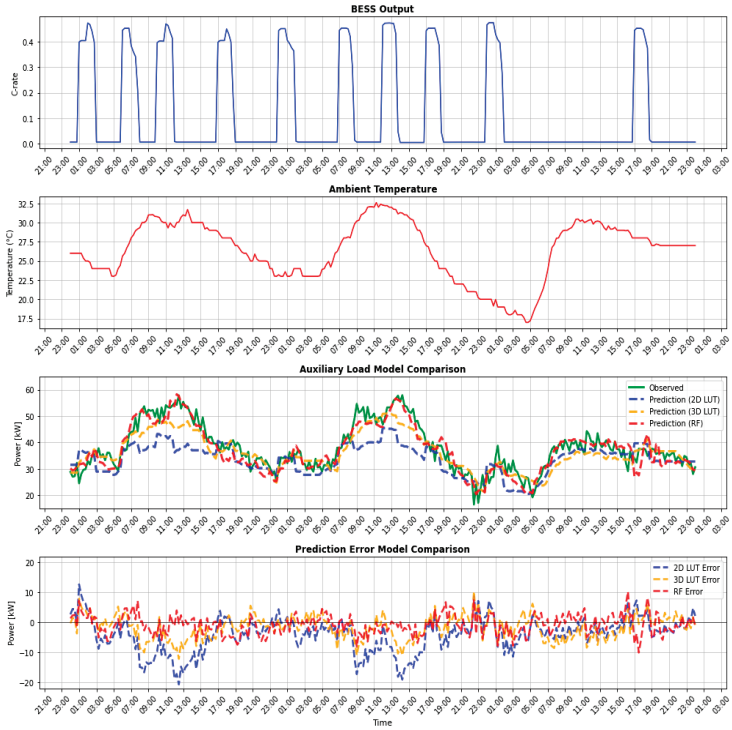

Figure 11. Time-series model performance comparison.

https://doi.org/10.3390/batteries12080288

5. Discussion and Conclusions

This paper proposed the modeling of auxiliary consumption in a utility-scale BESS using two distinct approaches: a three-dimensional LUT formulation, as well as a data-driven RF regression model. Moreover, a two-dimensional LUT approach from the literature was applied to the dataset to serve as a reference method. The three methods were evaluated using operational data from a real-world BESS installation in Italy. The results demonstrate that both approaches proposed are capable of capturing the main relationship between auxiliary consumption due to cooling needs, the utilization of the BESS represented by its power output, and ambient temperature, although they come with different strengths and limitations. On top of it, they showed a superior performance compared to the literature model.

First, the 2-D LUT method proposed by the literature was found insufficient to capture the correlation between the utilization of the BESS and the consumption of the auxiliaries. mainly due to its incapability to model the thermal inertia using only instantaneous values. Moving to the approaches proposed, they were found significantly more capable of modeling the system's thermal inertia. The 3-D LUT method provides a transparent and significantly more interpretable representation of the system behavior, allowing the relationship between variables to be directly visualized and analyzed, where final estimations can be obtained using algebraic calculations. However, this paper found that its performance is inherently constrained by the discretization of the feature space and the increasing dimensionality of the problem. This would most likely lead to data sparsity should additional predictors be introduced, as, even in the case analyzed, we were able to draw some conclusions about the data sparsity in certain bins, i.e., parts of the feature space. This, of course, is linked to the specific case under analysis and certainly could not be generalized. In contrast, the RF model demonstrates improved an predictive performance and a stronger ability to capture non-linear relationships in the data, making it particularly suitable for forecasting applications such as the day-ahead estimation of auxiliary consumption in a utility-scale BESS. The concept was validated by introducing a persistence-model-based forecast of the ambient temperature, arriving at reduced performances, but still very acceptable for potential applications. The advantages of the RF come from the fact that it is not constrained by selecting anything a priori, and by eventually forcing a fixed type of interpolation. On the other side, its downside is the limited interpretability, as the internal structure of an ensemble model such as the RF is significantly less transparent than the LUT-based method, bringing it close to a black-box approach. Nevertheless, the analysis in this paper included a multitude of analysis providing directions on how to shed light on aspects that may improve the forecast, and how to approach the analysis of specific use cases.

More broadly, this work highlights an important gap in the existing literature on grid-scale BESS operation. While significant attention has been devoted to modeling the battery at a cellular level, less attention has been directed towards modeling utility-scale batteries as a whole, and even less toward understanding auxiliary systems, their thermal inertia and cooling needs, and their impact on operation. The review of the existing state of the art in the auxiliary system characterization in utility-scale BESSs is still represented through simplified formulations, leaving room for more detailed data-driven approaches, such as those pursued in this paper. This study showed that auxiliary consumption can vary significantly depending on operating conditions and environmental factors, making it an important component for operational planning and energy accounting. As grid-scale BESS systems continue to expand in scale and deployment, accurately modeling these auxiliary loads becomes increasingly more important.

https://doi.org/10.3390/batteries12080288

Although the proposed approaches provide positive results and indications, improvements are certainly possible. In particular, two directions appear especially relevant. First, validating the proposed models on data from multiple BESS installations under different climatic and operational conditions would allow their generalization capability to be quantified beyond the single site analyzed in this paper. Second, analyzing the trade-off between the number of moving-average predictors and the risk of overfitting in the RF model, for instance, through cross-validated learning curves, would clarify when additional predictors stop improving performance. On top of it, even though it was outside of the scope of the paper, further hyperparameter tuning can be performed on the RF model to search for minor improvements in performance, as well as a further dimensionality analysis for the LUT approach. The 3-D LUT breakpoints were set using a Monte Carlo search, which finds a good configuration rather than a provably optimal one. Since the 3-D LUT is meant here as an interpretable baseline, not a model to be optimized in its own right, we did not systematically compare alternative strategies for breakpoint selection—that would be a worthwhile direction for future work. Despite these limitations, the presented framework certainly constitutes a step forward in the characterization and forecasting of auxiliary consumption in grid-scale BESSs.

Author Contributions: Conceptualization, M.M., G.G., and A.D.; methodology, M.M., M.S., and A.D.; software, A.D. and M.S.; validation, M.P.; data curation, M.P.; writing—original draft preparation, A.D. and G.C.; writing—review and editing, M.M. and L.P.; visualization, M.S. and G.C.; supervision, G.G. and L.P.; project administration, G.G. All authors have read and agreed to the published version of the manuscript.

Funding: This research was funded by Eni in the context of the Joint Research Center between Eni and Politecnico di Milano, Prot. Nr. 4310669608—Project BESSence.

Data Availability Statement: Data presented in this paper are available upon request. However, some of the data are commercially sensitive and can only be shared with the approval of Eni S.p.A. Furthermore, they are subject to applicable confidentiality agreements.

Conflicts of Interest: The authors declare that this study received funding from Eni S.p.A. The funder had the following involvement with the study: the collection of data, conceptualization, the writing of this article, and the decision to submit it for publication. Eni S.p.A. owns and operates the utility-scale Battery Energy Storage System installed in Italy discussed in this study.

Abbreviations

The following abbreviations are used in this manuscript:

BAU	Battery Administration Unit
BCU	Battery Cluster Unit
BESS	Battery Energy Storage System
BTMS	Battery Thermal Management System
CDF	Cumulative Distribution Function
EV	Electric Vehicle
HVAC	Heating, Ventilation and Air Conditioning
LFP	Lithium Iron Phosphate
LUT	Look-Up Table
MAE	Mean Absolute Error
OCV	Open-Circuit Voltage
PCS	Power Conversion system
RF	Random Forest
RMSE	Root Mean Squared Error
SoC	State of Charge

References

1. Ueckerdt, F.; Brecha, R.; Luderer, G. Analyzing major challenges of wind and solar variability in power systems. *Renew. Energy* **2015**, *81*, 1–10. [CrossRef]
2. Akdemir, K.Z.; Mongird, K.; Bracken, C.; Burleyson, C.D.; Kern, J.D.; Oikonomou, K.; Thurber, T.B.; Vernon, C.R.; Voisin, N.; Zhao, M.; et al. Evaluating grid stress and reliability in future electricity grids across a range of demand, generation mix, and weather trends. *Adv. Appl. Energy* **2025**, *20*, 100249. [CrossRef]
3. Suyambu, M.R.; Vishwakarma, P.K. Improving grid reliability with grid-scale Battery Energy Storage Systems (BESS). *Int. J. Sci. Res. Arch.* **2024**, *13*, 776–789. [CrossRef]
4. International Energy Agency. World Energy Outlook Special Report Batteries and Secure Energy Transitions. Available online: www.iea.org (accessed on 10 December 2025).
5. Hutchinson, A.J.; Harrison, C.M.; Bryden, T.S.; Alahyari, A.; Hu, Y.; Gladwin, D.T.; Radcliffe, J.; Rogers, D.J.; Patsios, C.; Forsyth, A. A comprehensive review of modeling approaches for grid-connected energy storage technologies. *J. Energy Storage* **2025**, *109*, 115057. [CrossRef]
6. Ledro, M.; Zepter, J.M.; Paludan, M.; Marinelli, M. Electrical modelling of a grid-connected battery energy storage system via EMS and BMS data. *Meas. Energy* **2025**, *6*, 100048. [CrossRef]
7. Moncecchi, M.; Brivio, C.; Mandelli, S.; Merlo, M. Battery energy storage systems in microgrids: Modeling and design criteria. *Energies* **2020**, *13*, 2006. [CrossRef]
8. Gholami, M.; Muyeen, S.M.; Abokhamis Mousavi, S. Optimal sizing of battery energy storage systems and reliability analysis under diverse regulatory frameworks in microgrids. *Energy Strategy Rev.* **2024**, *51*, 101255. [CrossRef]
9. Gatta, F.M.; Geri, A.; Lauria, S.; Maccioni, M.; Palone, F. Battery Energy Storage Efficiency Calculation Including Auxiliary Losses: Technology Comparison and Operating Strategies. In Proceedings of the 2015 IEEE Eindhoven PowerTech, Eindhoven, The Netherlands, 29 June–2 July 2015; pp. 1–6. [CrossRef]
10. Rancilio, G.; Lucas, A.; Kotsakis, E.; Fulli, G.; Merlo, M.; Delfanti, M.; Masera, M. Modeling a large-scale battery energy storage system for power grid application analysis. *Energies* **2019**, *12*, 3312. [CrossRef]
11. Rancilio, G.; Merlo, M.; Lucas, A.; Kotsakis, E.; Delfanti, M. BESS modeling: Investigating the role of auxiliary system consumption in efficiency derating. In *2020 International Symposium on Power Electronics, Electrical Drives, Automation and Motion (SPEEDAM), Online, 24–26 June 2020*; IEEE: Piscataway, NJ, USA, 2020; pp. 189–194. [CrossRef]
12. Rancilio, G.; Rossi, A.; Di Profio, C.; Alborghetti, M.; Galliani, A.; Merlo, M. Grid-scale BESS for ancillary services provision: SoC restoration strategies. *Appl. Sci.* **2020**, *10*, 4121. [CrossRef]
13. Ma, S.; Jiang, M.; Tao, P.; Song, C.; Wu, J.; Wang, J.; Deng, T.; Shang, W. Temperature effect and thermal impact in lithium-ion batteries: A review. *Prog. Nat. Sci. Mater. Int.* **2018**, *28*, 653–666. [CrossRef]
14. Spitthoff, L.; Shearing, P.R.; Burheim, O.S. Temperature, ageing and thermal management of lithium-ion batteries. *Energies* **2021**, *14*, 1248. [CrossRef]
15. Petrelli, M.; Fioriti, D.; Berizzi, A.; Poli, D. Multi-Year Planning of a Rural Microgrid Considering Storage Degradation. *IEEE Trans. Power Syst.* **2021**, *36*, 1459–1469. [CrossRef]
16. Saber, N.; Richter, C.P.; Unnthorsson, R. Review of Thermal Management Techniques for Prismatic Li-Ion Batteries. *Energies* **2025**, *18*, 492. [CrossRef]
17. Mdachi, N.K.; Choong-koo, C. Comparative Review of Thermal Management Systems for BESS. *Batteries* **2024**, *10*, 224. [CrossRef]
18. Kim, G.-H.; Pesaran, A. Battery Thermal Management Design Modeling. *World Electr. Veh. J.* **2007**, *1*, 126–133. [CrossRef]
19. Mądziel, M.; Campisi, T. Predicting Auxiliary Energy Demand in Electric Vehicles Using Physics-Based and Machine Learning Models. *Energies* **2025**, *18*, 6092. [CrossRef]
20. Pulvirenti, B.; Puccetti, G.; Semprini, G. Dynamic Energy Consumption Modeling for HVAC Systems in Electric Vehicles. *Appl. Sci.* **2025**, *15*, 3514. [CrossRef]
21. Cong, L.; Zhou, X.; Li, N.; Zhu, H.; Fan, Y.; Bu, L. Review of Research on System Thermal Inertia Modelling and Optimal Scheduling from the Perspective of Flexible Resources. *J. Phys. Conf. Ser.* **2022**, *2160*, 012051. [CrossRef]
22. Althnian, A.; AlSaeed, D.; Al-Baity, H.; Samha, A.; Dris, A.B.; Alzakari, N.; Abou Elwafa, A.; Kurdi, H. Impact of Dataset Size on Classification Performance: An Empirical Evaluation in the Medical Domain. *Appl. Sci.* **2021**, *11*, 796. [CrossRef]

Disclaimer/Publisher's Note: The statements, opinions and data contained in all publications are solely those of the individual author(s) and contributor(s) and not of MDPI and/or the editor(s). MDPI and/or the editor(s) disclaim responsibility for any injury to people or property resulting from any ideas, methods, instructions or products referred to in the content.

MDPI AG
Grosspeteranlage 5
4052 Basel
Switzerland
Tel.: +41 61 683 77 34

Batteries Editorial Office
E-mail: batteries@mdpi.com
www.mdpi.com/journal/batteries



Disclaimer/Publisher's Note: The title and front matter of this reprint are at the discretion of the Guest Editors. The publisher is not responsible for their content or any associated concerns. The statements, opinions and data contained in all individual articles are solely those of the individual Editors and contributors and not of MDPI. MDPI disclaims responsibility for any injury to people or property resulting from any ideas, methods, instructions or products referred to in the content.





Academic Open
Access Publishing

mdpi.com

ISBN 978-3-7258-8990-7